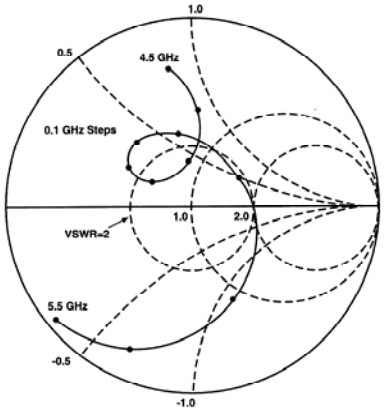

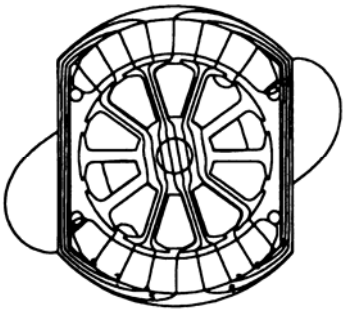

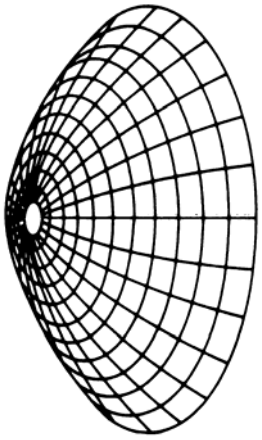

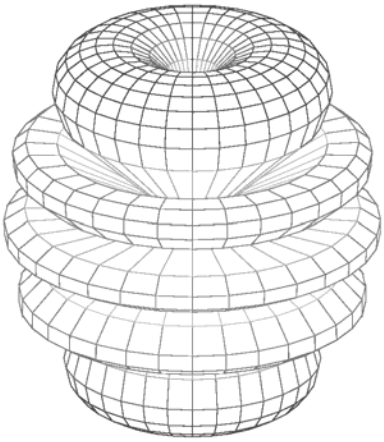

Applied Computational Electromagnetics Society Journal

Editor-in-Chief
Atef Z. Elsherbeni

July 2007
Vol. 22 No. 2
ISSN 1054-4887

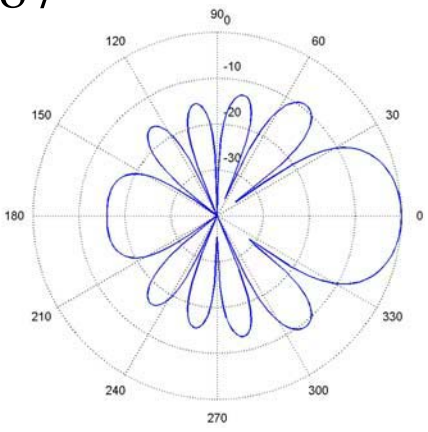

GENERAL PURPOSE AND SCOPE: The Applied Computational Electromagnetics Society ***(ACES)*** Journal hereinafter known as the ***ACES Journal*** is devoted to the exchange of information in computational electromagnetics, to the advancement of the state-of-the art, and the promotion of related technical activities. A primary objective of the information exchange is the elimination of the need to "re-invent the wheel" to solve a previously-solved computational problem in electrical engineering, physics, or related fields of study. The technical activities promoted by this publication include code validation, performance analysis, and input/output standardization; code or technique optimization and error minimization; innovations in solution technique or in data input/output; identification of new applications for electromagnetics modeling codes and techniques; integration of computational electromagnetics techniques with new computer architectures; and correlation of computational parameters with physical mechanisms.

SUBMISSIONS: The ***ACES Journal*** welcomes original, previously unpublished papers, relating to applied computational electromagnetics. Typical papers will represent the computational electromagnetics aspects of research in electrical engineering, physics, or related disciplines. However, papers which represent research in applied computational electromagnetics itself are equally acceptable.

Manuscripts are to be submitted through the upload system of ***ACES*** web site http://aces.ee.olemiss.edu See "Information for Authors" on inside of back cover and at ***ACES*** web site. For additional information contact the Editor-in-Chief:

Dr. Atef Elsherbeni
Department of Electrical Engineering
The University of Mississippi
University, MS 386377 USA
Phone: 662-915-5382 Fax: 662-915-7231
Email: atef@olemis.edu

SUBSCRIPTIONS: All members of the Applied Computational Electromagnetics Society who have paid their subscription fees are entitled to receive the ***ACES Journal*** with a minimum of three issues per calendar year and are entitled to download any published journal article available at http://aces.ee.olemiss.edu.

Back issues, when available, are $15 each. Subscriptions to ***ACES*** is through the web site. Orders for back issues of the ***ACES Journal*** and changes of addresses should be sent directly to ***ACES*** Executive Officer:

Dr. Richard W. Adler
ECE Department, Code ECAB
Naval Postgraduate School
833 Dyer Road, Room 437
Monterey, CA 93943-5121 USA
Fax: 831-649-0300
Email: *rwa@attglobal.net*

Allow four week's advance notice for change of address. Claims for missing issues will not be honored because of insufficient notice or address change or loss in mail unless the Executive Officer is notified within 60 days for USA and Canadian subscribers or 90 days for subscribers in other countries, from the last day of the month of publication. For information regarding reprints of individual papers or other materials, see "Information for Authors".

LIABILITY. Neither ***ACES***, nor the ***ACES Journal*** editors, are responsible for any consequence of misinformation or claims, express or implied, in any published material in an ***ACES Journal*** issue. This also applies to advertising, for which only camera-ready copies are accepted. Authors are responsible for information contained in their papers. If any material submitted for publication includes material which has already been published elsewhere, it is the author's responsibility to obtain written permission to reproduce such material.

APPLIED COMPUTATIONAL ELECTROMAGNETICS SOCIETY JOURNAL

Editor-in-Chief
Atef Z. Elsherbeni

July 2007
Vol. 22 No. 2
ISSN 1054-4887

The ACES Journal is abstracted in INSPEC, in Engineering Index, DTIC, Science Citation Index Expanded, the Research Alert, and to Current Contents/Engineering, Computing & Technology.

The first, fourth, and sixth illustrations on the front cover have been obtained from the Department of Electrical Engineering at the University of Mississippi.

The third and fifth illustrations on the front cover have been obtained from Lawrence Livermore National Laboratory.

The second illustration on the front cover has been obtained from FLUX2D software, CEDRAT S.S. France, MAGSOFT Corporation, New York.

THE APPLIED COMPUTATIONAL ELECTROMAGNETICS SOCIETY

JOURNAL

Vol. 22 No. 2 July 2007

TABLE OF CONTENTS

Numerical Examinations of the Stability of FDTD Subgridding Schemes

Shumin Wang

Laboratory of Functional and Molecular Imaging, National Institute of Neurological Disorders and Stroke, National Institutes of Health
10 Center Dr., 10/B1D728, Bethesda, MD 20892, U. S. A.
E-mail: james.wang@ieee.org

Abstract **–** The stability of two-dimensional Finite-Difference Time-Domain subgridding schemes was numerically examined. Both the same-time-step and the multiple-time-step schemes were considered. Results show that the multiple-time-step subgridding scheme is late-time unstable due to larger-than-unity eigenvalues. As to the same-time-step subgridding schemes, stability is related to the treatment of corner regions.

Keywords **–** FDTD method, subgridding, stability.

I. INTRODUCTION

Since the Finite-Difference Time-Domain (FDTD) method was introduced [1],[2], a major challenge is modeling locally fine structures and/or field singularities. To model fine features or resolve rapid field variations, small cells are required and the overall computational cost can be prohibitive by using the traditional FDTD method.

One attractive solution is subgridding, i.e., fine meshes are employed wherever needed and the rest of the computational domain is discretized by coarse meshes. The early version of subgridding applies the FDTD method twice in different regions, where the results in coarse region are used as boundary conditions for fine regions [3]. Due to the lack of timely feedback from fine regions, this approach only yields better results in fine regions. To improve the accuracy, fine regions are embedded into coarse regions and the timely feedback is provided by field coupling on boundaries [4]. In this scheme, two methods are possible to accommodate the stability requirement imposed by fine region cell size. One is to use the same time step (STS) size, which is dictated by the fine region cell size, in both regions. The other is to use different time step sizes determined by coarse and fine region cell sizes respectively. Thus one time step in coarse region corresponds to multiple time steps (MTS) in fine region. Accordingly, temporal interpolation is required for field coupling on the boundaries.

Despite the various accuracy-enhancement procedures [5]-[8], FDTD subgridding methods are notorious for their late-time instability, which typically happens after many iterations. To address this issue, spatial reciprocity on coarse-fine region boundaries has proposed as a necessary condition to achieve late-time stability [9]. However, its effectiveness remains unclear. In this paper, we provide numerical examinations of its sufficiency for both the STS and the MTS subgridding schemes.

The dominant eigenvalues of the system amplification matrices are examined as a key measure of stability. Meanwhile, corresponding numerical simulations are carried out for sufficient time steps to check the actual late-time behavior. For simplicity, 2D *TEz* wave was examined. The subgridding refinement ratio is 3:1. The odd ratio results in collocated coarse-fine region boundary values in space and in time. For other subgridding ratios, the analysis follows the same procedure. We note that the main purpose of this paper is to provide first-hand numerical examinations. Theoretical explanations are given tentatively based on known theories.

This paper is organized as follows. Section II presents the methodology and describes the numerical tests. Section III verifies the approach by the regular FDTD scheme. Sections IV and V show the results of the STS and the MTS schemes, respectively. Finally, conclusion remarks are drawn in section VI.

II. METHODOLOGY

The stability of FDTD subgridding schemes was first studied by the dominant eigenvalues of the system amplification matrices [2]. In the discretized Maxwell's equations

$$\begin{pmatrix} \vec{E}^{\,n} \\ \vec{H}^{\,n+1/2} \end{pmatrix} = [A] \cdot \begin{pmatrix} \vec{E}^{\,n-1} \\ \vec{H}^{\,n-1/2} \end{pmatrix}, \tag{1}$$

[A] denotes the system amplification matrix. To verify the late-time behavior, simulations were carried out inside Perfect Electric Conducting (PEC) boxes of various sizes. A magnetic point source near the lower-left corner was excited and the electric field at another location was monitored at each time step. The source is a differentiated Gaussian pulse and its peak

magnitude is less than one. Therefore, the observed electrical field magnitude should not be larger than one in a stable simulation. Whenever the above condition is violated, we claim that a simulation is unstable and that time step is recorded as the "critical point". Otherwise, the most recent observations were checked after ten million time steps. If they do not show any sign of growth, a scheme is claimed as numerically stable.

The fine region is placed at the center of the computational domain, which is denoted by $m \times n$, where m is the distance from the fine region boundary to the outer boundary of the entire computational domain and n the size of the fine region, both are in terms of the coarse region cell size.

We note that the maximum possible value at the observation is different with respect to different computational domain sizes. The "critical point" only indicates instability and its value should not be interpreted in the same way for different computational domains. Due of limited resources, we only considered small computational domains. However, stability is usually characterized asymptotically by assuming an infinitely large one. To examine the differences and verify our approach, we first study the regular FDTD method.

III. THE REGULAR FDTD METHOD

Figure 1 shows the dominant eigenvalues of the system amplification matrix of the regular FDTD method as a function of the Courant-Friedrichs-Levy (CFL) number, which is defined by $\Delta t\sqrt{2}v_p / \Delta h$. Here, v_p is the phase velocity, Δh is the cell size and Δt is the time-step size. The computational domain size is denoted by $m \times n$ in terms of cells, where m represents the length and n represents the width.

It is interesting to notice that simulations of very small computational domains can be stable even with a larger than one CFL number. For a 3 × 3 PEC box, the largest stable CFL number reaches to 1.15 (the CFL numbers are resolved to 0.01 in this article). As the computational domain size increases, the largest stable CFL number drops rapidly and becomes one when the computational domain size is equal to or larger than 12 × 12. These results were confirmed by simulations.

The above observations can be understood by the asymptotic nature of theoretical stability analysis, which only considers the worst case in the Von Neumman analysis [2]. It is well known that the time step size of 2D FDTD simulations is restricted by

$$\Delta t \le \frac{h}{v_p\sqrt{\sin^2\left(\frac{k_x h}{2}\right)+\sin^2\left(\frac{k_y h}{2}\right)}} \tag{2}$$

where k_x and k_y are associated with the discrete Fourier modes [10] and the worst case is $k_x h = k_y h = (2n+1)\pi$. In an infinitely large computational domain, there are infinite Fourier modes including the above worst case. When the computational domain size is limited, the discrete Fourier modes that can possibly exist are limited and they may not include the worst case. The stability condition determined directly by the dominant eigenvalues of small computational domains can be different from that of the Von Neumman analysis. Therefore, multiple tests with increasing computational domain sizes are suggested to estimate the asymptotic behavior of numerical stability.

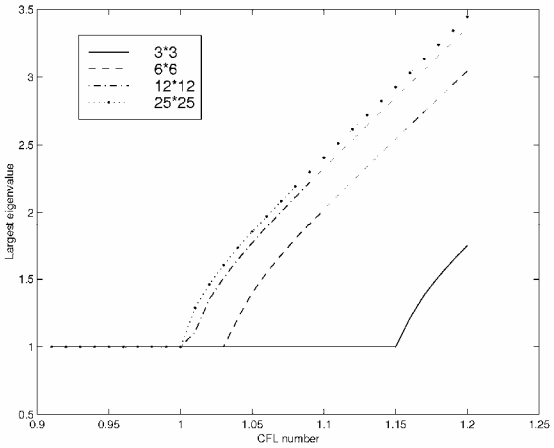

Fig. 1. Dominant eigenvalues of the system amplification matrix of the regular 2D FDTD method according to different CFL numbers and computational domain sizes.

IV. THE STS SUBGRIDDING SCHEME

In general, we can write the STS scheme as

$$\begin{pmatrix} \vec{U}^{\,n+1/2} \\ \vec{u}^{\,n+1/2} \end{pmatrix} = \begin{pmatrix} A_{CC} & A_{CF} \\ A_{FC} & A_{FF} \end{pmatrix} \cdot \begin{pmatrix} \vec{U}^{\,n-1/2} \\ \vec{u}^{\,n-1/2} \end{pmatrix} \tag{3}$$

where $\vec{U}^{\,n+1/2}$ contains all coarse region unknowns and $\vec{u}^{\,n+1/2}$ contains all fine region unknowns, both at the current time step. A_{CC} represents how the coarse region uses the previous coarse region values, A_{CF} represents how the coarse region uses the previous fine region values, A_{FC} represents how the fine region uses the previous coarse region values and A_{FF} represents how the fine region uses the previous fine region values.

Figures 2 and 3 depict a regular coarse-fine region boundary and a corner region respectively. In order to calculate the fine region boundary electric field, e.g. e_{y1}, we need the coarse region magnetic field, e.g. h'_{z1}. To

recover the missing values due to boundary truncation, the following linear interpolation is employed [8],

$$h'_{z1} = \frac{2}{3}H_{z1} + \frac{1}{3}H_{z2} \ , \tag{4}$$

$$h'_{z2} = \frac{1}{3}H_{z1} + \frac{2}{3}H_{z2} \ , \tag{5}$$

$$h'_{z3} = H_{z2} . \tag{6}$$

Instead of being half-cell away from the boundary electric field, the recovered magnetic field is 1.5-cell away. To keep at least first-order accuracy in space, we employed the unbalanced differencing scheme to update the boundary electric field, e.g.,

$$e^{n}_{y1} = e^{n-1}_{y1} + \frac{\Delta t}{2\Delta h\varepsilon}\left(h'^{\,n-1/2}_{z1} - h^{n-1/2}_{z1}\right) \tag{7}$$

where Δh is the fine region cell size. When calculating the coarse region boundary magnetic field, e.g. H_{z2}, we need the electric field along the coarse-fine region boundary, e.g. E_{y2}. They are obtained by enforcing spatial reciprocity [9], i.e.,

$$E_{y2} = \frac{1}{3}\left[\frac{1}{3}\left(e_{y1} + e_{y5}\right) + \frac{2}{3}\left(e_{y2} + e_{y4}\right) + e_{y3}\right]. \tag{8}$$

Note that the coarse region boundary magnetic field is calculated by central differencing scheme in the layout shown in Fig. 2. Another choice is to extend the fine region 1/3 coarse cell (or one fine cell) to the left, i.e., overlapping the coarse and fine regions by one fine cell. In that case, the coarse region boundary magnetic field is calculated by unbalanced differencing and the fine region boundary electric field is calculated by central differencing. Since unbalanced differencing scheme is first-order accurate, choosing fine region boundary electric field to be calculated by unbalanced differencing scheme is apparently more accurate.

As we shall see, the real difficulty is to treat corners, e.g., h'_{z1} and in h''_{z1} Fig. 3, by imposing spatial reciprocity. If we write

$$h'_{z1} = \frac{2}{3}H_{z1} + \frac{1}{3}H_{z3}, h''_{z1} = \frac{2}{3}H_{z2} + \frac{1}{3}H_{z3}, \tag{9}$$

the coarse region boundary electrical field can be obtained by spatial reciprocity as,

$$E_{x3} = E_{x3} + \frac{1}{9}e_{x1}, E_{y3} = E_{y3} + \frac{1}{9}e_{y1} . \tag{10}$$

This apparently introduces errors when calculating H_{z3} (also H_{z1} and in H_{z2}). To improve the accuracy, other corner layouts can be applied by shifting the fine region boundary field components and violating the reciprocity. Since spatial reciprocity is our major concern, we employ the layout shown in Fig. 3 and refer to it as "reciprocal with corner" treatment.

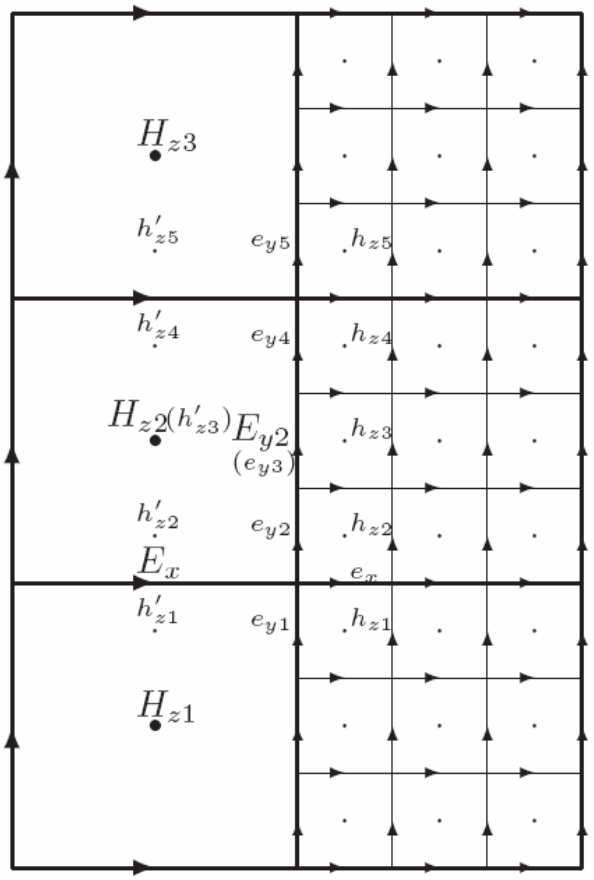

Fig. 2. The coarse-fine region boundary.

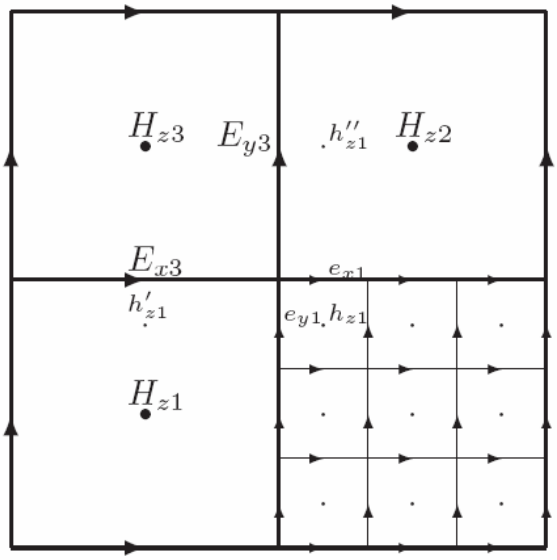

Fig. 3. The coarse-fine region boundary at a corner.

Alternatively, one may simply ignore corners and write

$$h'_{z1} = H_{z1}, h''_{z1} = H_{z2} . \tag{11}$$

This can be physically interpreted as treating H_{z1} and H_{z2} as the average in those cells. In the following, we refer to

this as "reciprocal without corner" treatment.

A. Reciprocal with Corner

An example of the system amplification matrix is illustrated in Fig. 4, which corresponds to a "3 × 3" subgridding region. The dominant eigenvalue of this example is 1.420754 when the CFL number is 1.03. As we decrease the CFL number, the dominant eigenvalue drops quickly and becomes 1.0 when the CFL number is 1.01. We further calculated the dominant eigenvalues of subgridding schemes with larger computational domain sizes (up to "10 × 10"). It was found that the results are all 1.0 when the CFL number is 1.0.

Although the dominant eigenvalues do not show any sign of instability for CFL=1, numerical simulations were unstable for all computational domains being tested. Moreover, the instability does not happen late. For example, the "3 × 3" case became unstable after 360 time steps. The "9 ×10" case is the most stable one, which only runs stably for 3689 time steps. This example shows that enforcing spatial reciprocity on coarse-fine region boundaries is not a sufficient condition for stability in general.

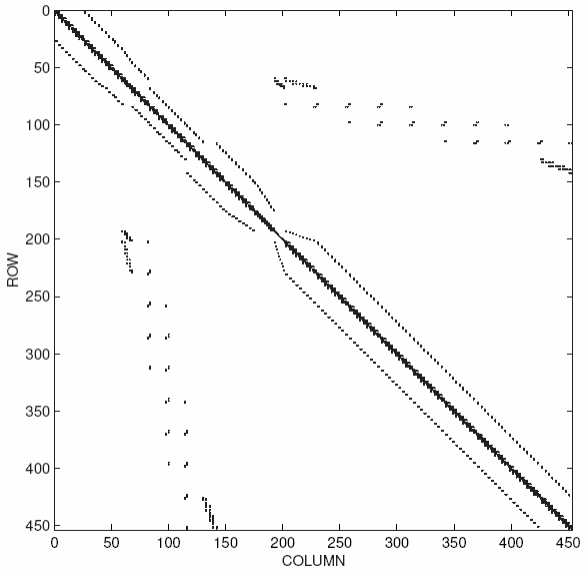

Fig. 4. An example of the system amplification matrix of the "reciprocal with corner" treatment.

B. Reciprocal without Corner

The same set of subgridding layout was examined. The system amplification matrices look similar to Fig. 4. The dominant eigenvalue of the "3 × 3" case is 1.420752 when the CFL number is 1.03. As we decrease the CFL number, the dominant eigenvalue drops quickly and becomes 1.0 when the CFL number is 1.01. For subgridding schemes with larger computational domain sizes (up to "10 ×10") the dominant eigenvalues are all 1.0 when the CFL numbers are 1.0.

Contrary to the previous case, numerical simulations were stable with ten million time steps for all computational domains being tested.

V. THE MTS SUBGRIDDING SCHEME

The major difference between the STS and the MTS subgridding schemes is the timing procedure involved in the latter case. Figure 5 illustrates the case where one coarse-region time-step corresponds to three fine-region time-steps. When calculating e^n and $e^{n+1/3}$ in fine region, we need $H^{n-1/6}$ and $H^{n+1/6}$ in coarse region for spatial interpolation. Also, when calculating $H^{n+1/2}$ by imposing reciprocity, we need e^n in fine region. These two requirements make accurate temporal interpolation, i.e., obtaining $H^{n-1/6}$ and $H^{n+1/6}$ by $H^{n-1/2}$ and $H^{n+1/2}$, difficult to implement if special reciprocity has to be enforced. One solution is to use temporal extrapolation, i.e., obtaining $H^{n-1/6}$ and $H^{n+1/6}$ by $H^{n-1/2}$ and $H^{n-3/2}$, etc. Alternatively, one may also use $H^{n-1/2}$ for $H^{n-1/6}$ and $H^{n+1/6}$ [9], which is frequently referred to as Zeroth Order Hold (ZOH) in digital signal processing [11]. ZOH inevitably introduces spectrum distortion to input signals. However, we chose ZOH because temporal extrapolation is more prone to instability in practice.

The implementation of the above timing procedure results in the following set of equations,

$$\vec{u}^{\,n-1/6} = A_{FF}\vec{u}^{\,n-1/2} + A_{FC}\vec{U}^{\,n-1/2}, \tag{12}$$

$$\vec{u}^{\,n+1/6} = A_{FF}^2\vec{u}^{\,n-1/2} + \left(A_{FF}+1\right)\cdot A_{FC}\vec{U}^{\,n-1/2}, \tag{13}$$

$$\vec{u}^{\,n+1/2} = A_{FF}^3\vec{u}^{\,n-1/2} + \left(A_{FF}^2 + A_{FF}+1\right)\cdot A_{FC}\vec{U}^{\,n-1/2}, \tag{14}$$

$$\begin{aligned}\vec{U}^{\,n+1/2} &= A_{CC}\vec{U}^{\,n-1/2} + A_{CF}\vec{u}^{\,n-1/6} \\ &= \left(A_{CC} + A_{CF}\cdot A_{FC}\right)\vec{U}^{\,n-1/2} \\ &\quad + A_{CF}\cdot A_{FF}\vec{u}^{\,n-1/2}\end{aligned} \tag{15}$$

where all symbols have the same meaning as in equation (3). Accordingly, the system amplification matrix is written as

$$A = \begin{bmatrix} A_{CC} + A_{CF}\cdot A_{FC} & A_{CF}\cdot A_{FF} \\ \left(A_{FF}^2 + A_{FF}+1\right)\cdot A_{FC} & A_{FF}^3 \end{bmatrix}. \tag{16}$$

Figure 6 illustrates the amplification matrix of the "3 × 3" case. Figure 7 shows the dominant eigenvalues vs. the CFL numbers for different sizes of computational domain and subgridding region. As we see, the dominant eigenvalues are always larger than 1.0 regardless of the CFL number. As the size of computational domain increases, the dominant eigenvalue for a given CFL

number decreases but never reaches 1.0. Numerical simulations further verified the above results, where the recorded "critical points" are shown in Fig. 8. These results correspond to the dominant eigenvalues in Fig. 7 well.

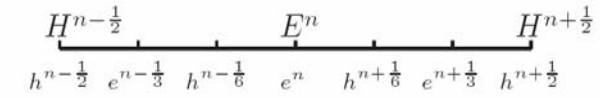

Fig. 5. Timing of the MTS subgridding scheme, where superscripts denote the time-step.

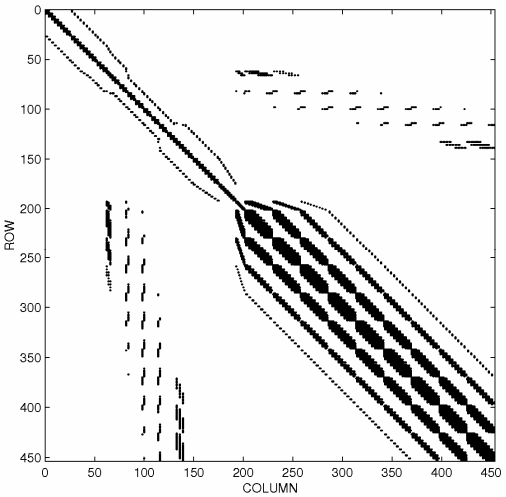

Fig. 6. An example of the system amplification matrix of the MTS subgridding scheme.

The MTS scheme is more efficient than the STS scheme. As demonstrated in Fig. 7, the dominant eigenvalues decrease with either an increasing computational domain size or a decreasing CFL number. Thus in practice, one may delay the late-time instability by either decreasing the CFL number or by increasing the computational domain size.

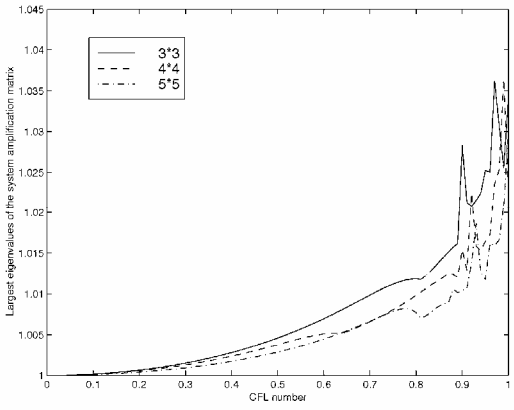

Fig. 7. Dominant eigenvalues of the MTS subgridding scheme.

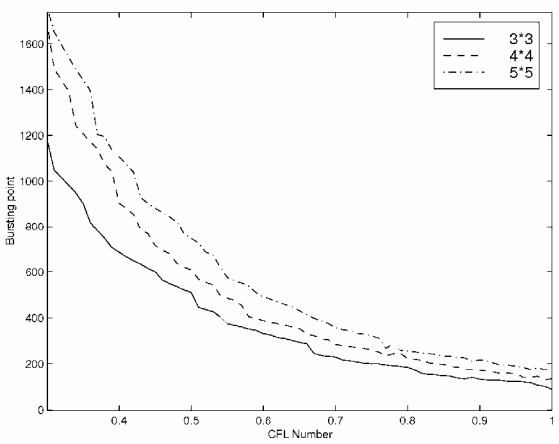

Fig. 8. "Critical points" of the MTS subgridding scheme with different computational domain sizes and different CFL numbers.

VI. CONCLUSIONS

We numerically examined the stability of both the STS and the MTS FDTD subgridding schemes. For the STS schemes, it was shown that enforcing spatial reciprocity does not guarantee stability in general, especially when corners must be handled in a reciprocal manner. As to the MTS subgridding schemes, the system is unstable due to eigenvalues that are out of the unit circle. Some practical considerations were also given with regard to the use of FDTD subgridding schemes. Future work involves developing stable FDTD subgridding schemes.

REFERENCES

[1] K. S. Yee, "Numerical solution of initial boundary value problems involving Maxwell's equation in isotropic media," *IEEE Trans. Antennas Propag*., vol. 14, no. 3, pp. 302-307, 1966.

[2] A. Taflove *Advances in computational electrodynamics: the finite-difference time-domain method*, Artech: Boston.

[3] K. S. Kunz and L. Simpson, "A technique for increasing the resolution of finite-difference solution of the Maxwell equation," *IEEE Trans. Electromagn. Compat*., vol. 23, no. 4, pp.419-422, 1981.

[4] I. S. Kim and W. J. R. Hoefer *A local mesh refinement for the time-domain finite-difference method using Maxwell's curl equations*, IEEE Trans. Microwave Theory Tech. 1990; 38(6):812-815.

[5] S. S. Zivanovic, K. S. Yee, and K. K. Mei, "A subgridding method for the time-domain finite-difference method to solve Maxwell's equations," *IEEE Trans. Microwave Theory Tech*.,

vol. 39, no. 3, pp. 471-479, 1991.

[6] M. Okoniewski, E. Okoniewski, and M. A. Stuchly, "Three-dimensional subgridding algorithm for FDTD," *IEEE Trans. Antennas Propag.*, vol. 45, no. 3, pp. 422-429, 1997.

[7] M. W. Chevalier, R. J. Luebbers, and V. P. Cable, "FDTD local grid with material transverse," *IEEE Trans. Antennas Propag*., vol. 45, no. 3, pp. 411-421, 1997.

[8] S. Wang, F. L. Teixeira, R. Lee, and J-F. Lee, "Optimization of subgridding schemes for FDTD," *IEEE Microwave and Wireless Components Lett*., vol. 12, no. 6, pp. 223-225, 2002.

[9] P. Thoma and T. Weiland, "A consistent subgridding scheme for the finite difference time domain method," *International Journal of Numerical Modeling: Electronic Network, Devices and Fields*, vol. 9, no. 5, pp. 359-374, 1996.

[10] J. W. Thomas *Numerical Partial Differential Equations: Finite Difference Methods*. Springer Verlag: New York.

[11] B. Porat *A course in digital signal processing*. John Wiley & Sons: New York.

Shumin Wang received the B.S. degree in physics from Qingdao University, and the M.S. degree in electronics from Peking University, China, in 1995 and 1998, respectively, and the Ph.D. degree in electrical engineering from The Ohio State University, Columbus, Ohio, in 2003. He is a Staff Scientist at the National Institutes of Health, Bethesda, Maryland. His research interests include time-domain differential equation based methods, integral equation methods, high frequency asymptotic methods and their applications to bio-medical and electromagnetic scattering problems.

Parallel ICCG Solvers for a Finite-Element Eddy-Current Analysis on Heterogeneous Parallel Computation Environment

T. Iwashita[1], M. Shimasaki[2], and J. Lu[3]

[1]Academic Center for Computing and Media Studies, Kyoto University, Japan

[2]Graduate School of Engineering, Kyoto University, Japan

[3]School of Microelectronic Engineering, Griffith University, Australia

iwashita@media.kyoto-u.ac.jp, simasaki@kuee.kyoto-u.ac.jp, J.Lu@griffith.edu.au

Abstract – This paper investigates fast electromagnetic field analysis on parallel computers mutually integrated by means of Grid computing technology. To utilize the heterogeneous parallel computation environment, we introduce four parallelized ICCG solvers: the block ICCG, load-balanced block ICCG, algebraic block red-black ordering, and recursive reordering methods. These solvers are evaluated in a finite edge-element eddy-current analysis on integrated parallel computers.

I. INTRODUCTION

Grid computing technology is one of the latest and most important technologies in the area of high-performance computing (see, e.g., [1]). The technology provides various functions related to computing, some of which have the possibility to significantly impact electromagnetic field computations. For example, access to non-limited computer resources enables much larger-scale numerical electromagnetic field simulation to be performed than with conventional analysis.

This paper investigates efficient utilization of heterogeneous parallel computation environments, which involve multiple parallel computers, on a finite-element electromagnetic field analysis. These computational environments are fundamental parts of the Grid computing technique. Here, we use the Globus toolkit that is a standard middleware for Grid computing and the MPICH-G communication library [2], [3]. These two tools provide us with easy access to the integrated multi-computer environment, in which standard MPI-based programs can be run. In this paper, we focus on a solution of a linear system of equations in a finite-element analysis, which is the most time-consuming part in whole FEM-based analysis.

This paper examines four parallelized ICCG (Incomplete Cholesky Conjugate Gradient) [4] solvers in a heterogeneous parallel computation environment. The ICCG method is the most popular solver for a linear system of equations arising in electromagnetic field analyses. While there are several parallelization ways of the ICCG method [5], [6], we focus on four techniques that have an advantage in communication cost. For example, the multi-color ordering method [7] that is one of conventional parallel ICCG methods needs much communication between processors. The first solver is the block ICCG method [8], which is based on localized incomplete factorization, and has the advantage of no communications in parallelized substitutions. The second solver is the load-balanced block ICCG method, in which a load-balancing technique is applied to the block ICCG method. The third solver is the algebraic block red-black ordering method [9], which has a superior convergence rate. The forth solver is the newly presented recursive reordering method. In this technique, in order to utilize both site-by-site and processor-by-processor parallelisms in integrated multi parallel computers, reordering techniques are recursively applied. While there are many variations in choosing reordering methods, we use algebraic block red-black ordering and multi-color ordering. This paper investigates parallel performance of these solvers in a multi parallel computer environment.

II. PARALLEL ICCG SOLVERS

The present paper solves a linear system of equations having a positive or semi-positive definite symmetric coefficient matrix arising in finite element electromagnetic field analyses. To efficiently utilize the Grid computing environment, we use four parallel ICCG solvers for solving this linear system: 1) Block ICCG method, 2) Load-balanced block ICCG method, 3) Algebraic block red-black ordering method, 4) Recursive reordering method. We briefly describe the procedure for each solver, while paying special attention to parallel processing of forward and backward substitutions. Other kernels of the ICCG method are easily parallelized.

A. Block ICCG Method

The block ICCG method is a well-known parallelization

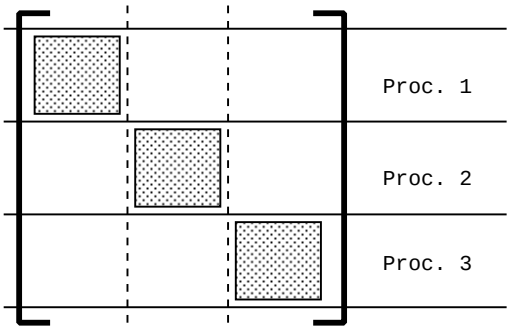

Fig. 1. Preconditioning matrix in block ICCG method (3 Processors).

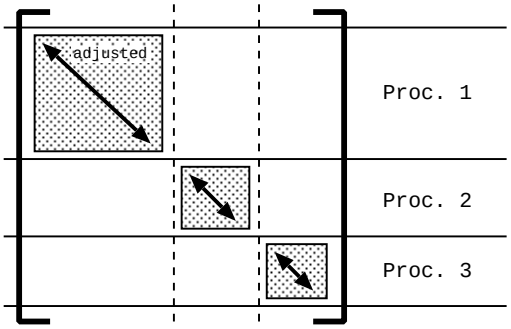

Fig. 2. Preconditioning matrix in load-balanced block ICCG method (3 Processors).

technique for incomplete Cholesky factorization preconditioning. The global matrix is divided into multiple parts that are distributed into processors. Since matrix entries between different processors are ignored in incomplete factorization, its preconditioning matrix can be treated in parallel among processors. Figure 1 shows the form of a preconditioning matrix in the block ICCG method. Forward and backward substitutions are performed in parallel without communications. Therefore, this method has an advantage in its communication cost, and is suitable for parallel computation environments based on lower grade network systems. However, the block ICCG method often suffers from a decline in convergence rate due to ignored matrix entries.

B. Load-Balanced Block ICCG Method

The load-balanced block ICCG method is the enhanced version of the block ICCG method. In a heterogeneous parallel computation environment, load-balancing often plays a key role. While there are several load-balancing techniques, our implementation method is: first, we execute a few iterations of the normal block ICCG method to obtain information about the computation environment. While we can use processor information obtained via Globus functions, we use performance data based on the actual execution. This is mainly because finite element electromagnetic field analysis is generally too complex to predict its computational time using limited information about processors. Next, the computational efforts on each processor are balanced by means of this performance information. The size of the block assigned to each processor is adjusted to the processor performance. Finally, block incomplete factorization is performed on each processor in parallel. Forward and backward substitutions are also parallelized in the same way as the block ICCG method. Fig. 2 depicts a preconditioning matrix in the load-balanced block ICCG method.

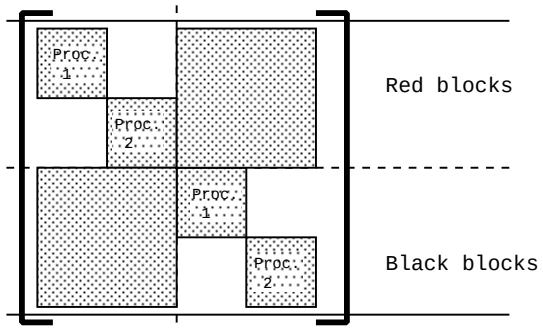

Fig. 3. Coefficient matrix in algebraic block red-black ordering method.

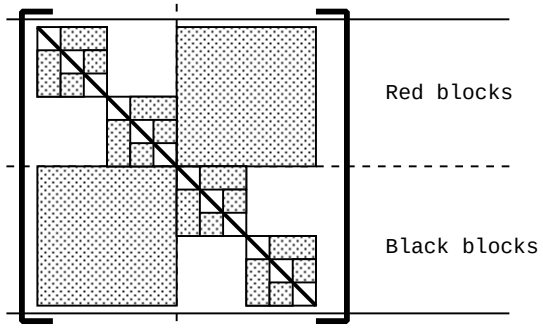

Fig. 4. Coefficient matrix in recursive reordering method.

C. Algebraic Block Red-Black Ordering Method

Reordering (parallel ordering) technique is one of the most popular techniques for parallel processing of the ICCG method. The algebraic block red-black ordering method, which is a relatively new technique, was proposed in [9]. In this method, a set of unknowns are divided into multiple groups (blocks). A well-known red-black ordering scheme is applied to the blocks. This method has two major advantages. The first advantage is

in its high convergence rate, which is generally higher than the block ICCG method, especially when the number of processors is increased. The second advantage is the low communication cost. In this method, only one synchronization point exists in parallelized forward (or backward) substitution. Although its communication cost is larger than the one of the block ICCG method that requires no communication in substitution, it is smaller than other reordering techniques, for example, multi-color ordering. Figure 3 shows a sample of reordered matrix based on algebraic block red-black ordering.

D. Recursive Reordering Method

In a Grid computing environment, the distance between computers is often significantly large. When multiple parallel computers far from each other collaborate with an analysis, the external computer-to-computer network has a large performance degradation compared with an internal network among processors in each parallel computer. The recursive reordering method is proposed for this computation environment. First, we reorder the coefficient matrix in order to distribute data and computations to each site. In this first reordering, the parallel ordering method that has an advantage in its communication cost is preferable. Next, in each parallel computer, another reordering technique is recursively applied to the distributed part of the coefficient matrix. The parallel ordering method that has fast convergence is appropriate to the second reordering technique. In our analysis, we use algebraic block red-black ordering and multi-color ordering for the first and the second reordering techniques, respectively. Figure 4 depicts the reordered matrix in the recursive reordering technique. In the implementation of the method, a hybrid programming tool is required; in the present analysis we use Open MP API (application programming interface) for internal parallel processing in each site, while the MPICH-G library is used for communications between different sites.

III. RESULTS

A. Test Model and Computation Environment

In the present analysis, we use the IEEJ standard benchmark model of 3-D eddy current analyses [10]. The analyzed model is discretized by first-order brick-type edge elements. Table I lists the discretization data. The electromagnetic field equations are solved by using the Galerkin method with *A*-formulation and the backward time difference method. The generated linear system of equations is solved by means of the shifted ICCG method.

The present analyses were implemented on two parallel computers connected via a Giga-bit local area network (see Fig. 5). Both computers are SMP-type parallel computers based on SPARC-compatible processors. First one is a Fujitsu HPC2500, and its peak performance is 5.2 GFlops per processor element. The second is a Fujitsu GP7000F model 900, and its peak performance is 1.2 GFlops per processor element. We used Globus 2.0 for the GRID computing middleware and MPICH-G 1.2.4 for MPI communications between the parallel computers. The parallelized program code is written by using FORTRAN and MPI. In the implementation of the recursive reordering method, we also use Open MP. The convergence criterion of the ICCG method is given by $||\boldsymbol{r}||_2/||\boldsymbol{b}||_2 < 10^{-7}$, where $\boldsymbol{r}$ and $\boldsymbol{b}$ are the residual vector and the right-hand side vector of the linear system, respectively.

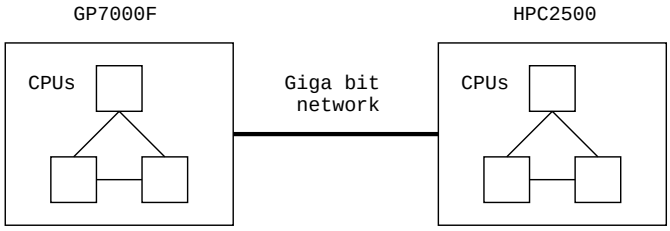

Fig. 5. Computation environment.

Table I. Discretization data.

Number of volume elements	327680
Number of nodes	342225
Number of unknowns	1011920
Time step	1 msec

B. Parallel Performance

Tables II-V list the number of iteration and the elapsed time in the four solvers. In the case of the block ICCG method, the elapsed time is reduced by increasing the number of processors. It is also indicated that the effect of the faster processor (HPC2500) is more significant than that of the processor of the GP7000. This result is caused not only by the performance difference between processors but also by the difference of the internal network performance. In the block ICCG method, the number of iterations is affected by the total number of processors. Table II shows that an increased number of processors leads to a decline in convergence. Accordingly, when more processors are used, the method may suffer from further convergence deterioration.

The results of the load-balanced block ICCG method are examined next. Table VI lists the elapsed time in one iteration of the block ICCG method and the load-balanced block ICCG method. It is shown that the load-balancing technique effectively reduces computational time in all

cases. However, in Table III, the load-balanced block ICCG method does not always obtain a better result than the normal block ICCG method. This is due to a side-effect of the convergence rate of the load-balancing technique. Since the block size assigned to a processor is dynamically changed, the preconditioning effect, i.e., the number of iterations may change in each execution of an analysis. While the side-effect also has the possibility of improving convergence, it does however cause a decline in convergence in the present analysis. Since the side-effect depends on the problem to solve, it should be examined before any given production run.

Next, we examine the results of the algebraic block red-black ordering method. Table IV indicates that the algebraic block red-black ordering technique has a better convergence rate than the block ICCG method. This superior convergence has been reported in [9]. However, it is shown that the elapsed time of the present method is longer than that of the block ICCG method. This is due to overheads of the communications between the two computers. Accordingly, the algebraic block red-black ordering method suffers from a trade-off problem between convergence and time of the present method is longer than that of the block ICCG method. This is due to overheads of the communications between the two computers. Accordingly, the algebraic block red-black ordering method suffers from a trade-off problem between convergence and communication cost in a Grid computing environment.

Finally, we examine the results of the recursive reordering technique. In the present analysis, we used 100-color ordering for the secondary reordering technique. An advantage of this method is that the number of iterations does not depend on the total number of processors. However, Table V indicates that the recursive reordering method cannot obtain a satisfactory solver performance. This is mainly due to an overhead of multi-thread parallel computation, which is a synchronization cost among processors. In particular, since the GP7000F computer is not equipped with a hardware barrier function, the synchronization cost is large, which results in the deterioration of the total solver performance. In future, when the synchronization function has been improved, this method is expected to obtain a far better solver performance.

In the present analysis, the block ICCG method, in most cases, showed the best performance among the four solvers. This result implies that communication cost is often more significant than convergence in electromagnetic field analyses in a Grid computing environment. On the other hand, the numerical results indicate that the load-balancing technique is effective for reducing computational time of one iteration. The load-balanced block ICCG method obtained the best solver performance among all cases when one GP7000F processor and three HPC2500 processors were used. However, the load-balancing technique has the possibility

Table II. Results of block ICCG method.

# of CPUs on GP7000	# of CPUs on HPC2500	Number of iterations	Elapsed time (sec)
1	1	468	1160
1	2	515	997
1	3	525	825
2	1	515	912
2	2	526	808
2	3	554	787
3	1	525	1080
3	2	553	1203
3	3	545	753

Table III. Results of load-balanced block ICCG method.

# of CPUs on GP7000	# of CPUs on HPC2500	Number of iterations	Elapsed time (sec)
1	1	656	1088
1	2	520	651
1	3	563	610
2	1	672	995
2	2	723	878
2	3	724	797
3	1	783	1177
3	2	853	1357
3	3	740	904

Table IV. Results of algebraic block red-black ordering method.

# of CPUs on GP7000	# of CPUs on HPC2500	Number of iterations	Elapsed time (sec)
1	1	378	1515
1	2	374	1214
1	3	383	1215
2	1	375	1356
2	2	383	1205
2	3	405	1237
3	1	383	1324
3	2	405	1323
3	3	391	1233

of suffering the side-effect of deterioration of convergence. The algebraic block red-black ordering method and the recursive ordering method do not attain better solver performances than the block ICCG method due to their higher communication costs. Since both methods have the advantage of high convergence rates, further development of network technology may improve their solver performances.

Table V. Results of recursive reordering method.

# of CPUs on GP7000	# of CPUs on HPC2500	Number of iterations	Elapsed time (sec)
1	1	504	2792
1	2	504	2757
1	3	504	2752
2	1	504	2330
2	2	504	2349
2	3	504	2283
3	1	504	2181
3	2	504	2265
3	3	504	2276

Table VI. Effect of load-balancing technique. (Time in one ICCG iteration (sec))

# of CPUs on GP7000	# of CPUs on HPC2500	Block ICCG method	Load-balanced block ICCG
1	1	2.48	1.66
1	2	1.93	1.25
1	3	1.62	1.08
2	1	1.77	1.48
2	2	1.53	1.21
2	3	1.42	1.10
3	1	2.06	1.50
3	2	2.17	1.59
3	3	1.38	1.22

IV. CONCLUSION

This paper investigates four parallel ICCG solvers in a multi parallel computer environment in the context of finite element electromagnetic field analyses. The results can be summarized as follows:

- In parallel ICCG solvers for Grid computation environment, a reduction of communication cost is important for getting satisfactory parallel solver performance. Although the block ICCG method is a conventional solver, it is effective in a multi computer environment due to its lower communication cost.
- The load-balancing technique is effective for the reduction of computational time in one ICCG iteration. The technique, however, affects the convergence rate of the solver.
- Although the algebraic block red-black ordering and the recursive ordering techniques have higher convergence rates than the block ICCG method, they can not attain better solver performance due to their communication or synchronization costs.

Further investigation of electromagnetic field analyses in Grid computing environments will be performed in the future; numerical tests on larger numbers of CPUs and computers will be performed for larger models.

ACKNOWLEDGMENT

A part of this work was supported by MEXT (Japan) Grant-in-Aid for Young Scientists (B) (16700060).

REFERENCES

[1] F. Berman, G. Fox, and A. Hey, *The Grid: past, present, future in Grid Computing*. Ed. West Sussex: John Wiley & Sons Ltd., pp. 9-50, 2003.

[2] I. Foster and C. Kesselman, "The Globus project: a status report," *Future Generation Computer Systems*, vol. 15, pp. 607-621, 1999.

[3] N. T. Karonis, B. Toonen, and I. Foster, "MPICH-G2: A Grid-enabled implementation of the Message Passing Interface," *Journal of Parallel and Distributed Computing*, vol. 63, pp. 551-563, 2003.

[4] J. Meijerink and H. A. van der Vorst, "An iterative solution method for linear systems of which the coefficient matrix is a symmetric M-matrix," *Mathematics of Computation*, vol. 31, pp. 148-162, 1977.

[5] Y. Saad, *Iterative Methods for Sparse Linear Systems*, Second ed., SIAM, Philadelphia, PA, 2003.

[6] H. A. van der Vorst and T. F. Chan, "Parallel Preconditioning for Sparse Linear Equations," *ZAMM. Z. angew. Math. Mech.*, vol. 76, pp. 167-170, 1996.

[7] T. Iwashita and M. Shimasaki, "Algebraic multi-color ordering for parallelized ICCG solver in finite element analyses," *IEEE Trans. Magn.*, vol. 38, pp. 429-432, 2002.

[8] C. Vollaire and L. Nicolas, "Preconditioning techniques for the conjugate gradient solver on a parallel distributed memory computer," *IEEE Trans. Magn.*, vol. 34, pp. 3347-3350, 1998.

[9] T. Iwashita and M. Shimasaki, "Algebraic block red-black ordering method for parallelized ICCG solver with fast convergence and low communication

costs," *IEEE Trans. Magn.*, vol. 39, pp. 1713-1716, 2003.

[10] T. Nakata, N. Takahashi, T. Imai, and K. Muramatsu, "Comparison of various methods of analysis and finite elements in 3-d magnetic field analysis," *IEEE Trans. Magn.*, vol. 27, pp. 4073-4076, 1991.

Takeshi Iwashita received the M.Eng. degree and the Ph.D. degree from the department of electrical engineering in Kyoto University, Japan, in 1995 and 1998, respectively. From 1998 to 1999, he worked as a research associate in Kyoto University for a Japanese national project (JSPS-RFTF project) on software for distributed parallel computing environment. In 2000, he joined the Data Processing Center in the same university. Since 2003 he has worked as an associate professor in the Academic Center for Computing and Media Studies, Kyoto University. From 2003 to 2004, he was a visiting fellow of Griffith University in Australia. His research interests include high performance computing, linear iterative solvers, and electromagnetic field simulations.

Masaaki Shimasaki received the M.Eng. degree from Department of Electronics and Ph.D. degree from Department of Electrical Engineering in Kyoto University, Japan, in 1968 and 1972, respectively. From 1978 to 1989, he worked as an associate professor of Kyoto University and from 1989 to 1997 he worked as professor of Kyushu University. Since 1997, he is a professor of Electrical Engineering of Kyoto University. In the 1974-75 academic years, he was an associate research scientist, Courant Institute of Mathematical Sciences, New York University. His research interests include high performance computing, linear iterative solvers, and electromagnetic field computation.

Junwei Lu graduated from the department of electrical engineering, Xian Jiaotong University, China, in 1976, the M.Eng. degree in electronic and computer engineering from the National Toyama University, Japan, in 1988, and Ph.D., degree in electrical and computer engineering from the National Kanazawa University, Japan, in 1991. From 1976 to 1984, he worked with the Institute of Qinhai Electric Power Testing and Research, China, where he was involved in the various national research projects for electrical power industry. Since 1985 he started his new academic study and research in the area of computational electromagnetics at the laboratory of electrical communications, Toyama University, Japan. Since 1988 he worked on the applied computational electromagnetics and involved in the development of magnetics devices with the laboratory of electrical energy conversion, Kanazawa University, Japan. He joined the School of Microelectronic Engineering, Griffith University in 1992, where he is now an associate professor and director of HPCV Lab. His fields of interest are computational and visual electromagnetics, EMC computer modeling and simulation, high performance cluster computing, smart mobile terminal antennas and RF/MW devices and circuits, and high frequency magnetics.

A New 3D Ray-Tracing Acceleration Technique for the Analysis of Propagation and Radiation in Complex Enviroments

I. González, C. Delgado, F. Saez de Adana, O. Gutiérrez, and M. F. Cátedra

Dept. Ciencias de la Computación. Universidad de Alcalá
28806 Alcalá de Henares (Madrid), Spain
Fax: +34 91 885 6646, E-mail: kiko.saez@uah.es

Abstract **–** A new 3D ray-tracing technique, based on the Angular Z-Buffer algorithm, [1] to speed-up reflection calculations is presented. The technique can be applied to the analysis of propagation in urban or indoor environments, or to the computation of radiation of antennas on-board complex structures amongst other applications. The technique is used in combination with the Uniform Theory of Diffraction (UTD) and shows a large reduction in CPU-time.

I. INTRODUCTION

Electromagnetic asymptotic ray-tracing techniques like UTD [1] have been used to obtain the electrical field at a point or in a direction as the addition of all the rays that reach that point or direction: direct, reflected, diffracted, etc [1 - 3].

Traditionally complex environments have been modeled with facets (hundreds or even thousands of them). Most of the CPU-time in the electromagnetic analysis is spent determining the facets of the environment that obstruct the ray path (shadowing test) and/or produce reflection or diffraction. Several ray-tracing acceleration techniques, such as Space Volumetric Partitioning (SVP), Binary Space Partitioning (BSP) and Angular Z-Buffer (AZB) have been developed which reduce the potential number of facets that need checking in the analysis of the shadowing of the ray-path [2]. In this way, the CPU-time required for the shadowing test is reduced. However, these techniques have been applied to complex environments modeled by flat facets. The proposed approach allows reducing the CPU time associated to the shadowing test for scenarios modeled by the combination or flat and curved facets. Moreover, the technique can be applied to the ray paths involved at the contribution of any kind of ray. In a reflection for instance, the test is performed to check whether any of the following ray-paths are obstructed: the path from the source to the reflection point and the one from the reflection point to the observation point.

Other important task in the ray tracing is to determine the flash-points (reflection or diffraction points) for each contribution. Although, as mentioned above, several fast algorithms have been used to reduce the computational cost associated to the shadowing test, there is not previous experience in the application of these algorithms, for the UTD analysis, to reduce the number of potential facets that must be considered in the effects of reflection of diffraction. The objective, in this case, is to select from all the potential surfaces, those which due to their orientation and position could create a reflection on the field at a point or in a direction. With this objective, an improvement on the AZB technique has been developed in this work in order to reduce the number of facets that are considered as potential reflecting surfaces when the coupling through a reflection is computed. The algorithm can be applied to the any effect in which a reflection is involved, as can be the simple reflection, double reflection, diffraction-reflection, etc. FASANT [3], a code based on UTD, has been updated using this technique for the analysis of antennas on-board complex structures, obtaining accurate results with a huge reduction in the CPU-time.

II. AZB TECHNIQUE FOR THE SHADOWING TEST

The shadowing test is very time consuming, particularly if it is applied to a large number of facets and when the facets are not flat. There is no analytical formula to obtain the intersection point between a ray and an arbitrary surface. In these cases minimization algorithms like the Conjugate Gradient (CG) must be used for the intersection testing. These algorithms are very time consuming; therefore, when the number of surfaces is high the ray-tracing acceleration techniques are needed to reduce the number of facets to test. The AZB technique [2] is based on the Light Buffer technique [4] used in Computer Aided Design (CAD) to find the objects contained in a scene that are visible from a given point (source). To analyze the shadowing of the rays that leave a source a “shadowing window” is defined. The window space is divided into several rectangles, called anxels that correspond to the angular regions which, taking as reference the source-point, cover the entire space seen from the source. The facets of the structure are classified depending on their positions within these anxels (see Fig. 1). Therefore, only the surfaces within the anxel where the ray is located are analyzed in the facet-intersection test to find

out if a given ray is shadowed. This previous selection of the facets which can shadow the ray produces an important reduction in the CPU time required for the ray-facets intersection test. The main advantage of the proposed approach is its applicability to scenarios modeled by the combination of flat and curved surfaces. This is very important, because, as mentioned above, the computation time associated to the shadowing test is significantly higher when curved facets are involved because minimization algorithms must be applied to perform this test.

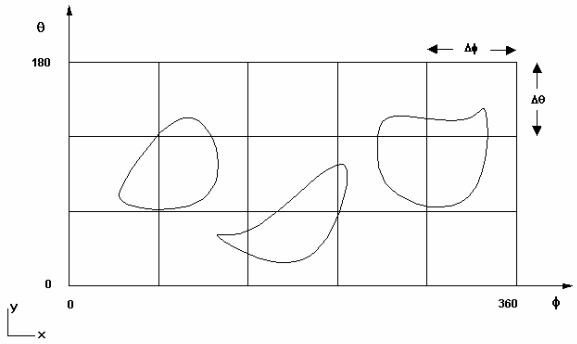

Fig. 1. Curves stored in the AZB plane from the shadowing source window.

The AZB technique can also be applied to speed up the computation of other effects such as of the reflection, diffraction, double-reflection and so on, reducing the time required for the shadowing test associated to each effect. In its original version, the AZB technique was used in combination with the image method to speed up the computation of the shadowing of the reflected fields. The procedure consists on using the image of the transmitter antenna as source [2]. Therefore, a reflection window can be determined for each facet to analyze the potential shadowing of the ray that after reflection leaves the facet.

III. AZB TECHNIQUE FOR THE REFLECTION TEST

As mentioned above, in this work, not only the computation time associated to the shadowing test is reduced but also the time necessary to determine the reflection points associated to the ray path. The objective, in this case, is to perform a previous selection of the facets that, due to their shape, orientation and position may contribute through reflection to the total field. This test is complementary to the shadowing test, because it provides a CPU time reduction to the other part of the ray tracing, as it is the determination of the ray paths using the minimization of the distance. Figure 2 illustrates the problem of the determination of the reflection points in a double reflection. As curved facets are involved, the determination of the points can not be done analytically, but they must be determined from the minimization of the ray distance from the source to the observer (d_1+d_2+d_3 in Fig. 2) based on the Fermat´s principle [1]. This distance, in the case of the double reflection, depends on four variables (u_1, v_1, u_2, and v_2, the parametric coordinates which define a curved surface [5]) and its computational cost is very high. If the complexity of the scenario under studio is high, the number of minimization tests necessary increase considerably and the reduction of this number seems very important if the analysis needs to be perform in a reasonable time.

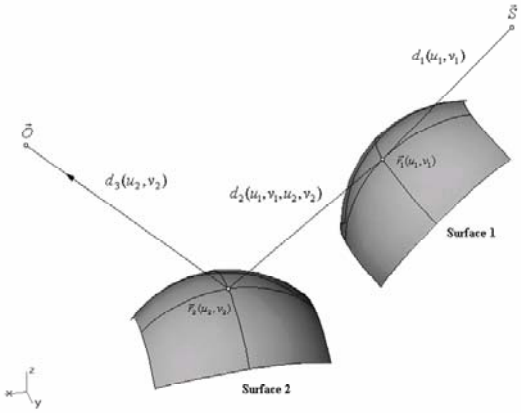

Fig. 2. Example of ray-tracing for a double reflection problem.

In this section the application of the AZB to the reflection test is explained. New AZB windows are defined for this test. The AZB reflection windows divide the space into anxels, which contain the facets that may contribute to the reflected field in the angular sector corresponding to that anxel. The so called reflecting source window is employed to analyze simple reflections. This window divides the space into angular regions, which contain the facets that may contribute to the reflected field in those regions. Only the facets located in the anxel of the reflecting source window that contains a given direction are tested to obtain all the reflected rays in that direction. As in the shadowing check, a lot of CPU-time is saved by not having to test for reflection facets that do not contribute to the reflected fields in that direction, particularly for curve facets, for which there is no analytical formula to find the reflection point. The following procedure can be used to find the anxel or anxels where a facet should be located in the reflecting source window:

1. Five sample points are obtained on the facet: the four vertices and the middle point. The coordinates and the normal vector of these points are calculated.
2. The directions of the reflected rays are obtained for the five sampling points using the Snell law (see Fig. 3). The anxel or anxels corresponding to those directions are identified and stored in a file.
3. The visibility from the source of the facet is checked: if there are one or more sample points not shadowed by any other facet, then the facet should

be included in the reflection source window. If the five points are shadowed, the facet is not included in the reflecting source window.

4. The facet is included in the set of anxels obtained in step 2.

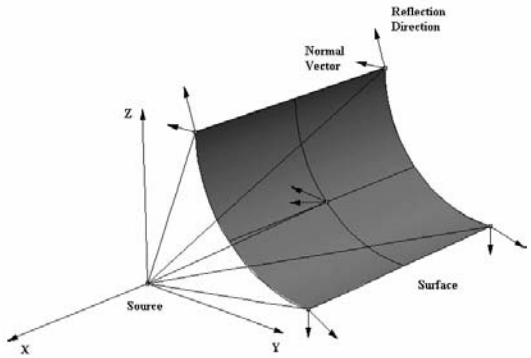

Fig. 3. Direction of the reflected rays for the five sample points of the curved facet.

Only five sampling points are necessary to create the AZB matrix because the facets are not supposed to be convex and concave at the same time. In this case, five points would not be enough. A previous division of the surfaces is performed to avoid that situation. The idea is to have, after the division, facets that are only convex or concave.

The technique, explained above, can be extended to speed up double-reflection field calculations. A reflecting window is associated to each facet in this case. This window allows obtaining efficiently all the facets that may contribute to the double-reflection in a specified observation direction. This window is also divided into anxels that contain the facets that could potentially contribute to the double-reflection in the angular sector corresponding to each anxel. The reflecting window of an arbitrary facet, that will be called facet *i*, can be obtained as follows

1. Using the shadowing window of facet *i*, all the visible surfaces from this one are obtained.

2. The box which encloses the surface is obtained and the eight vertices are used as source points (see Fig. 4).

3. Eight partial reflection windows are obtained (one for each vertex). Each window is determined by its spherical coordinates (θ_{l_max}, θ_{l_min}, ϕ_{l_max} and ϕ_{l_min}) $_{l=1,2,\ldots 8}$.

4. Once determined the partial angular windows, the total angular window (θ_{max}, θ_{min}, ϕ_{max} and ϕ_{min}) is obtained by means of an OR operation between the eight partial windows.

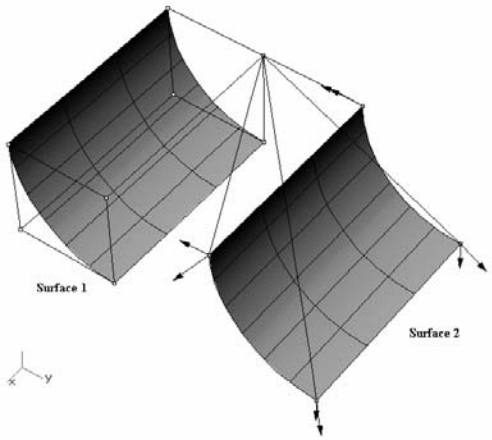

Fig. 4. Example of the estimation of the angular margin of one vertex of the enclosing box.

IV. RESULTS

This ray-tracing technique has been implemented in a computer code called FASANT, [3], developed previously for the analysis of antennas on board complex structures like ships, satellites, etc. This tool is based on UTD and can work with surfaces of arbitrary form modeled by Bezier patches. The electromagnetic kernel of FASANT is divided into two modules: flat and curve modules. In the previous version of FASANT, the flat module included a ray-tracing acceleration technique based on the AZB to efficiently treat the shadowing test problem, while the curve module only had the back-face culling test implemented in order to reject non-visible facets [3]. The new version of FASANT includes the AZB to treat the shadowing and reflection problems in both flat and curve modules.

First of all, a comparison between the results obtained from the proposed approach and measurements of a real scale mock-up of a satellite called Stentor are shown to prove the validity of the method. The measurements were performed by the French institution CNES (Centre National d'Estudes Spatiales, National Center of Space Studies in English). A picture of the mock-up can be seen in Fig. 5 In the left-bottom part of the satellite a GPS antenna is placed. The antenna is pyramidal-shaped as can be seen in Fig. 6 and its free-space radiation pattern is as depicted in Fig. 7. The frequency of analysis is 1.575 GHz.

The geometrical model of the Stentor is shown in Fig. 8. It has 83 flat surfaces and 11 curves. The datellite is completely metallic. The dimensions are 2.3 m × 1.8 m × 0.65 m. The phase centre of the antenna is placed at (-0.815, 1-.24, 0.13).

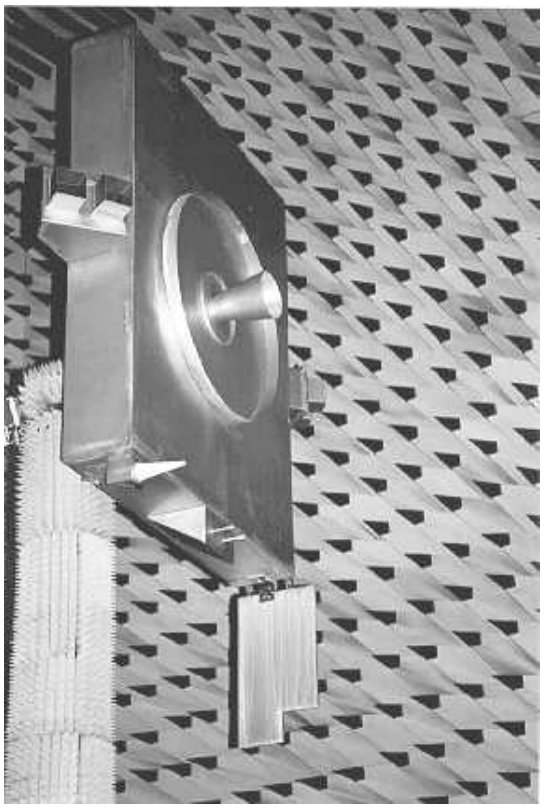

Fig. 5. Real mock-up of the Stentor satellite incide the CNES anechoic chamber.

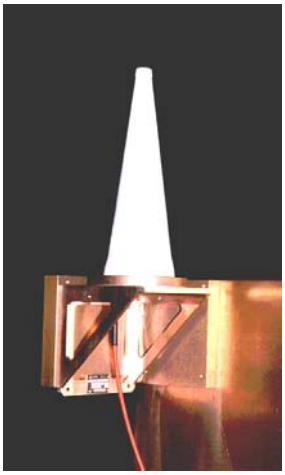

Fig. 6. Pyramidal antenna placed onboard the satellite.

Figures 9 and 10 show the comparison between the measurements and the simulation with FASANT for the theta and phi components of the electric field for a cut with ϕ = 11.25º and θ varying from –180º to 180º. As can be seen, there is good agreement between the measurements and the simulation results.

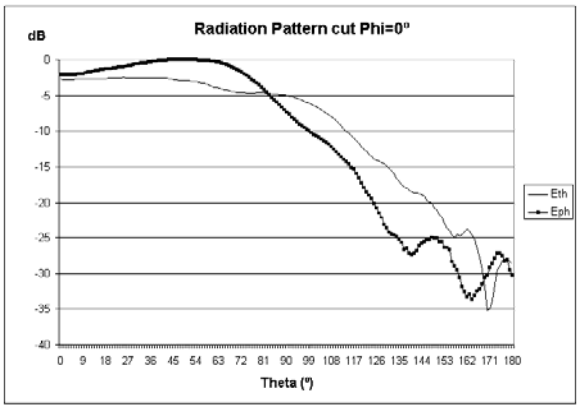

Fig. 7. Free-space radiation pattern of the pyramidal antenna (cut ϕ=0º).

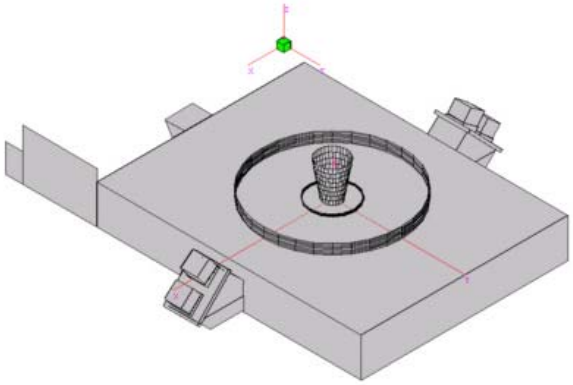

Fig. 8. Geometrical model of the Stentor and position of the antenna.

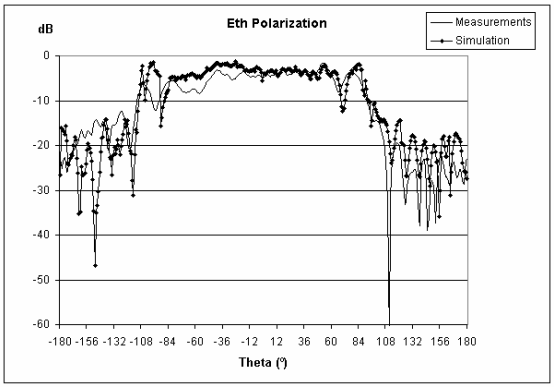

Fig. 9. Comparison between measurements and simulation for the Stentor satellite (Etheta).

On the other hand, several cases of analysis of on-board antennas with different complex structures have been tested to prove the CPU-time reduction provided by the present approach. In all the results, a previous test was performed to check that the final results are the same for both the original and modified versions of FASANT. The only difference between both is the CPU-time required, due to the more advanced ray-tracing acceleration technique introduced in the new version. In all the cases tested, the new version reduces

the CPU-time by order of magnitude. In this section, the CPU-time reduction for the analysis of antennas on-board the HISPASAT satellite mock-up is discussed. The computer used was a Pentium IV 1.8 GHz with 1 GB memory PC-800.

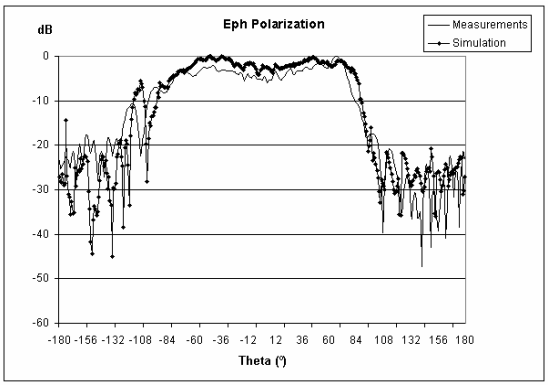

Fig. 10. Comparison between measurements and simulation for the Stentor satellite (Ephi).

The HISPASAT model used has 75 flat facets and 12 curve facets as shown in Fig. 11. To check the increase in speed of FASANT with the new ray-tracing algorithm, simple and double reflections have been selected. In the simulations using both versions of FASANT the antenna was placed in position with Cartesian coordinates 0.5, 0.5, 0.5, as shown in Fig. 3. Two cuts in ϕ have been calculated with angles 90º, 270º. The angular sweep in θ for simple-reflection is of 181 points, from 0º to 180º. For double-reflection, 30 points from 0º to 90º have been considered for the angular sweep in θ 2037 rays were traced for simple reflection and 948 for double reflection.

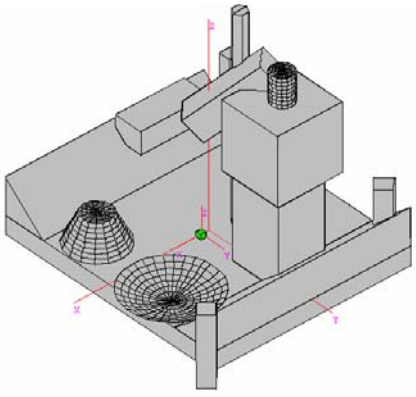

Fig. 11. HISPASAT satellite mock-up.

In the comparison shown in Table I, only the computation time associated to simple and double reflections has been considered. The reason is that the presented approach is only applicable for the reduction of the time associated to the reflections. At the moment, the diffraction is treated in FASANT without any AZB based algorithm to reduce its computational cost. An algorithm applicable to the diffraction effect is being developed at this moment.

Table I. Comparison of the CPU-time used with the two versions of FASANT.

Code	Simple-Reflection	Double-Reflection
Original FASANT	3 min: 21 s	43 min: 21 s
New FASANT	33 s	12 min: 46 s

V. CONCLUSIONS

A new version of the Angular Z-Buffer technique for accelerating the computation of reflected rays in complex environments has been presented. This technique has been tested with the FASANT code, showing a reduction in CPU-time by the order of magnitude. The technique is easily applicable to mobile communications propagation. In this case, the geometrical models will be one or two orders of magnitude higher, but the method is perfectly scalable and, therefore, the time reduction will be similar. The approach can also be applicable for situations in which two or more sources are present. The only difference is that the AZB matrices associated to the method must be created for each source.

ACKNOWLEDGEMENTS

The authors would like to thank to the CNES (France) for the measurements of the Stentor mock-up.

This work has been supported in part by Comunidad de Madrid and Universidad de Alcalá, projects PI2005/069 and CAM-UAH 2005/005.

REFERENCES

[1] D. A. McNamara, C. W. I. Pistorius, and J. A. G. Maherbe *Introduction to the Uniform Geometric Theory of Diffraction,* Norwood , MA: Arctech House, 1990.

[2] F. Cátedra, J. Pérez-Arriaga, *Cell planning for wireless Communications*. Artech House Publishers, Boston London, 1999.

[3] J. Pérez. F. Saez de Adana, O. Gutiérrez, I. González, M. F. Cátedra, I. Montiel, and J. Guzmán "FASANT: Fast Computer Tool for the Analysis of Antennas on Board," *IEEE Antennas and Propagation Magazine*, vol. 41, no. 2, April 1999.

[4] E. A. Hines and D. P. Greenberg "The Light Buffer: A Shadow-Testing Accelerator," *IEEE CG&A*, pp. 6 – 16, Sep. 1986.

[5] G. Farin *Curves and surfaces for computer aided geometric design*. Academic Press, 1988.

Iván González Diego was born in Torrelavega, Spain in 1971. He received the B.S. and M.S. degrees in telecommunications engineering from the University of Cantabria, Spain, in 1994 and 1997 respectively, and the Ph.D degree in telecommunications engineering from the Univeristy of Alcalá , Madrid, Spain in 2004.
He worked in the Detectability Laboratory of the National Institute of Technical Aerospace (INTA), Madrid, Spain and as an Assistant Researcher at the University of Alcalá. He currently works as Assistant Professor in this university. He has participated in several research projects with Spanish and European companies, related with analysis of on board antennas, radio propagation in mobile communications, RCS computation, etc. His research interests are in numerical methods applied to the electromagnetic problems, like genetic algorithms and numerical methods to represent complex bodies for the electromagnetic techniques.

Carlos Delgado was born in Guadalajara, Spain, in 1979. He received the MS degree in Telecommunications Engineering from the University of Alcalá, Spain, in 2002, and the Ph. D. in Telecommunications Engineering in 2006. He is currently with the Computer Science Department, Universidad de Alcalá, Spain. His research interests include numerical methods applied to scattering and radiation problems, hybridization of high frequency and numerically rigorous methods and fast computational techniques applied to electromagnetics.

Francisco Saez de Adana was born in Santander, Spain, in 1972. He received the BS, MS and PhD. degrees in Telecommunications Engineering from the University of Cantabria, Spain, in 1994, 1996 and 2000, respectively. Since 1998 he works at the University of Alcalá, first as assistant professor and since 2002 as professor. He has worked as faculty research at Arizona State University from March 2003 to August 2003.
He has participated in more than forty research projects with Spanish, European, American and Japanese companies and universities, related with analysis of on board antennas, radio propagation in mobile communication, RCS computation, etc. He has directed two Ph. D. Dissertations, has published sixteen papers in referred journals and more than 40 conference contributions at international symposia. His research interests are in areas of high-frequency methods in electromagnetic radiation and scattering, on-board antennas analysis, radio propagation on mobile communications and ray-tracing acceleration techniques.

Oscar Gutiérrez Blanco was born in Torrelavega, Spain, in 1970. He received the BS and MS degrees in Telecommunications Engineering from the University of Cantabria, Spain, in 1993 and 1996, respectively. From 1995 to 1998, he was with the Communications Engineering Department of the Cantabria as Research assistant. He received the Ph.D. degree in Telecommunication from the Alcala university, Spain, in 2002. From 1998 to 2000, he was with the Signal Theory and communications Deparment of the Alcala University, Madrid. In 2001, he is currently an assistant professor in the Computational Science Department in the Alcalá University, Madrid.
He has participated in more than 40 research projects, with Spanish and European companies, related with analysis of on board antennas, radio propagation in mobile communication, RCS computation, etc. His research interests are in high-frequency methods in electromagnetic radiation and scattering, and ray-tracing acceleration techniques.

Manuel F. Catedra received his M.S. and Ph. D. degrees in Telecommunications Engineering from the Polytechnic University of Madrid (UPM) in 1977 and 1982 respectively. From 1976 to 1989 he was with the Radiocommunication and Signal Processing Department of the UPM. He has been Professor at the University of Cantabria from 1989 to 1998. He is currently Professor at the University of Alcalá, in Madrid, Spain.
He has worked on about 60 research projects solving problems of Electromagnetic Compatibility in Radio and Telecommunication Equipment, Antennas, Microwave Components and Radar Cross Section and Mobile Communications. He has developed and applied CAD tools for radio-equipment systems such as Navy-ships, aircraft, helicopters, satellites, the main contractors being Spanish or European Institutions such as EADS, ALCATEL, CNES, ALENIA, ESA, DASA, SAAB, INTA, BAZAN, INDRA, the Spanish Defence Department.
He has directed about 15 Ph D. dissertations, has published about 45 papers (IEEE, Electronic Letters, etc), two books, about 10 chapters in different books, has given short courses and has given around a hundred and thirty presentations in International Symposia.

On the Convergence Properties of the Multiple Sweep Method of Moments

D. Çolak, R. J. Burkholder and E. H. Newman

The Ohio State University Dept. of Electrical and Computer Engineering
ElectroScience Laboratory, 1320 Kinnear Rd., Columbus, Ohio 43212

Abstract–This paper investigates the convergence properties of the Multiple Sweep Method of Moments (MSMM), both analytically and numerically, and presents some numerical results for various 2D scattering geometries, such as a strip, a cylinder, and a rough surface with and without a target on it. The MSMM is an $\mathcal{O}(N^2)$ iterative method for solving the large matrix equations which arise in the method of moments (MM) analysis of electrically large bodies. In the MSMM, the body is split into P sections and the currents on these sections are found in a recursive fashion. Although the MSMM is a frequency domain solution, it has a time domain interpretation. The first sweep includes the dominant scattering mechanisms and each subsequent sweep includes higher order mechanisms. A connection between the MSMM and classical iterative methods is established in this paper. Under certain conditions, the MSMM is shown to be mathematically equivalent to a block Jacobi preconditioned system of equations that results from the moment method, and solved via the method of symmetric successive over-relaxation (SSOR) with relaxation factor $\omega = 1$. Based on this connection, the convergence is analyzed by examining the eigenvalue distribution of the iteration matrix for different classes of 2D geometries, and for electric and magnetic field integral equation formulations and TE_z and TM_z polarizations. In addition, the MSMM is compared with other recently used iterative methods for rough surface scattering problems, namely the Method of Ordered Multiple Interactions (MOMI), or the Forward-Backward (FB) Method. The results show that the MSMM converges for some problems for which the MOMI (and FB) fails to converge, e.g., the rough surface with a target on it, or when the surface becomes multi-valued which causes large off-diagonal elements in the interaction matrix.

Keywords–Iterative methods, Integral equations, Moment methods, Convergence, Numerical methods.

Dr. Çolak is currently with the King Faisal Specialist Hospital and Research Centre, MBC03, P.O. Box 3354, Riyadh 11211, Saudi Arabia. E-mail: DColakKaya@Kfshrc.edu.sa.

I. INTRODUCTION

The frequency domain method of moments (MM) has been one of the most reliable and widely used numerical methods for the analysis of radiation and scattering from bodies of simple or complex shape [1]-[3]. In the MM, the scattered or radiated field is generated by a set of equivalent currents which replace the physical structure. The current on a body is expanded in terms of N expansion functions, and the N unknown coefficients in this expansion are obtained as the solution of an order N matrix equation. The standard MM is often limited by the $\mathcal{O}(N^3)$ CPU time required to solve the matrix equation by direct methods, such as LU decomposition. Over the past several years many methods have been developed to improve the computational efficiency of the MM, and thus allow it to be applied to electrically larger bodies [4]. Iterative solution of the MM matrix equation has received considerable attention since the CPU time is reduced to $\mathcal{O}(N^2)$ [5], [6].

A considerable effort has been directed toward the solution of scattering of electromagnetic waves from rough surfaces at low grazing angles since it has important applications in remote sensing of ocean and land profiles [7]. Monte Carlo simulations of rough surface scattering problems using direct numerical solutions have become popular with the growth of modern computers and the development of the fast methods. Iterative techniques developed for solving general systems of linear equations have been applied to systems resulting from electromagnetic rough-surface scattering problems [8]-[18]. One approach, called the Kirchhoff iterative method (also known as the Neumann expansion) [8]-[10], has been shown to be useful, but that the method may fail to converge for surfaces with large slopes or for large incidence angles [9].

Recently, a new iterative technique termed the Forward-Backward (FB) method has been proposed by Holliday *et al.* [14]. A functionally identical approach, the Method of Ordered Multiple Interactions (MOMI), has been developed by Kapp and Brown [15]. These approaches have been shown to be very

effective for the solution of the magnetic field integral equation (MFIE) for the scattering from perfectly conducting (PEC) surfaces that are single valued and rough in one dimension (two-dimensional scattering). The limitation of the MOMI (and the FB method) is that the convergence of the method is very much dependent on the sequential ordering of the current elements along a certain direction. Hence convergence may be a problem, especially for two-dimensional (2D) rough surfaces (three-dimensional scattering). Tran [16] applied MOMI to the scattering from a 2D rough surface and showed that the convergence of the iterative process depends strongly on the order in which the current elements are updated. With some orderings it did not converge, and it was found that in one case it did not converge even though the optimal ordering was used.

The MOMI is shown to be mathematically equivalent to a point Jacobi preconditioned system of equations that results from the moment method, and solved via symmetric successive over-relaxation (SSOR) with relaxation factor $\omega = 1$ (i.e., Forward Backward Gauss-Seidel method) [17]. West and Sturm [17] tested the performance of the method through application to a series of 1D surface profiles (2D scattering) that approximate breaking ocean waves, and 2D perfectly conducting circular cylinder problems. They found that the method diverges for some breaking wave profiles, as well as for the closed circular cylinder. Pino *et al.* [18] applied the FB method to scattering from targets on 1D ocean-like rough surfaces. They also came to the conclusion that the method does not exhibit a convergent behavior if there is a target on the rough surface, and developed a generalization of the FB method to handle this case.

Recently, a new technique termed the *Multiple Sweep Method of Moments (MSMM)* has been introduced for the analysis of the radiation and scattering from electrically large, perfectly conducting bodies [19]-[21]. The MSMM is an extension or modification of the Spatial Decomposition Technique (SDT) developed by Umashankar *et. al.* [22]. In both methods, the electrically large body is split into P sections containing approximately N/P unknowns per section. The currents on the P sections are found in a recursive fashion until they (hopefully) converge to the exact result. The main difference between the MSMM and the SDT is that the MSMM attempts to perform the recursion so that the first sweep accounts for the dominant mechanisms, while subsequent sweeps account for higher order mechanisms. Tapered resistive cards (R-cards) [20], [23], [24], [25] are used on the first sweep to minimize endpoint scattering from the junctions between sections. Subsequent sweeps are performed in the order in which currents would change with time so that the higher order sweeps correspond to higher order interactions.

In this paper, a connection between the MSMM and well-known classical iterative methods in mathematics is established so that the convergence properties of the MSMM can be investigated using matrix theory. Based on this connection, the convergence difficulties (such as for the closed cylinder) can be explained by the inherent limitations of the corresponding stationary iterative method. In addition, the MSMM can be compared with the recently used iterative methods for rough surface scattering problems (e.g., the MOMI, or FB Method) from both theoretical and numerical points of view.

The organization of this paper is as follows. Section II presents the description of the Multiple Sweep Method of Moments (MSMM) for the analysis of scattering from a 2D PEC strip. The formulation of the MSMM in matrix notation as a stationary iterative algorithm is derived in Section III. An *iteration matrix* is derived analytically, and based on that the convergence properties of the MSMM will be discussed. Section IV presents a numerical investigation of the convergence properties of the MSMM for the aforementioned various 2D scattering geometries (i.e., strip, cylinder, and rough surface with and without a target), by extracting and plotting the eigenvalue spectrum of the iteration matrix. The effect of the initial guess vector on the convergence of the method will be investigated numerically by using zero current, the physical optics current, and the MSMM first sweep current (which uses the R-cards), as starting solutions for the current vector. Finally, discussions and conclusions are included in Section V.

II. THE MSMM PROCEDURE

The basics of the original MSMM algorithm will be illustrated briefly on the MSMM solution for the current on a 2D PEC strip. Most of the material presented in this section is drawn from [20] and [21]. Figure 1 shows the MSMM procedure for the problem of TE_z scattering from a PEC strip. For the purposes of the standard MM solution, the strip is split into N segments of width $d = L/N$, and the $\hat{\mathbf{x}}$ directed current is expanded as

$$J = \sum_{n=1}^{N} i_n J_n \tag{1}$$

where the J_n are the known subsectional expansion functions and the i_n are the unknown coefficients. Hence,the standard MM solution can be written as the matrix equation

$$[Z]I = V^i \tag{2}$$

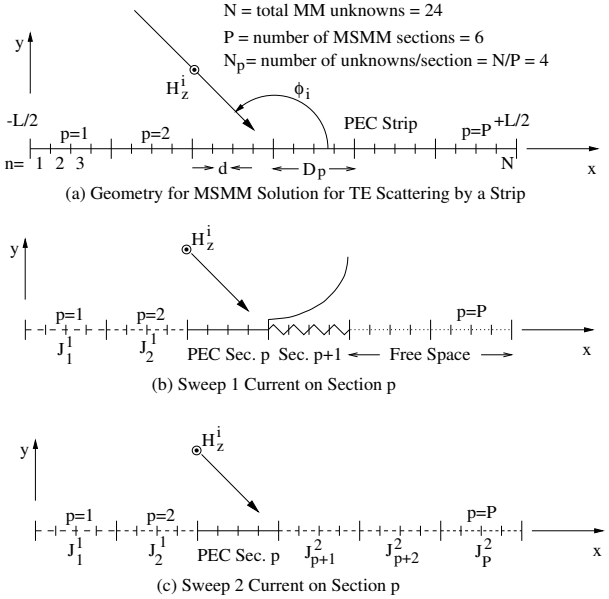

Fig. 1. For the MSMM solution a strip of width L is split into P sections with $N_P = N/P$ unknowns per section.

where [Z] is the $N \times N$ impedance matrix (also called "the interaction matrix"), V^i is the length N voltage vector due to the incident field, and $I = [i_1, i_2, \ldots, i_N]^T$ is the current vector. For the MSMM purposes, the strip is split into P equal sections of $N_P = N/P$ expansion functions per section, and of width D_P. Assuming the incident field propagates from left to right in Fig. 1, the first sweep ($k = 1$) begins by computing the current $J^{k=1}_{p=1}$ on section $p = 1$ excited by the incident field. At this point the remaining sections have no current, thus creating a non-physical truncation of the current at the end of section $p = 1$. To minimize that, the right-hand edge of the section $p = 1$ is terminated in an exponentially tapered R-card, as illustrated in Fig. 1(b). Once the current on section 1 has been determined, the next step is to compute the current $J^{k=1}_{p=2}$ on section $p = 2$ caused by the incident field plus the previously computed current $J^{k=1}_{p=1}$ on section 1. The process is continued for $p = 3, ..., P$ to complete Sweep 1.

Consider the computation of the first sweep current, $J^{k=1}_p$, on an arbitrary section p. As illustrated in Fig. 1(b), sections 1 to $p-1$ contain previously computed currents, section p is a PEC, the next section is tapered R-card, and the remaining sections are free space. Note that for the left hand edge of section p, the previously computed currents on section $p-1$ (approximately) enforce continuity of current at the junction, and thus from an electromagnetic viewpoint there is no edge. The currents on the PEC section p and the R-card section $p+1$ are produced by the superposition of the incident field plus the previously computed currents on sections 1 to $p-1$.

The second sweep is done in reverse order, since this is the natural order in which the currents would change with time. That is, section P is modified first, then section $P-1$, ..., and finally section 1. Hence, the second sweep will include reflections of the wave at the trailing edge. Figure 1(c) illustrates the computation of $J^{k=2}_p$, the Sweep $k = 2$ current on arbitrary section p. In computing the Sweep 2 current on section p, section p is a PEC, while all other sections are represented by their most recently computed currents. At this point in the Sweep 2 computation, sections $p+1$ to P have already been updated to the Sweep 2 currents, while sections 1 to $p-1$ still have the Sweep 1 currents. No R-cards are needed for this and subsequent sweeps because J^1_{p-1} and J^2_{p+1} approximately enforce continuity of current at the left and right edges of section p, respectively. The current on section p is the superposition of that due to the incident field plus the scattered component due to the previously computed currents.

All Sweeps $k > 2$ are identical to Sweep 2, except that odd numbered sweeps proceed from left to right while even numbered sweeps proceed from right to left as the MSMM solution attempts to model multiple interactions across the structure.

III. THE MSMM AS A STATIONARY ITERATIVE METHOD

The MSMM solution procedure has been described in Section II. The formulation of the MSMM in a matrix notation as a classical (or stationary) iterative algorithm is derived in this section. The term *stationary* indicates that the iterative equations do not change as the iterative algorithm is repeated [26], [27].

It is of interest to solve the following matrix equation:

$$\begin{bmatrix} [Z_{11}] & [Z_{12}] & \cdots & [Z_{1P}] \\ [Z_{21}] & [Z_{22}] & \cdots & [Z_{2P}] \\ \vdots & \vdots & \vdots & \vdots \\ [Z_{P1}] & [Z_{P2}] & \cdots & [Z_{PP}] \end{bmatrix} \begin{bmatrix} I_1 \\ I_2 \\ \vdots \\ I_P \end{bmatrix} = \begin{bmatrix} V^i_1 \\ V^i_2 \\ \vdots \\ V^i_P \end{bmatrix} \tag{3}$$

where $[Z_{pq}]$ is the $N_P \times N_P$ block containing the mutual impedances between expansion functions in sections p and q, V^i_p contains the N_P elements of the incident voltage vector V^i for section p, and I_p contains the N_P elements of the solution vector I for section p.

Here we will assume that the first forward sweep of the MSMM, which uses R-cards to isolate sections to obtain the dominant scattering mechanisms, is done to obtain an initial guess and is not part of the iterative method. The second sweep (the backward

sweep) of the MSMM can be written in terms of matrix notation as follows. As seen in Fig. 1(c), the second sweep current on section p is due to the superposition of the incident field and the scattered field due to the previously computed currents, i.e., J_1^1 through J_{p-1}^1 and J_{p+1}^2 through J_P^2, where J_p^k denotes the k^{th} sweep current on section p. Hence, the MSMM uses the most recently updated values of the current on each section as they become available. The current on section p is found as the solution of

$$[Z_{pp}]I_p = V_p^i + V_p^s \tag{4}$$

where V_p^s is the scattered field vector on section p due to the previously computed currents on all other sections, and is given by

$$\left[\ V_p^s\ \right] = -\left[\ [Z_{p1}] \quad [Z_{p2}] \quad \cdots \quad [Z_{pP}]\ \right] \begin{bmatrix} I_1 \\ I_2 \\ \vdots \\ I_P \end{bmatrix}. \tag{5}$$

In equation (5), I_1 through I_{p-1} includes currents from the previous sweep (the first sweep of the MSMM, or initial guess of the matrix iterative algorithm), $I_p = 0$, and I_{p+1} through I_P includes the currents from the present sweep. From equations (4) and (5), the second sweep can be written as

$$[Z_{pp}]\, I_p^{(2)} = V_p^i - \sum_{j=1}^{p-1} [Z_{pj}]\, I_j^{(1)} - \sum_{j=p+1}^{P} [Z_{pj}]\, I_j^{(2)} \tag{6}$$

where p goes from P to 1, i.e., a backward sweep. Similarly, the third sweep (forward sweep) can be written as

$$[Z_{pp}]\, I_p^{(3)} = V_p^i - \sum_{j=1}^{p-1} [Z_{pj}]\, I_j^{(3)} - \sum_{j=p+1}^{P} [Z_{pj}]\, I_j^{(2)} \tag{7}$$

where in this case p goes from 1 to P.

The remaining sweeps of the MSMM are identical to Sweep 2 except that odd numbered sweeps proceed from left to right while even numbered sweeps proceed from right to left, as the MSMM solution attempts to model the multiple scattering interactions. Hence, the generalization for an arbitrary Sweep $k = 2n$ or $k = 2n + 1$ is

$$[Z_{pp}]\, I_p^{(2n)} = V_p^i - \sum_{j=1}^{p-1} [Z_{pj}]\, I_j^{(2n-1)} - \sum_{j=p+1}^{P} [Z_{pj}]\, I_j^{(2n)}, \text{ for } p = P, ..., 1,$$

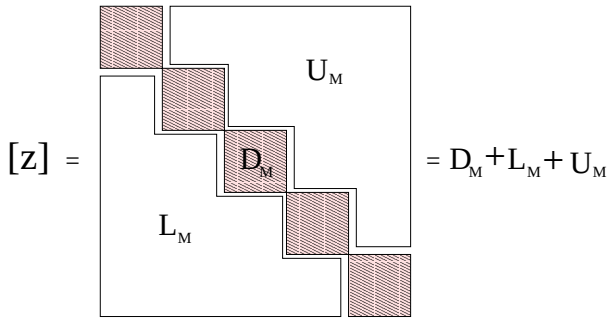

Fig. 2. Decomposition of $[Z]$ into a sum of block matrices.

$$[Z_{pp}]\, I_p^{(2n+1)} = V_p^i - \sum_{j=1}^{p-1} [Z_{pj}]\, I_j^{(2n+1)} - \sum_{j=p+1}^{P} [Z_{pj}]\, I_j^{(2n)}, \text{ for } p = 1, ..., P \tag{8}$$

The operational count of the MSMM is $\mathcal{O}(N^2)$ per iteration, assuming the $[Z_{pp}]$ matrices have been factorized before starting the iteration [19].

Now decompose $[Z]$ in terms of a sum of block matrices

$$[Z] = D_M + U_M + L_M \tag{9}$$

where D_M is a block diagonal matrix, and U_M and L_M are strictly upper and lower triangular block matrices of $[Z]$, respectively, as shown in Fig. 2. Hence, equation (8) can be written in terms of block matrices as,

Backward sweep:

$$D_M I^{(2n)} = V^i - U_M I^{(2n)} - L_M I^{(2n-1)},$$

Forward sweep:

$$D_M I^{(2n+1)} = V^i - L_M I^{(2n+1)} - U_M I^{(2n)}. \tag{10}$$

The form in equation (10) is equivalent to Forward-Backward block Gauss-Seidel (FB-GS, or equivalently, block SSOR with a relaxation factor $\omega = 1$) by considering two half iterations [5], [28]. This iterative algorithm is also equivalent to solving a block Jacobi preconditioned system of equations via forward-backward block GS iteration [29].

Equation (10) can be written in a similar format as that of the FB-GS in [5], [28]

$$\begin{aligned} (D_M + U_M) I^{(k+\frac{1}{2})} &= V^i - L_M I^{(k)} \\ (D_M + L_M) I^{(k+1)} &= V^i - U_M I^{(k+\frac{1}{2})}, \end{aligned} \tag{11}$$

where $I^{(k+\frac{1}{2})}$ is an intermediate solution of the iterate. The *iteration matrix* G [26] of a general stationary iterative system is defined from,

$$I^{(k+1)} \quad = \quad G\, I^{(k)} + V \tag{12}$$

where V is a constant vector. Hence, the iteration matrix of the MSMM can be found as

$$G_M = (D_M + L_M)^{-1} U_M (D_M + U_M)^{-1} L_M. \tag{13}$$

As shown in the numerical results of the next section, the spectral radius of this matrix determines the convergence rate.

One should note that as the MSMM section size reduces to the size of one cell (i.e., the size of a single MM expansion function), then $D_M \rightarrow D$, and the block FB-GS (or block SSOR with $\omega = 1$) becomes point FB-GS (or point SSOR with $\omega = 1$). West *et. al.* [17] showed that MOMI [15] (and hence Forward-Backward method [14]) is mathematically equivalent to a point Jacobi preconditioned system solved via point SSOR with $\omega = 1$, and zero initial guess vector. We showed above that the MSMM is mathematically equivalent to a block Jacobi preconditioned system solved via block SSOR with $\omega = 1$ (or equivalently block FB-GS), and the MSMM first sweep (which uses R-cards) as an initial guess vector. Therefore, we draw the conclusion that the MOMI is equivalent to the MSMM with MSMM section size reduced to one basis element (i.e., block $\rightarrow$ point) and with zero initial guess vector. It is also noted that the MSMM is a more general form of the generalized forward-backward method wherein block sections are only used to encompass the obstacles on the rough surface [18].

IV. NUMERICAL RESULTS

The spectral radius of the iteration matrix $\rho(G)$, which is the magnitude of the largest eigenvalue of G, controls the convergence of the iterative method. The iterative method is convergent if and only if $\rho(G) < 1$ [26]. Smaller values of $\rho(G)$ give higher convergence rates. This section presents a numerical investigation of the convergence properties of the MSMM for various 2D scattering geometries by extracting and plotting the eigenvalue spectrum of the iteration matrix G_M, which was derived in Section III. Examples will include a strip, a closed and open cylinder, and a rough surface with and without a target on it, as shown in Fig. 3. The effect of the initial guess vector on the convergence of the method is also investigated numerically by starting with zero current, the physical optics (PO) current, and the MSMM first sweep current which uses R-cards to isolate the sections. The electric and magnetic field integral equation formulations (EFIE and MFIE) and both polarizations (TE_z or TM_z) of the incident field are considered. The results are compared with the MOMI (or FB Method) which corresponds to the case when the MSMM section size (D_P) equals the cell size. In our results, we use a pulse-basis function cell size (MM segment size) of $\lambda/10$ and a frequency of 300 MHz.

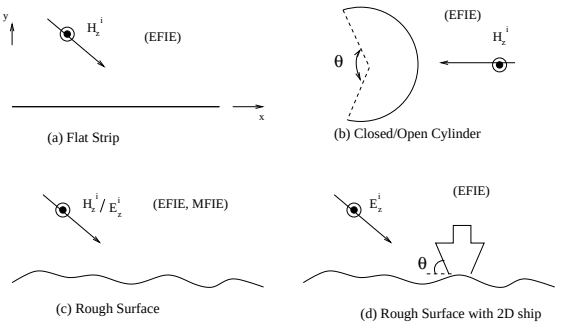

Fig. 3. The 2D problem geometries that are investigated for the convergence analysis.

The convergence of the iterative method is monitored by examining the residual error norm

$$R_k = \frac{\|r^{(k)}\|}{\|V^i\|} \tag{14}$$

where $r^{(k)} = V^i - ZI^{(k)}$ is the residual error vector at the k^{th} iteration. R_k is a direct measure of how well the matrix equation is satisfied by the k^{th} solution vector. This is important for integral equation problems because it is a measure of how well the boundary conditions are satisfied for a given set of testing functions. It is noted that the currents are not guaranteed to converge to the exact value [30]; however, for RCS problems one is more interested in the fields radiated by the currents and the enforcement of field boundary conditions.

A. Flat Strip

Figure 4 shows the eigenvalue spectrum of G_M for a 12.8λ PEC strip with various MSMM section sizes (denoted by D_P). The strip is illuminated by a TE_z polarized plane wave with an incidence angle of $\phi_i = 135°$ with respect to the x axis. As seen from the figure, as the section size becomes larger (i.e., the number of sections P of the MSMM gets smaller), the spectral radius of G_M gets smaller and the convergence is expected to be faster. It is also noticed that for $P \geq 32$ (or $D_P \leq 0.4\lambda$), the method diverges, i.e., $\rho(G_M) > 1$ as seen in Fig. 4(a). This is consistent with the result that was reported before in [19]. Hence, the EFIE formulation of TE_z polarized scattering from a strip is divergent if the section size

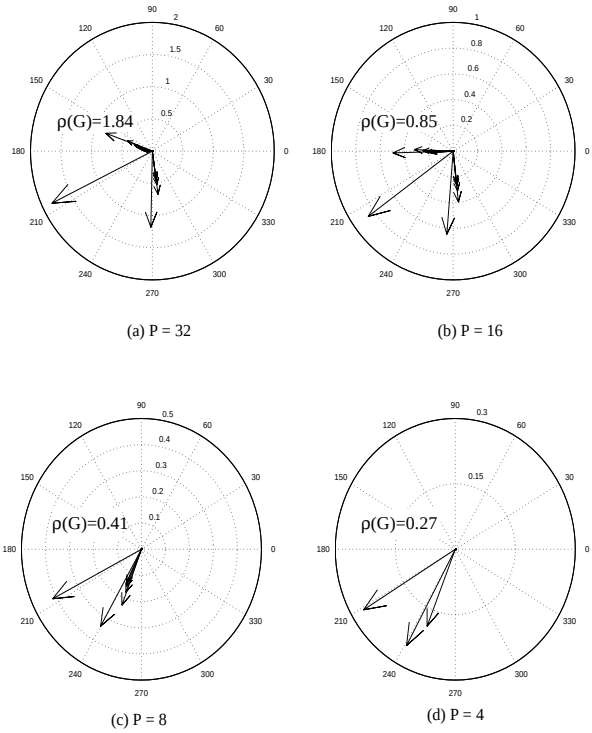

Fig. 4. Eigenvalue spectrum of G_M for various MSMM section sizes for a strip. (a) $D_P = 0.4\lambda$, (b) $D_P = 0.8\lambda$, (c) $D_P = 1.6\lambda$, and (d) $D_P = 3.2\lambda$.

in the MSMM is reduced without limit. This implies that the MOMI (or Forward-Backward method) solution (which corresponds to MSMM with $P = 128$, or $D_P = 0.1\lambda$) also diverges for this case.

The convergence in terms of the residual errors for various initial guess vectors is shown in Figs. 5 and 6 for section sizes of $D_P = 1.6\lambda$ and $D_P = 0.4\lambda$, respectively. As seen from the figures, using the MSMM first sweep current (which uses R-cards) as an initial guess vector for the iterative method results in the lowest error, and using the PO current as an initial guess gives slightly lower error than the zero initial guess vector. The MSMM first sweep has a physical interpretation, i.e., it includes the dominant interactions on the scattering geometry. Hence, it exhibits the lowest error for a given number of iterations compared with PO and zero initial guess vectors. As predicted by the eigenvalue spectrum of G_M for $D_P = 0.4\lambda$ in Fig. 4(a), the method is expected to diverge for any initial start vector, as verified in Fig. 6. As seen in both Figs. 5 and 6, the rate of convergence (or divergence) is relatively independent of the start vectors. So in some cases it may be more efficient to use PO as the start vector and perform a few more iterations than to use the more computationally complex R-card treatment.

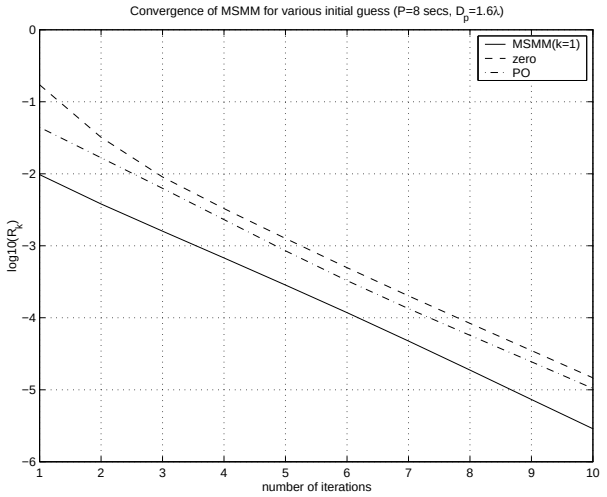

Fig. 5. Convergence of MSMM for various initial guesses for a strip with $P = 8$ ($D_P = 1.6\lambda$).

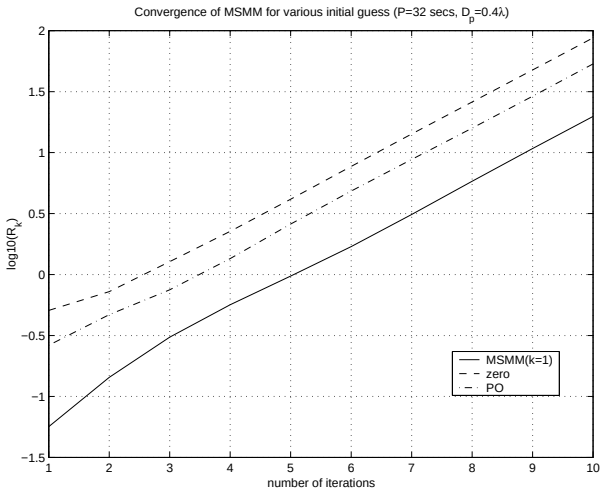

Fig. 6. Convergence of MSMM for various initial guesses for a strip with $P = 32$ ($D_P = 0.4\lambda$).

B. Circular Cylinder

In this section the effect of having various aperture sizes in the circular cylinder of Fig. 3(b) on the eigenvalue spectrum of the iteration matrix G_M is investigated. The cylinder is broken up into MSMM sections starting at the lower lip of the aperture and proceeding counter-clockwise around the cylinder boundary. Figure 7 shows the eigenvalue spectrum of G_M for two MSMM section sizes for a closed cylinder (no aperture) of radius $12\lambda/\pi$. In this case the method diverges for any choice of section size, even with only 2 sections. The reason may be partially due to the EFIE (or MFIE) formulation for closed surfaces which can result in a poorly conditioned or even singular system matrix $[Z]$, due to internal resonances. A combined field integral equation

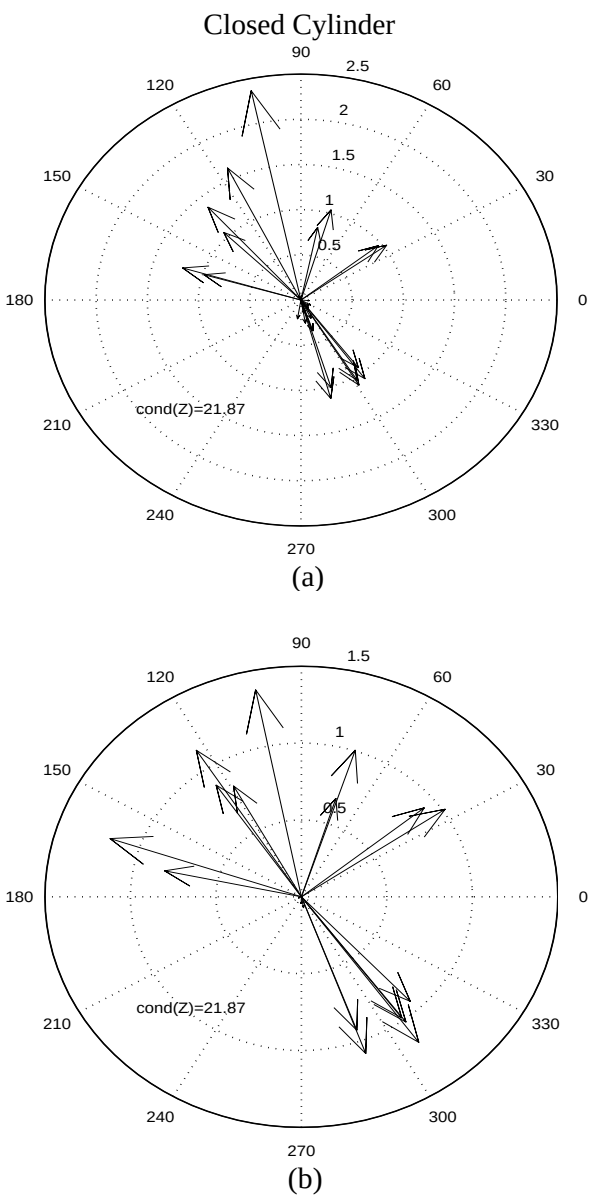

Fig. 7. Eigenvalue spectrum of G_M for two different numbers of MSMM sections for a closed cylinder. (a) $P = 12$, (b) $P = 2$.

(CFIE) formulation would be one way to avoid the internal resonance effects, and hence result in a better conditioned matrix [31]. A summary of various other approaches for overcoming the effect of internal resonances can be found in [32], [33].

The eigenvalue spectrum of G_M for the cylinder with an aperture opening of $\theta = 5°$, using $P = 2$ MSMM sections is shown in Fig. 8(a). The method still exhibits large eigenvalues, hence, the iterations show divergent behavior (i.e. $\rho(G_M) > 1$). Figures 8(b) and (c) show the eigenvalue spectrum of G_M for the aperture sizes of $\theta = 30°$ and $\theta = 60°$, respectively, with $P = 8$ MSMM sections. As the

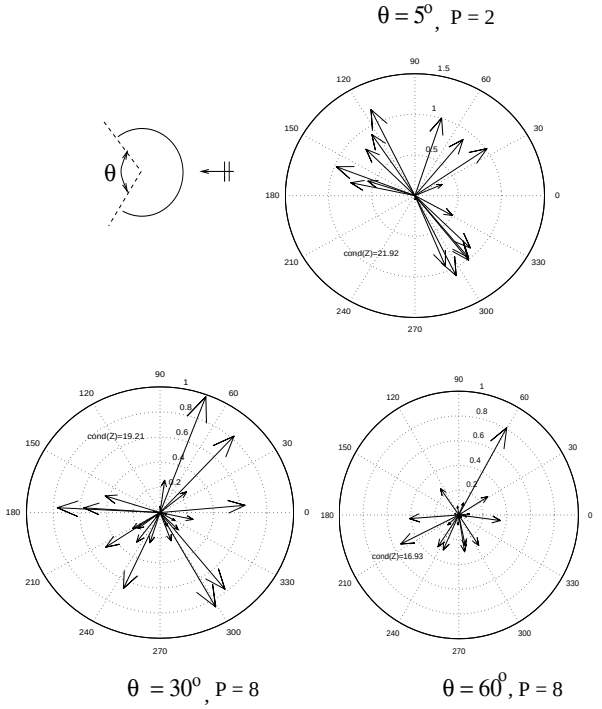

Fig. 8. Eigenvalue spectrum of G_M for open cylinder with (a) $\theta = 5°$, $P = 2$, (b) $\theta = 30°$, $P = 8$, (c) $\theta = 60°$, $P = 8$.

aperture size increases, the rate of convergence of the MSMM also increases, i.e., $\rho(G_M)$ gets smaller. This is due to the fact that increasing the aperture size reduces the interior resonance effects, or "ringing."

C. Rough Surface

The rough sea surface geometry sketched in Fig. 3(c) is a randomly generated realization of a Gaussian random process with a Pierson-Moskowitz ocean spectrum for a given wind speed [34]. The length of the surface is 12.8 m. We consider the following cases in this section:

Case 1: EFIE formulation for TE_z scattering,
Case 2: EFIE formulation for TM_z scattering,
Case 3: MFIE formulation for TE_z scattering.

For Case 1 the wind speed is 10 m/s which gives rise to an RMS surface roughness of 0.54 m. The results are shown in Fig. 9 for various MSMM section sizes. As the number of MSMM sections increases, the convergence rate of the MSMM decreases. Also, notice that if the number of sections is 32 or larger, the method diverges; therefore, MOMI cannot produce a convergent result for this case which would correspond to $P = N = 128$ sections.

A wind speed of 15 m/s (RMS roughness 1.106 m) is used for Cases 2 and 3. The results for Case 2 are shown in Fig. 10. It is seen that the method converges even if the section size is reduced to the cell

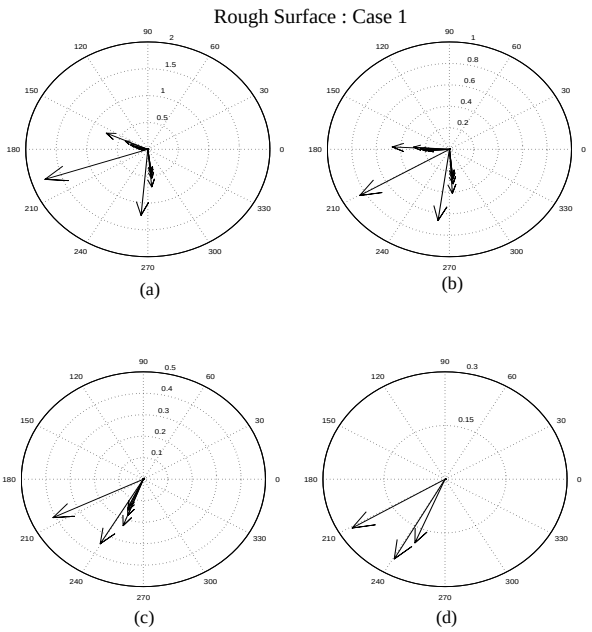

Fig. 9. Eigenvalue spectrum of G_M for the rough surface with 10 m/s wind speed. Case 1: EFIE for TE_z polarization. (a) $P = 32$, $D_P = 0.4\lambda$, (b) $P = 16$, $D_P = 0.8\lambda$, (c) $P = 8$, $D_P = 1.6\lambda$, (d) $P = 4$, $D_P = 3.2\lambda$.

size, i.e. $D_P = 0.1\lambda$, so the MOMI is also expected to converge for this case. It is interesting to note that the eigenvalues are closely grouped, suggesting that a more optimum iterative algorithm could be constructed [26].

The results for Case 3, which makes use of the MFIE formulation, is shown in Fig. 11. The spectral radius is very small compared with the EFIE formulation, so the convergence rate is greatly increased by using the MFIE. Also note that the method converges for $D_P = 0.1\lambda$, i.e., MOMI (or FB) also converges for this case. Hence, the MFIE formulation is well suited for these types of iterative methods. However, one should be aware that the MFIE formulation is technically valid only for closed surfaces, although it is often used for finite rough surface scattering problems.

D. Rough Surface with a Ship−Like Target

The problem geometry considered in this section is sketched in Fig. 3(d), and shown in Fig. 12. The EFIE formulation for TM_z scattering is used to produce the $[Z]$ matrix. The MSMM sections are assumed to have about the same number of modes. No attempt has been made to make the sections of the same length, and have varying numbers of modes on the sections. Therefore, the length of the section which has the target will be significantly smaller than

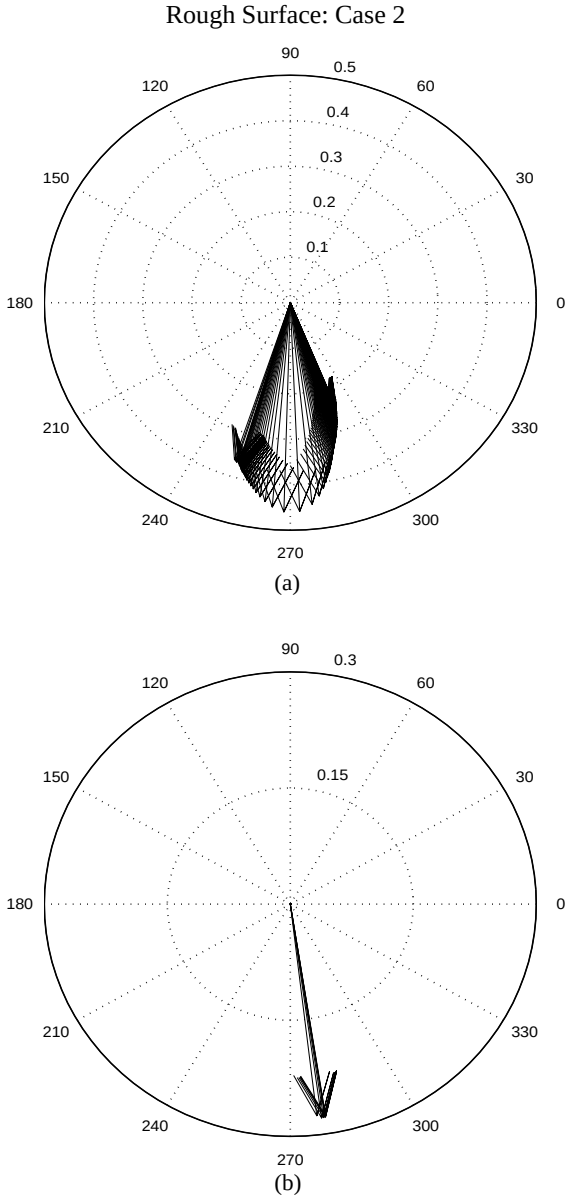

Fig. 10. Eigenvalue spectrum of G_M for the rough surface with 15 m/s wind speed. Case 2: EFIE for TM_z polarization. (a) $P = N = 128$, $D_P = 0.1\lambda$, (b) $P = 8$, $D_P = 1.6\lambda$.

the other sections which do not have the target. However, the three dimensional results that have been presented in [20] and [21] may have different numbers of modes on each section.

Figure 12 shows the eigenvalue spectrum for the MOMI (or FB method), i.e., the MSMM section size is $D_P = 0.1\lambda$. There are two large eigenvalues that cause the algorithm to diverge. However, as the section size is increased, the MSMM converges quite rapidly as seen in Fig. 13. In the case of Fig. 13(a) the ship-like geometry is part in one section, part in another, and the method still produces convergent

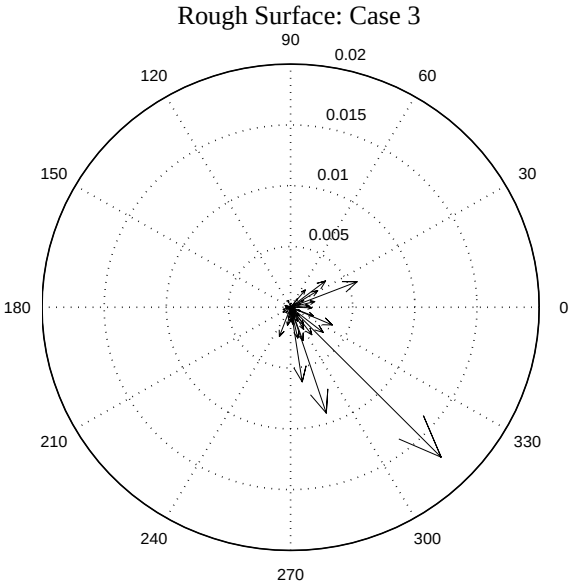

Fig. 11. Eigenvalue spectrum of G_M for the rough surface with 15 m/s wind speed. Case 3: MFIE for TE_z polarization. (a) $P = N = 128$, $D_P = 0.1\lambda$, (b) $P = 8$, $D_P = 1.6\lambda$.

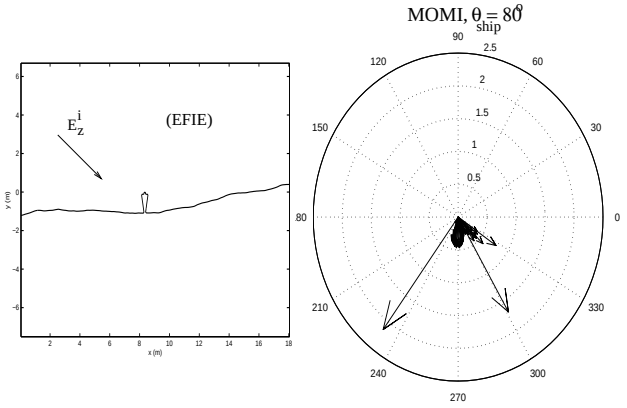

Fig. 12. MOMI: Eigenvalue spectrum of G_M for the rough surface with a 2D target. $P = N = 210$.

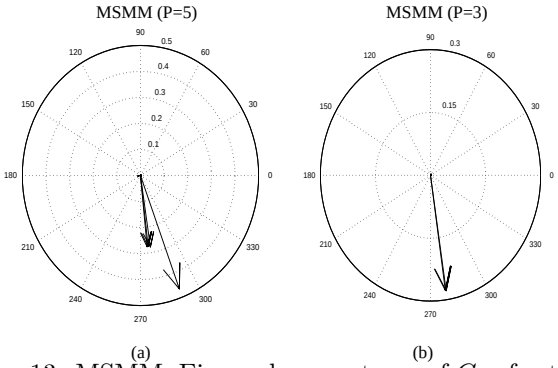

Fig. 13. MSMM: Eigenvalue spectrum of G_M for the rough surface with a 2D target. (a) $P = 5$, (b) $P = 3$.

results. However, the MOMI (or FB method) does not show convergent behavior if there is a target (or other strongly coupled region such as a breaking wave) on the surface.

V. CONCLUSIONS

The convergence properties of the Multiple Sweep Method of Moments (MSMM) has been studied both analytically and numerically for some classes of 2D scattering geometries. A connection between the MSMM and well-known classical iterative methods in mathematics is established so that the convergence properties of the MSMM can be investigated using matrix theory. The MSMM is shown to be mathematically equivalent to a block Jacobi preconditioned system of equations that results from the moment method, and solved via block symmetric successive over-relaxation (SSOR) with relaxation factor $\omega = 1$ (i.e., block Forward Backward Gauss-Seidel method). Based on this connection, the convergence difficulties (such as for the closed cylinder) can be explained by examining the eigenvalue distribution of the iteration matrix G defined for any stationary iterative method. In addition, the MSMM can be compared with other recently developed iterative methods for rough surface scattering problems such as the Method of Ordered Multiple Interactions (MOMI), or Forward-Backward (FB) Method, from both theoretical and numerical points of view. The results show that the MSMM converges for some problems for which the MOMI (and FB) fails to converge, e.g., the rough surface with a target on it, or a multi-valued surface which has large off-diagonal elements in the interaction matrix. It is also shown that the MSMM can be reduced to the MOMI if the block section size reduces to a single Method of Moments segment size, and the initial start vector is set to zero.

It has been shown in earlier works that the point SSOR (and hence MOMI and FB methods) is strongly effected by the ordering of the elements. It is because of the fact that changing the ordering of the elements results in a different iteration matrix G, that the iterative procedure may have different convergence properties. Hence, convergence may be a problem, especially for 2D surfaces (3D scattering problems) because a sequential ordering of elements is difficult to achieve. The convergence of the MSMM has no sensitivity to a change in the ordering of the elements because the ordering of groups becomes important rather than the elements. However, if the size of the blocks is reduced to the size of one element, the MSMM essentially becomes the MOMI and will have the same difficulties with convergence.

The effect of using different integral equation formulations (EFIE or MFIE) and the polarization of the incident field (TE_z or TM_z) on the convergence of the MSMM are also considered and the results are compared with the MOMI. The EFIE with TE_z polarization is found to have the worst divergence problem if a small block size is used, and the MFIE with TE_z polarization has extremely good convergence for any block size. The convergence is also affected by the geometry, and high Q structures such as the closed or partially open cylinder may not converge for any choice of block size (except, of course, when the entire geometry is in one block).

Guidelines for the implementation of the MSMM and some suggestions for the choice of an optimum P are presented in [35]. It has been found that as the MSMM section size increases (or the number of MSMM sections decreases) the rate of the convergence of the method also increases, i.e., $\rho(G_M)$ gets smaller. However, increasing the section size also increases the CPU time to factorize the $[Z_{pp}]$ block matrices. For the strip (also for the rough surface) the optimum section size is found to be $D_P \approx 1\lambda$. However, it is not easy to generalize this conclusion for an arbitrary geometry because every geometry has a different convergence behavior with respect to the section size. Furthermore, it is not easy to predict the $\rho(G_M)$ a priori for a given MSMM section size. As a rule of thumb, one can apply the following procedure. For a given a problem geometry, first include any target or high Q geometry in one MSMM section. As a result, the $[Z]$ matrix will have less significant off-diagonal blocks. Next, the smooth part of the geometry can be sectioned into $D_P = 1\lambda$ width MSMM sections. However, if the entire geometry is a high Q structure, such as a closed cylinder, then a better integral equation formulation could be used to make the MSMM converge.

REFERENCES

[1] R. F. Harrington, *Field Computation by Moment Methods*, Krieger, Malarbar FL, 1982.

[2] E. K. Miller, L. Medgyesi-Mitschang and E.H. Newman, *Computational Electromagnetics - Frequency-Domain Method of Moments,* IEEE Press, New York, 1992.

[3] R. C. Hansen, *Moment Methods in Antennas and Scattering,* Artech, Boston, 1990.

[4] E. H. Newman and I. Tekin, "An Overview of the Method of Moments Analysis of Large Systems," in *Nat. Res. Council Symp. Large-Scale Structures,* National Academy of Sciences, Washington, D.C., pp. 204-220, Sept. 1994.

[5] T. K. Sarkar, K. R. Siarkiewicz, and R. F. Stratton, "Survey of Numerical Methods for Solutions of Large Systems of Linear Equations for Electromagnetic Field Problems," *IEEE Trans. on An-*

tennas and Prop. vol. AP-29, pp. 847-856, Nov. 1981.

[6] T. K. Sarkar, and E. Arvas, "On a class of finite-step iterative methods (conjugate directions) for the solution of an operator equation arising in electromagnetics," *IEEE Trans. on Antennas and Prop.* vol. 33, no. 9, pp. 1058-1066, Oct. 1985.

[7] G. Brown (ed) "Special Issue on Low-Grazing-Angle Backscatter from Rough Surfaces", *IEEE Trans. on Antennas and Propagat.*, vol. 46, no. 1, Jan. 1998.

[8] E. I. Thorsos, and D. Jackson, "Studies of scattering theory using numerical methods," *Waves in Random Media* vol. 1, pp. 165-190, 1991.

[9] D. J. Wingham, and R. H. Devayya, "A note on the use of the Neumann expansion in calculating scatter from rough surfaces," *IEEE Trans. Antennas Propagat.*, vol. 40, pp. 560-563, May 1992.

[10] P. Tran, V. Celli, and A. A. Maradudin, "Electromagnetic scattering from a two-dimensional, randomly rough, perfectly conducting surface: Iterative methods," *J. Opt. Soc. Amer.* A. vol. 11, pp. 1686-1689, 1994.

[11] L. Tsang, C. H. Chang, K. Pak, and H. Sangani, "Monte Carlo simulations of large-scale problems of random rough surface scattering and applications to grazing incidence with the BMIA/canonical grid method," *IEEE Trans. on Antennas and Prop.* vol. 43, pp. 851-859, Aug. 95.

[12] J. T. Johnson, "On the canonical grid method for two-dimensional scattering problems," *IEEE Trans. on Antennas and Prop.* vol. 46, no. 3, pp. 297-302, March 1998.

[13] D. J. Donohue, H. C. Ku, and D. R. Thompson, "Application of iterative moment-method solutions to ocean surface radar scattering," *IEEE Trans. Antennas Propagat.*, vol. 46, no. 1, pp. 121-132 Jan. 1998.

[14] D. Holliday, L.L. DeRaad, and G. J. St-Cyr, "Forward-Backward: A new method for computing low-grazing angle scattering," *IEEE Trans. Antennas Propagat.*, vol. 44, pp. 722-729, May 1996.

[15] D. A. Kapp, and G. S. Brown, "A new numerical method for rough surface scattering calculations," *IEEE Trans. Antennas Propagat.*, vol. 44, pp. 711-721, May 1996.

[16] P. Tran, "Calculation of the scattering electromagnetic waves from a two-dimensional perfectly conducting surface using the method of ordered multiple interactions," *Waves in Random Media*, vol. 7, no. 3, pp. 295-302, July 1997.

[17] J. C. West, and J. M. Sturm, "On Iterative Approaches for Electromagnetic Rough-Surface Scattering Problems," *IEEE Trans. on Antennas and Prop.*, vol. 47, no. 8, pp. 1281-1288, August 1999.

[18] M. R. Pino, L. Landesa, J. L. Rodriguez, F. Obelleiro, and R. J. Burkholder, "The Generalized Forward-Backward Method for analyzing the scattering from targets on ocean-like rough surfaces," *IEEE Trans. Antennas Propagat.*, vol. 47, no. 6, pp. 961-969, 1999.

[19] D. Torrungrueng and E. H. Newman, "The Multiple Sweep Method of Moments (MSMM) Analysis of Electrically Large Bodies," *IEEE Trans. on Antennas and Prop.*, vol. 45, no. 8, pp. 1252-1259, Aug. 1997.

[20] D. Çolak, and E. H. Newman, "The Multiple Sweep Method of Moments (MSMM) design of wide-band antennas," *IEEE Trans. on Antennas and Propagat.*, vol. 46, pp. 1365-1371, Sept. 1998.

[21] D. Çolak, R. J. Burkholder, and E. H. Newman, "The Multiple Sweep Method of Moments Analysis of Electromagnetic Scattering from 3D Targets on Ocean-Like Rough Surfaces," *IEEE Trans. on Geoscience and Remote Sensing,* vol. 49, no. 1, pp. 241-247, January 2007.

[22] K. R. Umashankar, S. Nimmagadda, and A. Taflove, "Numerical Analysis of Electromagnetic Scattering by Electrically Large Objects Using Spatial Decomposition Technique," *IEEE Trans. on Antennas and Propagat.*, vol. AP-40, pp. 867-877, Aug. 1992.

[23] E. H. Newman and J. L. Blanchard, "TM Scattering by an Impedance Sheet Extension of a Parabolic Cylinder," *IEEE Trans. on Antennas and Prop.,* vol. AP-36, pp. 527-534, April 1988.

[24] T. B. A. Senior and J. L. Volakis, "Sheet Simulation of a Thin Dielectric Layer," *Radio Sci.*, vol. 22, pp. 1261-1272, Dec. 1987.

[25] T. B. A. Senior, "Backscattering from Resistive Strips," *IEEE Trans. on Antennas and Prop.*, vol. AP-27, pp. 808-803, Nov. 1979.

[26] G. H. Golub, and C. F. Van Loan, Chapter 10 in Matrix Computations, Second Edition, The Johns Hopkins University Press, Baltimore, 1989.

[27] R. Barrett, M. Berry, T. Chan, J. Demmel, J. Donato, J. Dongarra, V. Eijkhout, R. Pozo, C. Romine, and H. van der Vorst, *Templates for the solution of linear systems: Building blocks for iterative methods,* SIAM, Philadelphia, PA, 1994.

[28] R. J. Burkholder, "On the use of classical iterative methods for electromagnetic scattering problems" in 4^{th} *Conf. on Electromag. and Light Scat. by Nonspherical Particles: Theory and Applications (Digest)*, pp. 65-72, Sept. 1999.

[29] D. M. Young, *Iterative Solution of Large Linear Systems,*, Academic Press, New York, 1971.

[30] G. Dudley, "Error Minimization and Conver-

gence in Numerical Methods," *Electromagnetics,* vol. 5, no. 2-3, pp. 89-97, 1985.

[31] R. J. Adams, and G. S. Brown, "A combined field approach to scattering from infinite elliptical cylinders using the method of ordered multiple interactions," *IEEE Trans. on Antennas and Prop.,* vol. 47, no. 2, pp. 364-375, Feb. 1999.

[32] R. Mittra, and C. A. Klein, "Stability and Convergence of Moment Method Solutions," Chapter 5, in *Numerical and Asymptotic Techniques in Electromagnetics*

[33] A. F. Peterson, S. L. Ray, and R. Mittra, *Computational Methods for Electromagnetics*, Institute of Electrical and Electronics Engineers, New York, 1998.

[34] W. J. Pierson and L. Moskowitz, "A proposed spectral form of fully developed wind seas based on the similarity theory of S. A. Kitaigorodskii," *J. Geophys. Res.* vol. 69, pp. 5181-5190, 1964.

[35] D. Colak, "The Multiple Sweep Method of Moments (MSMM) Analysis of Three Dimensional Radiation and Scattering Problems," *Ph.D. Dissertation*, The Ohio State University, Dec. 2000.

Dilek Colak received the B.S. and M.S. in electrical and electronics engineering from Bilkent University, Ankara, Turkey, in 1991 and 1993, respectively, and Ph.D. degree in electrical engineering from The Ohio State University, Columbus in 2000. She worked at Bell Laboratories, Lucent Technologies, Murray Hill, NJ in 2000-2002 as a professional scientist. She is currently working at Biostatistics, Epidemiology and Scientific Computing of the King Faisal Specialist Hospital and Research Centre as a scientist. Her research interests are in the areas of computational electromagnetics, wireless communications, computational bioinformatics, and development of new methodologies for the analysis of high throughput data. She is currently working on the development and application of statistical and computational methods for the analysis of biomedical and genomic data, assessing reliability/agreement of new measurement scales/methods, bioequivalence studies, and computational bioinformatics. Dr. Colak was a recipient of the Young Scientist Award of the International Union of Radio Science (URSI) at the 24th General Assembly in 1993. She is a member of IEEE and Applied Computational Electromagnetic Society.

Robert J. Burkholder received the B.S., M.S., and Ph.D. degrees in electrical engineering from The Ohio State University, Columbus, in 1984, 1985, and 1989, respectively. Since 1989, he has been with The Ohio State University ElectroScience Laboratory, Department of Electrical and Computer Engineering, where he currently is a Senior Research Scientist and Adjunct Professor. Dr. Burkholder has contributed extensively to the EM analysis of large cavities, such as jet inlets/exhausts, and the scattering from targets over a rough sea surface. He is currently working on the more general problem of EM radiation, propagation and scattering in realistically complex environments. His research specialties are high-frequency asymptotic techniques and their hybrid combination with numerical techniques for solving large-scale electromagnetic radiation and scattering problems. Dr. Burkholder is a Fellow of the IEEE, an elected Full Member of URSI, Commission B, a member of the American Geophysical Union, and a member of the Applied Computational Electromagnetics Society. He is currently serving as an Associate Editor for IEEE Antennas and Wireless Propagation Letters.

Edward H. Newman was born in Cleveland Ohio on July 9, 1946. He received the BSEE, MS, and PhD degrees in electrical engineering from The Ohio State University in 1969, 1970, and 1974, respectively. Since 1974 he has been a member of the Ohio State University, Department of Electrical Engineering, ElectroScience Laboratory, where he is currently a Professor. His primary research interest is in the development of method of moments techniques for the analysis of general antenna or scattering problems, and he is the primary author of the "Electromagnetic Surface Patch Code" (ESP). Other research interests include electromagnetic shielding and antennas on automobiles, aircraft and similar platforms. He has published over 60 journal articles in these areas, and is a coauthor of the IEEE Press book "Computational Electromagnetics (Frequency Domain Method of Moments)". Dr. Newman is a Fellow of the IEEE, and is a member of Commission B of URSI and the Electromagnetics Institute. He is a recipient of the 1986 and 1992 College of Engineering Research Award, and is a past chairman of the Columbus sections of the IEEE Antennas and Propagation and Microwave Theory and Techniques Societies.

Semi-analytical Approach to Sensitivity Analysis of Lossy Inhomogeneous Structures

†Shirook M. Ali, ‡Natalia K. Nikolova, and ‡Mohamed H. Bakr

† Research In Motion Ltd.
Waterloo, Ontario, N2L 3L3, Canada

‡ Department of Electrical and Computer Engineering, McMaster University
Hamilton, Ontario, L8S 4K1, Canada

E-mail: shali@rim.com, talia@mcmaster.ca, mbakr@ece.mcmaster.ca

Abstract **–** We propose an adjoint-variable technique for sensitivity analysis with structured-grid EM solvers, which can handle lossy inhomogeneous materials. In previous discrete adjoint-based approaches, the response derivatives with respect to shape parameters require the solution of a perturbed geometry, which has to be approximated. Here, we improve the algorithm by proposing a semi-analytical sensitivity formula where the system matrix derivatives consist of an analytical and a finite-difference term. It allows the use of the solution of the unperturbed structure with no approximation, which improves the accuracy. Applications are based on a frequency-domain solver based on the transmission line method.

Index Terms – Sensitivity analysis, adjoint variable method, lossy dielectrics, complex permittivity, and frequency-domain transmission line method.

I. INTRODUCTION

The adjoint variable method (AVM) is the most efficient method for sensitivity analysis, see, e.g., [1] - [6]. Discrete adjoint-based techniques (DAVM) have been proposed for implementation with high-frequency structured-grid time-domain [3] -[5] and frequency-domain [6]], [7] solvers. The response gradient is computed with two full-wave simulations – of the original problem and the adjoint problem – regardless of the number of parameters of interest.

All preceding discrete adjoint-based techniques have been developed for implementation exclusively with loss-free homogenous problems, where the parameters of interest are either shape parameters of perfectly conducting details [3] - [6] or dielectric details [5], [7]. All these techniques require either the solution of the perturbed original problems [6], [7] or the solution of the perturbed adjoint problems [3] - [6]. The solution to these perturbed problems is approximated using a simple mapping between the original and the perturbed field solutions [3], [4], [6]. This is necessary to avoid the K additional full-wave analyses, K being the number of parameters of interest.

Most practical problems involve lossy inhomogeneous mediums. Examples include detection of tumors in the human body, nondestructive testing and evaluation (NDT/NDE) [8], etc. The solution to these problems often employs optimization algorithms whose efficiency is significantly improved by the availability of the response gradient.

In this paper, we address the sensitivity analysis for problems involving lossy inhomogeneous materials. We first investigate the application of our preceding discrete adjoint-based technique [6], [7] to the sensitivity analysis of lossy inhomogeneous problems. Such an investigation is carried out for the first time. This technique requires the approximation of the solutions of the perturbed original problems. Next, we propose an improvement of this technique based on a semi-analytical sensitivity formula. The newly developed formula requires the solution of the original unperturbed problem only. Hence, it avoids any solution approximations. This approach allows us to obtain sensitivities with respect to shape parameters using the complex permittivity as well as its real or imaginary part as intermediate variables in the new sensitivity expression.

We start by giving a brief description of the frequency-domain transmission line method and its implementation with lossy and inhomogeneous materials in section II. In section III, we give a brief background of preceding adjoint-based techniques. Our proposed semi-analytical formula for sensitivity analysis is given in section IV. Verification results are presented in section V. Conclusions are drawn in section VI.

II. THE FREQUENCY-DOMAIN TLM METHOD WITH LOSSY DIELECTRICS

The frequency-domain transmission line method (FDTLM) [9] carries out a sequence of scattering and connection processes among its TLM symmetrical condensed node(s) (SCN) in a similar way as in the time-domain transmission line method (TDTLM) [10]. An equation is written for each link of the SCN relating its voltages to those from neighboring nodes. These voltages are delayed through propagation factors of the type $e^{-\gamma_l \delta/2}$ where δ is the node size along the lth link. The propagation constant γ_l is

$$\gamma_l = j\omega\sqrt{\mu\tilde{\varepsilon}} \tag{1}$$

where

$$\tilde{\varepsilon} = \varepsilon_o \varepsilon_r - j\,\sigma/\omega\,. \tag{2}$$

In equation (1), ω is the angular frequency; $\tilde{\varepsilon}$, ε_r, μ and σ are the complex permittivity, the relative permittivity, the permeability and the conductivity, respectively. Local variations in the material properties are modeled by modifying the propagation constants of the node links. With lossy materials, the voltage waves are multiplied by a complex exponential factor.

When the equations for all the links in all the nodes are put together, we arrive at

$$\boldsymbol{A}\cdot\boldsymbol{v} = \boldsymbol{V}_s\,. \tag{3}$$

Here, $\boldsymbol{A} \in \mathbb{C}^{12N_t \times 12N_t}$ is the system matrix, $\boldsymbol{v} \in \mathbb{C}^{12N_t \times 1}$ is the solution vector containing all incident voltages in the computational domain, and $\boldsymbol{V}_s \in \mathbb{C}^{12N_t \times 1}$ is the excitation. All quantities in equation (3) are complex with N_t being the total number of TLM nodes in the computational domain.

III. BACKGROUND

Our objective is to efficiently compute the sensitivity of a response function $f\left(\boldsymbol{x}, \boldsymbol{v}(\boldsymbol{x})\right)$ with respect to changes in the vector of parameters $\boldsymbol{x} = [x_1 \ldots x_K]^T$, i.e., $\nabla_{\boldsymbol{x}} f$. Note that $\nabla_{\boldsymbol{x}}$ is defined as a row operator [1],

$$\nabla_{\boldsymbol{x}} f = \left[\frac{df}{dx_1} \;\cdots\; \frac{df}{dx_K}\right]. \tag{4}$$

The elements in $\boldsymbol{x}$ could be related to the material parameters of the structure and/or to its shape. We introduce in this section possible implementations of the AVM for sensitivity analysis with full-wave frequency-domain solvers.

A. The Exact AVM

With the exact AVM, the response derivative with respect to the kth parameter x_k is obtained as [2], [6]

$$\frac{df}{dx_k} = \frac{\partial f}{\partial x_k} + \boldsymbol{\lambda}^H \cdot \left[\frac{\partial \boldsymbol{V}_s}{\partial x_k} - \frac{\partial \boldsymbol{A}}{\partial x_k}\cdot\boldsymbol{v}\right], \quad k = 1,\ \ldots,\ K. \tag{5}$$

In equation (5), $\partial/\partial x_k$ represents an explicit dependence on x_k; $\boldsymbol{v}$ is the solution of equation (3); and $\boldsymbol{\lambda}^H$ is the Hermitian of the adjoint variable vector $\boldsymbol{\lambda}$. It is the solution of the adjoint problem

$$\boldsymbol{A}^H \cdot \boldsymbol{\lambda} = [\nabla_{\boldsymbol{v}} f]^H\,. \tag{6}$$

Here, $\boldsymbol{A}^H$ is the Hermitian of the system matrix $\boldsymbol{A}$. $\nabla_{\boldsymbol{v}} f$ is the adjoint excitation, which is the gradient of the response f relative to the state variables in $\boldsymbol{v}$.

The sensitivity equation (5) is exact in the sense that all three required derivatives – including the system matrix derivative $\partial\boldsymbol{A}/\partial x_k$ – are exact, i.e., analytic. The accuracy of the computed sensitivities is affected by the accuracy of the solution vectors $\boldsymbol{\lambda}$ and $\boldsymbol{v}$, which depends on the accuracy of the numerical solver.

It is straightforward to use equation (5) for sensitivity estimates with respect to material parameters of the structure such as the constitutive parameters ε_r and σ. Its implementation with shape parameters, however, is very limited [7].

B. The Discrete AVM

With structured grid solvers $\partial\boldsymbol{A}/\partial x_k$ is rarely available analytically for shape parameters. The discrete AVM (DAVM) overcomes this limitation. It determines the derivative with respect to the kth parameter x_k as in [7],

$$\frac{df}{dx_k} \approx \frac{\partial f}{\partial x_k} + \boldsymbol{\lambda}^H \cdot \left[\frac{\Delta_k \boldsymbol{V}_s}{\Delta x_k} - \frac{\Delta_k \boldsymbol{A}}{\Delta x_k}\cdot\tilde{\boldsymbol{v}}_k\right], \quad k = 1,\ \ldots,\ K. \tag{7}$$

Here, $\Delta_k \boldsymbol{A}$ is the difference matrix due to a stepwise perturbation of $\Delta x_k = \delta$ in x_k. The difference ratio $\Delta_k \boldsymbol{A}/\Delta x_k$ is, in general, not a good approximation of $\partial\boldsymbol{A}/\partial x_k$, and using it directly with equation (5) leads to unacceptable errors. Therefore, the solution of the kth perturbed problem $\tilde{\boldsymbol{v}}_k$ is required with such discrete perturbations. The perturbed solutions $\tilde{\boldsymbol{v}}_k$, $k = 1,\ \ldots,\ K$, are not obtained by actually solving the problems, since this would require K additional system analyses. They are approximated through

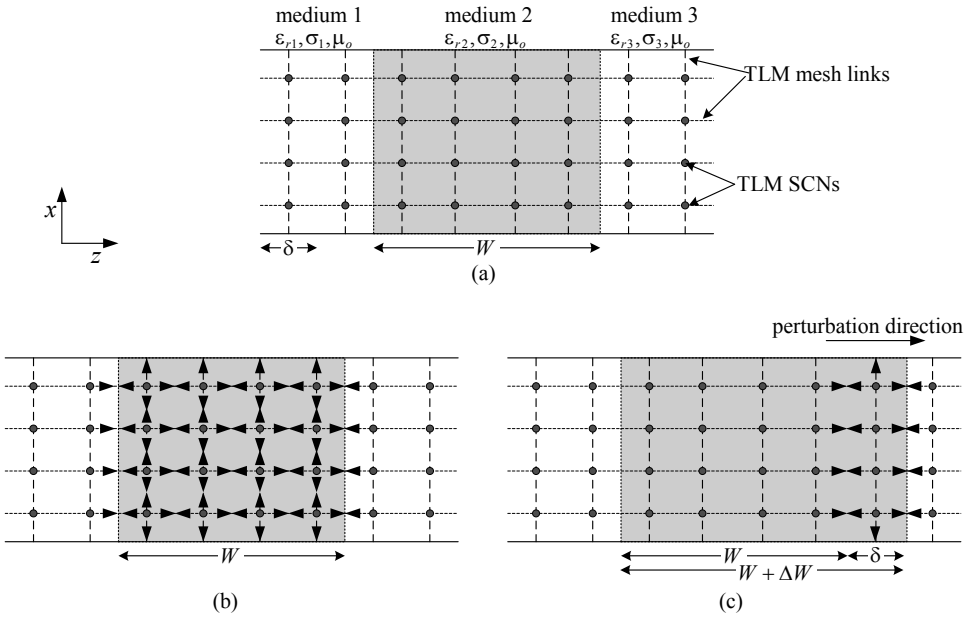

Fig. 1. Computing the analytical derivative of the system matrix $\partial \boldsymbol{A}/\partial\tilde{\varepsilon}$ for response sensitivity evaluation (2D view): (a) the unperturbed problem, (b) the nonzero elements of $\partial \boldsymbol{A}/\partial\tilde{\varepsilon}$ when computing $df/d\tilde{\varepsilon}$ with the exact AVM approach, and (c) the nonzero elements of $\partial \boldsymbol{A}/\partial\tilde{\varepsilon}_n$ when computing df/dW with the semi-analytical AVM approach.

mappings of the solution of the unperturbed problem (3). Hence, equation (7) requires K approximations of $\tilde{\boldsymbol{v}}_k$ ($k = 1, \ \ldots, \ K$) [7].

The discrete sensitivity, equation (7), is advantageous over the exact, equation (5), because of its versatility. It can be used for sensitivities with respect to material-related parameters as well as shape parameters. Its implementation with lossy materials deserves special consideration and is addressed here for the first time.

IV. THE SEMI-ANALYTICAL SENSITIVITY FORMULA

An appealing feature of the TLM solver in the frequency domain is the direct analytical relation between the system matrix $\boldsymbol{A}$ and the constitutive parameters of the SCNs. This relation is identified through the propagation factor γ_l as well as the transmission and reflection coefficients at the boundaries between the different regions in the computational domain, see equations (1) to (3). This feature allows us to derive an alternative approach to equation (4) in the case of lossy dielectric discontinuities. The approach combines the exact AVM and the DAVM. It employs the analytical dependence of the system matrix on the material properties of the SCNs. No approximations are required as in equation (7) and, unlike equation (5), it is versatile as it can be implemented with shape and material parameters.

Let $\{1, \ ..., \ m\}$ be the set of node indices whose dielectric properties change as the shape parameter x_k changes. We rewrite equation (5) as

$$\frac{df}{dx_k} = \frac{\partial f}{\partial x_k} + \boldsymbol{\lambda}^H \cdot \left[\frac{\partial \boldsymbol{V}_s}{\partial x_k} - \sum_{n=1}^{m} \left(\frac{\partial \boldsymbol{A}}{\partial \tilde{\varepsilon}_n} \frac{\partial \tilde{\varepsilon}_n}{\partial x_k} \right) \cdot \boldsymbol{v} \right], \quad k = 1, \ \ldots, \ K. \tag{8}$$

As before, the adjoint variable $\boldsymbol{\lambda}$ is the solution of equation (6). The matrix $\partial \boldsymbol{A}/\partial\tilde{\varepsilon}_n$ is the analytical derivative of the system matrix with respect to the dielectric constant of the *n*th perturbed node. This matrix is different from its analogous matrix in equation (5) as it is not a full matrix. It is a sparse matrix with nonzero elements only at locations corresponding to the *n*th node links.

Figure 1*a* illustrates a possible TLM discretization of a lossy inhomogeneous structure. The structure is composed of three dielectric mediums. Consider first the case when x_k is $\tilde{\varepsilon}_2$, or ε_{r2}, or σ_2. Here, the exact sensitivity, equation (5), can be directly applied with the term $\partial \boldsymbol{A}/\partial x_k$ obtained analytically, i.e., using common rules of differentiation. The nonzero elements in $\partial \boldsymbol{A}/\partial x_k$ correspond to all the links of the related

medium, i.e., medium 2, plus those at the boundary interfaces of medium 2 with medium 1 and medium 3 (see the arrowed links in Fig. 1b).

Now, consider another case when the thickness of the second medium W is the shape parameter of interest, i.e., we want to compute df/dW. Here, the exact sensitivity equation (5) can not be applied (refer to section III). Our semi-analytical equation (8), however, can be applied making use of the available $\partial \boldsymbol{A}/\partial\tilde{\varepsilon}$ values. In this case, a discrete perturbation of $\Delta W = \delta$ in W results in a derivative matrix $\partial \boldsymbol{A}/\partial\tilde{\varepsilon}_n$ with nonzero coefficients only at locations that correspond to the arrowed links shown in Fig. 1c. These are the links at the right-hand side of medium 2 affected by the discrete perturbation. The material change at these border cells is described mathematically in the sensitivity expression through the term $\left(\partial \boldsymbol{A}/\partial\tilde{\varepsilon}_n\right)\cdot\left(\partial\tilde{\varepsilon}_n/\partial x_k\right)$, see equation (8).

Note that equation (8) cannot be exact with structured grid solvers when x_k is related to a shape parameter such as *W*. This is because $\partial\tilde{\varepsilon}_n/\partial x_k$ is computed for each link of the *n*th perturbed node with $dx_k \approx \Delta x_k = \delta$ (stepwise change). Therefore, we approximate the analytical derivative $\partial\tilde{\varepsilon}_n/\partial x_k$ by its difference ratio $\Delta\tilde{\varepsilon}_n/\delta$, i.e., formula (8) becomes

$$\frac{df}{dx_k} = \frac{\partial f}{\partial x_k} + \boldsymbol{\lambda}^H \cdot \left[\frac{\partial \boldsymbol{V}_s}{\partial x_k} - \sum_{n=1}^{m}\left(\frac{\partial \boldsymbol{A}}{\partial\tilde{\varepsilon}_n}\frac{\Delta\tilde{\varepsilon}_n}{\delta}\right)\cdot \boldsymbol{v}\right], \quad k = 1, \ \ldots, \ K. \tag{9}$$

Despite this approximation, the semi-analytical sensitivity, equation (9) is still advantageous over equation (7) because the analytical derivative $\partial \boldsymbol{A}/\partial\tilde{\varepsilon}_n$ allows us to use the solution of the unperturbed problem (3). Thus, when the structure contains lossy dielectrics, we can use equation (9) and avoid the *K* approximations used in equation (7).

When x_k is related to a material parameter of the structure such as ε_r and σ, sensitivity equation (9) reduces to the exact equation (5).

Since all the elements of $\boldsymbol{A}$ are analytic functions of $\tilde{\varepsilon}$, see equations (1) to (2), the Cauchy-Riemann relations hold, allowing the use of $\tilde{\varepsilon}$, or ε_r, or σ in equation (9),

$$\frac{\partial \Re \boldsymbol{A}}{\partial \Re\tilde{\varepsilon}} = \frac{\partial \Im \boldsymbol{A}}{\partial \Im\tilde{\varepsilon}}, \quad \frac{\partial \Re \boldsymbol{A}}{\partial \Im\tilde{\varepsilon}} = -\frac{\partial \Im \boldsymbol{A}}{\partial \Re\tilde{\varepsilon}}. \tag{10}$$

Here, $\Re$ and $\Im$ denote the real and the imaginary part of the complex quantity, respectively. Consider, for example, the coefficients of the system matrix $\boldsymbol{A}$ that correspond to the links within the dielectric. According to the Cauchy-Riemann relations, equation (10), their analytical derivatives with respect to the constitutive parameters relate as

$$\begin{aligned}\frac{\partial \boldsymbol{A}}{\partial \varepsilon_r} &= \frac{\partial \Re \boldsymbol{A}}{\partial \varepsilon_r} + j\frac{\partial \Im \boldsymbol{A}}{\partial \varepsilon_r} \\ &= j\omega\varepsilon_0\left[\frac{\partial \Im \boldsymbol{A}}{\partial \sigma} - j\frac{\partial \Re \boldsymbol{A}}{\partial \sigma}\right] \\ &= \omega\varepsilon_0\left[\frac{\partial \Re \boldsymbol{A}}{\partial \sigma} + j\frac{\partial \Im \boldsymbol{A}}{\partial \sigma}\right] \\ &= \omega\varepsilon_0\frac{\partial \boldsymbol{A}}{\partial \sigma}.\end{aligned} \tag{11}$$

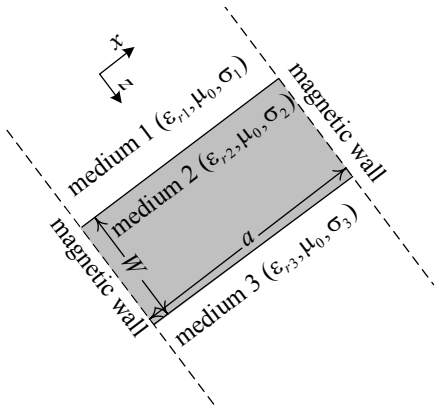

Fig. 2. 2D top view of the structure under study.

V. RESULTS AND DISCUSSION

The different AVM approaches discussed in sections III and IV are verified through the response sensitivity in a problem of a plane wave normally incident on a three-layer structure see Fig. 2. The structure is of width a = 30 mm and is discretized using a uniform 1 mm mesh cell, i.e., δ = 1 mm. The first layer of the structure, medium 1, has relative permittivity $\varepsilon_r = \varepsilon_{r1}$, permeability of free space μ_0, and conductivity σ=σ_1. The second layer, medium 2, is characterized by the constitutive parameters ε_{r2}, μ_0, σ_2, and is of thickness W. The third layer, medium 3, has the same constitutive parameters as medium 1, i.e., $\varepsilon_{r3} = \varepsilon_{r1}$, $\mu_3 = \mu_0$, and $\sigma_3 = \sigma_1$. The sensitivity of the response function f is measured with respect to variations in the vector of parameters $\boldsymbol{x} = [\varepsilon_{r2} \ \sigma_2 \ W]^T$ using applicable sensitivity expressions (5) to (9).

First, the response function f is defined as the complex electric field polarized in the *y*-direction

($f = E$) at the output port (medium 3). In this case, mediums 1 and 3 are set to be loss-free, i.e., $\sigma_1 = \sigma_2 = 0$, with $\varepsilon_{r1} = \varepsilon_{r3} = 1$. Medium 2 is lossy with nominal values $\varepsilon_{r2} = 5$ and $\sigma = 0.05$ S/m. The thickness is $W = 16$ mm. The sensitivities are computed at frequency 3.0 GHz.

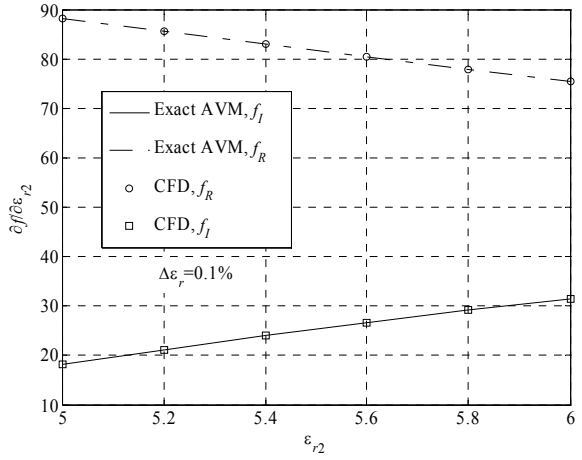

Fig. 3. Response sensitivity of $f = E$ with respect to ε_{r2} at the nominal value of $\tilde{\varepsilon}$, $f_R = \Re E$ and $f_I = \Im E$.

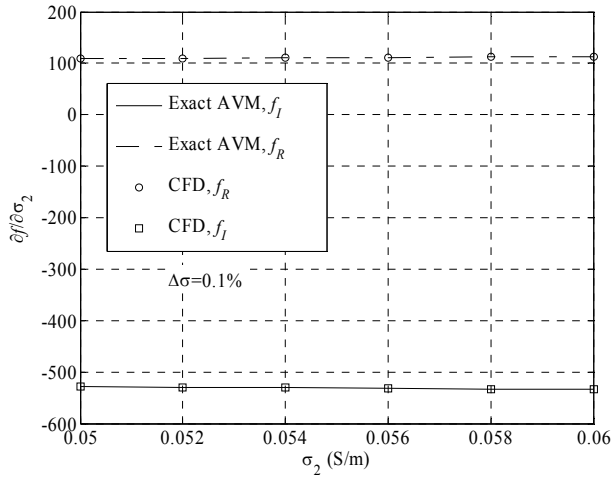

Fig. 4. Response sensitivity of $f = E$ with respect to σ_2 at the nominal value of $\tilde{\varepsilon}$, $f_R = \Re E$ and $f_I = \Im E$.

Figures 3 and 4 show the sensitivity of f with respect to the material parameters ε_{r2} and σ_2 computed using equation (5). These sensitivities are exact because the derivatives $\partial \boldsymbol{A}/\partial\varepsilon_{r2}$ and $\partial \boldsymbol{A}/\partial\sigma_2$ are analytic. Comparisons with response-level central finite difference (CFD) derivatives are also made using a finite perturbation of 0.1 percent. As expected, the agreement is excellent.

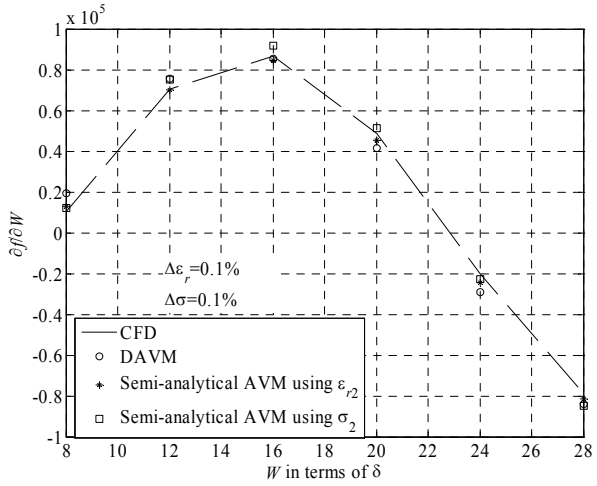

Fig. 5. Response sensitivity of $f_R = \Re E$ with respect to W at the nominal value of $\tilde{\varepsilon}$.

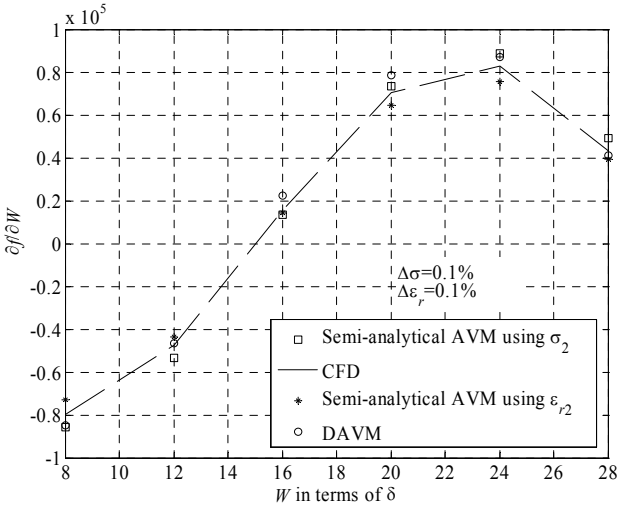

Fig. 6. Response sensitivity of $f_I = \Im E$ with respect to W at the nominal value of $\tilde{\varepsilon}$.

Figures 5 and 6 show the sensitivity of f with respect to the shape parameter W computed using: (i) response-level CFD; (ii) the DAVM sensitivity equation (7); (iii) the semi-analytical AVM equation (9) with $\partial \boldsymbol{A}/\partial\varepsilon_{r2}$ computed analytically and $d\varepsilon_{r2}/dW$ approximated as $\Delta\varepsilon_r/\delta$; and (iv) the semi-analytical AVM equation (9) with $\partial \boldsymbol{A}/\partial\sigma_2$ and $d\sigma_2/dW \approx \Delta\sigma_2/\delta$. The agreement is good.

Notice that for a complex objective function $f = f_R + jf_I$,[1] the derivative of the magnitude $|f|$ and phase ϕ can be easily extracted when $\partial f_R/\partial x_k$

[1] f_R and f_I are the real and imaginary parts of the complex function f, respectively.

and $\partial f_I / \partial x_k$ are known [12],

$$\frac{\partial |f|}{\partial x_k} = \frac{1}{|f|} \Re\left\{ f^* \cdot \frac{\partial f}{\partial x_k} \right\}, \tag{12}$$

and

$$\frac{\partial \phi}{\partial x_k} = \frac{1}{|f|^2} \Im\left\{ f^* \cdot \frac{\partial f}{\partial x_k} \right\}, \tag{13}$$

where

$$\frac{\partial f}{\partial x_k} = \frac{\partial f_R}{\partial x_k} + j \frac{\partial f_I}{\partial x_k}. \tag{14}$$

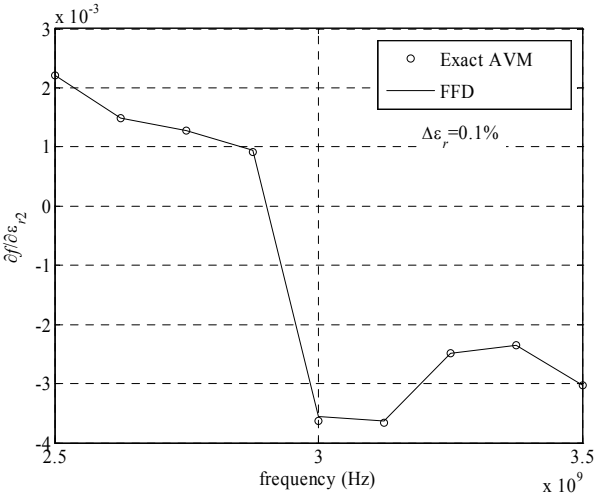

Fig. 7. Response sensitivity of $f = |\rho|^2$ with respect to ε_{r2} at nominal value of $\tilde{\varepsilon}$.

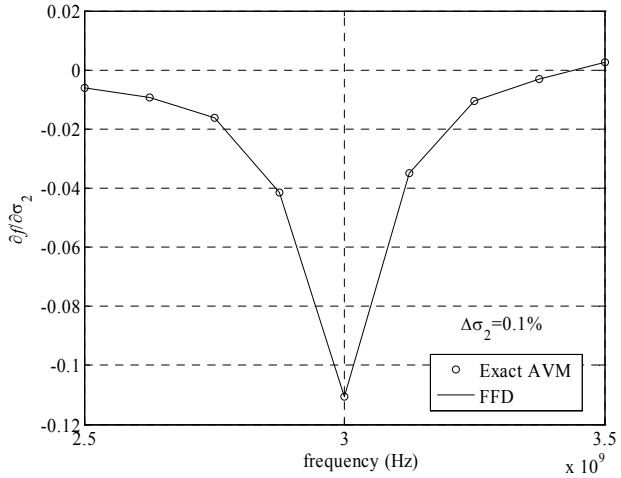

Fig. 8. Response sensitivity of $f = |\rho|^2$ with respect to σ_2 at nominal value of $\tilde{\varepsilon}$.

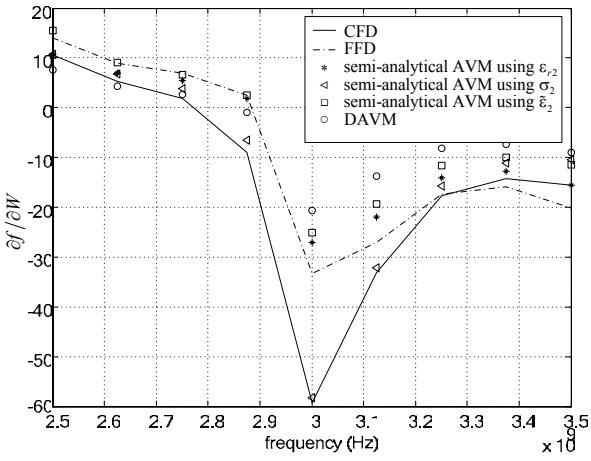

Fig. 9. Response sensitivity of $f = |\rho|^2$ with respect to W at the nominal value for $\tilde{\varepsilon}$.

For example, the sensitivity of $f = |\rho|^2$ where ρ is the reflection coefficient, is computed as $\partial |\rho|^2 / \partial x_k = 2\Re\{\rho^* \cdot \partial \rho / \partial x_k\}$.

We next verify the AVM approaches by computing the sensitivity of f when $f = |\rho|^2$. All three mediums in this case are lossy [see Fig. 2]. The first and third mediums have $\varepsilon_{r1} = \varepsilon_{r3} = 15$ and $\sigma_1 = \sigma_3 = 0.15$ S/m. The second medium has $\varepsilon_{r2} = 80$ and $\sigma_2 = 4.0$ S/m. The sensitivity is measured with respect to changes in the parameters of the second medium $\boldsymbol{x} = [\varepsilon_{r2} \ \sigma_2 \ \ W]^T$ for a frequency sweep from 2.5 GHz to 3.5 GHz.

Figures 7 and 8 show the sensitivity of f with respect to the constitutive parameters computed using the exact AVM equation (5). The results are also compared with response-level forward finite difference (FFD) estimates using a finite perturbation of 0.1 percent. Excellent agreement is obtained.

The sensitivity of f with respect to the shape parameter W is shown in Fig. 9. It is computed using: (i) response-level central and forward finite differences; (ii) the semi-analytical AVM equation (9) with $\partial \boldsymbol{A} / \partial \varepsilon_{r2}$ computed analytically and $\partial \varepsilon_{r2} / \partial W$ approximated as $\Delta \varepsilon_r / \delta$; (iii) the semi-analytical equation (9) with $\partial \boldsymbol{A} / \partial \sigma_2$ and $\partial \sigma_2 / \partial W \approx \Delta \sigma_2 / \delta$, (iv) the semi-analytical equation (9) with $\partial \boldsymbol{A} / \partial \tilde{\varepsilon}_2$ and $\partial \tilde{\varepsilon}_2 / \partial W \approx \Delta \tilde{\varepsilon} / \delta$, and (vi) the DAVM equation (7).

A number of observations can be made with respect to Fig. 9. Firstly, we notice that the disparity between the forward and central response level sensitivities is noticeable. The difference comes as a result of the finite discretization step δ. A finer discretization may improve the accuracy, however, this is not necessarily so. This has always been considered the major drawback of response-level sensitivities.

Secondly, due to the semi-analytical nature of the newly proposed approach, the accuracy of the computed sensitivities can substantially improve compared to the preceding DAVM approach. This is provided that the right choice of the intermediate variable in the semi-analytical formula is made. For example, the sensitivities computed in case (ii) employed ε_{r2} as the intermediate variable, sensitivities computed in case (iii) employed σ_2 as the intermediate variable, and those computed in case (iv) employed $\tilde{\varepsilon}_2$ as the intermediate variable. In general, using $\tilde{\varepsilon}_2$ yields the most accurate results.

A final remark concerns a shape parameter, which relates to a region where $\omega\varepsilon_0\varepsilon_r \leq \sigma$, i.e., the shape parameter relates to a geometrical detail, which is a good conductor. The large values of σ cause the corresponding $\boldsymbol{A}$-matrix coefficients to almost vanish resulting in numerical errors. Hence, in this case, the DAVM technique is the only approach for sensitivity analysis with respect to such details. Obviously, this is also the case when the detail is a perfect conductor.

Thirdly, the disparity between the results computed using the semi-analytical approach with ε_{r2} and σ_2 as intermediate variables and those computed using $\tilde{\varepsilon}_2$ is also noticeable. This is a result of the nonlinearity of f, the discretization step size δ, and the fact that all three mediums are lossy with large contrast between their constitutive parameters. In general, when the adjacent mediums have very different constitutive parameters, it is recommended to use $\tilde{\varepsilon}$ in equation (9) and not ε_r or σ. That is because $\tilde{\varepsilon}$ takes into account the change in both the permittivity and the conductivity of the affected links at the same time.

There are cases where only ε_r can be used as the intermediate variable in the semi-analytical sensitivity expression. An example of such cases is when the adjacent mediums at a perturbed boundary have different permittivities but the same or no conductivity.

Alternatively, if the two adjacent mediums at a perturbed boundary have the same permittivity but different conductivities, only σ can be used as an intermediate variable.

Here, we make some general remarks with regard to the numerical sensitivity analysis with shape parameters. The accuracy of the estimated sensitivities (exact or discrete) with any numerical analysis technique can be only as good as that of the response function. The accuracy of the latter depends on the setup and the convergence of the numerical solution.

Also, the difference between the values of the constitutive parameters of the neighboring mediums is a factor affecting the accuracy of the computed sensitivities. This factor is interrelated with the discretization step size δ. In the case of the finite-difference estimation of the response sensitivity, these two factors influence the accuracy of the estimates through round-off errors. On one hand, smaller δ typically leads to improved accuracy of the numerical solution for the response calculation. On the other hand, a shape perturbation of one δ for adjacent mediums of very similar constitutive parameters may produce a response, which is practically identical to the response of the original unperturbed structure. In such a case, the finite-difference estimate is very unreliable. Possible remedy is a perturbation of several δ. There is, however, no generally valid prescription for a proper value of the perturbation with the finite-difference approach at the response level. This, together with the obvious numerical inefficiency of the finite-difference approach, is its main drawback.

For a given δ, the accuracy of our adjoint-based techniques is better or equivalent to that of the finite difference approaches because they are less prone to round-off errors. Consider, for example, the semi-analytical adjoint-based equation (9). The only difference term $\Delta\tilde{\varepsilon}$ is not affected by round-off errors because, in practice, when two materials are considered different, the difference in their constitutive parameters is far more significant than the machine error. For the same reason, with the DAVM, the different constitutive parameter values produce significantly different coefficients of the system matrix $\boldsymbol{A}$. Subsequently, the elements of the difference matrix $\Delta\boldsymbol{A}$ in equation (7) are never very small.

VI. CONCLUSIONS

For the first time, we present adjoint-based approaches for efficient sensitivity analysis of high-frequency structures developed for lossy inhomogeneous materials. The approaches are applicable in the case of material and shape parameters. The first approach is an approximate discrete adjoint-based approach adapted from our preceding technique. It was originally developed for lossless homogenous problems. The approach is investigated here for the first time with lossy inhomogeneous materials. It requires field approximations of the perturbed problems. We improve this approach by proposing a semi-analytical formula. The newly developed formula utilizes the analytical dependence of the system matrix elements on the constitutive parameters of the structure materials. This approach avoids the approximations needed in the preceding technique leading to simplification in the implementation and improvement in the accuracy. We show that the accuracy of the proposed semi-analytical approach is affected by the variation between the constitutive parameters of the neighboring mediums.

We also show that this effect can be reduced by using the complex permittivity as the intermediate variable in the semi-analytical expression.

REFERENCES

[1] E. J. Haug, K. K. Choi, and V. Komkov, *Design Sensitivity Analysis of Structural Systems.* Orlando, Florida: Academic Press, Inc. 1986.

[2] N. K. Nikolova, J. W. Bandler, and M. H. Bakr, "Adjoint techniques for sensitivity analysis in high-frequency structure CAD," *IEEE Trans. Microwave Theory Tech.,* vol. 52, no. 1, pp. 403-419, Jan. 2004.

[3] N. K. Nikolova, H. W. Tam, and M. H. Bakr, "Sensitivity analysis with the FDTD method on structured grids," *IEEE Trans. Microwave Theory Tech.*, vol. 52, no. 4, pp. 1207-1216, April 2004.

[4] M. H. Bakr and N. K. Nikolova, "An adjoint variable method for time domain TLM with fixed structured grids," *IEEE Trans. Microwave Theory Tech.*, vol. 52, no. 2, pp. 554-559, Feb. 2004.

[5] P. A. W. Basl, M. H. Bakr, and N. K. Nikolova, "Efficient estimation of sensitivities in TLM with dielectric discontinuities," *IEEE Microwave and Wireless Components Lett*., vol. 15, no. 2, pp. 89-91, Feb. 2005.

[6] S. M. Ali, N. K. Nikolova, and M. H. Bakr, "Recent advances in sensitivity analysis with frequency-domain full-wave EM solvers," *Applied Computational Electromagnetics Society Journal*, vol. 19, no. 3, pp. 147-154, Nov. 2004.

[7] S. M. Ali, N. K. Nikolova, and M. H. Bakr, "Sensitivity analysis with full-wave EM solvers based on structured grids," *IEEE Trans. Magnetics*, vol. 40, no. 3, pp. 1521-1529, May 2004.

[8] R. Zoughi, *Microwave Nondestructive Testing and Evaluation*. Dordrecht: Kluwer Academic Publishers, 2000.

[9] D. Johns and C. Christopoulos, "New frequency-domain TLM method for numerical solution of steady-state electromagnetic problems," *IEE Proc. Sci. Means Technol*., vol. 141, pp. 10-316, 1994.

[10] C. Christopoulos. *The Transmission-line Modeling Method TLM.* New York: IEEE press, 1995.

[11] D. Pasalic, R. Vahldieck, and J. Hesselbarth, "The frequency-domain TLM method with absorbing boundary conditions," *IEEE MTT-S Int. Microwave Symposium Dig*., pp. 1669-1672, 1999.

[12] J. Dobrowolski, *Computer-Aided Analysis, Modeling, and Design of Microwave Networks*, Boston: Artech House, Inc., pp. 96, 1996.

Shirook M. Ali received the B.Sc. degree in Communication engineering from University of Baghdad, Iraq, in 1993, and the M.Sc. degree in electrical engineering from Jordan University of Science and Technology, Jordan, in 1999. In 2004 she received her Ph.D. degree in electrical and computer engineering from McMaster University, Canada. She joined the Computational Electromagnetic Laboratory as a Post Doctoral Fellow in 2005. Dr. Ali is currently an RF/EM Researcher at Research in Motion Ltd. (RIM). Her research interests include computational electromagnetics, time domain analysis for high-frequency structures and antennas, optimization, and CAD methods.

Dr. Ali currently holds an Industrial Research Fellowship of NSERC.

Natalia K. Nikolova received the Dipl. Eng. degree from the Technical University of Varna, Bulgaria, in 1989, and the Ph.D. degree from the University of Electro-Communications, Tokyo, Japan, in 1997. From 1998 to 1999, she held a Postdoctoral Fellowship of the Natural Sciences and Engineering Research Council of Canada (NSERC), during which time she was initially with the Microwave and Electromagnetics Laboratory, DalTech, Dalhousie University, Halifax, Canada, and, later, for a year, with the Simulation Optimization Systems Research Laboratory, McMaster University, Hamilton, ON, Canada. In July 1999, she joined the Department of Electrical and Computer Engineering, McMaster University, where she is currently an Associate Professor. Her research interests include theoretical and computational electromagnetism, high-frequency analysis techniques, as well as CAD methods for high-frequency structures and antennas.

Mohamed H. Bakr received a B.Sc. degree in Electronics and Communications Engineering from Cairo University, Egypt in 1992 with distinction (honors). In June 1996, he received a Master's degree in Engineering Mathematics from Cairo University. In 1997, he was a student intern with Optimization Systems Associates (OSA), inc. From 1998 to 2000, he worked as a research assistant with the Simulation Optimization Systems (SOS) research laboratory, McMaster University, Hamilton, Ontario, Canada. He earned the Ph.D. degree in September 2000 from the Department of Electrical and Computer Engineering, McMaster University. In November 2000, he joined the Computational Electromagnetics Research Laboratory (CERL), University of Victoria, Victoria, Canada as an NSERC Post Doctoral Fellow. Dr. Bakr is a recipient of a 2003 Premier's Research Excellence Award (PREA) from the province of Ontario, Canada. His research areas of interest include optimization methods, computer-aided design and modeling of microwave circuits, neural network applications, smart analysis of microwave circuits and efficient optimization using time/frequency domain methods. He is currently an Assistant Professor with the Department of Electrical and Computer Engineering, McMaster University.

Model-Based Parameter Estimation (MBPE) for Metallic Photonic Crystal Filters

[1]K. Tavzarashvili, [1]Ch. Hafner, [1]Cui Xudong, [1]R. Vahldieck, [2]D. Karkashadze, and [2]G. Ghvedashvili

[1] Laboratory for Electromagnetic Fields and Microwave Electronics
Gloriastrasse 35, ETH Zentrum, 8092 Zurich
e-mail: k.tavzarashvili@ifh.ee.ethz.ch

[2] Laboratory of Applied Electrodynamics, Tbilisi State University
3, Chavchavadze Ave., 0128, Tbilisi, Georgia
e-mail: davidkarkashadze@laetsu.org

Abstract **–** An efficient method for the accurate computation of the response of photonic crystal filters is obtained when Model-Based Parameter Estimation (MBPE) is combined with accurate field solvers. In this paper, MBPE is combined with Multiple Multipole Program (MMP) and the Method of Auxiliary Sources (MAS) and the results are compared with results obtained from a commercial field solver. When metals are present in photonic crystal filters, strong material dispersion at optical frequencies cause nonlinearity of the filter response. It is demonstrated that MBPE is still useful although it is originally designed for linear systems.

Keywords – Model-Based Parameter Estimation; PhC filters; MMP, MAS.

I. INTRODUCTION

Photonic Crystals (PhCs) consist of dielectric or metallic structures [1] arranged on a regular lattice like the atoms in a natural crystal. Mainly because of the Photonic Band Gap (PBG) - that is observed when the contrast between the materials used for fabricating the PhC is high enough - PhCs are very promising for integrated optics. In fact, the PBG is the photonic counter part to the electronic band gap of semiconductors. By doping PhCs one can easily introduce resonators (point defects) and waveguides (line defects) in a PhC. By combining both one can obtain useful components such as filters. PhC filters may be embedded in PhC waveguides but also in classical waveguides. The simplest PhC filter is a PhC slab illuminated by a plane wave. Such filters are currently intensively studied to determine their limitations and practical value. The main problem is that no simple design rules are available. Therefore, efficient numerical methods for the analysis and optimization of PhC filters are highly desirable. Model-Based Parameter Estimation (MBPE) [2 - 4] is an auxiliary technique that may be added to any field solver for obtaining the entire frequency response from the calculation of the response in a small number of frequency points. This means that the field solver only computes the filter for m discrete (real or complex) frequency points s_k (k=1…m) and MBPE then provides a very fast approximation for any desired frequency s.

Model-Based Parameter Estimation - also called Cauchy method [5] - was originally designed for linear PhC filters: The frequency response of linear filters is known to be best represented by a fraction of two polynomials (Cauchy formula) and MBPE takes advantage of this representation.

In the following it is demonstrated that MBPE is also useful and efficient for PhC filters made of dispersive materials, namely, PhC filters that include metal with strongly frequency-dependent complex permittivity at optical frequencies. As a particular case, filter analysis in the optical frequency range is considered. The electrodynamic problem of the PhC filter structure - containing silver rods - was solved by using the frequency domain solvers Multiple Multipole Program (MMP) [6], [7], [10], [11] and the Method of Auxiliary Sources (MAS) [8], [9].

II. MODEL-BASED PARAMETER ESTIMATION (MBPE)

Most EM phenomena require essentially a continuous representation of the system response over a specific frequency range. The computation of the observables (S parameters, transmission and reflection coefficients, field strengths in certain points of space, etc.) with sufficient resolution can be expensive especially when sharp resonances are present. MBPE allows us to obtain the system response over the entire frequency range by using a relatively small number of frequency samples.

The main concept of MBPE is the following. In the frequency domain, the response of a linear system may be optimally represented by Cauchy's method, i.e.,

$$F(s) = \frac{N(s)}{D(s)} + Error(s) = \frac{\sum_{i=0}^{n} N_i s^i}{\sum_{i=0}^{d} D_i s^i} + Error(s), \qquad (1)$$

where F is the response of the system and s the complex frequency that also may be limited to the radian frequency $i\omega$. The error of this approximation depends on the maximum orders n and d of the power series expansions in the nominator N and denominator D as well as on the method that determines the parameters N_i and D_i.

A simple technique to compute the parameters is to multiply equation (1) by D and rewrite equation (1) in a set of m frequency points s_k:

$$F(s_k)\sum_{i=0}^{d} D_i s_k^i - \sum_{i=0}^{n} N_i s_k^i = Error(s_k)\sum_{i=0}^{d} D_i s_k^i = E_k, \qquad (2)$$
$$k = 1,..,m$$

where E is an unknown error vector. When F is known in $m \geq n + d + 1$ points s_k, equation (2) is a linear system of m equations. One then can evaluate the parameters D_i and N_i in such a way that the square norm of the error vector is minimized. Before this is done, one should note that not all parameters are independent because nominator and denominator in equation (1) may be scaled with an arbitrary factor. For this reason, one of the parameters may be set equal to 1. It is reasonable to set D_d=1. One then obtains,

$$F(s_k)\sum_{i=0}^{d-1} D_i s_k^i - \sum_{i=0}^{n} N_i s_k^i = -F(s_k)s_k^d + E_k = R_k + E_k, \quad (3)$$
$$k = 1,..,m$$

where R is a known, right-hand-side vector. Note that equation (3) can be solved in such a way that the error vector E is zero when $m=m_0=n+d+1$, because one then obtains a square matrix system. This does not imply that $Error(s)$ becomes zero as well. Especially when the sample values $F(s_k)$ are only approximately known – which is always the case in practice – it is more reasonable to work with an overdetermined system of equations with $m > m_0$. Reasonable overdetermination implicitly provides smoothing of "noise" and "ripples" caused by inaccurate Maxwell solvers. When highly accurate codes such as MMP and MAS are used, very weak overdetermination (with overdetermination factors m/m_0 around 1.1) is sufficient. This obviously reduces the number of frequency points required. Since the time-consuming part of the MBPE is the computation of the sample values by the Maxwell solver, weak overdetermination saves computation time.

The most difficult problem is to determine the required maximum orders n and d of the power series of the nominator and denominator. Both depend very much on the size of the frequency range of interest, the desired accuracy, and the complexity of the system. Since metals within Metallic Photonic Crystals (MPhCs) and Metallo-Dielectric Photonic Crystals (MDPhCs) are strongly dispersive at optical frequencies, MPhC and MDPhC filters are non-linear and may be linearized only over a sufficiently short frequency interval. Therefore, it is reasonable to limit the maximum orders n and d by a value of typically not higher than 10 and to subdivide the frequency interval into two or more parts when the MBPE approximation is not accurate enough.

The algorithm block scheme of the MBPE procedure used for the PhC filter analysis is presented in Fig. 1. The MBPE procedure is adaptive and starts with small orders, i.e., n and d values and with a small number of test points according to the overdetermination factor specified by the user. It then increases the order by 1 and compares the resulting MBPE approximations. When the differences

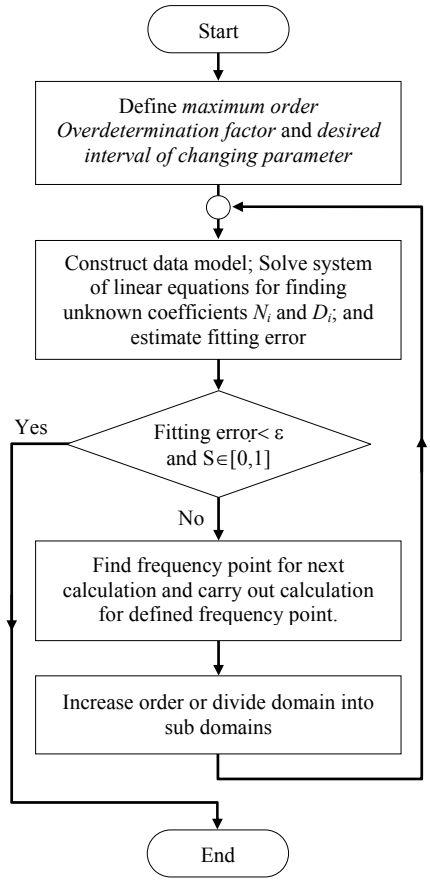

Fig. 1. MBPE procedure for PhC filters analysis.

between the two approximations are below a user-defined error bound over the entire frequency range and when all *S* parameters are within the range 0…1, the MBPE approximation is good enough and the procedure stops. Otherwise, it inserts new test points within the frequency range as follows: If an *S* parameter is out of the range, it inserts the new test point at the frequency where the biggest distance from the range 0…1 is encountered. Otherwise, it searches for the maximum difference between the current and previous MBPE approximation and sets the new test point at the corresponding frequency. The evaluation of the filter response, e.g., the *S* parameters, in the new test point is then performed by the field solver, for example, MMP or MAS. When the number of test points is high enough, the MBPE order is increased – provided that the user-defined maximum order is not yet reached. As soon as the maximum order is reached, the frequency interval is split into two intervals with half the length of the original interval and a separate MBPE approximation is started for each interval. This procedure is recursively continued if required.

One is often interested in the frequency dependence of several characteristic values, for example, the S parameters. Usually, the field solver can simultaneously evaluate all parameters with almost the same numerical costs as for a single parameter. Therefore, it is reasonable to implement an MBPE procedure that simultaneously evaluates the frequency response of several observables, for example, all S parameters. All that needs to be done for such a multi-parameter MBPE is to define the maximum fitting error over all model parameters – typically the sum of the square errors of all model parameters. Beside this, the procedure outlined in Fig. 1 remains the same.

To demonstrate how MBPE works for dispersive materials, we consider the problem of coupled metallic nanoparticles [11 - 13]. The first test system contains only two circular cylinders made of silver with a radius of 25 nm and a surface-surface separation of 5 nm (see Fig. 2), illuminated by an H-polarized plane wave. H-polarization is chosen, because plasmon resonances are obtained for this case. The electrodynamic problem was solved by the MAS. The MBPE procedure was started in 30 sample points and the overdetermination factor was set equal to 1.1. For the system response over the wavelength range 100 nm to 350 nm the adaptive MBPE algorithm requires only 63 frequency points for a maximum fitting error below 1%. In Fig. 2 the Scattering Cross Section (SCS) for the system is shown and Fig. 3 illustrates the field distribution at plasmon wavelengths. The Drude model is used for the frequency dependence of the permittivity of silver [10],

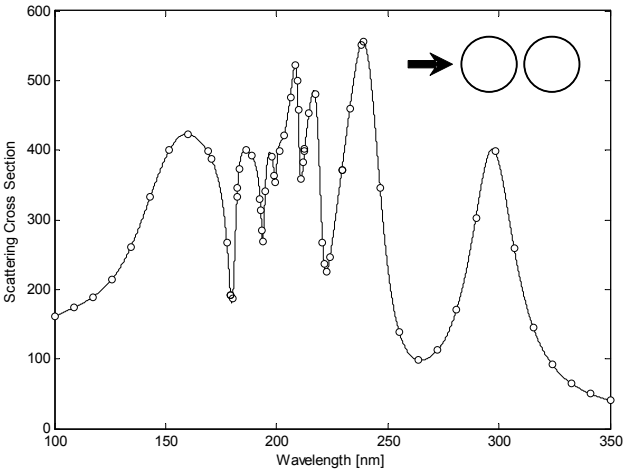

Fig.2. SCS for two intersecting cylinders made of silver with a radius of 25 nm at a surface-surface separation of 5 nm. The field is evaluated in 68 sample points marked by circles.

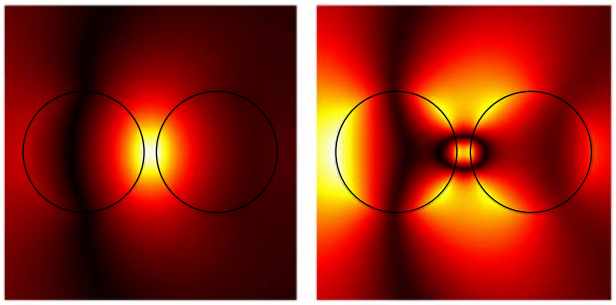

α) λ = 297 nm b) λ = 239 nm

Fig. 3. Near-Filed around coupled circular nanoparticles illuminated by an H-polarized plane wave incident from the left side.

$$\varepsilon(\nu) = 1 + \frac{i\tau\omega_p^2}{2\pi\nu(1 - i2\pi\tau\nu)}, \tag{4}$$

with $\tau = 1.45 \times 10^{-14} s$ and $\omega_p = 1.32 \times 10^{16} s^{-1}$. Note that this frequency dependence is only approximate and not very accurate. For more realistic results, experimental values should be used [14]. The value used here just serves as a demonstration how the MBPE can handle dispersive materials. Furthermore, this allows us to compare the results with time-domain solvers that only can handle dispersive materials described by simplified mathematical models such as the Drude model. Figure 4 illustrates the real and imaginary part of the permittivity of the Drude model for silver together with the different MBPE domains. The second and third domains are small

compared with other ones although the frequency dependence of the material properties is rather smooth everywhere. The reason for this is that plasmon resonances occur when the real part of the permittivity is close to -1, i.e., the adaptive MBPE has correctly located the critical frequency range. Note that the number of plasmon resonances depends on the material characteristics and on the geometry. Therefore it is usually not possible to precisely foresee the locations of the resonances.

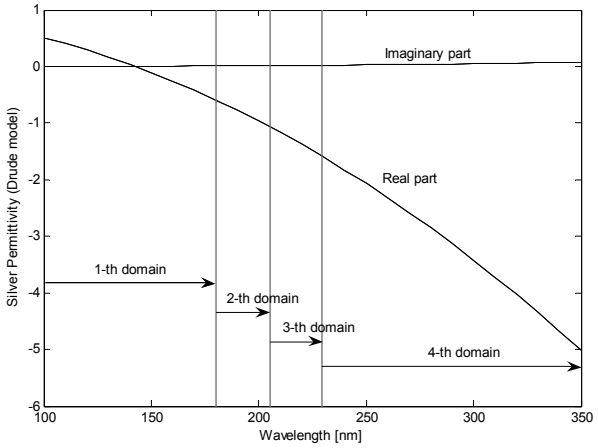

Fig.4. Frequency dependence of the permittivity of silver (Drude model). The vertical grey lines indicate the MBPE domains obtained from the automatic procedure. In each domain a Cauchy approximation of order 10 was used.

III. 2D METALLIC PHC SLAB

The PhC filter structure considered in the following consists of a 2D PhC with 5 layers of circular silver wires arranged on a square lattice. This structure extends to infinity in x direction and is finite in y direction, as illustrated in Fig. 5. The wire radius is 73.3 nm and lattice constant is 820 nm. E_z polarization is considered because metallic PhCs have a fundamental band gap for this polarization.

Numerical methods can take advantage of the periodic symmetry in x direction in different ways.

1) The MMP code introduces fictitious boundaries that separate a single "fundamental" cell from its neighbors as illustrated in Fig. 5. Along these boundaries, periodic (Floquet) boundary conditions are imposed [11]. It is then sufficient to compute the field in a single cell. Since this cell extends still to infinity in y direction, two additional fictitious boundaries are introduced that separate three areas: a) the upper half space with incident plane wave plus reflected zero and higher order Rayleigh expansions, b) the PhC area, and c) the lower half space with transmitted zero and higher order Rayleigh expansions. The areas a) and c) are modeled as for arbitrary gratings, whereas area b) has a finite size. Within b) the field is approximated by standard MMP expansions as an ordinary scattering problem.

Taking care of the periodic symmetry by means of periodic boundary conditions has the advantage of generality and simplicity in the implementation, i.e., any frequency-domain code that can handle simple scattering problems can handle periodic structures such as gratings and PhCs as soon as periodic boundary conditions are implemented. Within MMP, not only multipoles but a big library of analytic solutions of Maxwell's equations is available. All of these functions may then not only be applied for modeling scattering problems but also for modeling PhCs. For example, the field inside the wires is approximated by Bessel expansions rather than by multipoles.

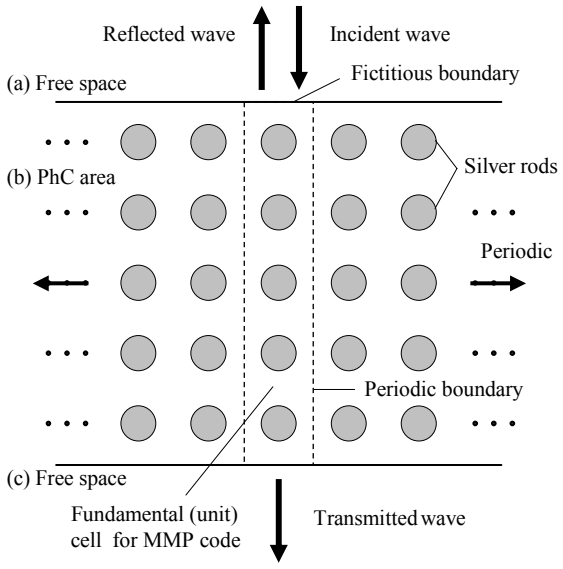

Fig. 5. The PhC filter structure for MMP code.

2) The Method of Auxiliary Sources (MAS) uses an approximation of the scattered field by a set of auxiliary sources, i.e., monopole sources, distributed along auxiliary lines that are always outside the physical area of the scattered field. Here, the periodic symmetry is taken into account by using periodic arrays of monopole sources as illustrated in Fig. 6. Thus, the periodic boundary conditions are automatically satisfied by the periodic expansions. Since only one type of relatively simple expansions – monopoles – is used, the implementation of a periodic set of expansions is not too difficult, but for an efficient implementation, a careful numerical analysis is

required. The functions describing the fields of auxiliary sources have the form

$$F_n(|\vec{r}_n - \vec{r}|) = \sum_{m=-\infty}^{\infty} \alpha \, \mathrm{H}_0^{(1)}(k\sqrt{(x - x_n - md)^2 + (y - y_n)^2}), \tag{5}$$

where d - is the period of the structure; α=1 for diffraction lattices and $\alpha = (-1)^m$ for waveguides with non-homogeneous filling. Now, the singularities are singled out in an explicit form. When the bad convergence of equation (5) is improved by use of the Poisson formula, an efficient algorithm is obtained. The amplitudes of each monopole array are computed in such a way that Floquet conditions are automatically met, i.e., no periodic boundary conditions are required. For the calculation of the reflected ($y>y_n$) and transmitted ($y<y_n$) fields for the 0 and p-th harmonic one has,

$$g_p = \frac{2\pi}{d} p, \quad h_p = \frac{2\pi}{d}\sqrt{D^2 - (p + D\cos\theta)^2}, \tag{6}$$
$$D = \frac{d}{\lambda}, \quad (p = 0, \pm 1, \pm 2, ...),$$

$$E_0(x, y) = \sum_{n=1}^{N} a_n \frac{\exp\left(ik\cos\theta(x - x_n)\right)}{k|\sin\theta|} \exp\left(ik|\sin\theta||y - y_n|\right), \tag{7}$$

$$E_p(x, y) = \sum_{n=1}^{N} a_n \frac{\exp\left(i(k\cos\theta + g_p)(x - x_n)\right)}{h_p} \exp\left(ih_p|y - y_n|\right) \tag{8}$$

where $\theta \in (0, \pi)$, is the incident angle of the plane wave; $\{a_n\}$, n=1..N are the amplitudes of the auxiliary sources, that must be calculated by imposing standard continuity conditions on the surface of the wires within one period in x direction.

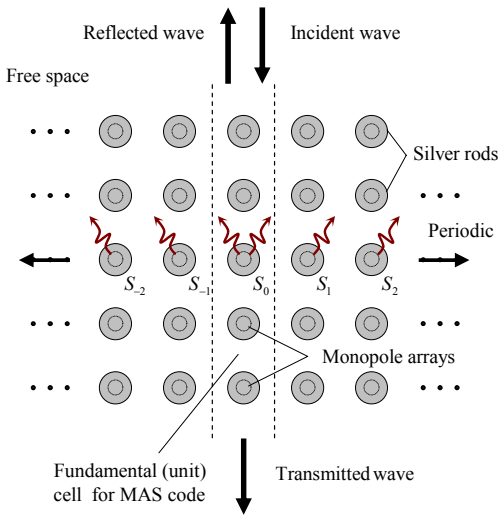

Fig. 6. The PhC filter structure for MAS code.

3) For time-domain methods such as FDTD and FIT [15] the appropriate handling of periodic symmetries becomes simple only for a vertically incident plane wave. One then may introduce electric or magnetic walls in y direction for separating the "fundamental" cell used in the MMP model.

Furthermore, absorbing boundary conditions may be imposed in the areas a) and c) for absorbing the reflected and transmitted waves (see Fig. 7). Consequently, FDTD (and FIT) codes discretize only a finite rectangular area b) like MMP. For the more general case of an obliquely incident plane wave, FDTD becomes more complicate and requires a complex formulation for taking the periodic boundary conditions accurately into account. Incidentally, material dispersion causes additional problems for time-domain codes. In order to avoid the time-consuming evaluation of convolution integrals, material models for dispersive materials are simplified, for example, by the Drude model given above. Despite of its inaccuracy, it is used for the following test case in order to obtain a comparison of MMP-MBPE and MAS-MBPE with commercial FDTD and FIT codes.

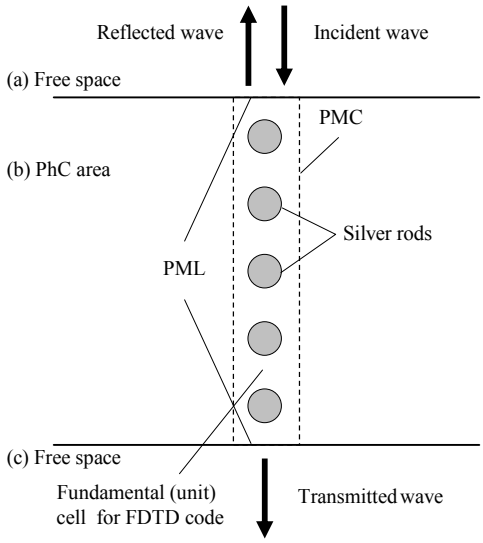

Fig. 7. The PhC filter structure for FDTD code.

IV. NUMERICAL TEST CASE: 2D METALLIC PHC SLAB

Figures 8 and 9 show the transmission characteristics of a PhC filter obtained with the three different methods outlined above. Excellent agreement is observed at sufficiently low frequencies (λ = 1.0 μm to 3.0 μm) (Fig. 8). The maximum difference between MMP brute-force, MMP-MBPE and MAS-MBPE is 0.02 % (there is no observable difference between curves plotted on graphs) and between MMP and FIT it is 0.1 %. For MMP-MBPE

and MAS-MBPE only 20 points were computed by MMP and by MAS, the remaining points were interpolated by MBPE (see Fig. 8, points with triangles). The total computation time for these MBPE solutions was below 1 minute on a PC and 5 minutes for the less accurate FIT solution.

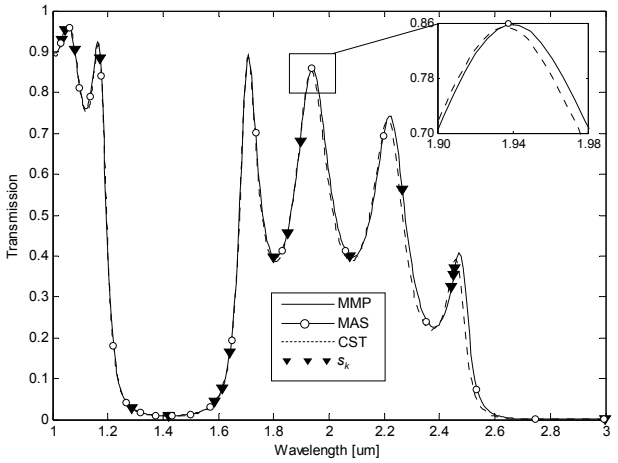

Fig. 8. MMP-MBPE, MAS-MBPE, and CST Microwave Studio (FIT) results of the test case at low frequency range. Only 20 frequency points s_k were computed and the remaining points were interpolated by MBPE.

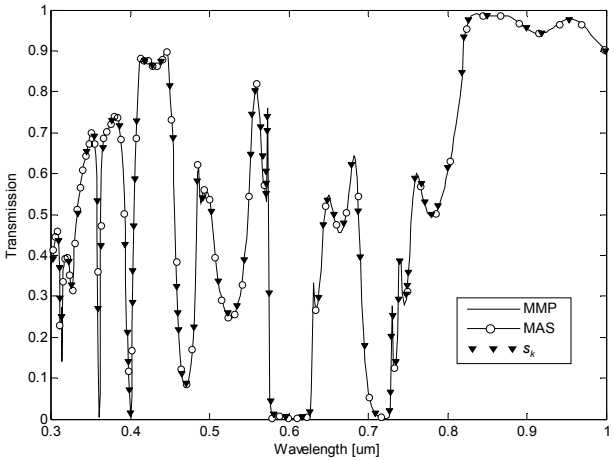

Fig. 9. MMP and MAS results with and without MBPE techniques. The maximum difference between MMP brute-force, MMP-MBPE and MAS-MBPE results is less then 0.02 %. Only 145 frequency points s_k were computed and the remaining points were interpolated by MBPE.

Excellent agreement between MMP and MAS is also observed for higher frequencies (λ = 0.3 μm to 1.0 μm) that cannot be handled correctly with the commercial FIT code (see Fig. 9). Only 145 frequency points were computed and the remaining points were interpolated by MBPE for higher frequency interval, while at least 2000 frequency points were required for getting a smooth curve using MMP or MAS without MBPE technique, i.e. the speed-up factor provided by the MBPE is more than 10.

Note that the computation time for FDTD and FIT codes for the more general case with oblique incidence and more accurate material models would strongly increase the computation time of the time domain codes, whereas it does not increase the computation time of the MMP-MBPE and MAS-MBPE solutions. The near field distribution for PhC filter is shown in Fig. 10.

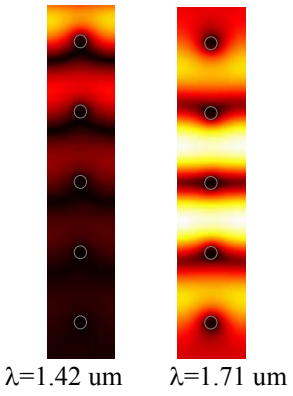

Fig. 10. Near-Filed for PhC filter.

The wavelength dependence of the permittivity (according to the Drude model with solid line and measurement fitting with doted line) is presented in Fig. 11 together with MBPE sample points where the field was evaluated. For long wavelength (λ = 1.0 μm to 3.0 μm) it was sufficient to use 20 sample points and the MBPE domain was not subdivided by the adaptive algorithm.

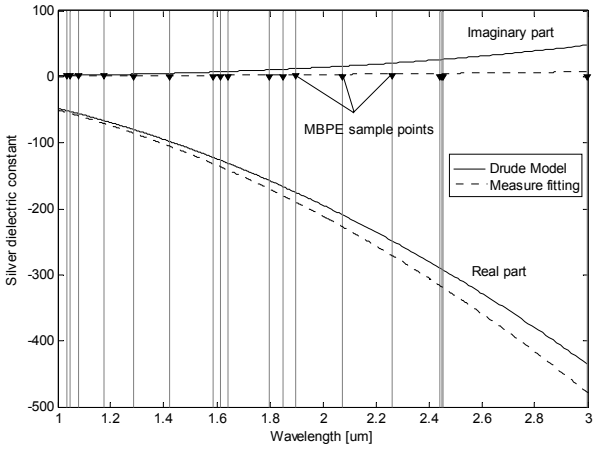

Fig. 11. Silver dielectric constant – Drude model. With vertical grey lines the MBPE sample point locations is plotted.

V. CONCLUSIONS

Adaptive MBPE algorithms may be added to any frequency domain field solver. These algorithms drastically reduce the numerical effort for the accurate computation of the filter response also when dispersive materials are present. It can simultaneously evaluate the frequency response of several observables. For the metallic photonic filter test case, excellent agreement between the MMP-MBPE and MAS-MBPE solutions is observed even at high frequencies, where the commercial FIT solver fails. This solver is outperformed by MMP-MBPE and MAS- MBPE even when simplified models are considered that cause no problems for FDTD and FIT.

VI. ACKNOWLEDGMENT

This work was supported by the INIT grant "Composite Doped Metamaterials" of the ETH Zurich and by SCOPES grant IB7320-110977 of the Swiss National Science Foundation.

REFERENCES

[1] C. Hafner, C. Xudong, and R. Vahldieck, "Metallic Photonic Crystals at Optical Frequencies," *J. Computational and Theoretical Nanoscience* vol. 2, pp. 1-11, 2005.

[2] E. K. Miller, "Model-Based Parameter Estimation in Electromagnetics: Part I. Background and Theoretical Development," *IEEE Antennas and Propagation Magazine* vol. 40, no. 1, Feb. 1998.

[3] E. K. Miller, "Model-Based Parameter Estimation in Electromagnetics: Part II. Applications to EM Observables," *IEEE Antennas and Propagation Magazine* vol. 40, no. 2, April 1998.

[4] E. K. Miller, "Model-Based Parameter Estimation in Electromagnetics: Part III. Applications to EM Integral Equations," *IEEE Antennas and Propagation Magazine* vol. 40, no. 3, June 1998.

[5] R. S. Adve, T. K. Sarkar, S. M. Rao, E. K. Miller, and D. R. Pflug "Application of the Cauchy Method for Extrapolating/Interpolating Narrow-Band System Responses" *IEEE Transactions on Microwave Theory and Techniques*, vol. 45, no.5, May 1997.

[6] C. Hafner, *Post-modern Electromagnetics*, John Wiley & Sons, Chichester, 1999.

[7] http://alphard.ethz.ch/hafner/MaX/max1.htm.

[8] D. Karkashadze and R. Zaridze, "The Method of Auxiliary Sources in Applied Electrodynamics," *Latsis Symposium on Computational Electromagnetics*, Zurich, Sept. 1995.

[9] R. Zaridze, G. Bit-Babik, K. Tavzarashvili, N. Uzunoglu, and D. Economou, "Wave Field Singularity Aspects Large-Size Scatterers and Inverse Problems," *IEEE Transactions on Antennas and Propagation*, vol. 50, no. 1, Jan. 2002.

[10] E. Moreno, D. Erni, Ch.Hafner, and R. Vahldieck, "Multiple Multipole Method with Automatic Multipole Setting Applied to the Simulation of Surface Plasmons in Metallic Nanostructures," *J. Opt. Soc. Am. A*., vol. 19, no. 1, Jan. 2002.

[11] C. Hafner "Multipole multipole program computation of periodic structures," *J. Opt. Soc. Am. A*., vol. 12, no. 5, May 1995.

[12] J. Kottmann and O. martin "Plasmon Resonant Coupling in Metallic Nanowires" *Optic Express*, vol. 8, no. 12, June 2001.

[13] C. Rockstuhl, M. Salt, and H. Herzig "Analyzing the scattering properties of coupled metallic nanoparticles," *J. Opt. Soc. Am. A*., vol. 21, no. 9, Sep. 2004.

[14] P. Johnson and R. Christy "Optical Constants of the Nobel Metals" *Physical Review B*, vol. 6, no. 12, Dec. 1972.

[15] http://www.cst.de/Content/Products/MWS/Overview.aspx.

Kakhaber Tavzarashvili was born in Tbilisi, Georgia, in 1974. He received Master Science in Microprocessors and Microprocessor Systems and Ph.D. in Radio-physics from Tbilisi State University (TSU), Georgia in 1996 and 1999 respectively. Since 1996 he has been working at the laboratory of Applied Electrodynamics (LAE), Department of Physics as Engineer. Since 2000 has been working as Scientific Researcher of the LAE. Since 2005 he is a postdoctoral research fellow in the Computational Optics group of the Laboratory for Electromagnetic Fields and Microwave Electronics at the ETH Zurich. His current research interest includes numerical field calculation, photonic crystal devices, antennas, optimization codes and development of EM software for engineering. Since 2002 he is IEEE Associate Member.

Christian Hafner was born in Zurich, Switzerland, in 1952. He received a Dipl. El.-Ing. Degree, Doctoral Degree, and Venia Legendi from Swiss Federal Institute of Technology (ETH), Zürich in 1975, 1980, and 1987 respectively. In 1999 he was given the title of Professor. Since 1976 he has been working at the ETH on the development of methods for computational electromagnetics and for optimization problems. He has developed the Multiple Multipole Program (MMP), the MaX-1 package, the Generalized Genetic Programming (GGP) code, and various optimization codes. He worked on various applications (electrostatics, EM scattering, antenna, waveguides and waveguide discontinuities, gratings, chiral media, etc.). His current focus is on photonic crystals, microstructured optical fibers, and Scanning Nearfield Optical Microscoes (SNOM). In 1990 he obtained the second prize of the Seymour Cray avard for scientific computing and in 2001 he has been awarded the 2000 Outstanding Journal Paper Award by the Applied Computational Electromagnetics Society. He is member of the Electromagnetics Academy.

Cui Xudong graduated from Beijing Institute of Technology, Beijing, China and received the M.S. degree in optics from Chinese Academy of Engineering Physics, Beijing, China. He is currently pursuing the Ph.D. degree from Swiss Federal Institute of Technology Zurich. His research interest includes X-ray optics, image processing, photonic crystal devices design and optimization, metamaterials, novel numerical methods for Electromagnetic problems.

Rüdiger Vahldieck (M'85-SM'86-F'99) received the Dipl.-Ing. and the Dr.-Ing. degrees in electrical engineering from the University of Bremen, Germany, in 1980 and 1983, respectively. From 1984 to 1986 he was a Postdoctoral Fellow at the University of Ottawa, Canada. In 1986 he joined the Department of Electrical and Computer Engineering at the University of Victoria, British Columbia, Canada, where he became a Full Professor in 1991. During Fall and Spring of 1992-'93 he was a visiting scientist at the Ferdinand-Braun-Institut für Höchstfrequenztechnik in Berlin, Germany. In 1997 he accepted an appointment as Professor for electromagnetic field theory at the Swiss Federal Institute of Technology, Zurich, Switzerland, and became head of the Laboratory for Electromagnetic Fields and Microwave Electronics (IFH) in 2003. His research interests include computational electromagnetics in the general area of EMC and in particular for computer-aided design of microwave, millimeter wave and opto-electronic integrated circuits.

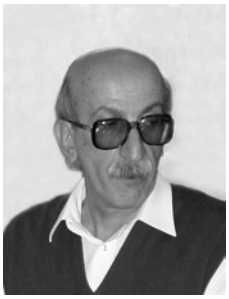

David Karkashadze was born in Tbilisi, Georgia in 1949. He received Master Science in Radio-physics and Quantum Electronics and Candidate of Science Degrees in Radio-physics and Quantum Electronics from Tbilisi State University (TSU), Georgia in 1971 and 1981 respectively. Since 1971 he has been working at the Department of Physics as a teacher, since 1985 to present General Physics Associate Professor (TSU). His current research interests include: numerical methods for solution diffraction and wave propagation problems; theoretical and experimental investigation, computer simulation of electrodynamics phenomena; ESD and Transient field calculation; theory and application of wave scattering and propagation in complex (Chiral and Bi-anisotropic) media; development of EM software for engineering.

Giorgi Ghvedashvili was born in Tbilisi, Georgia, in 1974. He received Master Science in Physics of Elementary Particles and Ph.D. in Radio-physics from Tbilisi State University (TSU), Georgia in 1996 and 2002 respectively. Since 2000 he has been working at the laboratory of Applied Electrodynamics (LAE), Department of Physics as Engineer. Since 2002 has been working as Scientific Researcher of the LAE. In 2004 he has been awarded the INTAS Young Scientists Postdoctoral Fellowship Grant. His current research interest includes numerical field calculation, antenna design and development of EM software for engineering. Since 2003 he is IEEE Associate Member.

Scattering by PEMC (Perfect Electromagnetic Conductor) Spheres using Surface Integral Equation Approach

Ari Sihvola, Pasi Ylä-Oijala, and Ismo V. Lindell

Electromagnetics Laboratory, Helsinki University of Technology,
P.O. Box 3000, FI–02015 TKK, Finland

Abstract– This article discusses bistatic scattering by totally reflecting spheres. The spheres are either perfect electric, magnetic, or electromagnetic conductors (PEMC). The PEMC medium is described by the parameter M with special cases of PMC (vanishing M) and PEC (infinite M). The scattering by a small sphere of such a material from incoming plane wave can be explained by the interplay of electric and magnetic dipoles. The special characteristics of the radiation of PEMC spherers (different from PEC and PMC) include cross-polarization which is especially marked in the backscattering direction. The radiation pattern is rotated by an angle that has a simple connection with the M parameter. Scattering patterns of PEMC spheres with size parameters up to $ka = 3$ are shown and they also display cross-polarized properties. The computations are based on a MoM software to solve the surface integral equation for the fields.

I. INTRODUCTION

The objective of the present paper is to analyze how the basic scattering characteristics and parameters of electromagnetic plane waves from a perfectly conducting (PEC) sphere are affected and changed when the material of the scattering sphere is made of a more general medium: perfect electromagnetic conductor (PEMC).

In the following, we first introduce the PEMC medium and connect it with the class of bianisotropic materials. Next we present the scattering properties of homogeneous spheres made of different materials. Then the scattering problems for spheres with different material and size parameters are solved by a surface integral equation software, developed in the Electromagnetics Laboratory of Helsinki University of Technology, and the results are given physical interpretation.

II. PEMC MEDIUM

The concept of perfect electromagnetic conductor (PEMC, [1, 2]) is a generalization of the much-used idealizations of perfect electric conductor (PEC) and perfect magnetic conductor (PMC). In PEC, the electric field and magnetic flux vanish, which can be modelled by assuming that its permittivity ϵ grows to infinity and the permeability μ decreases to zero. This behavior can be generalized: the response of PEMC media contains a scalar parameter M

$$\mathbf{D} = M\mathbf{B}, \quad \mathbf{H} = -M\mathbf{E} \tag{1}$$

in the constitutive relations linking the electric ($\mathbf{E}, \mathbf{D}$) and magnetic ($\mathbf{H}, \mathbf{B}$) field strengths and flux densities. Translating these quite strange-looking conditions (1) into field-versus-flux type relations, we can write the constitutive parameter matrix relation [3] in the following manner,

$$\begin{aligned} \begin{pmatrix} \mathbf{D} \\ \mathbf{B} \end{pmatrix} &= \begin{pmatrix} \epsilon & \xi \\ \zeta & \mu \end{pmatrix} \begin{pmatrix} \mathbf{E} \\ \mathbf{H} \end{pmatrix} \\ &= q \begin{pmatrix} M & 1 \\ 1 & 1/M \end{pmatrix} \begin{pmatrix} \mathbf{E} \\ \mathbf{H} \end{pmatrix}. \quad \text{with} \quad q \to \infty \end{aligned} \tag{2}$$

Even if the transformation between equations (1) and (2) is not immediately obvious, it can be checked by opening up the matrix: $\mathbf{D} = q(M\mathbf{E} + \mathbf{H})$ and $\mathbf{B} = q(\mathbf{E} + \mathbf{H}/M)$, which returns equation (1) as $q \to \infty$. Because $\mathbf{D}$ cannot reach infinity, the factor multiplying q has to vanish.

The admittance-like parameter M can be expressed in another convenient form by the angle ϑ,

$$M = \cot \vartheta. \tag{3}$$

It may hurt intuition that the material parameters of PEMC are infinite. In fact, this is the case for all four bi-isotropic parameters of PEMC. There is, however, the following restriction between them: $\epsilon\mu - \xi\zeta = 0$ as can be seen from equation (2). But as was noted, infinities are also encountered in PEC and PMC cases. T he PEC and PMC materials are special cases of relation (1).

For $M = \infty$ (corresponding to $\vartheta = 0$), we have $\mathbf{E} = 0$ and $\mathbf{B} = 0$ which is the requirement for PEC (electric field and magnetic flux cannot exist inside a perfect conductor). But because no restrictions are set on $\mathbf{D}$ and $\mathbf{H}$, we require $\epsilon \to \infty$ and $\mu \to 0$. Similarly, by duality [4], the case $M = 0$ (or $\vartheta = \pm\pi/2$) leaves us with PMC, as $\mathbf{H} = 0$ and $\mathbf{D} = 0$, in other words $\epsilon \to 0$ and $\mu \to \infty$.

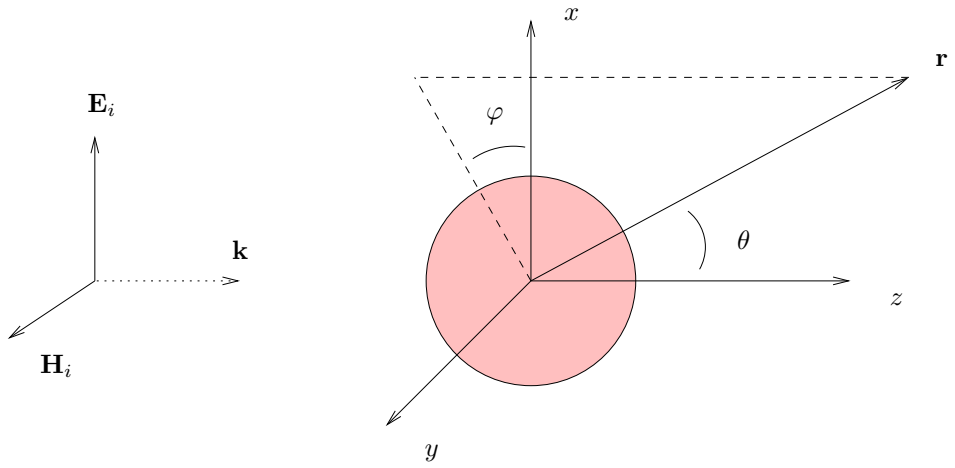

Fig. 1. Geometry of the problem: homogeneous sphere as an obstacle to the incident, linearly x-polarized electromagnetic wave which is propagating into the $+z$-direction. The scattering direction is defined by the angles θ, φ of the spherical coordinate system.

Inside PEMC media, a linear combination of the electric and magnetic fields vanishes identically: $\mathbf{H} + M\mathbf{E} = 0$. This means that on the interface between "ordinary" and PEMC materials, the boundary condition is ($\mathbf{n}$ is the unit normal)

$$\mathbf{n} \times \mathbf{H} = -M\mathbf{n} \times \mathbf{E}. \tag{4}$$

The properties of PEMC media, as the results of the present paper will show, promise quite interesting applications concerning polarization transformation, for example. A challenge which remains is how to fabricate PEMC materials in the real world. One possibility is a composite structure involving a gyrotropic (e.g., ferrite) material layer on a metal surface, with which a band-limited PEMC behavior can be simulated [5]. In today's electromagnetics research there are large-scale activities internationally concerning artificial metamaterials[1] which give hopes that new designs that behave according to more and more exotic material relations come into experimental and operative use.

In the following, we will study how an electromagnetic plane wave is scattered by a sphere which is made of PEMC material.

III. SCATTERING BY A SPHERE

The scattering of waves by a homogeneous sphere is a classical problem in electromagnetics. After the fundamental paper by Gustav Mie [7] and much preceding literature, the problem has been discussed thoroughly in textbooks; see, for example [8, 9, 10, 11].

In the following three-dimensional formulation, we shall use normalized field quantities: in terms of the SI-system electric and magnetic fields and flux densities $\mathcal{E}, \mathcal{H}, \mathcal{D}, \mathcal{B}$ with units V/m, A/m, As/m^2, Vs/m^2, respectively, we deal with fields and fluxes that are renormalized in order to have homogeneous units in each of them,

$$\mathbf{E} = \sqrt{\epsilon_0}\,\mathcal{E}, \quad \mathbf{H} = \sqrt{\mu_0}\,\mathcal{H}, \quad \mathbf{D} = \frac{\mathcal{D}}{\sqrt{\epsilon_0}}, \quad \mathbf{B} = \frac{\mathcal{B}}{\sqrt{\mu_0}} \tag{5}$$

with the free-space parameters ϵ_0, μ_0. This leaves the material parameters in equation (2) dimensionless. All four renormalized field quantities carry the dimension of square root of energy density: $\sqrt{\mathrm{VAs/m^3}} = \sqrt{\mathrm{J/m^3}}$.

A. Small scatterer

Let the geometry be fixed in such a way that the plane wave is incident in the $+z$ direction, its electric field is polarized along the x axis, and the magnetic field along the y axis, as shown in Fig. 1. The ordinary spherical angles are θ between the position vector and the z axis, and φ counted from the x axis up to the projection of the position vector onto the xy plane.

To begin with, consider the scattering by a small sphere. By a small sphere we mean a sphere the diameter of which is small compared to the wavelength of the incident field. No exact relative limit can be expressed for the object to be small; in practise, often the size around a tenth of the wavelength could be used as this limit. The results of the present paper will give more light into this question which determines when static and quasi-static considera-

[1] Such programs include the DARPA program in the USA (`www.darpa.mil/dso/thrust/matdev/metamaterials`) and the European Network of Excellence within the Union's 6th Framework programme *Metamorphose* (`www.metamorphose-eu.org`). For literature on electromagnetic metamaterials, see, for instance [6].

Fig. 2. The electric far fields radiated by an electric $(\mathbf{p}_e)$ and magnetic $(\mathbf{p}_m)$ dipole. The electric field of the electric dipole $\mathbf{E}_e$ is "longitudinal", meaning that it is in the plane spanned by the dipole and the position vector, whereas the electric field of the magnetic dipole $\mathbf{E}_m$ is "latitudinal," perpendicular to that. Note the arrow directions. The amplitude dependence of the radiated field is sine of the angle between the dipole and the position vector in both cases.

tions have to be replaced by dynamic analysis.

Let us start with the electromagnetic field radiated by dipoles. The far-field behavior of the electric field of the electric and magnetic Hertzian dipoles [12] is illustrated in Fig. 2.

Obviously, the amplitude of the radiated electric field decays with distance as r^{-1}. If the electric and magnetic dipoles vibrate in the same phase, their electric fields add up constructively. The vector characteristics (polarization) and radiation pattern in the far field can then be calculated using vector cross products,

$$\mathbf{E}_s = (\mathbf{p}_e \times \mathbf{u}_r - \mathbf{p}_m) \times \mathbf{u}_r \tag{6}$$

with $\mathbf{u}_r = \mathbf{u}_x \sin\theta\cos\varphi + \mathbf{u}_y \sin\theta\sin\varphi + \mathbf{u}_z \cos\theta$.

B. PEC and PMC spheres

The electric and magnetic dipole moments $\mathbf{p}_e, \mathbf{p}_m$ of a sphere which can have dielectric and magnetic properties are excited by the incident fields,

$$\mathbf{p}_e = \alpha_e \mathbf{E}_i, \quad \mathbf{p}_m = \alpha_m \mathbf{H}_i. \tag{7}$$

These dipole moments are determined by the normalized electric and magnetic polarizabilities [13]

$$\alpha_e = 3\frac{\epsilon - 1}{\epsilon + 2}, \quad \alpha_m = 3\frac{\mu - 1}{\mu + 2} \tag{8}$$

where ϵ is the relative permittivity and μ the relative permeability of the sphere.

For the PEC sphere $(\epsilon \to \infty, \mu \to 0)$, the normalized electric polarizability is 3 and the normalized magnetic polarizability is $-3/2$. Therefore we can calculate the scattered electric field of a small, perfectly conducting sphere from the vector (note that in our normalized system of electric and magnetic quantities, the electric and magnetic fields have the same unit and the free-space impedance is unity)

$$3(\mathbf{u}_x \times \mathbf{u}_r + \frac{1}{2}\mathbf{u}_y) \times \mathbf{u}_r \tag{9}$$

because the electric dipole is x-directed and the magnetic one y-directed according to Fig. 1. The resulting absolute value of the scattered field is illustrated in Fig. 3 in the two principal planes: E-plane (xz-plane) and H-plane (yz-plane). Note the greater backscattering compared to the forward scattering, and the null in the E-plane into the $\theta = 60^\circ$ direction. The threefold back-to-front ratio (ninefold in the power pattern) is a well-known fact [10, p. 157] for perfectly conducting scatterers. Of course the same behavior applies for magnetically perfectly conducting small spheres with the E- and H-plane patterns interchanged.

There is a significant qualitative difference of these patterns compared to the ordinary Rayleigh scattering diagram of a dielectric sphere (Fig. 4), with equal radiation to the front and back, and a null in the $\theta = 90^\circ$ in the E-plane. On the other hand, if the sphere has both arbitrary finite permittivity and permeability, the patterns again change. Especially, if the dielectric and magnetic material parameters are equal $(\epsilon = \mu)$, there is no reflection, but, rather, a strong forward scattering, as can also be seen in Fig. 4.

The polarization (vector direction of the electric field) of the scattering by a PEC sphere is shown in Fig. 5.

C. PEMC sphere

How does the scattering change if the sphere is made of homogeneous PEMC material where the material parameter is arbitrary $(0 < |M| < \infty)$? When the plane wave touches the sphere, dipole moments are created, just like in the cases dealt with in the previous section. The difference with the PEC and PMC cases is now that both the electric and magnetic dipole moments of the PEMC sphere are dependent on both the electric and magnetic incident fields.

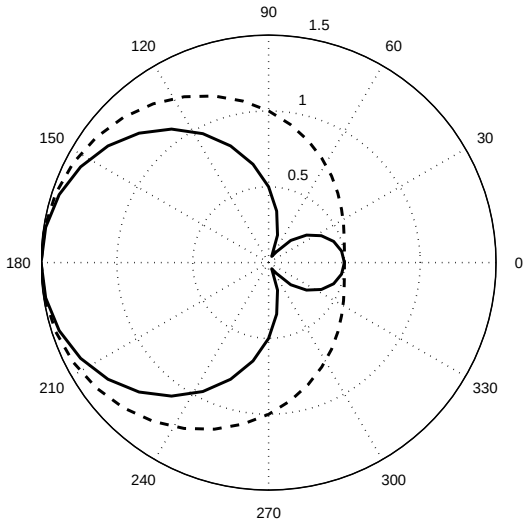

Fig. 3. The scattered far field pattern of a PEC sphere in the E-plane (solid line) and H-plane (dashed line). For the PMC sphere the patterns interchange. The incident wave is arriving from the left.

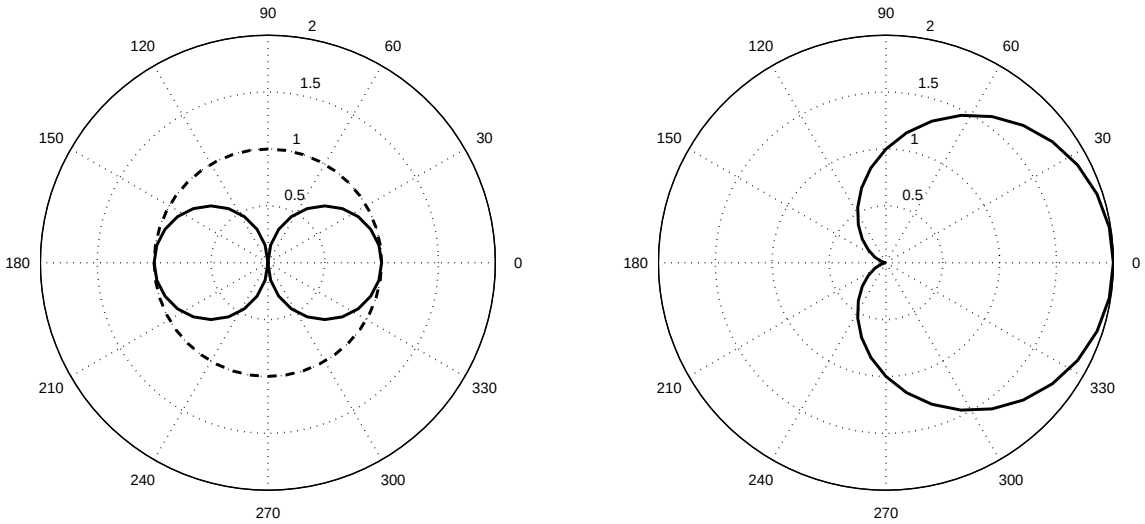

Fig. 4. Left-hand side: scattered far field pattern of a dielectric sphere in the E-plane (solid line) and H-plane (dashed line). On the right-hand side, the pattern for a reflection-matched sphere, $\epsilon = \mu$, in which case the pattern is the same in E and H planes. The incident wave is arriving from the left. Note that the amplitude of the permittivity and permeability only affects the overall magnitude of the scattering (here normalized to 1 and 2 in maximum field magnitude, respectively). However, regardless of the absolute amplitude of ϵ (which is equal to μ on the right-hand side), the radiation patterns are the same.

The polarizabilities and the dipole moments

$$\begin{aligned} \begin{pmatrix} \mathbf{p}_e \\ \mathbf{p}_m \end{pmatrix} &= \begin{pmatrix} \alpha_{ee} & \alpha_{em} \\ \alpha_{me} & \alpha_{mm} \end{pmatrix} \begin{pmatrix} \mathbf{E}_i \\ \mathbf{H}_i \end{pmatrix} \\ &= \mathsf{A} \begin{pmatrix} \mathbf{E}_i \\ \mathbf{H}_i \end{pmatrix} \end{aligned} \tag{10}$$

can be calculated from the material parameter matrix

$$\begin{aligned} \mathsf{C} &= \begin{pmatrix} \epsilon & \xi \\ \zeta & \mu \end{pmatrix} \\ &= \lim_{q \to \infty} q \begin{pmatrix} M & 1 \\ 1 & 1/M \end{pmatrix} \end{aligned} \tag{11}$$

with the infinite parameters for the PEMC material. The polarizability matrix can be calculated from the material

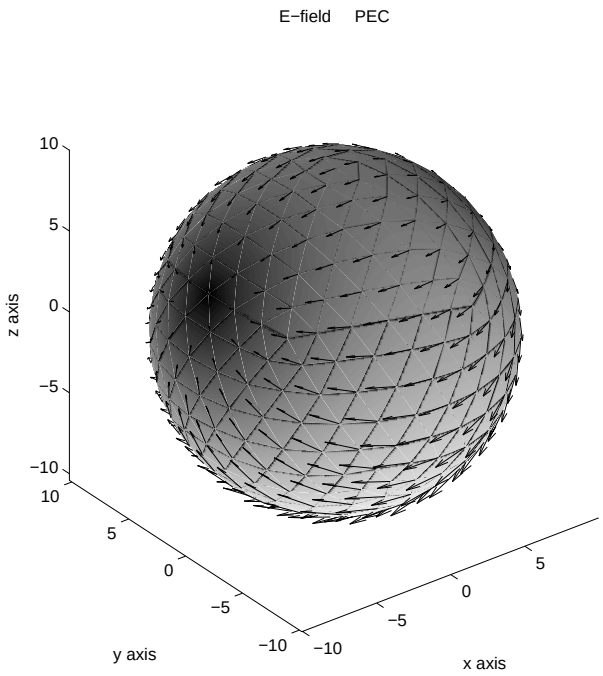

Fig. 5. The scattered far field of a small PEC sphere. Grayscale gives the amplitude and the arrows display the polarization of the radiated electric field. Note the zero in the radiation pattern in the E-plane (xz plane, cf. Fig. 3). Incident electric field is parallel to the x axis. (The figure has been calculated numerically with a dynamic solution for a sphere with the radius $a = 1$ m, and the (small) size parameter $ka = 0.1$. The radiated field has been calculated on a spherical surface with radius 10 m).

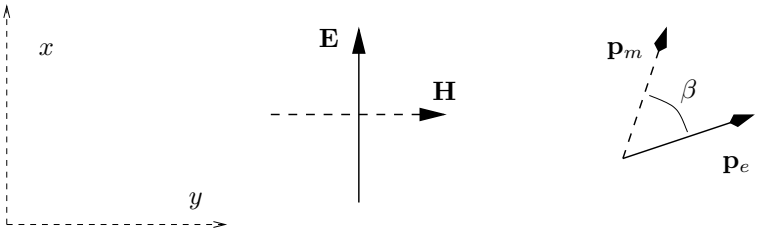

Fig. 6. The directions of the induced electric and magnetic dipole moments in the PEMC sphere are not in general parallel to the incident field vectors. The angle β between the moments depends on M. This case corresponds to $M = 1$.

parameter matrix [13] and turns out to be

$$\begin{aligned} \mathsf{A} &= 3(\mathsf{C}-\mathsf{I})\cdot(\mathsf{C}+2\mathsf{I})^{-1} \qquad (12)\\ &= \frac{3/2}{1+M^2}\begin{pmatrix} 2M^2-1 & 3M \\ 3M & 2-M^2 \end{pmatrix} \\ &= \frac{3}{4}\begin{pmatrix} 1 & 0 \\ 0 & 1 \end{pmatrix} \\ &\quad -\frac{9}{4}\begin{pmatrix} \cos 2\vartheta & -\sin 2\vartheta \\ \sin 2\vartheta & \cos 2\vartheta \end{pmatrix}\begin{pmatrix} -1 & 0 \\ 0 & 1 \end{pmatrix} \end{aligned}$$

where I is the 2×2 unit matrix. Note that despite the infinities on (11) of the four material parameters of PEMC, all polarizability components of (12) behave "reasonably." They remain finite for real values of M.

Now, both induced dipole moments contain components in x and y direction, due to the magnetoelectric coupling. The dipoles are rotated, depending on M; see Fig. 6. Furthermore, they are orthogonal only in the PEC or PMC case. The angle β between the dipoles obeys (cf. definition (3))

$$\begin{aligned} \cos\beta &= \frac{3M}{\sqrt{(1+4M^2)(4+M^2)}} \\ &= \frac{3\sin 2\vartheta}{\sqrt{(5-3\cos 2\vartheta)(5+3\cos 2\vartheta)}}. \qquad (13) \end{aligned}$$

The dependence of the angle β on the PEMC parameter

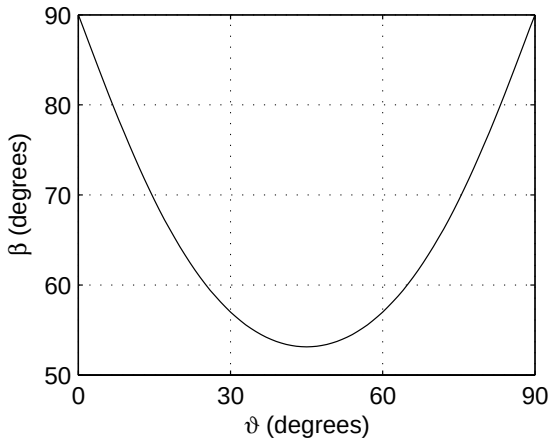

Fig. 7. The angle β as a function of the PEMC parameter ϑ. Note the orthogonality of dipoles in the PEC ($\vartheta = 0°$) and PMC ($\vartheta = 90°$) limits.

ϑ is illustrated in Fig. 7. In the PEC and PMC limit cases, the angle is obviously $90°$. The minimum angle $\beta = \arccos(3/5) \approx 53°$ comes in the case $M = \pm 1$ (corresponding to $\vartheta = \pm 45°$)

Now the scattered field can be calculated from equation (6). Figure 8 shows the radiated field for different values of the M parameter. We can observe a continuous transition from PMC to PEC as the radiation pattern rotates along with varying M. Also the polarization of the electric field changes gradually from the "longitudinal" field of the PEC case to the "latitudinal" PMC radiation field. For a general PEMC sphere, the far-field polarization pattern is helicoidal with handedness depending on the sign of M.

The rotation of the radiation pattern can be seen in Fig. 9, where the scattered field amplitude is shown in the xy-plane. Clearly the radiation of the PEMC sphere is somewhere between those of PEC and PMC.

D. Size-dependent effects

When the radius of the sphere is no longer small compared to the wavelength, the scattering characteristics of the object become decorated with more details. Of course, then the quasistatic calculations involving the electric and magnetic dipole moments with which the low-frequency results were calculated do not apply. We have used a full-wave numerical code to calculate the results.

The code is based on the surface integral equation method. The electric field integral equation, EFIE, is first written for both the electric surface currect density $\mathbf{J}_e = \mathbf{n} \times \mathbf{H}$ and magnetic $\mathbf{J}_m = -\mathbf{n} \times \mathbf{E}$ surface current density as

$$\left(\frac{-1}{i\omega\varepsilon_0} \left(\nabla\nabla\cdot + k_0^2 \right) \mathcal{S}(\mathbf{J}_e) - \nabla \times \mathcal{S}(\mathbf{J}_m) \right)_{\tan} = -\mathbf{E}^{\mathrm{inc}}_{\tan}. \tag{14}$$

Here

$$\mathcal{S}(\mathbf{F}) = \int_S G(\mathbf{r}, \mathbf{r}')\, \mathbf{F}(\mathbf{r}')\, dS' \tag{15}$$

and G is the free space Green's function. For $M \neq 0$, boundary condition (4) gives the following relation between $\mathbf{J}_e$ and $\mathbf{J}_m$ on the surface of a PEMC object

$$\mathbf{J}_m = \frac{1}{M} \mathbf{J}_e. \tag{16}$$

Using equation (16) $\mathbf{J}_m$ can be removed from equation (14) and the integral equation for $\mathbf{J}_e$ reads

$$\left(\frac{-1}{i\omega\varepsilon_0} \left(\nabla\nabla\cdot + k_0^2 \right) \mathcal{S}(\mathbf{J}_e) - M \nabla \times \mathcal{S}(\mathbf{J}_e) \right)_{\tan} = -\mathbf{E}^{\mathrm{inc}}_{\tan}. \tag{17}$$

In the PEC case, i.e., $M = \infty$, $\mathbf{J}_m$ vanishes and equation (17) reduces to the usual EFIE for the electric surface current. In the PMC case, $M = 0$, or for small values of M, instead of equation (16) we write

$$\mathbf{J}_e = M \mathbf{J}_m \tag{18}$$

and equation (14) is written for the magnetic current only. In both cases the resulting integral equations are solved numerically with the method of moments [14] using triangular rooftop basis and testing functions [15]. Details of the numerical implementations are similar as those presented in [16] and [17] in the case of PEC and dielectric objects. It should be noticed that, similarly as in the cases of PEC and PMC objects, also in the case of a PEMC

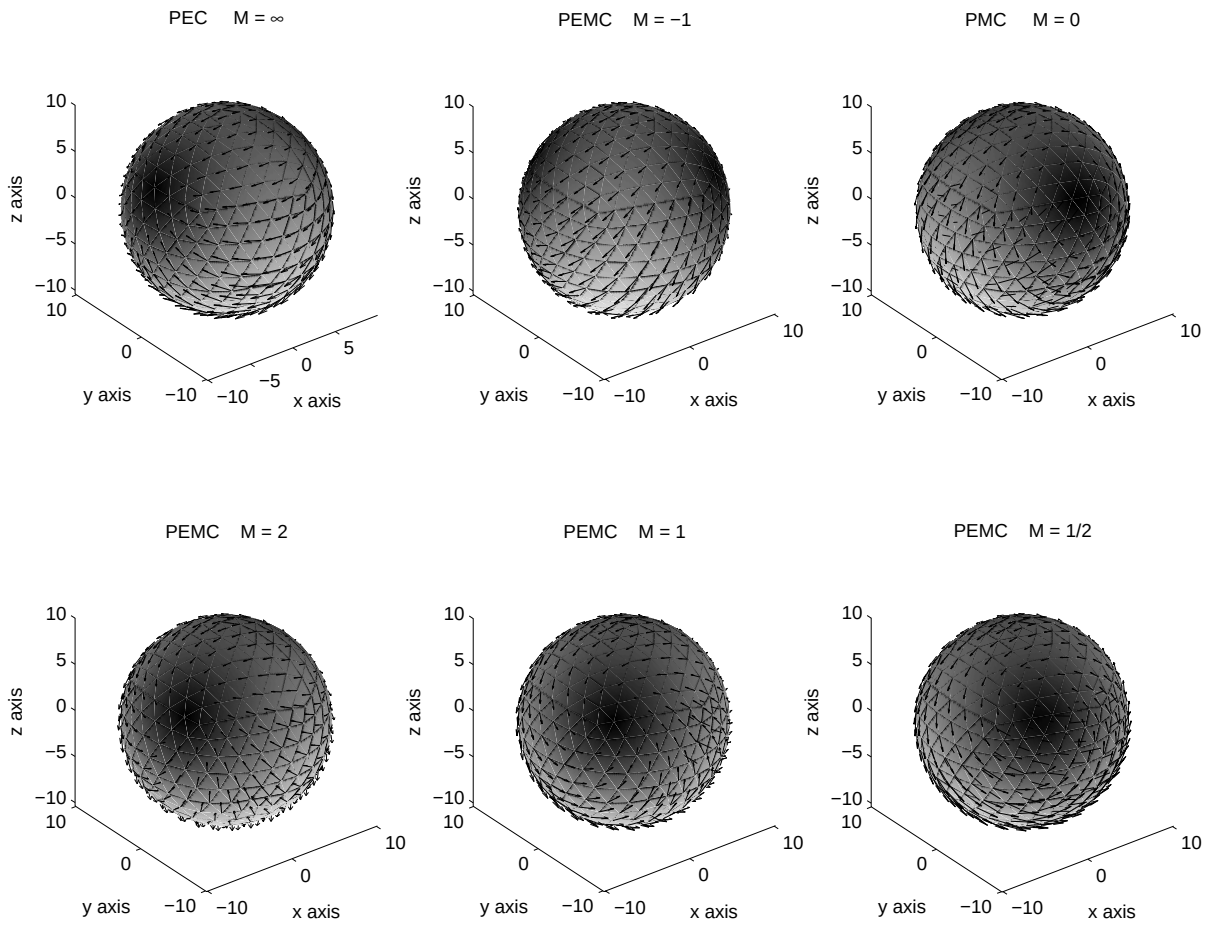

Fig. 8. The scattered far field of a small PEMC sphere with varying M parameters. $M = 0$ gives PMC and $M = \infty$ corresponds to PEC. Grayscale shows the amplitude and the arrows display the polarization of the radiated electric field. Incident electric field is parallel to the x axis.

object, a combined field integral equation formulation is needed to avoid problems with internal resonances.

The combined effects of the electrical size of the sphere and the PEMC parameter are shown in the set of Figs. 10 to 13, where the size of the sphere increases from $ka = 0.1$ to 3. These correspond to sphere diameters from $2a = 0.032\lambda$ to 0.95λ.

IV. DISCUSSION

We can draw several conclusions from the calculated results.

A. Co- and cross-polarization

The main property in the scattering behavior and characteristics of a PEMC sphere is the appearance of cross-polarization. Cross-polarization is strongest when the parameter $|M| = 1$ and also in the backscattering direction.

Quantitatively, the effect of the parameter M on backscattering is the following. The co- and cross-polarized components of the backscattered electric field as functions of the x and y components of the incident field read as

$$\begin{pmatrix} \mathbf{E}_x \\ \mathbf{E}_y \end{pmatrix}_s = \begin{pmatrix} \frac{1-M^2}{1+M^2} & \frac{2M}{1+M^2} \\ \frac{-2M}{1+M^2} & \frac{1-M^2}{1+M^2} \end{pmatrix} \begin{pmatrix} \mathbf{E}_x \\ \mathbf{E}_y \end{pmatrix}_i = -\begin{pmatrix} \cos 2\vartheta & -\sin 2\vartheta \\ \sin 2\vartheta & \cos 2\vartheta \end{pmatrix} \begin{pmatrix} \mathbf{E}_x \\ \mathbf{E}_y \end{pmatrix}_i . \quad (19)$$

The appearance of a cross-polarized component in reflection is a sign of non-reciprocity. From equation (19) we can observe that the reflection matrix is a rotation matrix defined by the angle $\pi - 2\vartheta$. For example, in the case $M = \pm 1$ (meaning that the angle of equation (3) is $\vartheta = \pm 45^\circ$) the reflection is fully cross-polarized, in other words the rotation is $180^\circ - 2\vartheta = \pm 90^\circ$. In the other limit, the cross-polarization vanishes for the PEC (180° rotation) and PMC (0° rotation) cases.

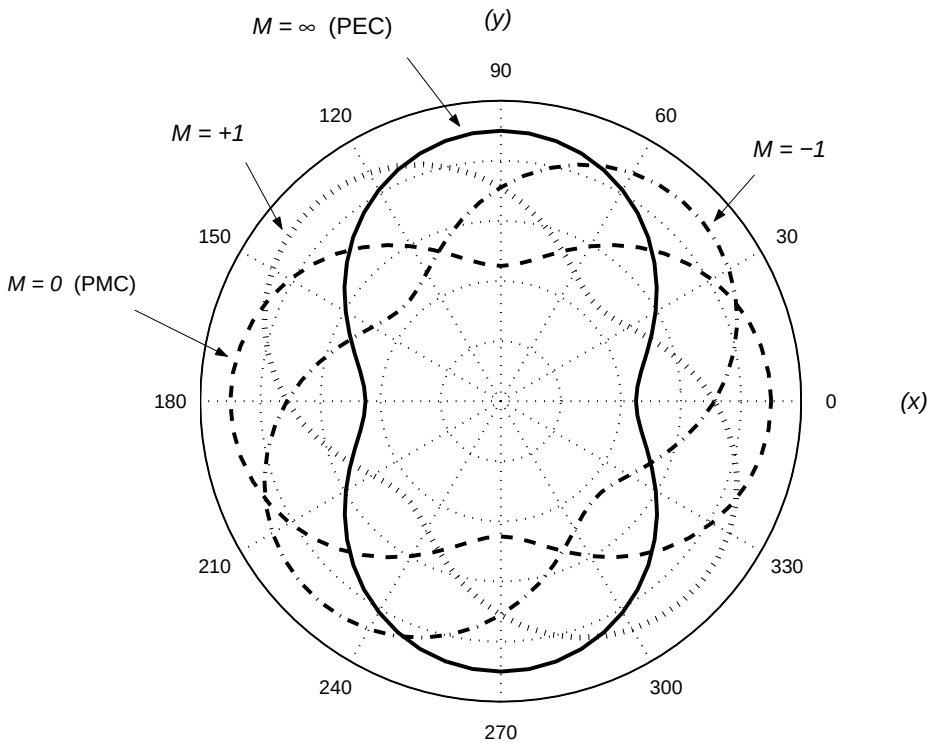

Fig. 9. The xy-plane far-field scattering plot of various spheres: PEC, PMC, and PEMC with $M = \pm 1$.

On the other hand, the forward-scattered field of a PEMC sphere with $|M| = 1$ is fully co-polarized. This is valid not only for electrically small spheres but also can be seen to hold when the sphere increases in the cases of $ka = 1, 2, 3$ (Figs. 11 to 13). When the M values starts to differ from unity, co-polarization appears in the backscattered radiation and cross-polarization in the forward direction. Of course, in the limits of both PEC and PMC, the scattering is fully co-polarized in both E and H planes.

This phenomenon of cross-polarization in reflection is important to notice. It is a sign of non-reciprocity (for this concept, see, for example [12, 18]). Whereas in transmission problems a rotation of polarization is perfectly consistent with reciprocity, the situation for the reflection problem is different. An example of reciprocal type of polarization rotation is the optical activity in chiral materials: a linearly polarized electromagnetic wave undergoes a uniform twist in the plane of the polarization the angle of which is proportional to the chirality parameter, frequency, and the distance propagated. The handedness of the material determines the sense (clockwise or counterclockwise) into which the rotation is space happens. (It is important not to confuse this polarization rotation with the Faraday rotation that can take place with wave propagation in magnetoplasma or ferrites. But there the external magnetic field makes the phenomenon anisotropic and non-reciprocal whereas the optical activity of chiral materials is isotropic and reciprocal [19].)

B. Radiation pattern and polarization

The phenomenon of cross-polarization is connected with the fact that the radiation pattern is rotated when the M parameter changes in the PEMC sphere, as can be seen for example in Figs. 8 and 9. The minimum radiation on the E-plane of a small PEC sphere moves continuously into the H-plane in the PMC case. The direction of the rotation depends on the sign of M.

Furthermore, the polarization of the radiated electric field changes continuously from the longitudinal electric-dipole type radiation (PEC), through a helicoidal pattern into the latitudinal magnetic-dipole type pattern in the PMC limit. This evolution is clear from Fig. 8.

C. Size dependence

When the size of the sphere increases so that it is no longer electrically small, the radiation pattern becomes more complex. This is a well-known fact from the theory of Mie scattering of "ordinary" spheres. For PEMC spheres, the effect of varying M parameter can be seen in Figs. 10 to 13. The expected increase into the forward

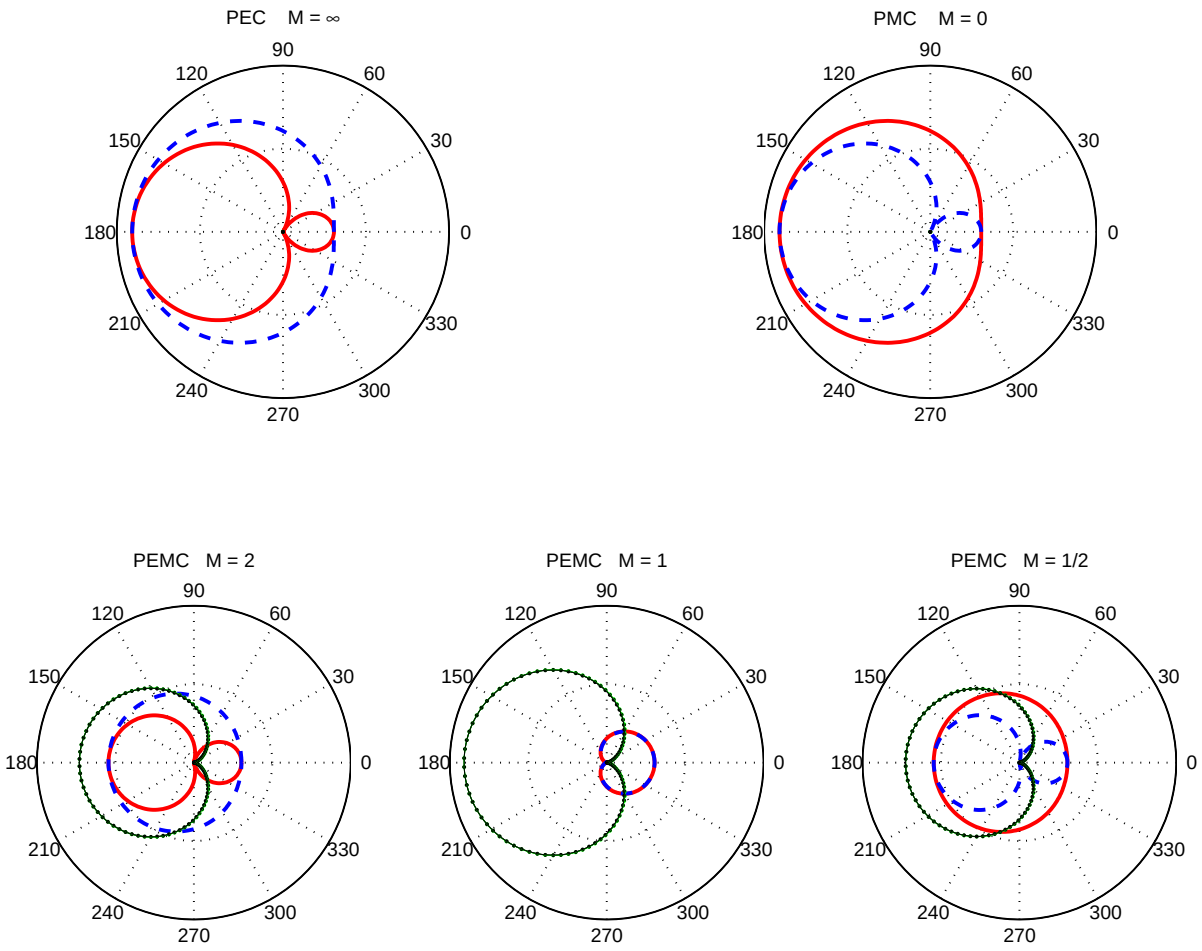

Fig. 10. The scattered far field power pattern of a small reflecting sphere $(ka = 0.1)$ with various values of the M parameter. Co-polarized in E-plane (solid line) and H-plane (dashed line). The dotted line shows the cross-polarized scattering (the same in both planes). The incident field is coming from the 180° direction.

scattering takes place regardless of the magnitude of M, as the size of the sphere increases from $ka = 0.1$ to 3. ($ka = 3$ means that the diameter of the sphere is around 95% of the wavelength.) But the results show clearly the cross-polarization in the backscattering direction, which is at its maximum for $|M| = 1$.

Another interesting observation is the following: for PEMC spheres, the radiated electric field is elliptically polarized in the E and H planes. As is known, this does not happen for PEC and PMC spheres even if the sphere is electrically large. This phenomenon can be seen in Figs. 14 to 15 which display the real and imaginary parts of the scattered electric field for a PEMC sphere with $ka = 1$. Both in the E and H planes we can observe that the real and imaginary parts are generally nonzero and are non-parallel, which implies that the temporal evolution of the electric field follows an ellipse.

D. Amplitudes

The preceding analysis has not paid any particular attention to the absolute amplitudes of the bistatic scattering cross section. This is because the behavior is quite uninteresting, as far as the effect of M parameter is concerned. Since the PEMC material is totally reflecting, in other words it is lossless and no field can penetrate into it, just like in the case of PEC and PMC, the scattered power remains independent of M. The effect is only on the distribution of power into the spatial directions and polarization states.

For example, the well-known [8, Sec. 10.61] result for the scattering efficiency of a small PEC sphere

$$Q_{\mathrm{sca}} = \frac{10}{3}(ka)^4 \tag{20}$$

is correct for a PEMC (and PMC) sphere with any real value of M.

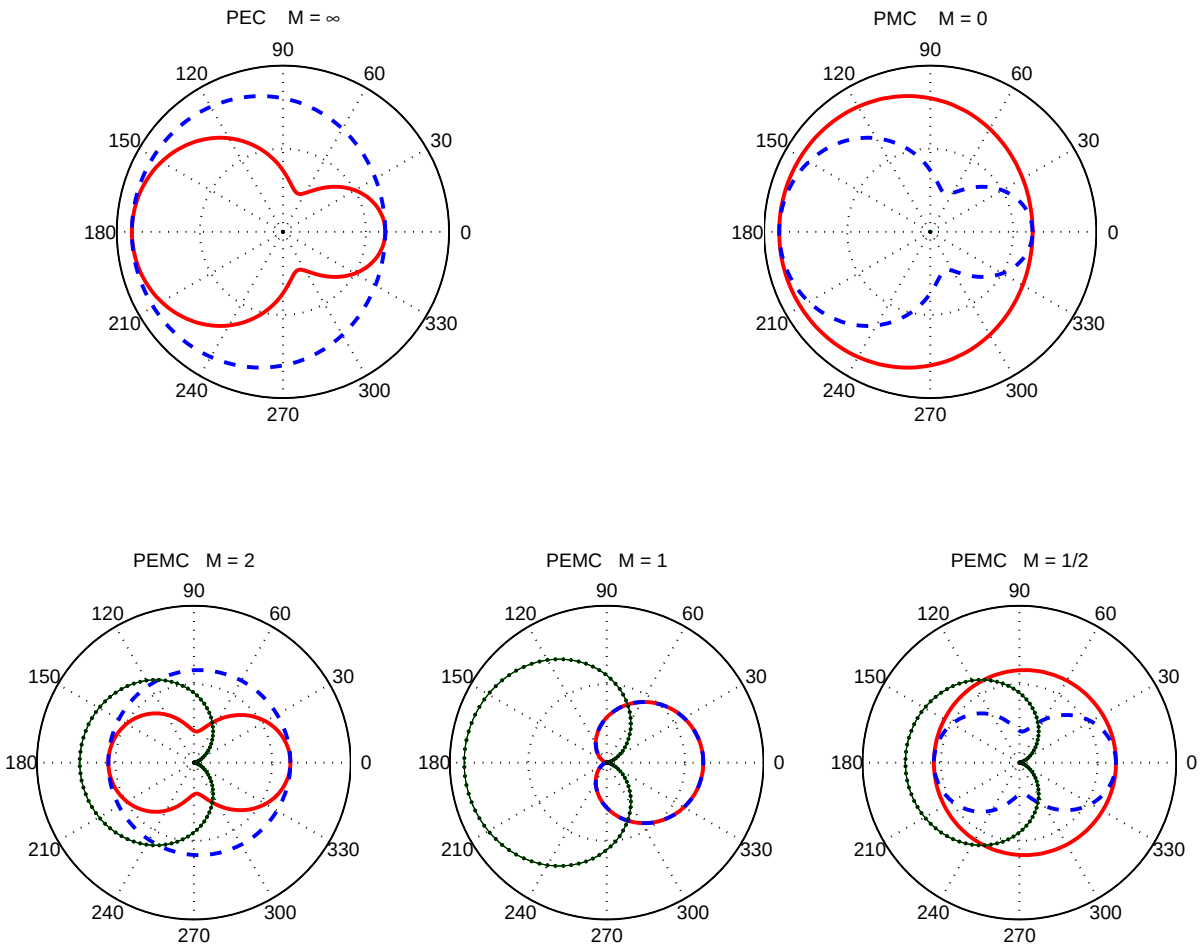

Fig. 11. The scattered far field power pattern of a small reflecting sphere $(ka = 1)$ with various values of the M parameter. Co-polarized in E-plane (solid line) and H-plane (dashed line). The dotted line shows the cross-polarized scattering (the same in both planes). The incident field is coming from the 180° direction.

V. CONCLUSIONS

The present paper has demonstrated that the scattering problem of particles made of rather complex materials can be solved. Using a computational surface integral equation software, where the required boundary condition is modified to account for the perfect electromagnetic conductor effect, the fields can be calculated. The results showed clearly the effect of the PEMC parameter on the scattering patterns: compared with a corresponding PEC scatterer, the polarization of the fields is rotated in reflection. The angle of rotation is determined by the PEMC amplitude between the limit cases of PEC and PMC materials. In the scattering patterns, this effect obviously manifests itself as cross-polarization which increases when the scattering direction deviates from the incident wave (forward) direction.

Because the polarization-rotating effect is present for all sphere sizes and the angle of rotation was seen to be independent of the size of the sphere relative to the wavelength, the results were only calculated for sphere sizes $ka = 0 \ldots 3$. If the size parameter becomes higher, the scattering pattern will display more and more sidelobes, as is well known. However, the effect of the M parameter of the scatterer on the patterns remains the same as for the lower frequency cases studied in this paper.

VI. ACKOWLEDGEMENT

The authors are grateful to Dr. Matti Taskinen for valuable help in formatting the article.

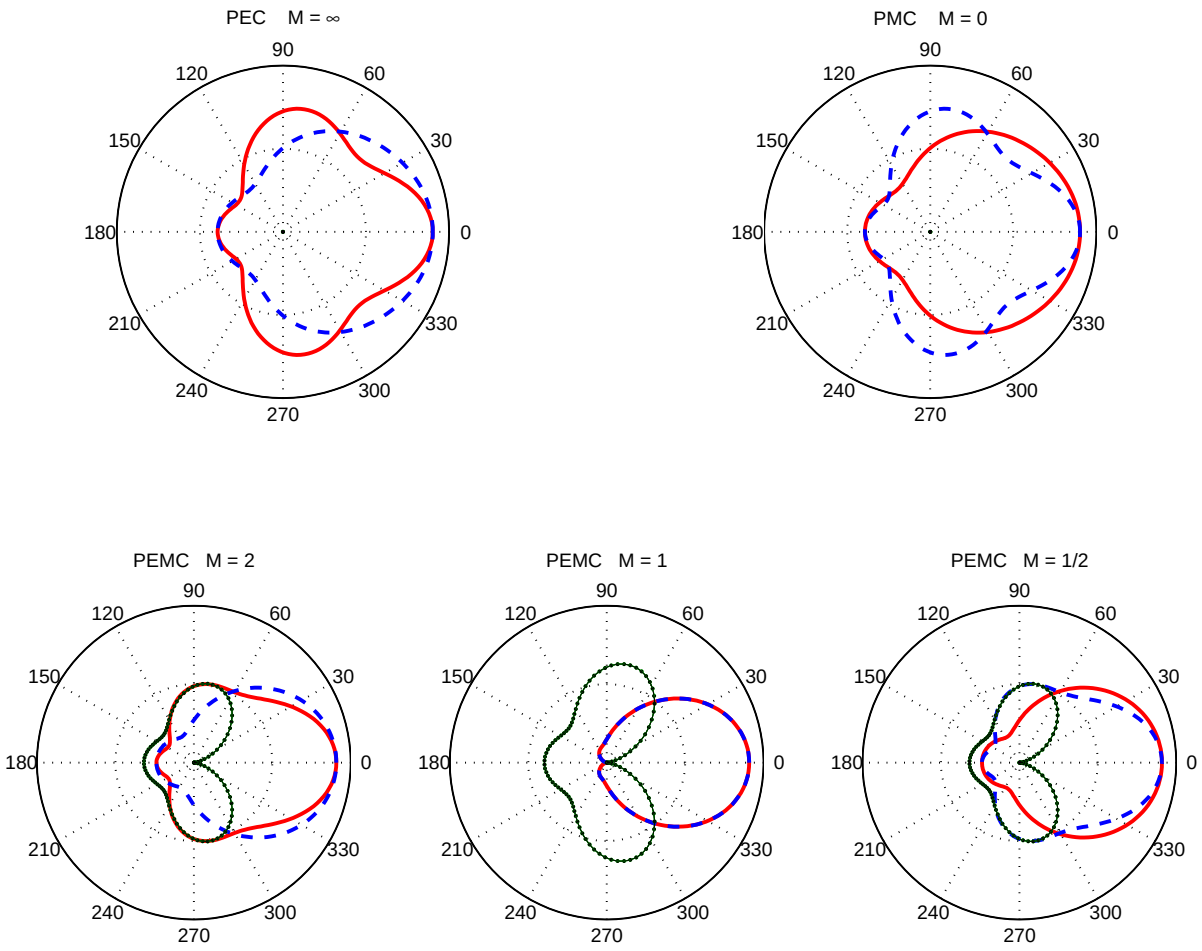

Fig. 12. The scattered far field power pattern of a small reflecting sphere $(ka = 2)$ with various values of the M parameter. Co-polarized in E-plane (solid line) and H-plane (dashed line). The dotted line shows the cross-polarized scattering (the same in both planes). The incident field is coming from the 180° direction.

REFERENCES

[1] I. V. Lindell and A. H. Sihvola, "Perfect electromagnetic conductor," *Journal of Electromagnetic Waves and Applications*, vol. 19, no. 7, pp. 861-869, 2005.

[2] I. V. Lindell and A. H. Sihvola, "Transformation method for problems involving perfect electromagnetic conductor (PEMC) structures ," *IEEE Transactions on Antennas and Propagation*, vol. 53, no. 9, pp. 3005-3011, 2005.

[3] I. V. Lindell, A. H. Sihvola, S. A. Tretyakov, and A. J. Viitanen, *Electromagnetic Waves in Chiral and Bi-isotropic Media*, (Artech House, Boston and London, 1994).

[4] I. V. Lindell, *Methods for Electromagnetic Field Analysis*, (Oxford and IEEE Press, New York, 1995).

[5] I. V. Lindell and A. H. Sihvola, "Realization fo the PEMC boundary," *IEEE Transactions on Antennas and Propagation*, vol. 53, no. 9, pp. 3012-3018, 2005.

[6] R. W. Ziolkowski and N. Engheta, (editors), *IEEE Transactions on Antennas and Propagation*, Special Issue on Metamaterials, vol. 51, no. 10, Part I, 2003.

[7] G. Mie, "Beiträge zur Optik trüber Medien, speziell kolloidaler Metallösungen," *Annalen der Physik*, vol. 25, pp. 377-445, 1908.

[8] H. C. Van de Hulst, *Light Scattering by Small Particles*, (Wiley, New York, 1957; Dover, New York, 1981).

[9] J. A. Stratton, *Electromagnetic Theory*, (McGraw Hill, New York, 1941).

[10] M. Kerker, *The Scattering of Light and Other Electromagnetic Radiation*, (Academic Press, New York, 1969).

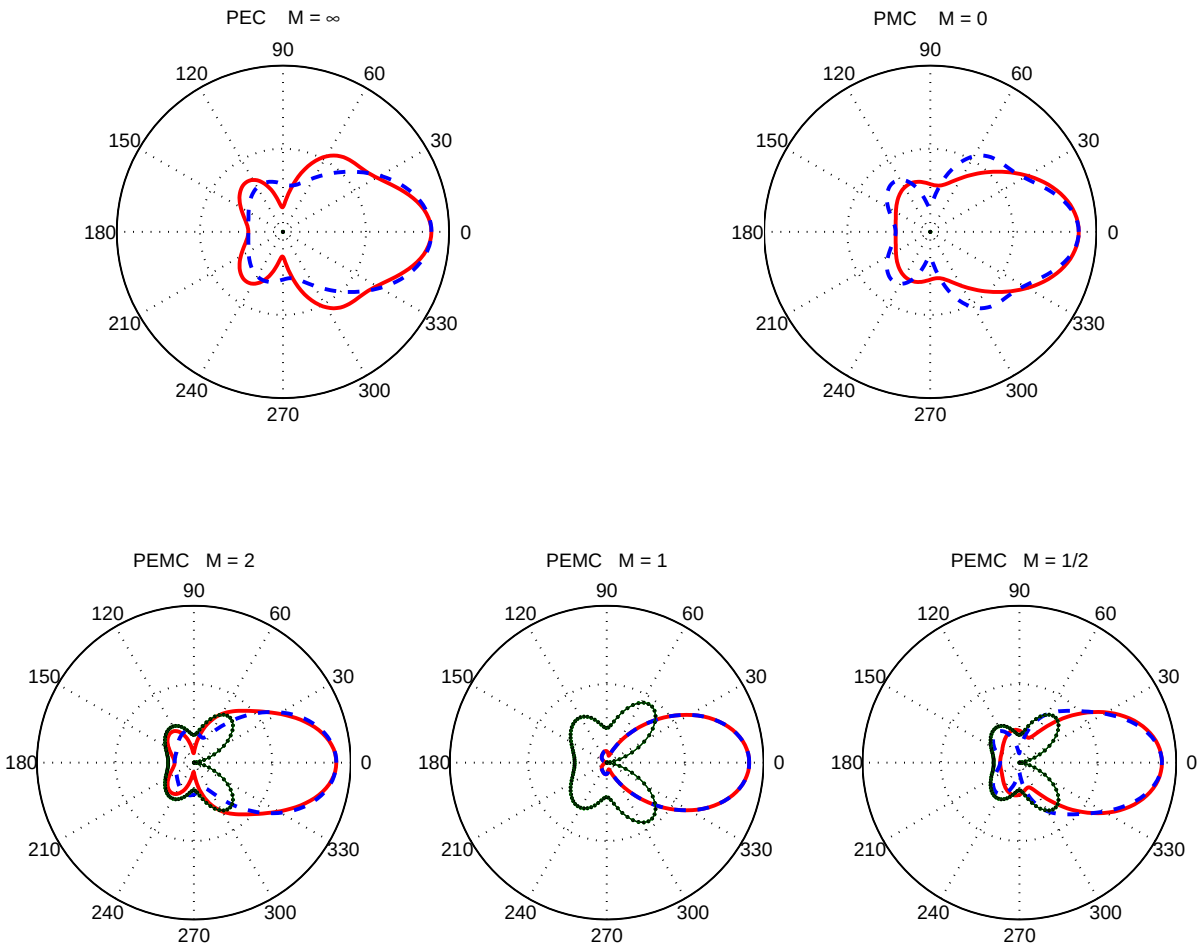

Fig. 13. The scattered far field power pattern of a small reflecting sphere $(ka = 3)$ with various values of the M parameter. Co-polarized in E-plane (solid line) and H-plane (dashed line). The dotted line shows the cross-polarized scattering (the same in both planes). The incident field is coming from the 180° direction.

[11] C. F. Bohren and D. R. Huffman, *Absorption and Scattering of Light by Small Particles*, (Wiley, New York, 1983).

[12] J. A. Kong, *Electromagnetic Wave Theory*, (Cambridge, Mass: EMW Publishing, 2000).

[13] A. Sihvola, *Electromagnetic Mixing Formulas and Applications*, (IEE Publishing, Electromagnetic Wave Series, London, 47, 1999).

[14] R. F. Harrington, *Field Computation by Moment Methods*, (Macmillan, New York, 1968).

[15] S. M. Rao, D. R. Wilton, and A. W. Glisson, "Electromagnetic scattering by surfaces of arbitrary shape," *IEEE Transactions on Antennas and Propagation*, vol. 30, pp. 409-418, 1992.

[16] P. Ylä-Oijala and M. Taskinen, "Calculation of CFIE impedance matrix elements with RWG and $\mathbf{n}\times$RWG functions," *IEEE Transactions on Antennas and Propagation*, vol. 51, pp. 1837-1846, 2003.

[17] P. Ylä-Oijala, M. Taskinen, and J. Sarvas, "Surface integral equation method for general composite metallic and dielectric structures with junctions," *Progress in Electromagnetic Research*, vol. 52, pp. 81-108, 2005.

[18] R. E. Collin, *Foundations for Microwave Engineering*, (Tokyo, McGraw–Hill, 1966).

[19] A. H. Sihvola and I. V. Lindell, "Material effects in bi-anisotropic electromagnetics," *IEICE Transactions on Electronics, (Japan)*, vol. E78-C, no. 10, pp. 1383-1390, 1995.

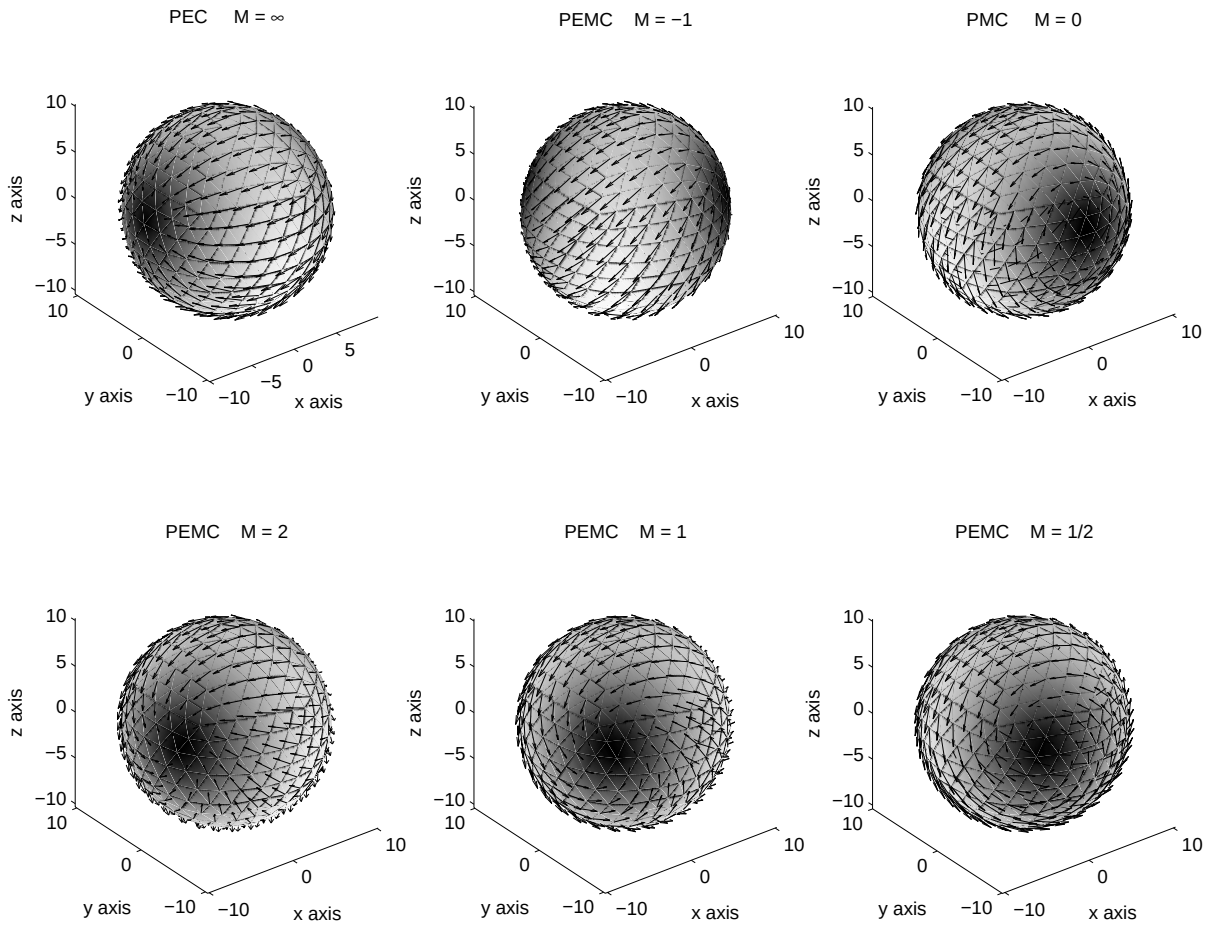

Fig. 14. The scattered far field of the PEMC sphere with varying M parameters: real part of the electric field. Grayscale shows the amplitude and the arrows display the polarization of the radiated electric field. Incident electric field is parallel to the x axis. The electrical size of the sphere is $ka = 1$.

Ari Sihvola is professor of electromagnetics at the Helsinki University of Technology (TKK), Espoo, Finland, and Academy Professor of the Academy of Finland. He received the degree of Doctor of Technology from TKK in 1987, and has been a visiting scientist and professor at the Massachusetts Institute of Technology (1985–1986), the Pennsylvania State University (1990-1991), Lund University (1996), and the Swiss Federal Institute of Technology, Lausanne (2000–2001). Ari Sihvola is the chairman of the Finnish National Committee of URSI (the International Union of Radio Science).

Pasi Ylä-Oijala received the M.Sc. degree in 1992 and the Ph.D. degree in 1999, both in applied mathematics in the University of Helsinki, Finland. Currently he is working as Academy Research Fellow in Electromagnetics Laboratory, Helsinki University of Technology, Finland. His field of interest includes numerical techniques in computational electromagnetics based on the integral equation methods.

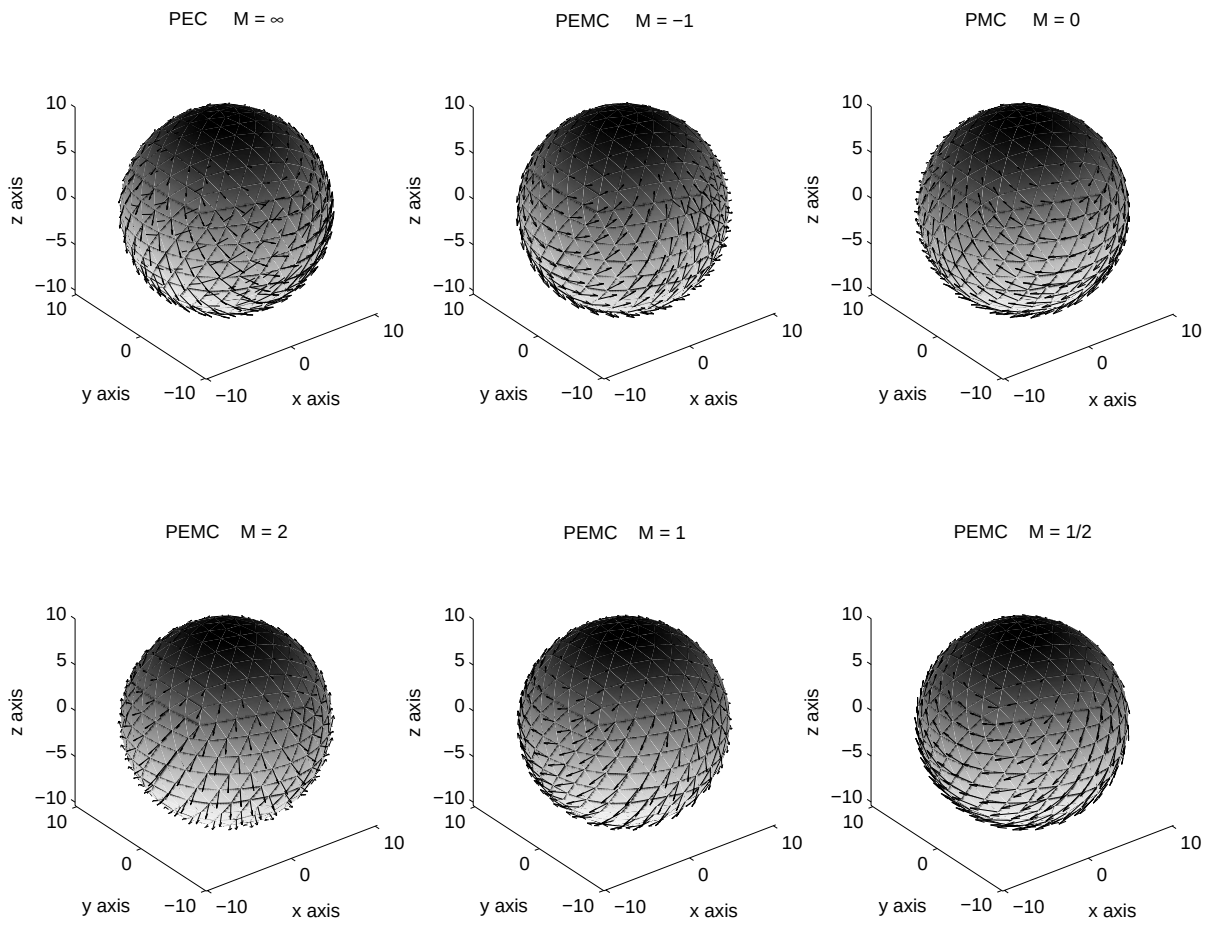

Fig. 15. The scattered far field of the PEMC sphere with varying M parameters: imaginary part of the electric field. Grayscale shows the amplitude and the arrows display the polarization of the radiated electric field. Incident electric field is parallel to the x axis. The electrical size of the sphere is $ka = 1$.

Ismo V. Lindell is professor emeritus at the Helsinki University of Technology, Espoo, Finland. He received the degree of Doctor of Technology in 1971. Besides having worked in TKK, he has served as visiting scientist and professor in University of Illinois and Massachusetts Institute of Technology. He served as the Academy Professor of the Academy of Finland during 1996–2001. Ismo Lindell is Life Fellow of the IEEE and the recipient of the IEEE S.A. Schelkunoff Prize (1987), the IEE Maxwell Premium (both 1997 and 1998), and the URSI Balthasar van der Pol Gold Medal (2005).

Fast Frequency Sweep Scattering Analysis for Multiple PEC Objects

C. Mingsheng, W. Xianliang, S. Wei, and H. Zhixiang

Key Lab of Intelligent Computing & Signal Processing
Anhui University, Ministry of Education
Hefei 230039, China

Abstract **–** The best polynomial approximation, performed by Chebyshev approximation , is applied to the scattering analysis of multiple arbitrary shaped perfectly electric conducting objects over a broad frequency band. For a given frequency band, the frequency points corresponding to the Chebyshev nodes are found by transformation of coordinates, and the surface electric currents at these points are computed by the method of moments. The surface current is represented by a polynomial function via the Chebyshev approximation, and the electric current distribution can be obtained at any frequency point within the given frequency band. Numerical examples show that the results generated by the presented approach agree to that provided by the method of moments at each of the frequency points, but the CPU time of the presented approach is reduced obviously without sacrificing much memory.

Index Terms **–** Method of moments (MOM), the best polynomial approximation, broad band radar cross section, multiple PEC objects.

I. INTRODUCTION

In many radar applications it is necessary to determine the scattering from objects over a broad frequency band. The solution of the electric field integral equation (EFIE) via the method of moments (MOM) has been one of the most popular tools for accurately predicting the radar cross-section (RCS) of arbitrarily shaped perfect electric conducting (PEC) objects in the frequency domain [1]. In MOM, the integral equation is reduced to a matrix equation by dividing the PEC body surface into sub-domains and employing a dispersed method. The RCS is computed from the surface currents obtained from the matrix equation.

To complete the scattering analysis over a wide frequency band using MOM, one has to repeat the calculation at each of the frequency points over the band of interest. If the far-field is highly frequency dependent, one needs to do the calculation at finer increment of frequency to get an accurate representation of the frequency response, which must be computationally intensive. To overcome this difficulty, the approximate solution techniques that can efficiently simulate frequency response over a wide band with acceptable computational time are desired.

Recently, the asymptotic waveform evaluation (AWE) technique has been successfully used in various electromagnetic problems especially in obtaining the broad band RCS [2], [3]. In the AWE technique, a Taylor series expansion is generated to approximate the equivalent surface current. And the rational function approach is applied to improve the accuracy of the numerical solution. As compared with using MOM at each of the frequency points, the AWE method is found to be superior in terms of the CPU time to obtain frequency response. However, the accuracy of the Taylor series is limited by the radius of convergence, and the memory needed is greatly increased on account of the high derivatives of the dense impedance matrix.

Based on this consideration, a more general approach using the best polynomial approximation is introduced in the follow sections. In the presented approach, the frequency points corresponding to the Chebyshev nodes are found by transformation of coordinates, and MOM is used to compute the electric currents at these points, then the electric currents at any point within the given frequency band can be obtained from the Chebyshev polynomial functions[4 - 6].
In the following sections, the theory of Chebyshev approximation is discussed, and numerical results are presented for a PEC sphere and other multiple PEC objects. Compared with the results obtained by direct solution, the presented approach is found to be superior in terms of the CPU time without sacrificing much memory.

II. THEORY AND FORMULATIONS

A. Electric Field Equation and MOM

Consider the problem of electromagnetic scattering of arbitrarily shaped three- dimensional body. Let S denotes the surface of the body. The boundary condition requires the tangential component of the total electric field to vanish on the surface of the PEC body,

$$(\mathbf{E}^{inc}+\mathbf{E}^{scat})_{\tan}=0 \tag{1}$$

where $\mathbf{E}^{inc}$ and $\mathbf{E}^{scat}$ denote incident and scattered electric field, respectively.

By MOM method with the Rao-Wilton- Glisson (RWG) basis functions introduced in [7 - 9], equation (1) will be reduced to a matrix equation

$$\mathbf{Z}(k)\mathbf{I}(k)=\mathbf{V}(k) \tag{2}$$

where k is the wavenumber, $\mathbf{Z}$ is a $N\times N$ impedance matrix containing information about the electromagnetic interaction between the basis functions, $\mathbf{V}$ is a vector of size N containing information about the incident field and $\mathbf{I}$ is a vector of size N that denotes the unknown coefficients in RWG basis functions.

B. Theory of Chebyshev Approximation

The electric current in equation (2) is calculated at a single frequency point. If one needs the RCS over a broad frequency band, this calculation must be repeated for different frequency points within interest band, which must be time consuming. Thus the Chebyshev approximation theory is introduced to complete the scattering analysis over a broad frequency band [10], [11].

For $H_n=span\{1,x,x^2,\cdots x^n\}$, $P_n(x)\in H_n$, $f(x)\in C[a,b]$, where $[a,b]$ is the range of investigation. The L^∞ error is defined as

$$\Delta(f,P_n)=\left\|f-p_n\right\|_\infty=\max_{a\le x\le b}\left|f(x)-P_n(x)\right| \tag{3}$$

and the infimum of $\Delta(f,P_n)$ is

$$E_n=\inf_{P_n\in H_n}\{\Delta(f,P_n)\}=\inf_{P_n\in H_n}\max_{a\le x\le b}\left|f(x)-P_n(x)\right|. \tag{4}$$

For $f(x)\in C[a,b]$, if there is a $P_n^*(x)\in H_n$ and $\Delta(f,P_n^*)=E_n$, then $P_n^*(x)$ is the best polynomial approximations in H_n for $f(x)$.

***Theorem 1*:** For a given $f(x)\in C[a,b]$, there always exists a unique $P_n^*(x)\in H_n(x)$, such that

$$\left\|f(x)-P_n^*(x)\right\|_\infty=E_n. \tag{5}$$

***Theorem 2*:** Let $f(x)\in C[a,b]$ be given, if there are $n+2$ points $a\le x_1\le x_2\le\cdots x_{n+2}\le b$ that satisfy

$$P(x_l)-f(x_l)=(-1)^l\sigma\left\|P(x)-f(x)\right\|_\infty \tag{6}$$

where $\sigma=\pm1$, then $P(x)$ will be the best polynomial approximations in H_n for $f(x)$.

The Chebyshev polynomial of degree n is denoted $T_n(x)$, which is given by the explicit formula

$$\begin{aligned}&T_0(x)=1,T_1(x)=x\\&T_{n+1}(x)=2xT_n(x)-T_{n-1}(x)\quad n\ge1.\end{aligned} \tag{7}$$

While the Chebyshev approximation formula for $f(x)\in C[-1,1]$ is given by

$$f(x)=-\frac{1}{2}c_0+\sum_{l=0}^{\infty}c_lT_l(x)=P_n(x)+\sum_{l=n+1}^{\infty}c_lT_l(x) \tag{8}$$

where $x\in[-1,1]$

hence $f(x)-P_n(x)\approx c_{n+1}T_{n+1}(x)$.

Since for $T_{n+1}(x)$ there are $n+2$ points

$$x_l=\cos(\frac{l\pi}{n+1})\quad(l=0,1,\cdots n+1)$$

which satisfies equation (6), the Chebyshev series would be the best polynomial approximations in $C[-1,1]$ by theorem 2.

C. Specified Formulations for Frequency Sweep Scattering Analysis

To introduce the theory into scattering analysis and illuminate the approach in detail, the specified formulations for frequency sweep analysis are presented in this section.

For a given frequency range $f\in[f_a,f_b]$, and the wavenumber $k\in[k_a,k_b]$, the transformation of coordinates is used as

$$\tilde{k}=\frac{2k-(k_a+k_b)}{k_b-k_a}, \tag{9}$$

such that $\tilde{k}\in[-1,1]$.

Then the electric current $I(k)$ will be calculated using

$$\mathbf{I}(k)=\mathbf{I}(\frac{\tilde{k}(k_b-k_a)+(k_b+k_a)}{2}) \tag{10}$$

and the Chebyshev approximation for $\mathbf{I}(k)$ is given by

$$\mathbf{I}(k)=\mathbf{I}(\frac{\tilde{k}(k_b-k_a)+(k_b+k_a)}{2})\approx\sum_{l=0}^{n}\mathbf{c}_lT_l(\tilde{k})-\frac{\mathbf{c}_0}{2}, \tag{11}$$

having

$$\mathbf{c}_l = \frac{2}{n+1}\sum_{i=0}^{n+1}\mathbf{I}(k_i)T_l(\tilde{k}_i) \tag{12}$$

where $\tilde{k}_i$ $(i=0,1,2,\cdots,n)$ are the Chebyshev nodes for $T_n(\tilde{k})$, and $k_i \in [k_a, k_b]$ can be obtained using

$$k_i = \frac{\tilde{k}_i(k_b-k_a)+(k_a+k_b)}{2} \tag{13}$$

To sum up, to get the Chebyshev approximation, the $n+1$ Chebyshev nodes for $T_n(\tilde{k})$ $(\tilde{k}\in[-1,1])$ must be computed firstly, then the wavenumbers k_i should be calculated using equation (13) and the surface electric current $\mathbf{I}(k_i)$ can be obtained by method of moments. Substituting $\mathbf{I}(k_i)$ into equation (12), one can obtain the Chebyshev series coefficients $\mathbf{c}_l$, and the surface electric current over the wide band is calculated using equation (11). Then the RCS over the given band is obtained.

III. NUMERICAL RESULTS

The Chebyshev approximation scheme described above has been applied to a sphere, two cubes, and three spheres, which are illuminated by a plane wave $\mathbf{E}^{inc} = \mathbf{e}_x e^{-jk_z z}$.

In Fig. 1, the radius of the sphere is chosen to be 0.3 cm, and the frequency band calculated is from 10 GHz to 55 GHz. The surface is discretized into 500 triangular elements. The CPU time for the direct solution of all output points is 4898.11 seconds, and that for AWE technique is 774.69 seconds, while the CPU time for the presented approximation approach is 756.43 seconds. The result is compared with that of AWE technique, and that of the direct solution of EFIE.

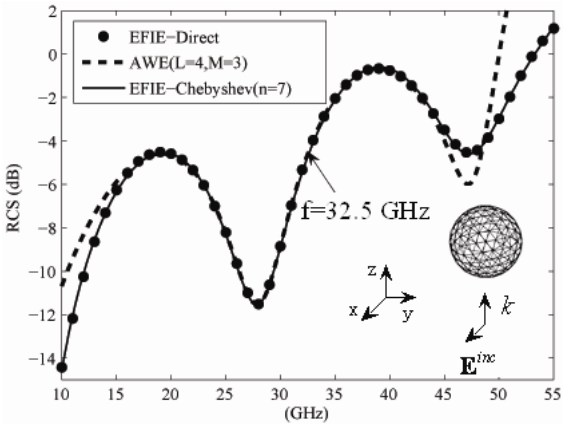

Fig. 1. RCS of a sphere from 10 GHz to 55 GHz.

It is found that the result obtained by Chebyshev method agree to that provided by direct solution very well, while the AWE technique does not. Where the order of the Chebyshev series is chosen to be 7, which is equal to the order of Taylor series. In figure 1, L and M denotes the order of the numerator and denominator in padé approximation.

As a second example, the RCS of two PEC cubes is considered, the length of each cube is chosen to be 0.5 cm, and the distance between them is 1 cm. The RCS is calculated from 5 GHz to 35 GHz, as shown in Fig. 2. The surface of the two cubes is discretized into 864 triangular elements resulting in 1296 RWG functions. The CPU times required for the direct solution and the approximation approach (n=7) are 6.6987 hours and 46.4 minutes, respectively.

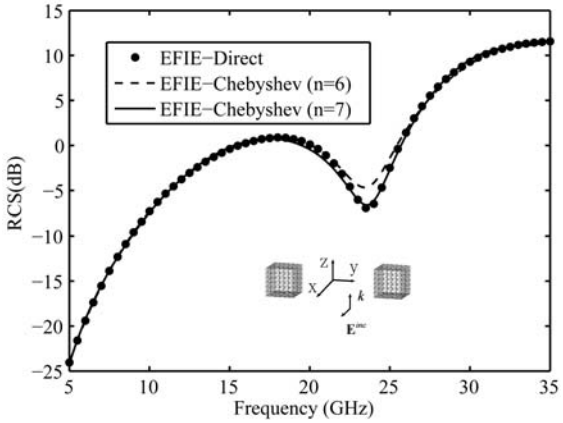

Fig. 2. RCS of two cubes from 5 GHz to 35 GHz.

Figure 3, represents the configuration of three PEC spheres that are uniformly placed on the y-axis. The radius of each sphere is 0.3 cm, and the center distance between any two neighbor spheres is 1 cm. The RCS starting from 16 GHz to 36 GHz is calculated and presented in Fig. 4. The CPU times for the direct solution and the approximation approach (n=8) are 5.5905 hours and 45.2 minutes, respectively.

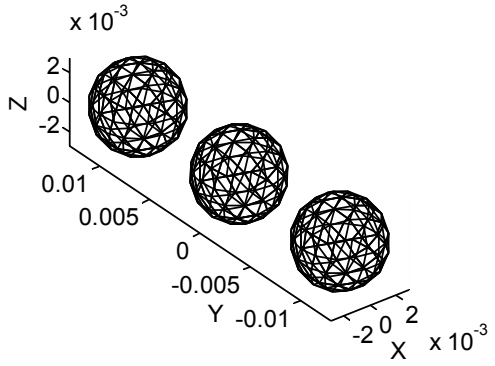

Fig. 3. Three PEC spheres placed along the y-axis.

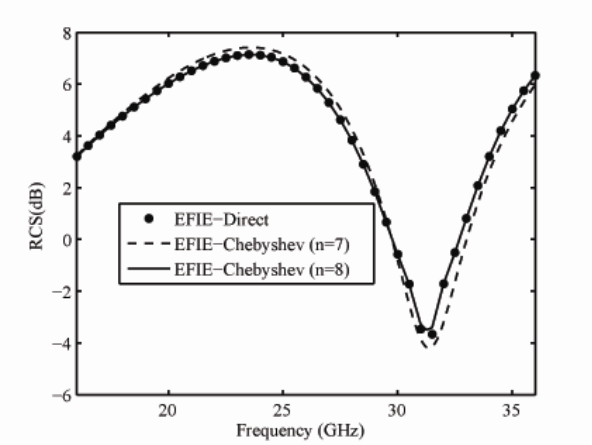

Fig. 4. RCS of three spheres from 16 GHz to 36 GHz.

It can be clearly observed from the data presented in Figs. 2 and 4, that the results obtained by the method presented vary with the value of n, and the accuracy is improved as the order increase.

All the computations reported are achieved by Matlab 7.0 on a PIV2.66G personal computer.

IV. CONCLUSION

The best polynomial approximation, implemented by Chebyshev approximation, for frequency sweep scattering analysis is presented. The RCS for different PEC objects are computed and compared with the direct solution by MOM at each of the frequency points, the presented approach is found to be superior in terms of the CPU time without sacrificing much memory. The accuracy of the presented approximation approach and its relation to the order of the best polynomial series are topics of interest for future research. With these topics addressed, the method presented will be of good application in obtaining the RCS over a desired frequency band using a frequency-domain technique.

REFERENCES

[1] R. F. Harrington, *Field Computation by Moment Methods*, Macmillan, 1968.

[2] D. Jiao, X. Y. Zhu, and J. M. Jin, "Fast and accurate frequency-sweep calculations using asymptotic waveform evaluation and combined-field integral equations," *Radio Science*, vol. 34, pp. 1055 - 1063, Sept. - Oct., 1999.

[3] C. J. Reddy, M. D. Deshpande, C. R. Cockrell, and F. B. Beck, "Fast RCS computation over a frequency band using method of moments in conjunction with asymptotic waveform evaluation technique," *IEEE Trans. Antennas Propagat.*, vol. 46, pp. 1229 - 1233, Aug. 1998.

[4] C. Lanczos, "Trigonometric interpolation of empirical and analytical functions," *J. Math. Phys.* vol. 17, pp. 99 - 123, 1938.

[5] S. Jokar and B. Mehri, "The best approximation of some rational functions in uniform norm," *Applied Numerical Mathematics,* vol. 55, pp. 204 - 214, 2005.

[6] H. D. Raedt, K. Michielsen, J. S. Kole, and M. T. Figge, "Solving the Maxwell equations by the Chebyshev method: a one-step finite-difference time - domain algorithm," *IEEE Trans. Antennas Propagat.*, vol. 51, pp. 3155 - 3160, Nov. 2003.

[7] S. M. Rao, D. R. Wilton, and A. W. Glisson, "Electromagnetic scattering by surfaces of arbitrary shape," *IEEE Trans.Antennas Propagat.,* vol. 30, pp. 409 - 418, May 1982.

[8] S. M. Rao, "*Electromagnetic scattering and radiation of arbitrarily-shaped surfaces by triangular patch modeling*," Ph.D. dissertation, Univ. of Mississippi, 1980.

[9] Y. O. Pasi and T. Matti. "Calculation of CFIE impedance matrix elements with RWG and n×RWG functions," *IEEE Trans. Antennas Propagat.,* vol. 51, pp. 1296 - 1301, Aug. 2003.

[10] T. J. Rilin, *The Chebyshev Polynomials*, Wiley, New York, 1974.

[11] M. J. D. Powell, *Approximation Theory and Methods*, Cambridge University Press, Cambridge, 1981.

Chen Ming-sheng was born in Anhui, China, in 1981. He is currently pursuing a Ph.D. degree in Anhui University. His research interests include wavelet transform, signal processing, and numerical methods for electromagnetics.

Wu Xian-liang was born in 1955. He is currently a professor of Anhui University, doctor advisor and the vice-president of Anhui University. His research interests cover wireless and mobile communication, microwave systems and components, signal processing, target tracking and numerical method for electromagnetics.

RCS Computation of Targets Using Three Dimensional Scalar Parabolic Equation

A. R. Mallahzadeh[1, 2], J. Rashed-Mohassel[3], and M. Soleimani[4]

[1]Faculty of Engineering, Shahed University, Tehran, Iran
[2]Iran Telecommunication Research Center, Tehran, Iran
[3]Faculty of Engineering, University of Tehran, Iran
[4]Iran University of Science and Technology, Tehran, Iran

Abstract **–** The parabolic equation (PE) method gives accurate results in calculation of scattering from objects with dimensions ranging from one to tens of wavelengths. Solving parabolic equation with the marching method needs limited computer storage even for scattering calculations of large targets. In this paper, the calculation procedure of radar cross section using scalar three dimensional parabolic equations is considered and the necessary equations are derived. In order to show the capabilities of the method two structures are analyzed. First scattered fields and RCS of an airplane in the forward direction are computed. Next, scattered fields and RCS of a reflector antenna in the backward direction are calculated. The obtained results are compared with physical optics results.

I. INTRODUCTION

Parabolic equation is an approximation of the wave equation which models energy propagating in a cone centered in a preferred direction, the paraxial direction. The parabolic equation was first introduced by Leontovich and Fock in order to study the diffraction of radiowaves around the earth [1]. By the advent of advanced computers closed form solution of the parabolic equation was replaced by numerical solutions. Since then, the parabolic equation is being applied to radar, sonar, acoustic and wave propagation. The parabolic equation has been recently used in scattering problems in acoustics [2] and electromagnetics [3].

II. THE PARABOLIC EQUATION FRAMEWORK

In this paper we concentrate on three dimensional analyses using parabolic equation. The time dependence of the fields is taken as $exp(-j\omega t)$. For horizontal polarization, the electric field $\vec{E}$ has only the non-zero component E_z, while for vertical polarization, the magnetic field $\vec{H}$, has the only H_z component. The reduced function u is defined as

$$u(x, y, z) = \exp(-ikx)\psi(x, y, z). \quad (1)$$

In which $\psi(x, y, z)$ is the E_z component for horizontal polarization and H_z component for vertical polarization. The paraxial direction is taken along the x axis. Assuming n, as the refractive index of the medium, the field component ψ satisfies the following three dimensional wave equation

$$\frac{\partial^2\psi}{\partial x^2}+\frac{\partial^2\psi}{\partial y^2}+\frac{\partial^2\psi}{\partial z^2}+k^2n^2\psi=0. \quad (2)$$

Using equations (1) and (2), the wave equation in terms of u is

$$\frac{\partial^2 u}{\partial x^2}+\frac{\partial^2 u}{\partial y^2}+\frac{\partial^2 u}{\partial z^2}+2ik\frac{\partial u}{\partial x}+k^2(n^2-1)u=0. \quad (3)$$

Considering $Q=\sqrt{\frac{1}{k^2}\frac{\partial^2}{\partial y^2}+\frac{1}{k^2}\frac{\partial^2}{\partial z^2}+n^2}$, equation (3) is reduced to

$$\frac{\partial^2 u}{\partial x^2}+2ik\frac{\partial u}{\partial x}+k^2(Q^2-1)u=0 \quad (4)$$

which can be written as

$$\left[\frac{\partial}{\partial x}+ik(1+Q)\right]\left[\frac{\partial}{\partial x}+ik(1-Q)\right]u=0. \quad (5)$$

Decomposing equation (5), the following pair of equations is obtained

$$\frac{\partial u}{\partial x}=-ik(1-Q)u, \quad (6\text{-}1)$$

$$\frac{\partial u}{\partial x}=-ik(1+Q)u. \quad (6\text{-}2)$$

The solution to equation (6-1) corresponds to forward propagating waves, while that of equation (6-2) concerns the backward waves.

III. SCATTERED FIELD CALCULATION

The simplest approximation of equation (6-1) is obtained using few terms of the Taylor series expansion. Using this approximation, the standard parabolic equation is obtained. Assuming Q as

$$Q = \sqrt{Y + Z + 1} \tag{7}$$

in which

$$Y = \frac{1}{k^2}\frac{\partial^2}{\partial y^2}\,,\; Z = \frac{1}{k^2}\frac{\partial^2}{\partial z^2} + n^2 - 1\,,$$

and using the Feit and Fleck approximation to decouple Y and Z [4], one will have

$$\sqrt{Y + Z + 1} \sim \sqrt{Y + 1} + \sqrt{Z + 1} - 1\,. \tag{8}$$

Using the first order Taylor series of each square root of equation (8) and substituting in equation (6-1) one finds

$$\frac{\partial u}{\partial x} = \frac{ik}{2}(Y + Z)u\,. \tag{9}$$

With regard to the definition of Y and Z, equation (9) is reduced to

$$\frac{\partial u}{\partial x} - \frac{i}{2k}\left(\frac{\partial^2 u}{\partial y^2} + \frac{\partial^2 u}{\partial z^2}\right) - \frac{ik}{2}(n^2 - 1)u = 0\,. \tag{10}$$

This equation is the standard parabolic equation and is a narrow angle approximation of parabolic equation in three dimensions which calculates the total field in the forward direction. Integration domain is considered as a box which embraces the object. This domain must be truncated in the transverse plane. PML has been used as an absorbing boundary condition to solve parabolic equation by Collino [5]. The main advantage of PML is its efficiency for all incident angles by using it in few grid points of integration domain. Integration domain with a PML absorbing boundary condition is shown in Fig. 1.

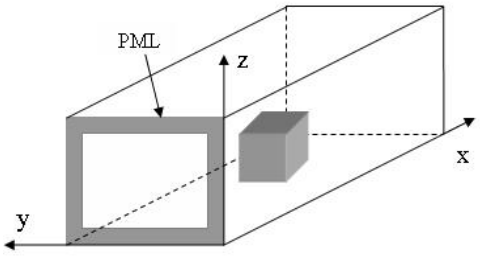

Fig. 1. Integration domain with a PML absorbing boundary condition.

We discretize equation (10) on rectangular grid by using finite difference method. In order to discretize parabolic equation usually Crank-Nicolson scheme is utilized. In this paper we use another scheme which shows better stability compared to the Crank-Nicolson scheme [6]. We define region $(m\Delta x, y, z)$ as range m. Despite Crank-Nicolson's scheme, in which second order derivatives with respect to y and z are calculated by averaging between range m and range m-1, this scheme calculates second order derivatives just in range m. This process decreases the accuracy of discretizing scheme with respect to the Crank-Nicolson and requires a smaller Δx, however the stability of the scheme is improved [6], [8]. The boundary of the object must be modeled accurately in scattering problems, therefore a smaller Δx is needed. Discretizing equation (10) for free space yields

$$\frac{u_{i,j}^m - u_{i,j}^{m-1}}{\Delta x} = \frac{i}{2k}\left(\frac{u_{i-1,j}^m - 2u_{i,j}^m + u_{i+1,j}^m}{\Delta y^2} + \frac{u_{i,j-1}^m - 2u_{i,j}^m + u_{i,j+1}^m}{\Delta z^2}\right). \tag{11}$$

By using equation (11), we can calculate fields in range m versus range m-1. Positions of grid points, while can be determined regarding equation (11), are shown in Fig. 2. In a two dimensional analysis by parabolic equation, we have to invert a triangular matrix to obtain u at range x_m. In the three dimensional case, the coefficient matrix is a very large sparse matrix and can not be solved with direct inversion. The conjugate gradient method is used to calculate u at range x_m in our work [7].

In order to calculate fields in all points of integration domain, first, the fields should be determined at range x_0. The incident field is assumed as a plane wave with unit amplitude as

$$u(x, y, z) = e^{(ik(x(\cos\theta - 1) + y\sin\theta\cos\varphi + z\sin\theta\sin\varphi))}\,, \tag{12}$$

in which θ and φ are the angles of incident plane wave with x and y axes, respectively.

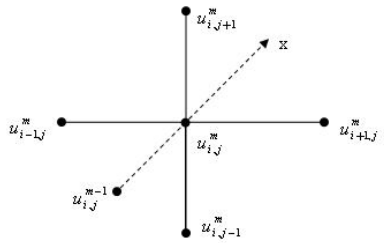

Fig. 2. Positions of grid points associated with equation (11).

The incident wave can be calculated at all points of integration domain using equations (11) and (12). Total fields in the forward direction can be calculated from equations (11) and (12) when the object is within the integration domain. Subtracting incident fields from total fields yields scattered fields in the forward direction. To compute the backward scattered fields we develop a two dimensional version in which the object is treated as a sequence of reflecting facets [3]. Modeling of the object boundary within the parabolic equation for scattering calculations has been shown in figure 3. In this case, the analysis is initiated from some range beyond the object, setting the initial scattering fields to zero. Boundary conditions on each facet are given by the appropriate polarization dependent reflection coefficients, which may vary along the scattering object.

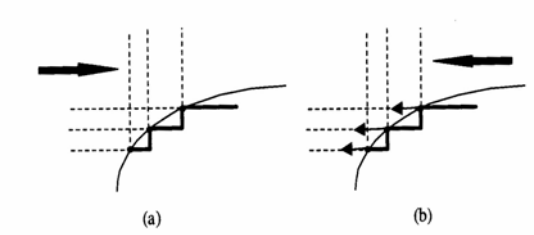

Fig. 3. Modeling of the object boundary within the parabolic equation for scattering calculations a) forward and b) backward [3].

IV. COMPUTATION OF RADAR CROSS SECTION

After the calculation of fields over the entire computational domain, we can compute the fields within any arbitrary domain x as a function of the fields in x_0 in free space as follows [8]

$$u(x,y,z) = -\frac{1}{2\pi}\times \int_{-\infty}^{+\infty}\int_{-\infty}^{+\infty} u(x_0,y',z')\left[\frac{ik(x-x_0)}{d(y',z')} - \frac{1}{d(y',z')}\right]\times \frac{e^{ikd(y',z')}}{d(y',z')}dy'dz' \tag{13}$$

in which

$$d(y',z') = \sqrt{(x_0-x')^2+(y-y')^2+(z-z')^2}\ .$$

The radar cross section is defined as

$$\sigma(\theta,\varphi) = \lim_{r\to\infty} 4\pi r^2 \left|\frac{u^s(x,y,z)}{u^i(x,y,z)}\right|^2 \tag{14}$$

in which we have

$$x = r\cos\theta\ ,\ y = r\sin\theta\cos\varphi\ ,\ z = r\sin\theta\sin\varphi\ .$$

Tending (x,y,z) to infinity along a given direction in equation (13), and assuming a unit amplitude for the incident wave, equation (14) yields [8]

$$\sigma(\theta,\psi) = \frac{k^2\cos^2\theta}{\pi}\times \left|\int_{-\infty}^{+\infty}\int_{-\infty}^{+\infty} u_s(x_0,y',z')e^{-ik\sin\theta(y'\cos\varphi+z'\sin\varphi)}dy'dz'\right|^2, \tag{15}$$

in which $u_s(x,y,z)$ is the scattered field.

V. NUMERICAL RESULTS

In this section, scattered fields and RCS of an airplane and a reflector antenna, which have been computed in forward and backward directions respectively, are presented. The incident wave is a plane wave with horizontal polarization and a wavelength equal to 1 meter. Moreover the angle of incident wave is assumed to be zero.

In order to calculate the scattered fields from the airplane, its staircase model is utilized. Dimensions of airplane and its staircase model are shown in Figs. 4 and 5, respectively.

In order to calculate scattered fields from the airplane the size of the integration domain has been considered as 40λ, 30λ and 30λ in the x, y, and z directions respectively. In addition the grid spacing in the x, y and z directions are assumed to be $\lambda/4$, $\lambda/5$, and $\lambda/5$, respectively. The run time of the program on a Pentium IV with 256 MB of RAM was 15 minutes. Near field results in planes $z = 11.3m$ and $x = 25m$ are shown in Figs. 6 and 7, respectively. RCS results of airplane in $\varphi = 0^\circ$ plane are presented in Fig. 8. Solid lines represent parabolic equation results and diamond markers represent physical optics (PO) data.

Backward scattered fields from the reflector antenna have been calculated using a staircase model for the antenna within the parabolic equation. Dimensions of reflector antenna and its staircase model are shown in Figs. 9 and 10, respectively. The size of integration domain has been considered as 3.5λ, 10λ, and 10λ in the x, y and z directions respectively. Moreover the grid spacing in the x, y, and z directions are assumed to be 0.01λ, 0.05λ, and 0.05λ, respectively. The run time of the program in this case was about 2 hours. Near field results in $y = 5m$ and $x = 0$ planes are shown in Figs. 11 and 12, respectively. RCS results of reflector antenna in $\varphi = 0^\circ$ plane are presented in Fig. 13. Solid lines represent parabolic equation results and circle markers represent physical optics data.

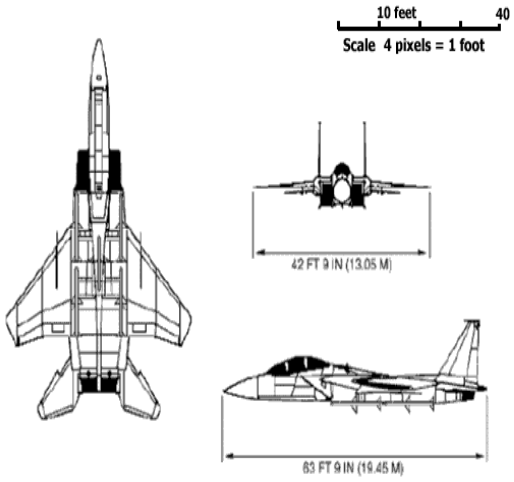

Fig. 4. The geometry of an actual airplane and its dimensions.

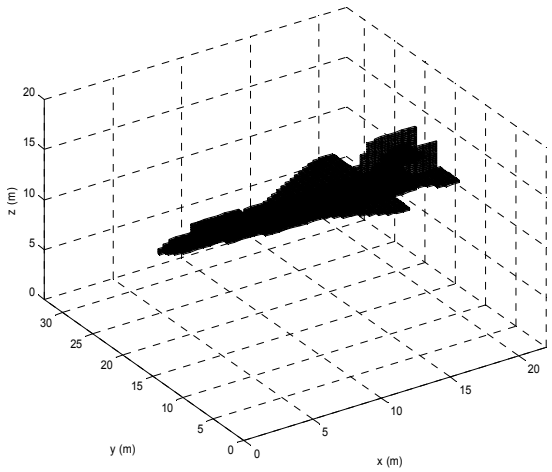

Fig. 5. Airplane staircase model (dimensions are in meters).

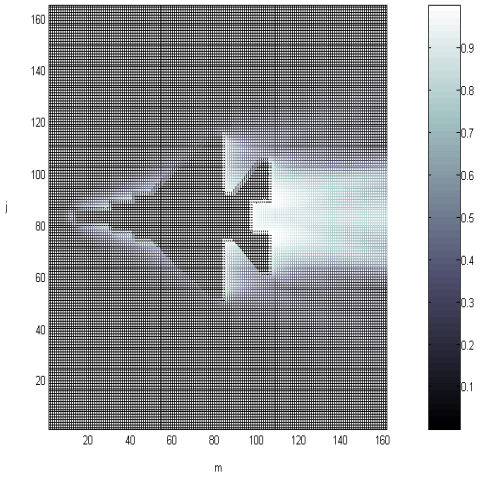

Fig. 6. Amplitude of the forward scattered field $u_s(m,i,j)$ from the airplane for z = 11.3 m and f = 300 MHz.

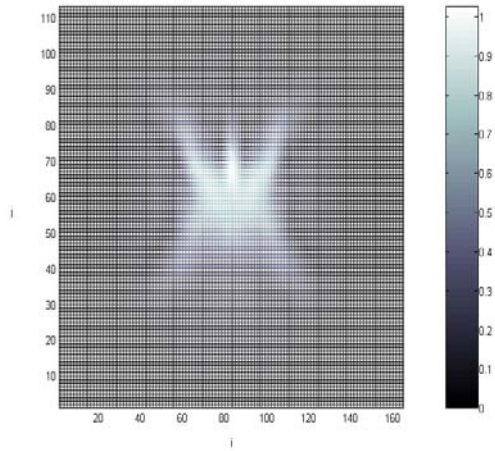

Fig. 7. Amplitude of the scattered field $u_s(m,i,j)$ from the airplane for x = 25m and f = 300 MHz.

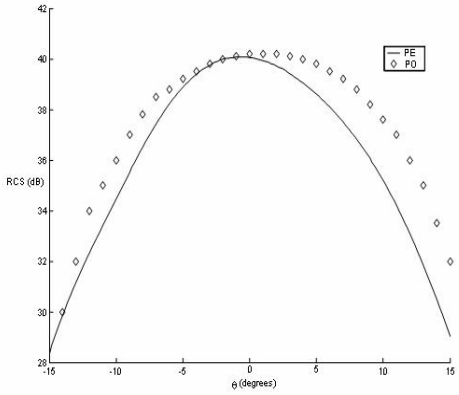

Fig. 8. Forward RCS of airplane in $\varphi = 0^\circ$ plane for f=300 MHz.

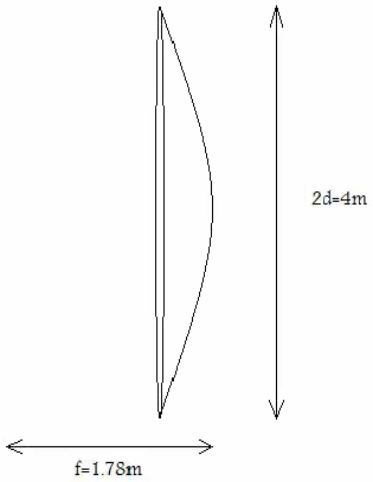

Fig. 9. The actual structure of the reflector antenna and its dimensions.

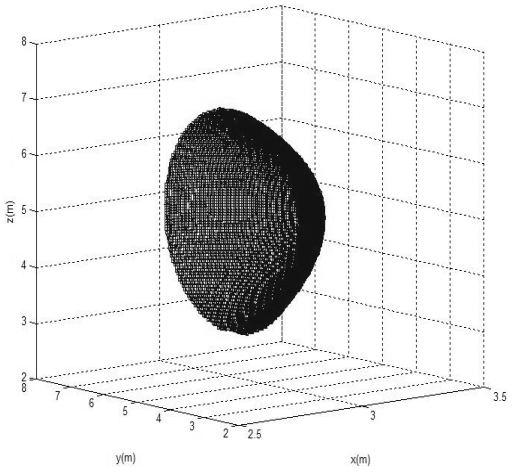

Fig. 10. Reflector antenna staircase model (dimensions are in meters).

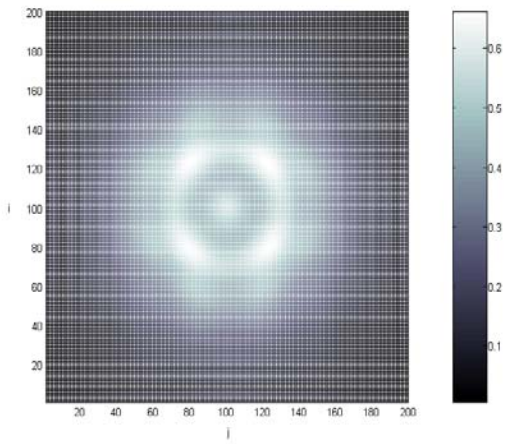

Fig. 11. Amplitude of the backward scattered field $u_s(m,i,j)$ from the reflector antenna for $x = 0$ and f = 300 MHz.

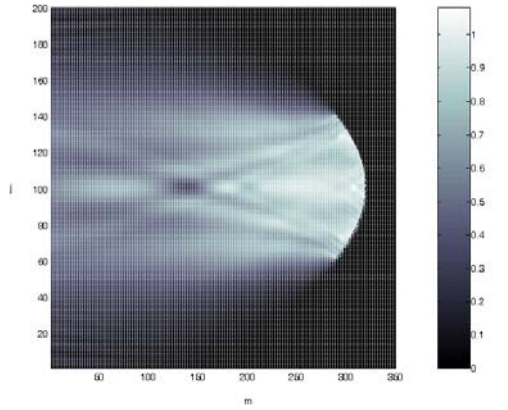

Fig. 12. Amplitude of the backward scattered field $u_s(m,i,j)$ from the reflector antenna for $y = 5\ m$ and f = 300 MHz.

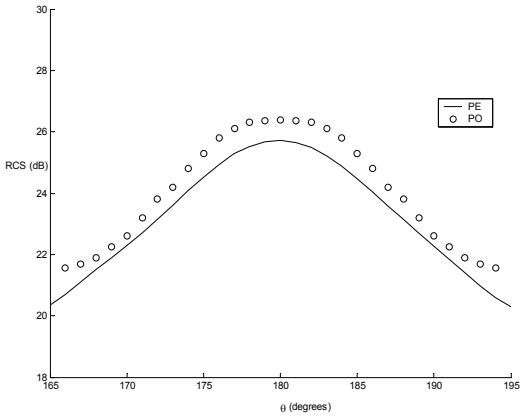

Fig. 13. Backward RCS of the reflector antenna in $\varphi = 0^\circ$ plane for f = 300 MHz.

VI. CONCLUSION

Parabolic equation method is an efficient tool in calculating scattered fields from objects with dimensions large compared to the wavelength. A three dimensional scalar parabolic equation technique was used for RCS calculation of two structures in this paper. First scattered fields and RCS of an airplane in the forward direction were computed and the results were compared with physical optics results. There is a good agreement between the physical optics results and the parabolic equation data. Next, scattered fields and RCS of a reflector antenna in the backward direction were calculated and the results were compared with physical optics data. Close agreement between the two results is observed.

REFERENCES

[1] M. A. Leontovich and V. A. Fock, "Solution of propagation of electromagnetic waves along the Earth's surface by the method of parabolic equations," *J. Phys. USSR*, vol.10, pp. 13 - 23, 1946.

[2] M. F. Levy and A. A. Zaporozhets, "Target scattering calculations with the parabolic equation method," *J. Acoust. Soc. Am.*, vol. 103, pp. 735 - 741, 1998.

[3] M. F. Levy and P. P. Borsboom, "Radar cross-section computations using the parabolic equation method," *Electron. Lett.*, vol. 32, pp. 1234 - 1235, 1996.

[4] M. D. Feit and J. A. Fleck, "Light propagation in graded-index fibers," *Appl. Opt.,* vol. 17, pp. 3990 - 3998, 1978.

[5] F. Collino, "Perfectly matched absorbing layers for the paraxial equations," *J. Comp. Phys.*, vol. 131, pp. 164 - 180, 1997.

[6] G. D. Smith, *Numerical Solution of Partial Differential Equations*, Clarendon, London, 1985.

[7] R. Barret, M. Berry, T. F. Chan, J. Demmel, J. M. Donato, J. Dongarra, V. Eijkhout, R. Pozo, C. Romine, and H. Van der Vorst, *Templates for the Solution of Linear Systems: Building Blocks for Iterative Methods* , SIAM, Philadelphia, 1994.

[8] M. F. Levy, *Parabolic Equation Methods for Electromagnetic Wave Propagation*, IEE Press, London, 2000.

Alireza Mallahzadeh was born in Bushehr, a beautiful city in the south of Iran in 1977. He received the B.S. degree in electrical engineering from Isfahan University of Technology, Isfahan, Iran, in 1999 and the MSc. degree in electrical engineering from Iran University of Science and Technology, Tehran, Iran, in 2001, and the PhD. degree in electrical engineering from Iran University of Science and Technology, Tehran, Iran, in 2006. He is a member of academic staff, Faculty of Engineering, Shahed University. He is interested in numerical modeling, antennas and microwaves.

Jalil Rashed-Mohassel is a member of academic staff, Faculty of Engineering, Tehran University. Formerly he was with the university of Sistan and Baluchestan, Zahedan, Iran, where he held several academic and administrative positions. In 1994 he joined University of Tehran where he is doing teaching and research as a professor in antennas, EM theory and applied mathematics. He served as the academic Vice-Dean, Faculty of Engineering and is currently academic Vice-Chairman of ECE department, member of Center of Excellence on Applied Electromagnetic Systems and the director of the microwave laboratory. He received his MSc. in Electronics Engineering from University of Tehran in 1976 and his PhD. degree in Electrical Engineering in 1982 from University of Michigan, Ann Arbor.

Mohammad Soleimani received the B.S. degree in electrical engineering from University of Shiraz, Shiraz, Iran, in 1978, the MSc. degree in electrical engineering from Pierre and Marie Curie University, Paris, France, in 1980, the PhD. degree in electrical engineering from Pierre and Marie Curie University, Paris, France, in 1983. He is currently professor of electrical engineering at Iran University of Science and Technology, Tehran, Iran. His research interest fall in antennas and high frequency.

Application of Quasi-static Method of Moments for the Design of Microwave Integrated Circuits and Antennas

Chun-Wen Paul Huang, Samir Hammadi, Jeannick Sercu*, Jian-Wen Bao, and Shihab Kuran

Anadigics, Inc., 35 Technology Drive, Warren, New Jersey, 07059, USA
*Agilent Technologies, EEsof EDA, Lammerstraat 20, 9000 Ghent, Belgium

I. INTRODUCTION

With the recent advancements in computer-aided design (CAD) technology, circuit simulators are being capable of simulating complex designs in a reasonably short time. To reduce the design cycle and development costs, design simulation is becoming a necessity for today's microwave and millimeter wave (mmW) integrated circuit (IC) designs. Besides operating at microwave and mmW frequencies, those designs are fairly complex. Accurate prediction of circuit performance before fabrication becomes a must for shortening design cycles and for lowering engineering cost. High-speed digital fiber optic integrated circuits, such as OC-192 (10 Gbit/s) and OC-768 (40 Gbit/s) are broadband circuits. They operate at frequencies ranging from the kHz range to a minimum of 10 GHz and from the kHz range to a minimum of 40 GHz, respectively. Such bandwidths are required to maintain low signal distortion levels. Therefore, accurate design simulations not only rely on the accuracy and robustness of transistor models, but also the passive layout models. These required models are due to the parasitic inductance, transmission line effects of the interconnections, and resonance of capacitors and inductors above microwave frequencies. Recently, several papers described the application of electromagnetic (EM) analysis tools for the design of the layouts in millimeter wave integrated circuits [1], [2]. However, these applications are limited to circuits of low complexity or periodic structures. For complicated circuits, the parasitic extraction method is widely applied to model the layouts of complicated IC's [3], that provides fast results and reasonable accuracy. However, it is difficult for parasitic extraction tools to model the resonance of capacitors and inductors at microwave frequencies, transmission line effects, and the air-bridge crossover capacitance [4]. Incomplete consideration of layout effects may result in peaking and sagging in the bandwidth of wideband circuits. A global circuit/layout modeling technique, based on the 2.5-D planar quasi-static Method of Moments (MoM) [5], [6], was presented and validated experimentally for its effectiveness for mmW IC applications in [7]. In this paper, the theory of quasi-static MoM is reviewed and presented for completeness. Comparative analyses of quasi-static MoM and conventional MoM approaches including convergence speed enhancements and computational requirements are also presented. The global layout analysis method in conjunction with vertical bipolar inter-company (VBIC) transistor models is applied to a complicated 10-Gbit/s broadband amplifier (see Fig. 1). Excellent agreements between simulated and measured results are observed in both frequency and time domains. Applications of quasi-Static MoM for microwave antenna designs are also presented. This method provides the first-order solutions of antenna resonance in a short computational time. Based on the fast quasi-static solutions, refined simulations with full-wave simulations for accurate bandwidths and radiation pattern analysis at specific frequencies can be made, which greatly shortens design cycle.

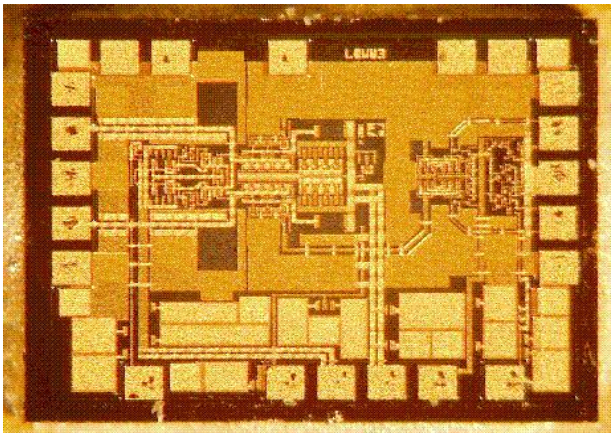

Fig. 1. OC-192 (10 Gbit/s) GaAs Amplifier.

II. FORMULATION OF QUASI-STATIC METHOD OF MOMENTS

The quasi-static Method of Moment technique was partially presented in [5], [6], and later the methodology was adopted in Agilent's EEsof Momentum RF [8]. In

this section, the theory of quasi-static MoM for free space problems is presented for completeness. This review is an expansion from the work presented in [5], [6]. This method is based on Mixed Potential Integral Equations. The relationship between the Mixed Potential Moment Matrix ([Z(ω)]) and the unknown currents |I(ω)> can be expressed as

$$[\mathrm{Z}(\omega)]\left|\mathrm{I}(\omega)\right\rangle = \left|\mathrm{V}(\omega)\right\rangle \tag{1}$$

where |V (ω)> is the voltage impressed by the sources or subject to the boundary conditions. The Moment Matrix can be re-expressed as,

$$[\mathrm{Z}(\omega)] = [\mathrm{R}(\omega)] + \mathrm{j}\omega[\mathrm{L}(\omega)] + 1/\mathrm{j}\omega\,[\mathrm{C}(\omega)]^{-1} \tag{2}$$

where [R (ω)], [L (ω)], and [C (ω)] represent the frequency dependent resistance, inductance, and capacitance matrices, respectively. A full-wave MoM can be developed based on equations (1) and (2). The explicit forms of the elements in [R (ω)], L [(ω)], and [C (ω)] matrices can be expressed in equations (3) to (5) as shown,

$$\begin{aligned} Z_{ij}^{R} &= R_{ij}(\omega) \\ &= Z_s(\omega)\iint_{S_i} ds \iint_{S_j} ds'\ \delta(\mathbf{r}-\mathbf{r}')\ \mathbf{B}_i(\mathbf{r})\cdot\mathbf{B}_j(\mathbf{r}') \end{aligned} \tag{3}$$

$$\begin{aligned} Z_{ij}^{L} &= j\omega L_{ij}(\omega) \\ &= \iint_{S_i} ds \iint_{S_j} ds'\ \mathrm{G_m}(\omega,\mathbf{r}-\mathbf{r}')\ \mathbf{B}_i(\mathbf{r})\cdot\mathbf{B}_j(\mathbf{r}'), \end{aligned} \tag{4}$$

$$\begin{aligned} Z_{ij}^{C} &= 1/\,j\omega C_{ij}(\omega) \\ &= \iint_{S_i} ds \iint_{S_j} ds'\,\mathrm{G_e}(\omega,\mathbf{r}-\mathbf{r}')\ \nabla\cdot\mathbf{B}_i(\mathbf{r})\ \nabla\cdot\mathbf{B}_j(\mathbf{r}'), \end{aligned} \tag{5}$$

where G (ω, **r-r'**) and **B(r)** are the Green's and the basis functions, respectively. The Green's function can be expressed in a Taylor series as,

$$G(\omega,\mathrm{r},\mathrm{r}') = e^{-jkR}/R = \frac{1}{R}\left(1 - jkR - (kR)^2/2! \cdots\right) \tag{6}$$

where k is the free-space wave number and R = |r-r'|. At low frequencies or when the structures are electrically small, the higher order terms in (6), that govern radiation, can be ingored. The quasi-static Green's functions can be expressed as,

$$G(\mathrm{r},\mathrm{r}') \approx \frac{1}{R}. \tag{7}$$

Based on equation (7), equations (4) and (5) can be simplified to obtain frequency scalable expressions. Therefore, the Moment matrix equation (2) can be simplified as

$$[\mathrm{Z}(\omega)] = [\mathrm{R}(\omega)] + \mathrm{j}\omega[\mathrm{L}] + 1/\mathrm{j}\omega\,[\mathrm{C}]^{-1}. \tag{8}$$

Instead of re-computing the entire Moment Matrix at each frequency, equation (8) provides a scalable Moment matrix, which greatly reduces the computational time. The maximum usable frequency is computed based on the requirement that the diagonal (D) of the structure is less than half of the free-space wavelength of the maximum frequency. The expression for the maximum frequency is

$$f_{\max} < \frac{150}{D(mm)}. \tag{9}$$

From equation (8), at low frequency the impedance matrix will tend to break down due to a zero of the inductive impedance matrix and an infinite capacitive impedance matrix. Therefore, instead of using traditional rooftop basis functions, the loop and star basis functions are adopted to ensure low frequency stability and enable mesh reduction [5], [6]. These features ensure shorter computational time and less memory requirements for complicated structures, in comparison with traditional 2.5-D full-wave MoM.

III. GLOBAL CIRCUIT/LAYOUT MODELING TECHNIQUES

The quasi-static MoM provides faster results and requires less memory, which enables EM modeling of complex IC layouts. The layout simulation is done using Agilent's Momentum RF and the circuit simulation is done by Agilent's Advanced Design System (ADS). Custom programs were built to integrate the layout tool, circuit simulator, and EM simulator for the global circuit/layout modeling. The technique is explained in this section. By setting up the layer mapping protocols, the circuit layouts can be correctly transferred between the layout tool and the EM simulator via Graphic Data System II (GDSII) or other standard layout data files. When modeling a layout, all transistors and resistors are removed in the layout tool by the custom programs. Transistors and resistors will be modeled in the circuit simulator with VBIC and transmission line models, respectively. Because the required computational time is a function of number of the unknowns square, the custom programs also enable the layout tool to generate layout partitions of a complicated layout to reduce the computational time. Partitioned layouts are exported to the EM simulator for layout modeling. After partitioned layouts are modeled, the EM simulator exports multi-port S-parameter layout models with look-alike symbols into the circuit simulator for circuit/layout co-simulations. When modeling a complicated layout, the layout models should be partitioned based on the coupling effects between the circuit stages and

elements. It is inadequate just to partition the layout based on the boundaries of circuit functional stages. One has to look at the coupling effects between various stages due to layout proximity. For this, the current visualization is an excellent vehicle for tracing the lines of minimum coupling. This coupling analysis is done using a global current visualization of a layout section using a low meshing density (shown in Fig. 2). Multiple ports were used in the layout simulation to emulate the current distribution around the transistor cells. The brighter color traces indicate higher EM coupling density, and the darker region indicates the low coupling between traces. This provides fast, first order results for the coupling effects. The partitioned layout models are simulated with fine meshing resolution. For modeling IC passive circuitry and interconnections, the meshing frequency and density need to be higher than those for the RF board and antenna applications to generate adequate current samples for small IC traces.

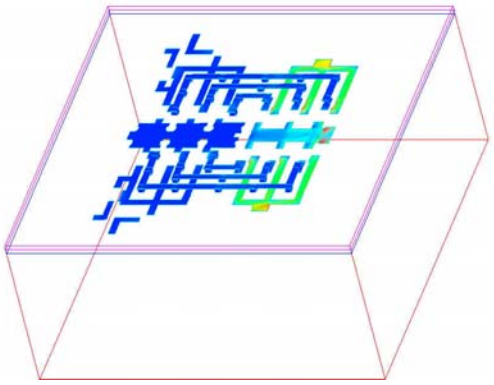

Fig. 2. Global visualization of induced currents between interconnections for the localization of layout modeling.

IV. VALIDATION FOR MICROWAVE CIRCUITS AND ANTENNA APPLICATIONS

Most quasi-static methods are used for modeling low frequency or electrically short structures. In this section, the quasi-static MoM is validated for modeling millimeter wave IC passive circuitry, a complex microwave IC, and electrically long structures. Its extended applications for the predictions the resonances of microwave antennas of arbitrary shapes are also presented. Analyses of the computational time and memory versus traditional MoM are also provided.

A. OC-768 Millimeter Wave IC Applications

For the OC-768 application, integrated circuits are required to operate at 40 Gbit/s. Therefore, the IC passive circuitry is also an important part of IC designs. Two examples are presented and verified with measurements. Modeling skills using quasi-static MoM at mmW IC passive are also presented.

Two 1.9-mm coplanar waveguides are printed side by side with a 50 μm separation on an Indium Phosphide (InP) wafer, shown in Fig. 3(a). The electrical lengths of waveguides are similar to those of typical traveling wave amplifiers (TWA) for OC-768 applications. The waveguide is filled with Benzocyclobutene (BCB) low dielectric material, which has a dielectric constant of 2.7 and loss tangent of 0.008. To accurately model a CPW with mmW with 2.5-D EM simulator, the thick metal strip model, composed of top and bottom strips and a via, are used to emulate the side-wall effects of finite-thickness metal strips (see Fig. 3 (b))[9]. Dielectric 2 is the substrate InP and the dielectric 1 is the over-mold material, which is BCB in this example. The extracted Z_o of infinitely thin strip model is 82.7 Ω, which is overestimated compared with 69 Ω from the thick metal model. The effectiveness of the quasi-static MoM for millimeter Wave applications is observed in Fig. 4. The spikes in S-parameter magnitude measurements and simulations, found at 24 GHz, are caused by higher order modes, which are confirmed by inspecting the magnitudes and phases of the measured S-parameters of both waveguides. However, the resonances in the measurements are weaker than those in simulations. Hence, the effectiveness of the quasi-static MoM is validated.

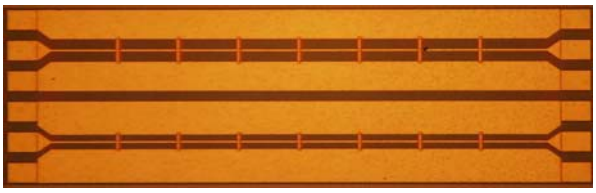

(a)

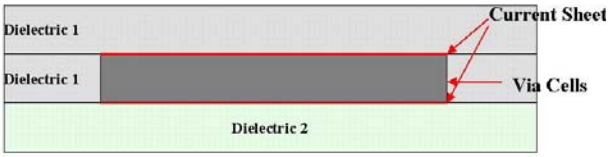

(b)

Fig. 3. (a) InP coplanar waveguides for OC-768 (40 Gbit/s) applications; (b) Thick metal model for a 2.5-D MoM simulator.

Table I shows the convergence of Z_o and R_{dc} for this example as a function of meshing density using Quasi-static MoM. Table II shows the required computational resources of the quasi-static MoM. Fast convergence and minimum computational requirements are observed compared with full-wave MoM. Both full-wave and quasi-static demonstrated the similar accuracy

compared with measurement shown in Table I. The quasi-static MoM requires 40 % to 90 % of the memory needed by the conventional 2.5 D MoM and simulates the circuit in 1/8 to 1/6 of the time. The relation between the computational time and memory requirements versus the unknown number (N) for quasi-static MoM can be expressed as follows

$$CPU \quad Time \quad = 5x10^{-6} N^{2.2}, \tag{10}$$

$$Memory \quad = 1.8x10^{-3} N^{1.47}. \tag{11}$$

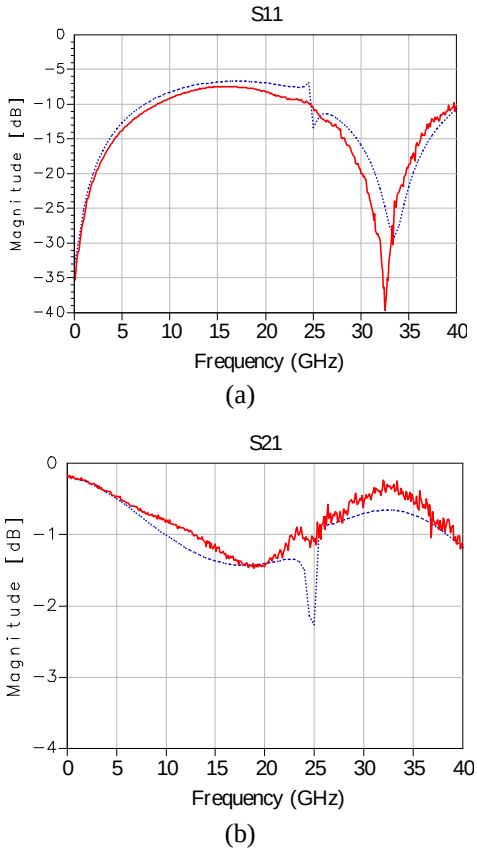

Fig. 4. Measurements (solid line) versus quasi-static MoM simulations (dotted line) (a) Return Loss (dB); (b) Insertion Loss (dB).

The relation between the computational time and memory requirements versus the unknown number (N) for a full-wave 2.5-D MoM can be expressed as follows

$$CPU \quad Time \quad = 1x10^{-6} N^{2..5}, \tag{12}$$

$$Memory \quad = 110e^{0.0002N}. \tag{13}$$

From Tables I and II, and equations (10) to (13), the computational speed improvement of quasi-static MoM is a result of both the reduction of the number of unknowns and the frequency scalable Moment matrix.

Another OC-768 application of a capacitive loaded electrode design of Electro-Optical Modulator [10] is also presented. As shown in Fig. 5 (a), the electrodes of the modulator are composed of a CPW with T-rail capacitors and two optical waveguides underneath the center conductor of the CPW. The Modulator is fabricated on a GaAs wafer with 1cm electrodes. To accurately characterize the electrically long and periodic electrodes, the electrodes were modeled in a 2 mm cell with extended feeds for S-parameter extraction. The GDSII file of the layout is imported into the EM simulator. The modeling method is similar to the previous example, and the thick metal strip model in the previous example was used to ensure the accuracy. The extended feeds are used to minimize the abrupt transitions at the excitation planes of the unit cell and provide more accurate S-parameter extractions. The 2 mm cell is about one wavelength at 40GHz, and the extended feeds are de-embedded from the simulated S-parameters. Comparisons of the simulated and measured phase velocity (V_{ph}), characteristic impedance (Z_o), and attenuation are shown in Fig. 5 (b). Excellent agreements between simulation and measurements are observed.

For electrically long transmission structures, the division of layout models should be made based on the localized coupling effects and appropriate electrical length. EM models of both examples have electrical lengths more than a half wavelength. The characteristics of both structures are determined by transmission

Table I. Convergence Test of Quasi-static MoM.

Mesh Density (cell/λ @ 40 GHz)	5	15	25	50
Zo @ 40 GHz (Measured Zo = 70.6 Ω)	72	69.7	69.2	69.1
R @ DC (Measure R = 2.02 Ω)	2.3	2.29	2.20	2.12

Table II. Quasi-Static MoM (RF) versus Full-wave MoM (MW) in Required Computational Resources on a 450 MHz Workstation.

Mesh Density (cell/λ @ 40 GHz)	5		15		25		50	
Type of MoM	RF	MW	RF	MW	RF	MW	RF	MW
Unknowns	1516	3054	1898	3515	2570	4332	4771	6988
Memory (MB)	90.37	216.65	119.98	218.60	195.69	269.75	416.91	488.64
CPU Time (min)	61.25	550.03	95.05	761.32	197.97	1300.53	785.74	4304.8

characteristics and localized couplings instead of far-end couplings. Therefore, quasi-static models for transmission structures can be used beyond the limit specified in equation (9). To re-confirm this statement, a 1.5 inch coupler is simulated and measured (see Fig. 6).

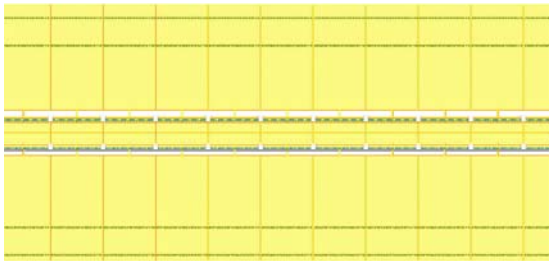

(a)

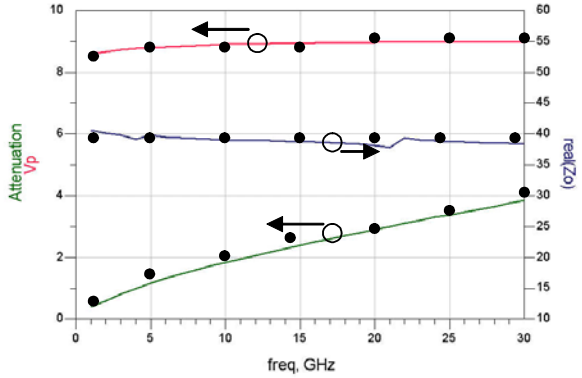

(b)

Fig. 5. (a) The top view of a 40 Gbit/s Electro-Optical Modulator; (b) Measurements (symbol) versus quasi-static MoM simulations (solid line) of electrode phase velocity (cm/ns), attenuation (dB/cm), and characteristic impedance (Ω).

The coupler is only terminated at the two diagonal ports, which results in the strongest coupling effects. Equation (9) indicates the maximum usable frequency of 3.71 GHz, but good agreement between measurement and simulation was observed up to 9 GHz (1.5 wavelength). This experiment shows that weak-radiating structures can be accurately characterized by quasi-static MoM model beyond the half-wave length limit in equation (9). Therefore, the effectiveness and efficiency of quasi-static MoM for millimeter wave IC applications are proven.

B. Complex Microwave IC Layout Modeling

The global layout analysis in conjunction with VBIC transistor models and transmission line resistor models is applied to a 10 Gbit/s fiber optic amplifier (Fig. 1). The layout model partitioning analysis is applied to the circuit layout. Cross-talk analysis of a gain-stage layout is shown in Fig. 2. The color densities at different regions show the intensities of electromagnetic field couplings. Fig. 2 indicates low cross-talk between the

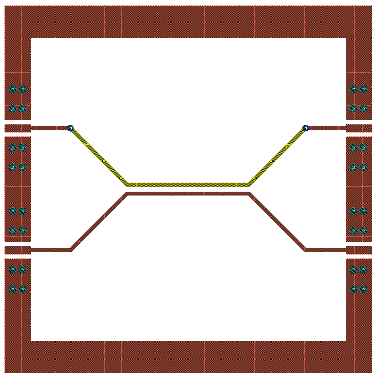

(a)

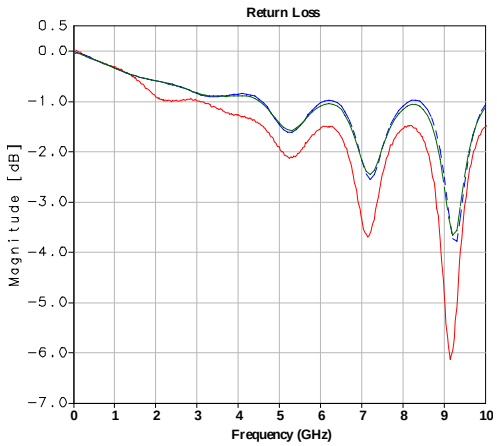

(b)

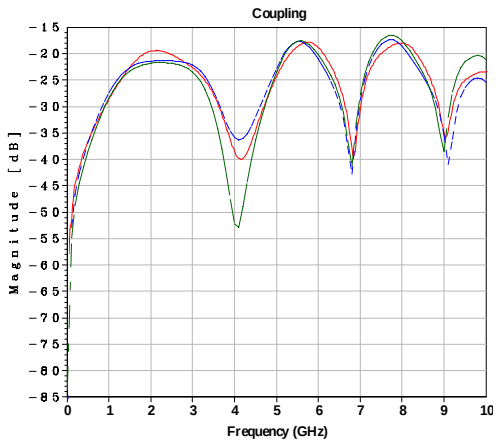

(c)

Fig. 6. Comparison of measured (solid line), full-wave 2.5-D MoM simulation (dash dot line), and quasi-static MoM simulation (dash line) of a 1.5-inch multilayer oupler. (a) Test structure; (b) Simulated and measured return loss; (c) Simulated and measured coupling.

two transistor arrays and hence the possibility of dividing this layout into two localized models. The transmitted and coupled current distributions were indicated by the color density of the visualization. The dark regions indicate low current distribution regions, and the brighter regions are indication the strong current crowdedness.

To support the circuit/EM co-simulation in fiber optic simulations, layout models are required for the low frequency stability, and the related elements can be biased with DC sources. Indeed, most EM simulators are incapable for accurate low frequency simulations. As previously indicated, the quasi-static MoM adopts the loop and star basis function instead of traditional rooftop basis function to ensure low frequency stability. In Fig. 7, a commonly used through-via multilayer interconnect is simulated with quasi-static and traditional full-wave MoM. The quasi-static MoM shows strong low frequency stability compared with full-wave MoM with rooftop basis functions. This feature provides the feasibility of bias through EM layout models and low frequency accuracy. Small signal validation is verified by comparing the magnitudes of the measured and simulated S-parameter results of the entire circuit, which is shown in Fig. 8.

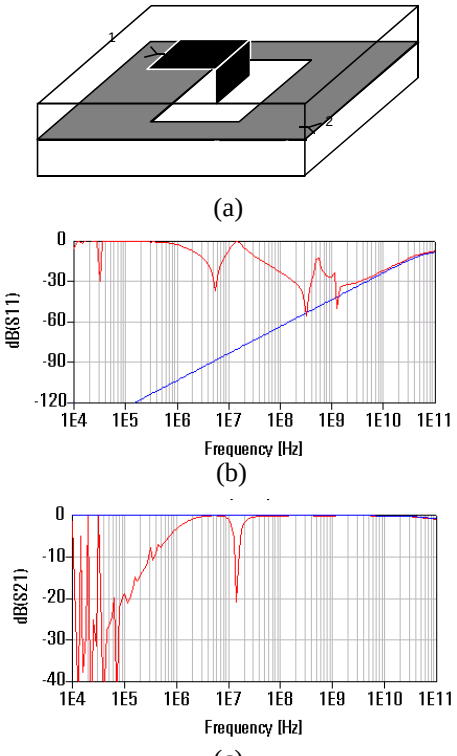

Fig. 7. Low frequency breakdown analysis of the rooftop basis function (solid line) and loop and star basis function (dotted line). (a) The test structure; (b) Simulated return Loss (dB); (c) Simulated insertion Loss (dB).

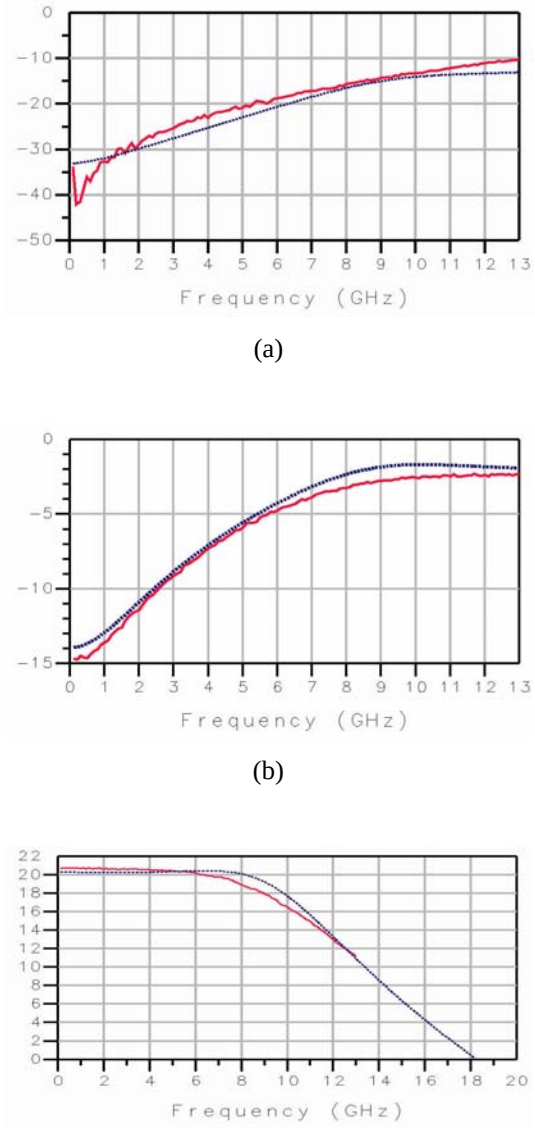

Fig. 8. Measured (solid line) versus simulated (dotted line) magnitudes of S-parameters for the OC-192 amplifier in Figure 3. (a) S11 (dB); (b) S22 (dB), and (c) S21 (dB).

To support time domain simulations of fiber optics circuits, sufficient frequency resolutions and maximum frequency are required based on the rise and fall time of the input pulse. For the 10 Gbit/s circuit simulations, a frequency resolution of 100 MHz and a maximum frequency of 20 GHz are used. Excellent agreement is observed. Large signal validation is verified by comparing transient simulation and measurement using eye diagrams, which is shown in Fig. 9. Good agreement in rise time, fall time and transient waveform is observed.

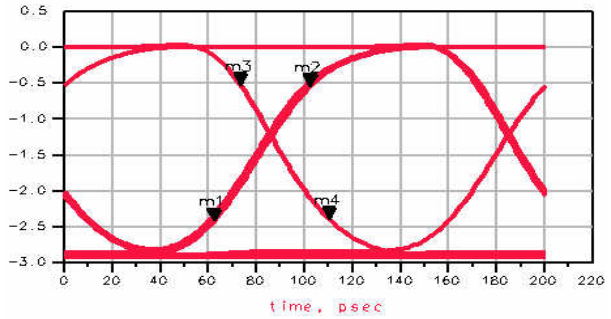

(a)

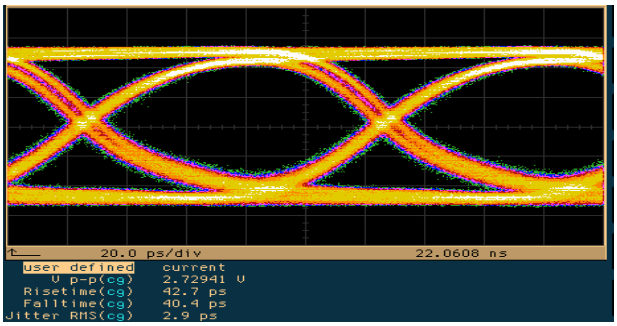

(b)

Fig. 9. Eye diagram of the 10Gbit/s GaAs amplifier. (a) Simulated eye diagram; (b) Measured eye diagram.

C. Predictions of Microwave Antenna Resonances

Equation (7) manifests the quasi-static assumption of neglecting the higher order terms in Greens' function, which enables the frequency scalable Moment matrix. However, the antenna impedance is mainly determined by the near fields instead of the far fields. Therefore, the quasi-static assumptions should is able to provide the first order solution of antenna resonances. Resonance frequencies, impedance bandwidths, and radiation pattern syntheses are the major antenna design parameters. For simple antenna structures, analytical solutions or simple numerical programs are often available. However, for designing antennas of arbitrary geometries, a more sophisticate numerical code is required to provide accurate results. Instead of using a full-wave EM simulator searching antenna operating modes within a wide bandwidth, the quasi-static MoM can predict the vicinities of antenna resonances in a much shorter computation time. Based on the quasi-static solutions, refined full-wave simulations for the impedance bandwidth and radiation pattern analyses within desired frequency bandwidths can be made. In this section, a ground backed planar antenna and a linear wire antenna were simulated and measured.

The first example is a circular patch antenna with a diameter of 4.22 cm printed on a 1.5 mm thick dielectric substrate with the permittivity of 2.55 [11]. This structure is simulated with both 2.5-D full wave and quasi-static MoM simulators. In [11], this antenna was measured from 4.9 to 5.5 GHz, at the vicinity of 3rd series resonance, which resonates at 5.18 GHz with 170 MHz operation bandwidth and antenna gain of 4.2 dB. The full-wave simulation for the antenna impedance bandwidth (see Fig. 10 (a) and (b)) shows agreement with the measurement in [11] but with a higher simulated gain of 4.6 dB. From Fig. 10 (a) and (b), quasi-static solutions predict the vicinities of usable resonances. The simulated impedance bandwidths of quasi-static MoM in Fig. 10 (a) provide relative levels, but the absolute values of impedance deviate from the full-wave simulations. The computational time for full-wave MoM is 86 minutes for 1541 unknowns, and the computational time for quasi-static MoM is 11 minutes for 958 unknowns. It is practical to use quasi-static MoM to locate the vicinities of usable antenna resonances.

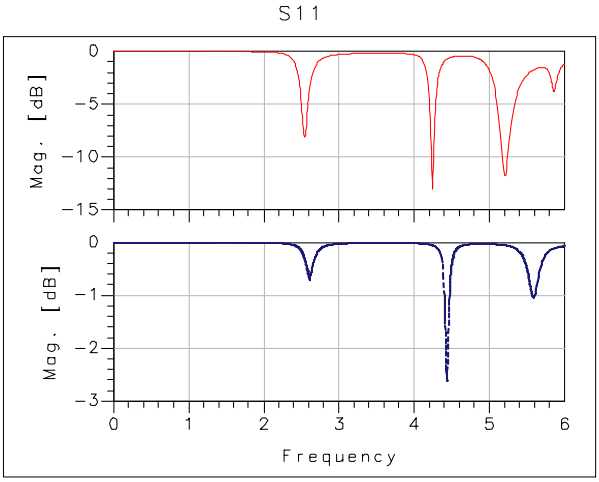

(a)

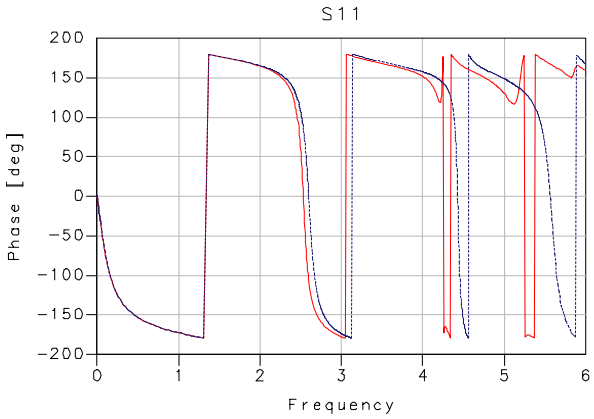

(b)

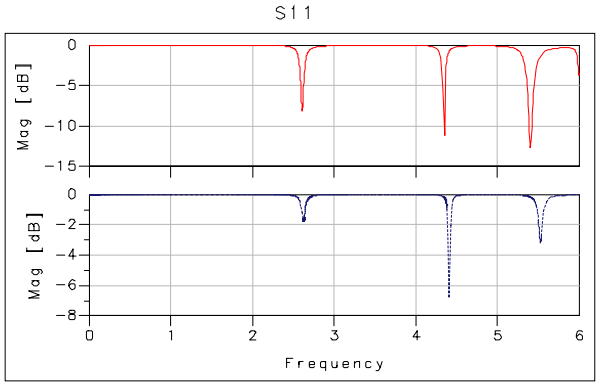

(c)

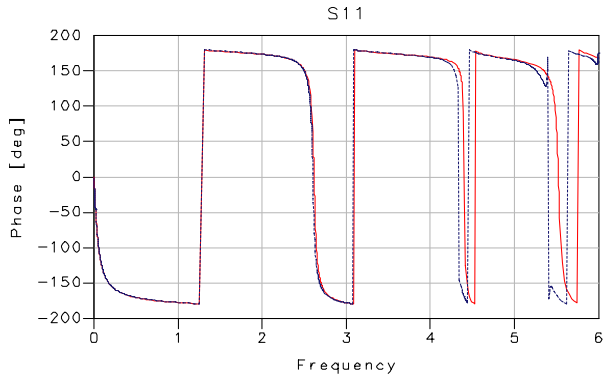

(d)

Fig. 10. Comparison of full-wave (solid line) and quasi-static (dash line) MoM simulations. Simulation of the circular patch antenna on a 1.5-mm thick substrate: (a) Magnitude of S11 and (b) Phase of S11. Comparison of full-wave (solid line) and quasi-static (dash line) MoM simulations. Simulation of the circular patch antenna on a 0.5-mm thick substrate: (c) Magnitude of S11 and (d) Phase of S11.

According to equation (9), the maximum frequency of quasi-static solution of this structure is 2.53 GHz, which also explains the deviation between full wave and quasi-static results increases after this frequency. When the substrate height is reduced from 1.5 mm to 0.5 mm, the agreement between full-wave and quasi-static simulations is improved shown in Fig. 10 (b). However, from full-wave simulations, the reduction of substrate thickness from 1.5 mm to 0.5 mm greatly decreases the radiation efficiency by 30 %.

The second example is a dual-sleeve meander line antenna (see Fig. 11 (a)), which is designed to operate at multiple operational modes [12]. The antenna is simulated and measured at an infinite ground plane. The quasi-static MoM captures the first 5 operational resonances. The impedance of this antenna is mainly determined by the mutual capacitance between segments, so the agreement is better than that of the ground-backed planar antennas. From Fig. 11, the full-wave solution shows better agreement with the measurement. However, the computational cost is much higher than quasi-static solutions. The required computational time of quasi-static MoM is 35 minutes for 978 unknowns, but the full-wave MoM requires 188 minutes for 1404 unknowns.

(a)

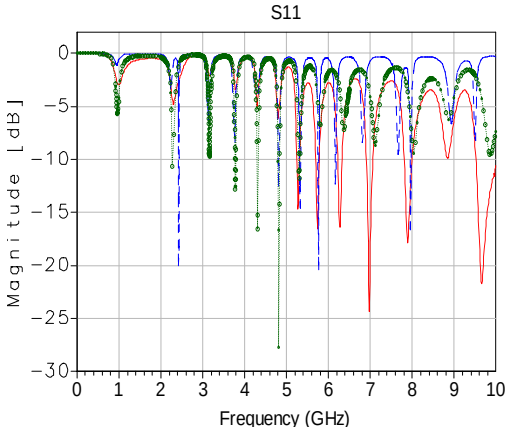

(b)

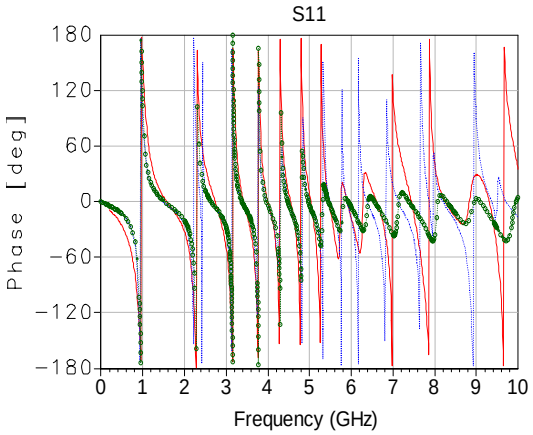

(c)

Fig. 11. Quasi-static (dash line) and full-wave (symbol) simulations versus measurement (solid line). (a) A dual-sleeve meander line antenna; (b) Magnitude of S11; (c) Phase of S11.

V. CONCLUSION

A novel global layout modeling technique based on a quasi-static MoM for complex IC designs is presented. The theory of quasi-static MoM is reviewed and its effectiveness and efficiency for microwave and millimeter wave IC applications is validated. This technique reduces the required memory size 10 to 60 % and decreases the simulation time by a factor of 6. Due to low radiation effects in MICROWAVE IC's, excellent agreement between simulated and measured results is observed. In addition, the low frequency stability of this method provides the accuracy of DC and wideband simulated results of EM/circuit model co-simulations, which is essential for complex microwave IC designs. Custom programs were generated to link layout CAD tool, the quasi-static MoM simulation engine, and a circuit simulator seamlessly, which greatly reduces design cycle. Effectiveness for modeling electrically long (>0.5 wavelength) structures is also proven. Its extended application for antenna resonance prediction is also presented, which provides the first order solutions for usable antenna resonances in a much shorter simulation time.

ACKNOWLEDGEMENT

The authors wish to express the appreciation to Dr. Charles E. Smith, the professor of the Electrical Engineering Department at The University of Mississippi, for his helpful technical discussions and Dr. Wei Zhong at Anadigics Inc. for providing the VBIC models.

REFERENCES

[1] J. W. Archer et al, "An InP MMIC amplifier for 180-205 GHz," *IEEE MICROWAVE and Wireless Comp. Letters*, vol. 11, no. 1, pp. 4-6, Jan. 2001.

[2] V. Radisic et al, "164-GHz MMIC HEMT Doubler," *IEEE MICROWAVE and Wireless Comp. Letters*, vol. 11, no. 6, pp. 241-243, Jun. 2001.

[3] W. H. Kao, C.-Y. Lo, M. Basel, R. Singh, "Parasitic extraction: current state of the art and future trends," *Proceedings of the IEEE*, vol. 89, no. 5, pp. 729-739, May 2001.

[4] T. M. Weller et al., "Three-Dimensional high-freuency distrubuted netowks, Part I: Optimiazation of CPW discontinuities," *IEEE Trans. Microwave Theory and Tech.*, vol. 48, no. 10, pp. 1635-1642, Oct. 2000.

[5] J. Sercu, "Inductance and capacitance modeling of RF board and high speed packaging interconnects based on planar EM simulation," *2nd MINT Millimeter-wave International Symposium*, Seoul, South Korea, Feb. 15-16, 2001.

[6] L. Knockaert, J. Sercu, and D. D. Zutter, "Generalized polygonal basis functions for the electromagnetics simulation of complex geometrical planar structures," *2001 IEEE International Microwave Symposium*, Phoenix, AZ, June 2001.

[7] C. P. Huang, J. Bao, N. Dwarakanath, and S. Al-Kuran, "Applications of quasi-static method of moments for the designs of OC-192 and OC-768 fiber optic integrated circuits," *IEEE 2002 RFIC Symposium*, pp. 97-100, June 2002.

[8] Agilent EEsof EDA, Advanced Design System 1.5 Momentum, Palo Alto, CA 94304, December 2000.

[9] C. P. Huang, S. Hammadi, J. Lott, and S. Al-Kuran, "Characterization of multiple-via interconnections for multilayer chip and module designs," *IEEE 2001 AP-S International Symposium*, July 2001.

[10] R. Spickermann, "High speed allium arsenide/aluminum gallium arsenide traveling wave electrop-optic modulators, *Ph.D. Dissertation, University of California at Santa Babara*, 1996.

[11] Y. J. Guo, A. Paez, R. A. Sadeghzadeh, and S. K. Barton, "A circular patch antenna for radio LAN's," *IEEE Trans. on Antennas and Propagation*, vol. 45, no. 1, pp. 177-178, Jan. 1997.

[12] C. P. Huang, A. Z. Elsherbeni and C. E. Smith, "Analysis and design of tapered meander line antennas for mobile communications," *Journal of Applied Computational Electromagnetics Society, Special Issue on Wireless Communications*, vol. 15, no. 3, pp. 159-166, 2000.

New Heating Characteristics of a Radio Frequency Rectangular Resonant Cavity Applicator Using Various Antennas for Hyperthermic Treatment

Yutaka Tange [1], Yasushi Kanai [2], Yoshiaki Saitoh [3], and Tatsuya Kashiwa [4]

[1] Graduate School of Science and Technology
Niigata University, Niigata, 950-2181, Japan

[2] Department of Information and Electronics Engineering
Niigata Institute of Technology, Kashiwazaki, 945-1195, Japan

[3] Department of Biocybernetics, Faculty of Engineering
Niigata University, Niigata, 950-2181, Japan

[4] Department of Electrical and Electronic Engineering
Kitami Institute of Technology, Kitami, 090-8507, Japan

Abstract **–** The heating characteristics of a radio frequency rectangular resonant cavity applicator excited by various antennas are investigated for use in hyperthermic treatment. The coupled electromagnetic and heat-transfer equations are solved to obtain the heating characteristics. Two types of antennas and three types of dielectric phantoms are used in the calculations and measurements. Clear differences in the heating characteristics are observed for these phantoms and antennas. Previously, we were only able to heat up the surface or end regions of the phantom, while it is now possible to uniformly heat up the deeper regions with the current applicator. Therefore, this applicator is suitable for hyperthermic treatment.

Keywords **–** Cavity resonators, dielectric phantom, FDTD methods, finite element methods, and hyperthermia.

I. INTRODUCTION

World Health Organization (WHO) statistics suggest that six million humans in the world die of cancer and ten million new patients are added every year [1].

Hyperthermia is a cancer treatment which exposes human tissues to high temperatures in order to irreparably damage or kill cancer cells. The treatment focuses on the difference in heat sensitivity between nomal (alive until $44\,^{\circ}C$) and cancer cells (dead above $42.5\,^{\circ}C$) [2]. In this method, the region around the tumor including healthy tissue is heated by, for example, electromagnetic energy. By comparison with a surgical cure, radiation therapy, and anticancer drug therapy, hyperthermia has the possibility of decreasing cancer patients' pain and suffering.

Many heating applicators for hyperthermia have been developed. For example, radio frequency heating [3] and microwave heating [4] applicators have been used for clinical treatment. However, these heating methods have several problems since the heating region is limited to areas near the surface of the body and moreover there are the effects of blood flow and complex human organs. Annular phased array (APA) systems, using the principle of phased arrays [5], [6], can heat deep-seated tumors selectively. However, it is difficult to control the phases and the amplitudes of multiple antennas in order to focus the electromagnetic energy [7], [8].

We have previously reported the analysis of, and experiments on, a reentrant resonant cavity applicator for hyperthermic treatment [9]-[11]. The applicator was able to heat a deep-seated region of a disk-shaped dielectric phantom, but a torso-shaped dielectric phantom similar in length to a human body could not be heated. Therefore, we developed a rectangular resonant cavity applicator using two antennas to realize heating of a deep region for a torso-shaped dielectric phantom. In our previous papers, the antennas were not modeled but the magnetic energy was supplied at a single point [12], [13]. Therefore, it is possilbe to obtain more accurate solutions if the antennas are modeled more precisely. In addition, we had no proper phantom with regard to electrical properties, especially electrical conductivity leading to poor experimental results. Note that we had already considered the various organs and metabolism including blood flow, and found that the

most critical issue is the design of the heating system, in particular, how the electromagnetic energy is directed towards the targeted region [11].

In this paper, we describe the analysis and the experiments of the heating technique for a deep-seated region in an RF rectangular resonant cavity applicator. In the experiments, we prepared TX-151 (a commercial powder for dielectric phantom fabrication designed with electrical and thermal constants close to muscle), clay, and the original phantoms and measured the frequency and temperature dependencies of the electrical constants. Then, dipole and L-type antennas were constructed and placed inside the applicator. First, two kinds of phantoms (TX-151 and clay phantoms) were used because we wanted to investigate how electrical constants affect the heating patterns. Next, we applied the original phantoms that have electrical constants close to that of human muscle by adjusting the initial temperature. It is possible to heat the center of the phantom if the antenna is moved appropriately. In addition, we had already found that the applicator fed by two antennas was better at heating the deeper region [13]. Therefore, we moved the antennas away from the applicator's center. In the analyses, the coupled electromagnetic and heat-transfer equations are solved to obtain the heating characteristics by using the FD-TD method [14] and FEM [10], [11], [13]. The antennas were modeled exactly. The experiments demonstrate the validity of the electromagnetic-heat transfer calculations and the possibility of heating deep-seated tumors.

II. RF HYPERTHERMIC SYSTEM AND RESONANT CAVITY APPLICATOR

As shown in Fig. 1, the system consisted of a signal generator (Tokyo HY-Power Labs., Inc. G1057VG), a set of high frequency electric power amplifiers (Niigata Tsushinki Co., Ltd., PA2000J), two power meters (BIRD Electronic Corp., Model 43), three custom impedance matching boxes, a set of dipole antennas or a set of L-type antennas, a custom balloon [15] with a coaxial line (Kyowa Ltd., 10D2V) used for dividing the RF power into two parts of the antenna, and a resonant cavity applicator. One L-type antenna, one matching box, and the balun are removed to make a single L-type antenna system.

The arrangement of the setup is shown in Fig. 2. The resonant cavity applicator is formed from 0.5 mm thick copper with dimensions 1300 mm × 1450 mm × 1500 mm. The wooden table consisted of a top plate with dimensions 1200 mm × 35 mm × 400 mm and four legs 70 mm in diameter and 555 mm in length. The dielectric phantom was placed on the table. The dipole antennas were placed beside the phantom at the center of the applicator in the x-direction. We were able to heat the distal parts (surface or end regions) of the phantom [13] and it was possible to heat the center of the phantom if the antennas were displaced appropriately [16]. Therefore, we placed the antenna 450 mm from the center with regard to the x-axis, as shown in Fig. 3. In addition, we had already found that the applicator fed by two antennas was better able to heat the deeper region [13]. We placed the antennas 450 mm and – 450 mm from the center with respect to the x-axis, as shown in Fig. 4. A dielectric phantom was used for the experiments to heat the deeper region before considering the clinical stage. The resonant state and the heating process for the rectangular cavity are discussed in the next section.

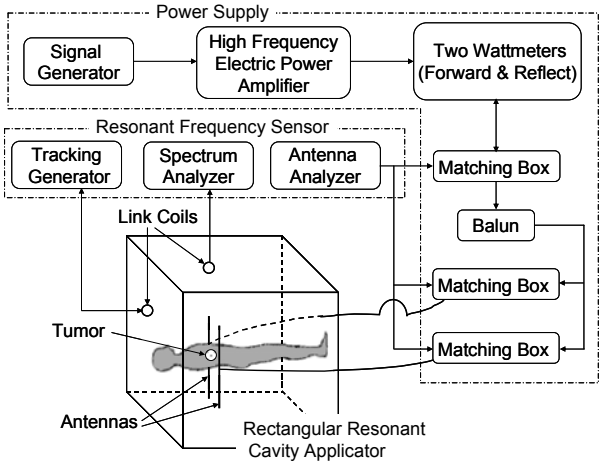

Fig. 1. Hyperthermic system schematic drawing.

III. VARIOUS DIELECTRIC PHANTOMS

We prepared three types of static dielectric phantoms: a TX-151 dielectric phantom 280 mm in diameter and 1200 mm in length, a clay phantom 300 mm in diameter and 1000 mm in length and an original dielectric phantom 280 mm in diameter and 1200 mm in length. The original dielectric phantom was composed of TX-151 solidifying powder (12.8 %) (Oil Center Research, Inc.), water (85.7 %) and additional agar powder (1.5 %) (Junsei Chemical Co., Ltd.). As compared to the TX-151 phantom, this original phantom has electrical properties similar to human muscle for a wide temperature range. As shown in Fig. 5, the temperature dependences of the electrical properties for these phantoms were measured using our measurement system prior to the calculations [17]. The electrical conductivity σ and the relative permittivity ε_r of human muscle in the RF range are approximately 0.7

S/m and 70, respectively [18]. Therefore, proper electrical constants are obtainable when the original dielectric phantom temperature is approximately $20\,°C$. Before the experiments, we kept both the room temperature and the dielectric phantom's temperature at approximately $20\,°C$ for more than 12 hours by using an air conditioner. The properties were measured at the resonant frequencies (50 MHz, 60 MHz, and 85 MHz) in the cavity as shown in section 2. The thermal properties of these phantoms are shown in Table 1 [10], [19]. The electrical properties of the wooden table, only used for electromagnetic field analysis were assumed to be $\varepsilon_r = 1.88$ and $\sigma = 0.0003$ S/m [20].

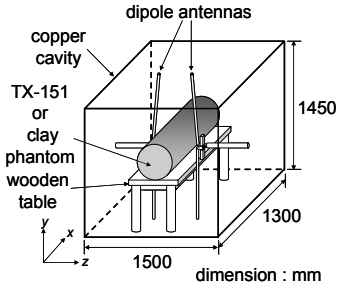

(a) A set of dipole antennas.

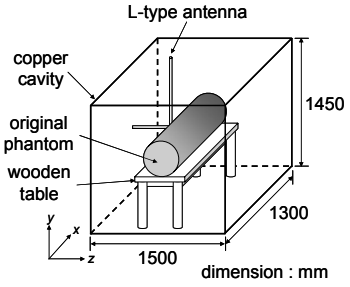

(b) L-type antenna.

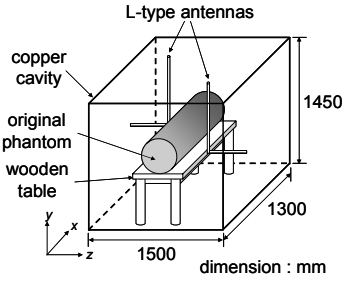

(c) A set of L-type antennas.

Fig. 2. Arrangement of a rectangular resonant cavity applicator, a phantom, an antenna(s), on the wooden table.

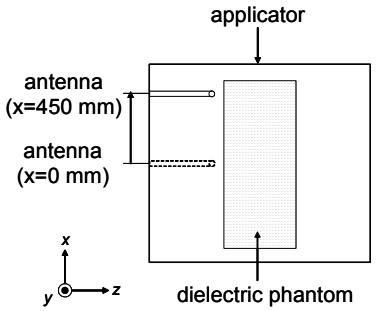

Fig. 3. Two locations of the L-type antenna (x = 0 mm and 450 mm): x = 450 mm from the center with respect to the x-axis was found to be appropriate.

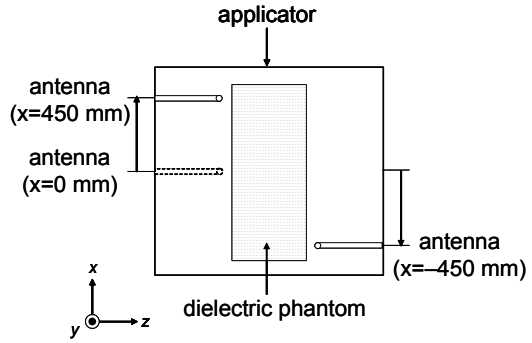

Fig. 4. Two locations for the L-type antennas (x = 450 mm and – 450 mm).

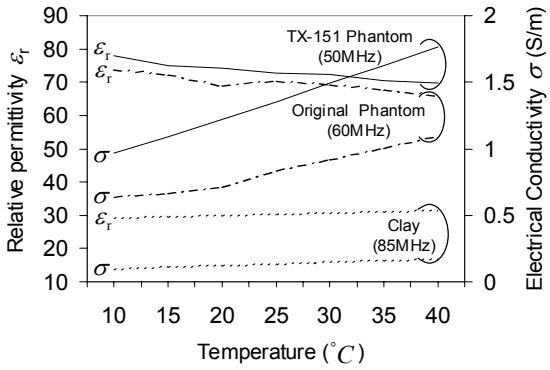

Fig. 5. Measured relative permittivity and electrical conductivity of the three phantoms.

IV. CALCULATION METHOD

The flow diagrams of the electromagnetic field calculations and heat-transfer calculations are shown in Fig. 6. We have modeled the cavity containing the dielectric phantom, the antenna(s), and the wooden table for the electromagnetic calculations. Note that the cavity walls were assumed to be perfect electrical

conductors.

We have used the three-dimensional finite-difference time-domain (FDTD) method [14] to solve Maxwell's equations:

$$\nabla \times \mathbf{E} = -\mu \frac{\partial \mathbf{H}}{\partial \mathrm{t}}, \tag{1}$$

$$\nabla \times \mathbf{H} = \sigma \mathbf{E} + \varepsilon \frac{\partial \mathbf{E}}{\partial \mathrm{t}} \tag{2}$$

where, μ, σ, and ε are respectively permeability, electrical conductivity, and permittivity. A current excitation source with a load impedance of 50 Ω at the gap was assumed for the dipole antennas. A voltage source with a pure sinusoidal wave was applied to the L-type antenna. Thin wire approximation [21] was used to model the dipole and L-type antennas. The whole volume of the cavity applicator was divided by our automatic mesh generator [22] into regular cells with a side length of 25 mm, as shown in Fig. 7.

After analyzing the electromagnetic field distributions, the electromagnetic energy applied to the phantom was evaluated as,

$$\dot{\mathrm{Q}} = \frac{1}{\mathrm{T}} \sigma \int |\mathbf{E}|^2 \mathrm{dt}\,. \tag{3}$$

The output data $\dot{\mathrm{Q}}$ were interpolated at regular intervals of 12.5 mm.

The heat-transfer equations

$$\rho c \frac{\partial \mathrm{T}}{\partial \mathrm{t}} = \lambda \nabla^2 \mathrm{T} + \dot{\mathrm{Q}}, \tag{4}$$

$$\mathrm{q} = \alpha_{\mathrm{c}} \left(\mathrm{T} - \mathrm{T}_{\mathrm{c}} \right) \tag{5}$$

are solved using three dimensional FEM because it is easier to set boundary conditions for FEM than for FDM. ρ, c, λ, q, α_{c}, and T_{c} denote respectively volume density of mass, specific heat capacity, thermal conductivity, heat flux, heat transfer coefficient, and the external temperature. The thermal constants of the TX-151 and original phantom were assumed to be as shown in Table 1 as both phantoms consisted of mostly water. In the heat-transfer calculations, only the phantom was modeled as it was discovered that the wooden table did not affect the temperature distributions. Brick elements 12.5 mm on each side were used, as shown in Fig. 8, such that the calculated electromagnetic energy from the FDTD calculation could be transferred precisely. That is, the average value of the eight-point nodal data obtained by FDTD analysis is considered to be the data of one element for FEM analysis.

Table 1. Thermal constants of dielectric and clay phantom.

TX-151 or Original Phantom	Volume density of mass	1030 (kg/m³)
	Specific heat capacity	3150 (J/kg°C)
	Thermal conductivity	0.555 (W/m°C)
	Heat transfer coefficient	5 (W/m²°C)
	Relative permeability	1
Clay Phantom	Volume density of mass	1700 (kg/m³)
	Specific heat capacity	1800 (J/kg°C)
	Thermal conductivity	1.2 (W/m°C)
	Heat transfer coefficient	5 (W/m²°C)
	Relative permeability	1

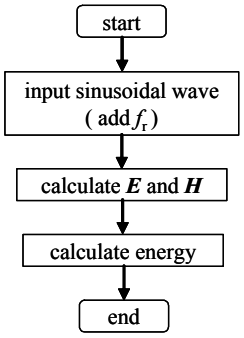

(a) Electromagnetic field analysis.

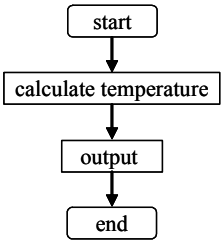

(b) Heat-transfer analysis.

Fig. 6. Flow diagrams of electromagnetic field and heat-transfer analysis.

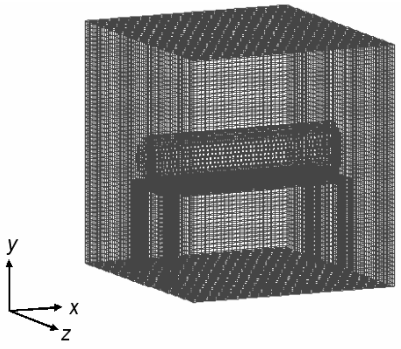

Fig. 7. FDTD mesh used for electromagnetic field analyses, where a resonant cavity applicator, dielectric phantom, a wooden table, and L-type antennas are modeled.

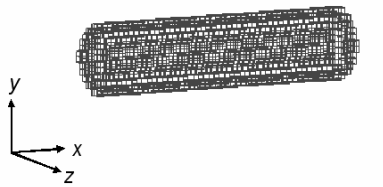

Fig. 8. FEM mesh used for heat-transfer analyses. Only the dielectric phantom is modeled.

V. EXPERIMENTAL PROCEDURE

Electromagnetic energy of 400 watts in the frequency range of 50 MHz – 85 MHz at the amplifiers' terminal was generated from the amplifiers. While the phantom is heated, the reflected power increases because of the temperature dependencies of the material properties. The amount of reflected power is minimized by adjusting the matching box during the heating process, i.e. the resonant state is maintained by changing the capacitance of the matching box. After a heating process of 30 minutes, the phantom was cut, and the temperature distribution was observed using a thermograph (Fujitsu Infra-Eye210).

VI. RESULTS AND DISCUSSION

A. Validity of Calculation

In electromagnetic analysis using finite-difference time-domain methods, a stable condition exists if the following relationship is valid [23],

$$\text{mesh size} \leq \lambda_{\text{wavelength}} / 10 \qquad (6)$$

where $\lambda_{\text{wavelength}}$ is the wavelength inside the dielectric phantom. A mesh size of 25 mm in our calculation is sufficient to satisfy this condition as a minimum value to achieve a stable condition in this case is 60 mm.

B. Comparison of Measured and Calculated Results

The measured and calculated results obtained in this study are shown in Figs. 9 and 10 for TX-151 and clay phantoms. The experimental conditions, starting temperature T_0 of the phantoms, surrounding temperature T_c, and resonant frequency f_r, are shown in the figure captions.

Whereas the tendencies of the measured temperature distributions for the TX-151 phantom and the original phantom agree with the calculated ones, the result for the clay phantom varies from the calculated one.

The major reasons for this discrepancy in temperature distributions are most likely caused by the differences in thermal properties of the clay phantom and deformation of the TX-151 and original phantoms between the experiments and calculations. It is also seen, from Fig. 10 (a), that the deep region of the phantom exhibiting low electrical conductivity can be heated up easily as we have noted previously [10].

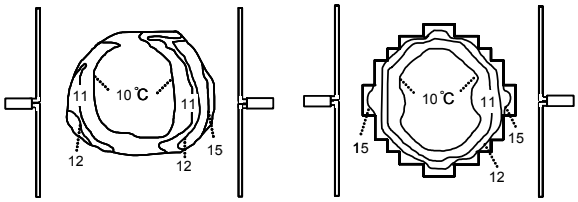

(a) Measured result (f_r = 51.37MHz – 51.45 MHz)

(b) Calculated result (f_r = 51.37 MHz)

Fig. 9. Measured and calculated temperature distributions of the center of the cross section in the dielectric phantom fed by two antennas with opposite phase, where initial temperature of the phantom T_0 and external temperature T_c were $10\,°C$ and $15\,°C$, respectively.

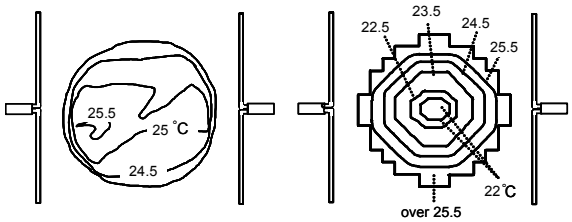

(a) Measured result (f_r = 84.80 MHz)

(b) Calculated result (f_r = 84.80 MHz)

Fig. 10. Measured and calculated temperature distributions of the center of the cross section in the clay phantom fed by two antennas with opposite phase, where T_0 and T_c of the clay were $21.8\,°C$ and $23.5\,°C$, respectively.

Measured and calculated temperatures are compared in Figs. 11 through 13 for an original phantom where the antenna was located at x = 0 mm in Fig. 11 and at x = 450 mm in Figs. 12 and 13. Note that the electrical conductivity and the relative permittivity of human muscle in the RF range are approximately 0.7 S/m and 70, respectively [18]. Therefore, the starting temperatures were set such that the phantoms' electrical conductivities were closer to that of human muscle. The increases in temperature of the deep region from the original state in Figs. 11 and 12 were $0.2\,°C$ and $1.9\,°C$, respectively. Therefore, it is very important to move the L-type antenna away from the applicator's center to achieve heating of the deep region. Comparing

Figs. 12 and 13 reveals that a small difference in starting temperature greatly alters the heating pattern, that is, the heating properties are sensitive to the initial electrical constants.

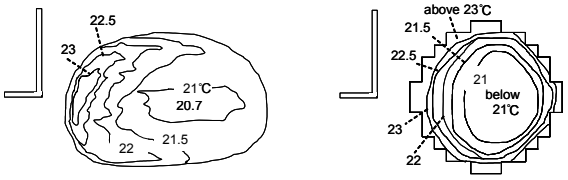

(a) Measured result (f_r = 61.62 MHz)

(b) Calculated result (f_r = 61.62 MHz)

Fig. 11. An L-type antenna (solid line) was placed at x = 0 mm. Calculated and measured temperature distributions on a cross section at x = 0 mm, where T_0 and T_c were 20.5 °C and 20.8 °C, respectively.

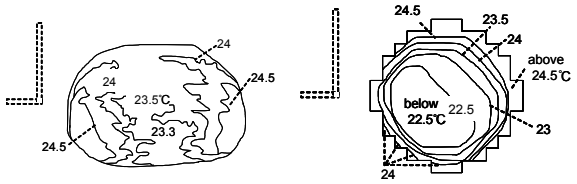

(a) Measured result (f_r = 62.23 MHz – 62.27 MHz)

(b) Calculated result (f_r = 62.27 MHz)

Fig. 12. An L-type antenna (dotted line) was placed at x = 450 mm. Calculated and measured temperature distributions on a cross section at x = 0 mm, where, T_0 and T_c were 21.4 °C and 21.5 °C, respectively.

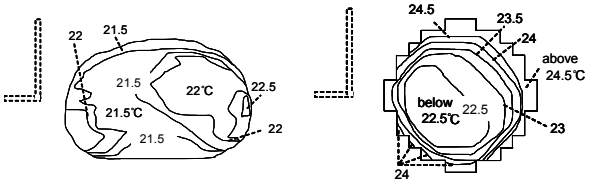

(a) Measured result (f_r = 62.20 MHz)

(b) Calculated result (f_r = 62.20 MHz)

Fig. 13. An L-type antenna (dotted line) was placed at x = 450 mm. Calculated and measured temperature distributions on a cross section at x = 0 mm, where T_0 and T_c were 19.6 °C and 19.9 °C, respectively.

The measured and calculated results fed by two antennas with the same and opposite phases of voltage distribution are shown respectively in Figs. 14 and 15 for the original phantom. Note that opposite phase implies that the two energies with a phase difference of 180^o are applied to two antennas. The increases in temperature of the deeper region from the original state in Figs. 14 and 15 were 1.9 °C and 1.8 °C, respectively. Comparison of the results of the single antenna and a set of L-type antennas with the same and opposite phases showed that the applicator, fed by two antennas with the same phase, heated the deeper region more uniformly. These results indicate that better heating patterns were obtained than in the previous results [9] - [13].

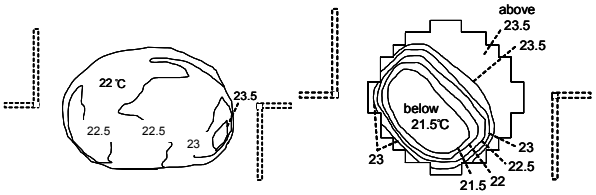

(a) Measured result (f_r = 62.82 MHz)

(b) Calculated result (f_r = 62.82 MHz)

Fig. 14. A set of L-type antennas (dotted line) fed by the same phase of voltage distribution were placed at x = 450 mm and x = – 450 mm. Calculated and measured temperature distributions on a cross section at x = 0 mm, where T_0 and T_c were 20.1 °C and 20.4 °C, respectively.

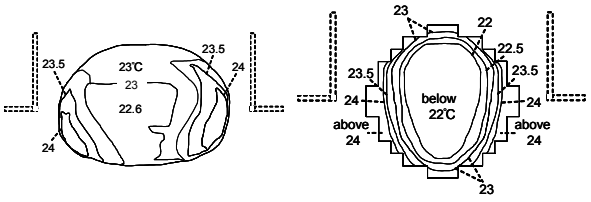

(a) Measured result (f_r = 61.81 MHz)

(b) Calculated result (f_r = 61.81 MHz)

Fig. 15. A set of L-type antennas (dotted line) fed by the opposite phase of voltage distribution were placed at x = 450 mm and x = – 450 mm. Calculated and measured temperature distributions on a cross section at x = 0 mm, where T_0 and T_c were 20.3 °C and 21.3 °C, respectively.

The measured and calculated results shown here are only for the cross section located at x = 0 mm, and note that the other cross sections as well as the central cross section (x = 0 mm) were also heated. If the temperature of the external parts of the dielectric phantom is higher than the internal parts, then the cooling method using pure water can be applied [10], [11].

In the future, calculations considering the organs and blood flow are necessary with finer FD-TD cells as well as measurements to obtain a better heating pattern that is capable of treating deep-seated cancer tumors.

VII. CONCLUSION

The heating characteristics of an RF hyperthermia applicator for deep-seated regions have been investigated using both calculated and experimental results. We have also prepared various dielectric phantoms. The initial temperature was adjusted so that the torso-shaped phantoms used for the experiments had electric characteristics similar to that of human muscle. We have constructed dipole and L-type antennas and placed them at appropriate positions in a rectangular resonant cavity applicator.

Better heating patterns, exhibited by uniformly heating a deeper region can be obtained by moving the antenna away from the applicator's center. In addition, it was found that the applicator, fed by a set of L-type antennas with the same phase, heated the deeper region more uniformly. Better heating patterns with regard to heating in a deep-seated region were obtained when compared to our previous work.

In the future, calculations considering the organs and blood flow are necessary as well as measurements to obtain a better heating pattern that treats deep-seated cancer tumors before the clinical stage can be undertaken.

ACKNOWLEDGMENT

The authors would like to acknowledge Messrs Hiroki Ishiwatari, Tsuyoshi Satoh, and Hiroaki Shimazaki of our laboratory in Niigata University for their experimental and related assistance and Mr. Tsukasa Shiga of Niigata Institute of Technology for supplying the calculated results.

REFERENCES

[1] World Health Organization web site [Online]. Available : (http://www.who.int/cancer/en/).

[2] W. C. Dewey, and L. E. Hopwood, "Cellular responses to combinations of hyperthermia and radiation," *Radiology*, vol. 123, pp. 463-474, 1977.

[3] H. Takahashi, R. Tanaka, M. Watanabe, K. Kakinuma, T. Suda, S. Takahashi, H. Masuda, A. Saito, and T. Nakajima, "Clinical results of RF interstitial hyperthermia for malignant brain tumors," *Japanese Journal of Hyperthermic Oncology*, vol. 11, no. 1, pp.61-67, March 1995 (in Japanese).

[4] C. H. Durney, and D. A. Christensen, *Introduction to Bioelectromagnetics*, Boca Raton: CRC, pp. 151-153, 1999.

[5] P. F. Turner, "Regional hyperthermia with an annular phased array," *IEEE Trans. on Biomed. Eng.*, vol. 31, no. 1, pp. 106-114, Jan. 1984.

[6] N. Terada and Y. Amemiya, "The performance of the dipole array applicator for radiofrequency hyperthermia," *The IEICE Transactions on Communications*, vol. J67-B, no. 2, pp. 163-170, Feb. 1984 (in Japanese).

[7] N. Siauve, L. Nicolas, C. Vollaire, A. Nicolas, and J. A. Vasconcelos, "Optimization of 3-D SAR distribution in local RF hyperthermia," *IEEE Trans. on Magn*., vol. 40, no. 2, pp. 1264-1267, Mar. 2004.

[8] P. Wust, B. Hildebrandt, G. Sreenivasa, B. Rau, J.Gellermann, H. Riess, R. Felix, and P. M. Schlag, "Hyperthermia in combined treatment of cancer," *The LANCET Oncology*, vol. 3, pp. 487-497, Aug. 2002.

[9] K. Kato, J. Matsuda, and Y. Saitoh, "A re-entrant type resonant cavity applicator for deep-seated hyperthermia treatment," *Proc. Annual Int'l Conf. of the IEEE Eng. in Medicine and Biology Society*, vol. 11, pp. 1712-1713, Nov. 1989.

[10] Y. Kanai, T. Tsukamoto, K. Toyama, Y. Saitoh, M. Miyakawa, and T. Kashiwa, " Analysis of a hyperthermic treatment in a reentrant resonant cavity applicator by solving time-dependent electromagnetic- heat transfer equations," *IEEE Trans. on Magn*., vol. 32, no. 3, pp. 1661-1664, May 1996.

[11] Y. Kanai, T. Tsukamoto, Y. Saitoh, M. Miyakawa, and T. Kashiwa, "Analysis of a hyperthermic treatment using a reentrant resonant cavity applicator for a heterogeneous model with blood flow," *IEEE Trans. on Magn*., vol. 33, no. 2, pp. 2175-2178, Mar. 1997.

[12] S. Soeta, S. Yokoo, M. Shimada, Y. Kanai, and J. Hori, "Eigenmode analysis of a parallelepiped resonator for hyperthermic treatment by using FD-TD method," *10th Niigata Branch Regional Meeting of IEE Japan*, III-21, Nov. 2001 (in Japanese).

[13] Y. Tange, Y. Kanai, and Y. Saitoh, "Analysis and development of a radio frequency rectangular resonant cavity applicator with multiple antennas

for a hyperthermic treatment," *IEEE Trans. on Magn.,* vol. 41, no. 5, pp. 1880-1883, May 2005.
[14] D. Sullivan, "Three-dimensional computer simulation in deep regional hyperthermia using the finite-difference time-domain method," *IEEE Trans.* on *Microwave Theory Tech.*, vol. 38, no. 2, pp. 204-211, Feb. 1990.
[15] G. Badger, "New class of coaxial-line transformers," *ham radio*, pp. 18-29, Mar. 1980.
[16] Y. Tange, Y. Kanai, and Y. Saitoh, "Heating characteristics of an RF hyperthermia for deep-seated region," *Proc. Annual Int'l Conf. of the IEEE Eng. in Medicine and Biology Society*, 271, 2005.
[17] S. Hoshina, Y. Kanai, and M. Miyakawa, "A numerical study on the measurement region of an open-ended coaxial probe used for complex permittivity measurement," *IEEE Trans. on Magn*., vol. 37, no. 5, pp. 3311-3314, Sep. 2001.
[18] Federal Communications Commission web site [Online]. Available, (http://www.fcc.gov/fcc-bin/dielec.sh/).
[19] JSME, *JSME Data Book, Heat transfer*, 4th ed., Tokyo: JSME Press, p. 321, 1986 (in Japanese).
[20] A. R. von Hippel, *Dielectric Material and Applications*, 3rd ed., Boston: The M.I.T. Press, p. 359, 1961.
[21] K. R. Umashankar, A. Taflove, and B. Beker, "Calculation and experimental validation of induced currents on coupled wires in an arbitrary shaped cavity," *IEEE Trans. on Antennas Propagat*., vol. 35, no. 11, pp. 1248-1257, Nov. 1987.
[22] Y. Kanai and K. Sato, "Automatic mesh generation for 3D electromagnetic field analysis by FD-TD method," *IEEE Trans. on Magn*., vol. 34, no. 5, pp. 3383-3386, Sep. 1998.
[23] T. Uno, *Finite difference time domain method for electromagnetic field and antennas*, Tokyo: Corona Publishing, 2000, pp. 50-55 (in Japanese).

Yutaka Tange received his B. E. and M. E. degrees in mechanical engineering from Toyohashi University of Technology in 2001 and 2003. From 2003, he has been a Ph.D. candidate at Niigata University. His research theme is the development of hyperthermia systems for deep-seated tumor. He is a member of Japanese Society of Hyperthermic Oncology (JSHO), IEICE and Journal of the Japan Society of Mechanical Engineers (JASME).

Yasushi Kanai was born in Niigata, Japan in 1959. He received the B. E., M. E. and Dr. Eng. degrees from Niigata University in 1982, 1984 and 1989, respectively. In 1984, he joined Alps Electric, Co., Ltd., Japan and worked as a research engineer until 1992. From 1992 to 1995, he was with Niigata University as an Associate Professor. In 1995, he joined Niigata Institute of Technology. Since 1999, he has been a Professor at the Department of Information and Electronics Engineering, Niigata Institute of Technology. His main research interests are numerical computations of electromagnetic fields and magnetic recording. He received The Valued Service Award from ACES in March 2003. Prof. Kanai is an ACES Journal Associate Editor, a Member of IEEE and a Founder Member of International Compumag Society.

Yoshiaki Saitoh received his B.E. degree in electrical engineering from Niigata University in 1963, and M.E. and Ph.D. degrees in electrical engineering from Hokkaido University in 1965 and 1970. In 1965, he joined the staff of the Department of Electronics, Niigata University, as an instructor, and had been a professor in the Department of Information Engineering since 1980. He is currently a professor in the Department of Biocybernetics. His recent research interests include measurements and stimulation of human organs, hyperthermia systems, and biomedical signal processing. He is a Senior Member of IEEE and the Japan Society of Medical Electronics and Biological Engineering.

Tatsuya Kashiwa graduated from the Department of Electrical Engineering of Hokkaido University in 1984 and completed the M.S. program in 1986. Before completing the doctoral program, he became a research associate in Department of Electrical Engineering in 1988. He has been an associate professor in the Department of Electrical and Electronic Engineering of Kitami Institute Technology since 1996. His research area is the analysis of electromagnetic fields and acoustic fields. He received an IEEE AP-S Tokyo Chapter Young Engineer Award in 1992. He is a coauthor of *Handbook of Microwave Technology* (Academic Press) and *Antenna and Associated System for Mobile Satellite Communications* (Research Signpost). He is a reviewer for IEEE MTT. He holds a Dr. Eng. degree, and is a member of IEICE and IEEE.

RF Coil Design for MRI Using a Genetic Algorithm

J. Rock Hadley[1], Cynthia M. Furse[2], and Dennis Parker[1]

[1]Utah Center for Advanced Imaging Research
[2]Electrical and Computer Engineering
University of Utah
50 S Campus Drive 3280 MEB
Salt Lake City, Utah 84112
cfurse@ece.utah.edu
www.ece.utah.edu/~cfurse

Abstract – In this work a Genetic Algorithm (GA) was used to optimize single and dual array Radio Frequency (RF) coils for imaging vasculature structures using Magnetic Resonance Imaging. Quasi-static equations were used to simulate sample noise and signal sensitivity profiles of the coil elements. Coil to sample and coil to coil interactions were taken into account, and the relative signal-to-noise ratio in the structure of interest was used as the cost function for the GA optimization.

Key words – Genetic Algorithm, Magnetic Resonance Imaging, phased array coils.

I. INTRODUCTION

Previous work has shown that substantial improvement in Magnetic Resonance (MR) image quality can be obtained using receiver coils that are specifically designed for the region of interest [1 - 46]. However, it is often difficult to fully optimize RF coils (eg. their sizes and positions) for specific objects or anatomies because of the complex nature of coil/sample and coil/coil interactions. Obtaining the exact geometric configuration that will optimize image quality over the region of interest is complicated. Also, the optimal geometric parameters can vary greatly depending on the sample volume or structure being imaged. There is a general rule that the coil diameter should be approximately equal to the depth of the voxel being imaged [38], but when that object is a large volume (such as the heart) or when the structure is a tortuous long and varies in depth like an artery, optimization is difficult. Many characteristics need to be taken into account when designing RF coils for specific anatomy such as object geometry (structure of interest, structure shape, and body surface geometry), coil coupling, coil sensitivity profile, interaction with the sample, relative positions of individual elements, patient comfort, parallel imaging factors, and image acquisition technique.

Stochastic optimization methods such as the genetic algorithm (GA) [47 - 49] are well suited for optimization problems of this nature, since they are able to find a global minimum when many local minima exist, they require no derivatives or gradients, and they are very flexible in their utility. Cost functions for GAs can be tailored to specific problems and can be implemented with other types of algorithms for accurate measurement or optimization purposes. GAs have previously been used to generate MRI related design parameters for various applications including split coil magnets, biplanar gradients, and some RF coil designs [50 - 55]. In this work, GA techniques are used to optimize coil parameters pertaining to single loop coil and phased array coil design for the purpose of imaging specific anatomic structures. The GA technique can provide optimum coil parameters including the number of coils in the array and the specific size and position of each element in the array for imaging the specific anatomy. The goal of this work is not to evaluate standard GA methods, as applied to RF coil design, nor to provide exact specifications for building application-specific coils. Rather the goal of this work is to show that the GA is well suited for optimizing coil design parameters and to define cost functions and methods to enable this optimization, allowing coil developers to assess trends and tradeoffs in relative signal-to-noise ratio (rSNR) during structure specific optimization.

II. THEORY

Genetic Algorithms

The genetic algorithm [47] is a search and optimization technique based on the concept of natural selection. This technique is particularly useful for optimization problems that have complicated cost functions with many local minima. GAs are also used in cases where it is difficult to formulate multiple derivatives of the cost function for use in algorithms such as the steepest descent algorithm. The GA computes a cost function for its individual

"chromosomes" or vectors of numbers that describe the optimization problem. The GA begins by computing the cost function for an initial population of chromosomes that are randomly chosen over the search space. The most favorable chromosomes are kept, and the worst chromosomes are discarded. Those chromosomes that are kept are "mated" with other "good" chromosomes to form "offspring" chromosomes that are then put into the population pool. There are multiple techniques for mating chromosomes and introducing mutations into the chromosome pool so that the GA is less likely to result in a local minimum when the global minimum is desired. Although there is no way to determine if the absolute global minimum has been obtained, GAs are typically more likely to find the global minimum for cost functions containing many local minima than standard minimum seeking algorithms.

Optimization Model

The model for these simulations consists of a large slab (80 cm × 80 cm × 40 cm) of a semi-conducting material with coils placed on the surface of the conducting model [38]. The slab is defined for (-40 < x < 40, -40 < y < 40, -40 < z < 0), and the coils are placed on the surface of the slab at z = 0 as shown in Fig. 1. The y-axis of the slab is defined to be parallel to the main DC magnetic field of the MR scanner, B_0. The sample has a conductivity of 0.3 S/m. Off-axis electromagnetic equations for rectangular coil elements are simulated using equations derived from the Biot-Savart law and presented by Smythe and Misakian [56], [57]. For a single loop, the dimensions are a × b, representing the side lengths of a rectangular coil in the x and y directions, respectively. The coil position is defined as (x, y) as shown in Fig. 1. The anatomic object of interest is embedded in the sample and consists of any collection of points that represent the particular structure over which rSNR calculations are made. The objects of interest in this work primarily consist of representations of different vessel structures and a heart shaped object.

The impedance, Z, for an RF resonating loop receiver coil is composed of several terms including the sample losses, R_s, coil ohmic losses, R_c, the connecting wire or cable losses R_w, the amplifier impedances, R_a, and the reactive inductance and capacitance terms, X,

$$Z_i = R_{si} + R_{ci} + R_{wi} + R_{ai} + jX_i. \tag{1}$$

The i represents the i^{th} coil, $j = \sqrt{-1}$. The sample noise R_s, for such a coil is defined as the integral of the squared magnitude of the magnetic vector potential, A, created by a unit current in the coil [58], multiplied by the sample conductivity, σ, and the squared radian frequency, ω, over the volume of the coil sensitivity [38], [56]

$$Rs_i = \omega^2 \sigma \int A_i \cdot A_i \partial v. \tag{2}$$

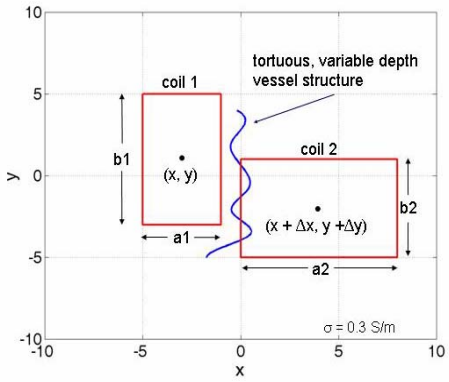

Fig. 1. Coil dimension and position definitions for a single and dual coil system positioned over the optimization sample space.

For this equation, it is assumed that the conductivity tensor is isotropic and uniform over the sample volume, and that only a ϕ component of the magnetic vector potential exists in the sample [56]. This satisfies the boundary conditions for the electric field at the sample boundary. The coil ohmic losses for the rectangular loop are [59]

$$Rc_i = \frac{4(a_i + b_i)}{\pi d}\sqrt{\frac{\mu_o 2\pi f}{2\sigma}}, \tag{3}$$

where μ_0 is the permeability of air, f is the frequency of the current in the conductor, and d is the diameter of the conductor. This work does not include the amplifier or cable losses based on the assumption that these losses are already minimized and are the same for all coils in the optimization algorithm. For a single loop, the reactive terms include the distributed capacitance and the loop self inductance terms that generally cancel out at resonant frequencies. However, the self inductance terms are useful in the coil optimization process. For a single rectangular loop coil of dimensions a × b, with a round wire diameter ρ, the self inductance is [60],

$$L_i = 0.004(a_i \log(2a_i/\rho) + b_i \log(2b_i/\rho) + 2\sqrt{a_i^2 + b_i^2}$$
$$-a_i \sinh^{-1}(a_i/b_i) - b_i \sinh^{-1}(b_i/a_i) - 2(a_i + b_i) + \frac{\mu}{4}(a_i + b_i)). \tag{4}$$

For the purposes of this work, the noise power, n, for a single coil is defined by equation (2) and equation (3) such that,

$$n_i = \mathrm{Re}\left(Z_i\right) \approx Rs_i + Rc_i. \tag{5}$$

The relative MR signal or coil sensitivity for a point in the sample space r is defined from the theory of reciprocity [58] as the transverse magnetic field produced by the coil with a unit current flowing in the conductor elements,

$$s_i(r) = B_\perp \approx (B_x(r) + jB_z(r)). \tag{6}$$

For a two coil system, the second rectangular loop has the dimensions of $a_2 \times b_2$, with a position of $(x + \Delta x, y + \Delta y)$ as depicted in Fig. 1. The second coil also has its own self inductance described by equation (4). There is also a mutual inductance term that describes the flux linkage between the two coils. This term is largely dependant on the geometrical relationship between the two coils and is expressed by,

$$M_{ik} = \frac{\mu_0}{4\pi} \iint \frac{\partial s_i \cdot \partial s_k}{|r_i - r_k|}, \tag{7}$$

where, s_i is a unit element of the conductor of coil i, and $|r_i - r_k|$ is the distance between the unit elements of the i^{th} and k^{th} coil.

The second coil also has sample noise and ohmic noise described by equations (2) and (3), respectively. If the two coils are in close proximity, a portion of the sample noise can be correlated between coils. This correlated noise power or noise that is shared between the two coils, through the sample, is described by,

$$Rs_{ik} = \omega^2 \sigma \int A_i \cdot A_k \partial v, \tag{8}$$

which is the general form of equation (2), including the inner vector product of the magnetic vector potential from both coils at each point in the sample space. These additional noise terms from coil k affect the noise of the overall system and the resulting noise as seen by coil i is,

$$n_{ti} = R_{si} + R_{ci} + \sum_{i \neq k} R_{ik} + \sum_{i \neq k} \left| \frac{\omega M_{ik}}{Z_k} \right|^2 \mathrm{Re}(Z_k^*), \tag{9}$$

where the subscript t represents the total noise from the i^{th} coil. The net signal or coil sensitivity for coil i, in the presence of coil k, then become,

$$s_i(r) = \left(Bx_i(r) + jBz_i(r)\right) + \sum_{i \neq k} \frac{M_{ik}}{L_i} \left(Bx_k(r) + jBz_k(r)\right). \tag{10}$$

The rSNR at any given point in the sample depends on combining the signals from coil i and coil k in the manner derived by Roemer [38]. Therefore, when the signals are combined to obtain maximized rSNR at every image point, the resulting maximum rSNR is,

$$rSNR = \sqrt{S^T \Psi^{-1} S^*}, \tag{11}$$

where S is the coil sensitivity vector, or the vector of coil sensitivities at the position for which the rSNR is being calculated. The T represents the matrix transpose, * represents the complex conjugate, and Ψ is the noise correlation matrix which includes the noise power terms from equation (2) as the diagonal elements, and the noise power terms from equation (8) as the off diagonal elements of its matrix.

III. METHODS

Genetic Algorithm

The GA chromosomes that describe the one and two coil systems consist of the geometrical parameters that express the sizes of the coils and their positions with respect to the sample being imaged (see Fig. 1). The chromosome for the two coil system is:

$$[a_1, b_1, x, y, a_2, b_2, \Delta x, \Delta y]. \tag{12}$$

For this work, these chromosome variables were continuous, although it would be equally valid to allow a fixed set of choices, which might speed up the GA convergence. The ranges for a and b define limitations on the smallest and largest coil sizes allowed in the optimization, and the limits on x, and y determined the limits of the coil position. The coils in this study are limited to a maximum a and b of 10 cm, and the center position of the search space is a 20 × 20 cm surface.

An initial set of 16 to 48 random chromosomes were compared based on their cost function values. The best half of the chromosomes were kept for mating (parents) and the rest of the chromosomes were discarded. The mating routine produced the same number of additional offspring chromosomes, which were sorted with the parent chromosomes according to their cost function values (their "fitness"). This iterative procedure was continued until convergence was achieved.

The cost function for each chromosome was computed as the average rSNR for the sample points in the object of interest,

$$\cos t = \frac{1}{N} \sum_{i=1}^{N} w_i \cdot rSNR(r_i). \tag{13}$$

For this equation, rSNR is defined by equation (11), r_i defines the position of the sample, point, N is the total number of sample points that define the anatomic structure of interest, and w_i is the weighting value of specific sample points ($w_i = 1$ for this work). For each rSNR calculation, the coil sample and ohmic losses were interpolated from pre-computed look up tables, eliminating the computation of time consuming volume

integrals over the sample space for each iteration. The coil signal sensitivity at all sample points was also computed for each coil, or set of coils, and for each GA iteration.

The original implementation of the two coil GA code used the equations as stated above to compute the cost functions of the chromosomes. However, the GA would quickly converge to local minimum solutions where the mutual inductance between coils was zero, but for which the coil shapes and positioning were not practical or intuitive for imaging the object of interest. Using continuous variables for the chromosome elements caused the solution space to be so large that it was difficult to find another local minima once the first set of $M_{12} = 0$ coils were determined. Consequently, the first local minimum found was generally the final result for this algorithm. These $M_{12} = 0$ solutions were very dominant over all other solutions and many such solutions (local minima) existed in the search space. Therefore, it was determined that the search space should be limited to solutions where the mutual inductance between coils was zero. This is commonly done in coil design without the GA, and it is reasonable to assume that it is also ideal for GA-optimized coils. This work used a simple binary search algorithm to shift coil 2, along a specified angle with respect to coil 1, to determine the Δx and Δy chromosome elements that would result in $M_{12} = 0$ between the two coils. Consequently, Δx and Δy can quickly be determined. Once this algorithm is complete, the Δx and Δy components of the two coil chromosome were set, and the relative position of coil 2 with respect to coil 1 was fixed. At that point, the correlated noise terms between the two coils were calculated, the individual coil sample noise terms were obtained from the lookup table, and the noise correlation matrix, Ψ, was defined for the two coil system. The binary search algorithm essentially eliminated two of the eight chromosome elements in the original 2 coil chromosomes. The next step that aided in significantly speeding up the algorithm, was the use of a nested GA to optimize the (x, y) position of coil 1 such that the average rSNR of the fixed two coil system was optimized for the object of interest. This nested GA was fast, because the only calculations needed for each iteration were the magnetic field and rSNR calculations for the object points at each (x, y) coil pair position. This technique resulted in a 4 element GA in an outer loop and a two element GA in an inner loop, and significantly reduced the chromosome pool search space to include only chromosomes that were relevant and practical for imaging the object of interest. This technique provides significant improvements in the speed of convergence over a single GA for all eight elements of the chromosome. Other factors that speed up convergence of the GA were to restrict the relative sizes of the two coils so that non-probable coil pairs were eliminated and the use of predetermined coil pair data that wais used in a look up table as the initial pool of chromosomes. All that wais needed for these initial chromosomes wais the inside GA loop to optimally position the coil pairs for imaging the object of interest. Finally, the option to fine tune the top chromosome wais included in the algorithm. This consists of adding chromosomes with incremental adjustments in the coil sizes and positions into the pool and helped to keep the GA from stagnating on a single chromosome for multiple iterations.

Coil Optimizations

Single coil GA simulations used a reduced chromosome length of 4 elements including the coil dimensions a and b, and the coil position x and y. Noise correlation and mutual inductance terms were not needed for these simulations, so convergence was quick. Single coil optimizations were performed to compare single and double coil rSNR results and to assess the relative improvements that can be gained by using two coils over a single coil for various vessel segments.

Several case studies were evaluated [79] and are discussed here. For each case a single and double coil GA optimization were performed. The case studies consisted of the following: case 1) a single sample point, representing a vessel segment of 1 cm length at a 3 cm depth, , case 2) a single sample point at 5 cm depth, case 3) a single sample point at 8 cm depth, case 4) a longer vessel segment of 4 cm length at a continuous depth of 3 cm, case 5) a longer vessel segment of 10 cm length at a 5 cm depth, case 6) a long vessel structure with a linear depth profile, with a length of approximately 11 cm, a depth of 2.5 cm at one end, a depth of 5 cm at the center and a depth of 7.5 cm at the deepest end, and case 7) a heart model consisting of approximately 300 points distributed on a stretched spheroidal surface with a center depth of 9 cm, a length of 10 cm, and a diameter of 7 cm.

IV. RESULTS

The results for all the single and dual coil optimizations for the various cases are presented in Table 1. This table shows that for a single vessel point at 3 cm depth, the optimal coil radius is approximately 1.9×1.9 cm, and as a consequence of the vessel point being positioned at (x, y, z) = (0, 0, -3) cm, the coil is positioned at (x, y) = (0, 0) cm. This is about 25 % different from the rule of thumb that the coil diameter should be 3 cm for a 3 cm deep voxel. The rSNR for this single point using the optimal single coil is 81.6.

For the same vessel point, using a two coil array, the dimensions of each coil were 1.6×2 cm with a 2.72 cm x-directed, patient left/right, or transverse offset

between the two coils. This is similar to the designs presented by Hayes where the coils are offset in the transverse direction for optimal rSNR [22], [23], [61]. This configuration of coils provided a 14.8 % improvement in the rSNR (93.7) over the single coil. Hayes has described this phenomenon and attributes this to the phase of the coil sensitivity profile at the point of interest [62]. Similarly for cases 2 and 3, the dual coil array provides similar rSNR improvement with coil elements offset in the transverse direction. These results also show the intrinsic rSNR loss that naturally occurs as the sample point increases in depth. For example, increasing the depth of the single sample point from 3 to 5 cm decreases the available rSNR using the two coil array by 65 %, and increasing the depth from 5 to 8 cm decreases the available rSNR by an additional 65 %.

Table 1. GA optimization results for case studies.

Case #	# coils	depth	length	a/2	b/2	x	y	rSNR	% chg
1. point	1	3	1	1.9	1.9	0	0	81.6	14.8
	2	3	1	1.6	2	-1.37	0	93.7	
				1.6	2	1.37	0		
2. point	1	5	1	2.7	2.7	0	0	27.9	15.1
	2	5	1	2.3	3	1.9	0.2	32.1	
				2.3	3	-1.9	-0.17		
3. point	1	8	1	4	4	0	0	9.8	15.3
	2	8	1	3.4	4.5	-2.84	-0.28	11.3	
				3.4	4.5	2.87	0.28		
4. vessel	1	3	4	1.8	2.5	0	0	71.1	17.4
	2	3	4	1.6	2.6	1.29	-0.21	83.5	
				1.6	2.6	-1.31	0.23		
5. vessel	1	5	10	2.5	5	0	0	20.6	26.2
	2	5	10	2.7	3.1	0.15	2.69	26	
				2.7	3.1	-0.15	-2.68		
6. vessel	1	2.5 – 7.5	11	2	3	0	2.7	29.7	26.3
	2	2.5 – 7.5	11	1.8	2	0	3.8	37.5	
				3	3.2	0	-0.6		
7. heart	1	9	10	4	6	0	0	6.7	23.9
	2	9	10	3.7	6.5	-3	0.29	8.3	
				3.7	6.5	3	-0.29		

For case 4, the vessel object is again at a 3 cm depth, and the length is increased to 4 cm, typical for a carotid bifurcation. For this case, use of a dual coil array provides approximately 17.4 % rSNR improvement over the single coil (see Fig. 2). It is also interesting to note that by optimizing coils over a larger volume or vessel length, there is a nearly 11 % reduction in available rSNR compared to a single point at the same depth (compare with case 1). This coil design might be considered to be a good coil design for applications where the object of interest is a single point somewhere along the artificial design vessel, and the goal of the coil design is to have improved flexibility in coil positioning for a tradeoff of nearly 11 % in rSNR.

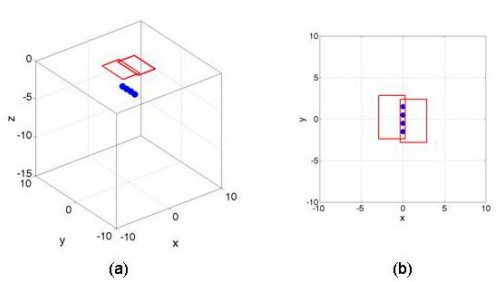

Fig. 2. Case 4 dual coil results show that the coils are still overlapped in the transverse direction and that there is a 17.4 % increase in rSNR compared to the single coil results.

The GA solution for case 5 indicates that the optimal dual coil configuration consists of two coils that are nearly the same size as an optimal single element coil for a single point at the design depth (see Fig. 3). However, rather than positioning the coils such that they are overlapped in the transverse direction, they are overlapped in the longitudinal direction, or patient superior/inferior direction. This configuration is known to have a subtle rSNR decrease under the overlap of the two coils as opposed to the known increase in rSNR under the overlap for coils overlapped in the transverse direction [62]. However, for the cost function used in this study, the net rSNR for the longitudinally overlapped pair is greater than for designs using the transverse overlapped pair. The GA technique can aid in determining where this break point might be found in determining the best approach for coil overlap for the imaging of specific structures. This case also demonstrates, as before, that designing a coil to cover such a long structure decreases the available rSNR of any one point on the structure by 19 % compared to a coil designed for a single point at the same depth (compare with case 2). However, this coil design is likely to be more flexible in positioning along the length of the structure.

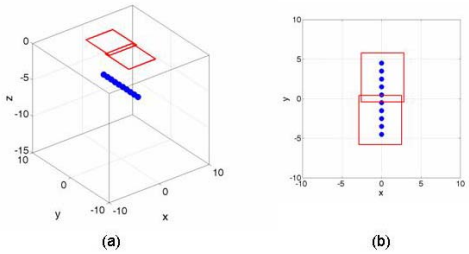

Fig. 3. Case 5: dual coil results show that the optimal overlap for this case is in the longitudinal direction. The dual coil provides a 26.2 % increase in rSNR over the single coil results.

The results for case 6 (see Fig. 4) give an indication of how the appropriate coil array should be designed to image structures that change in depth along the length of the structure. It would be difficult to use intuition alone to design a coil for such a purpose, however, using the GA to optimize the coils for this vessel structure provides a result that is intuitive and gives relative estimates of the dimensions and positions of a dual coil array that might be used to image a structure such as this. It is interesting to note how much rSNR improvement (~26 %) the GA indicates can be achieved using two coils rather than a single coil for these long vessel cases. This result also indicates that it may be important to use coils of arbitrary shape for the imaging of specific structures rather than standard circular or rectangular shaped coils.

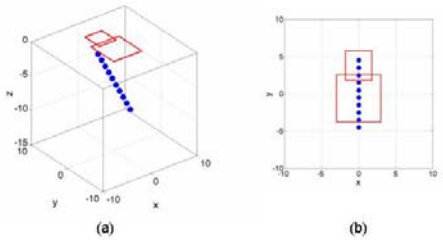

Fig. 4. Case 6: dual coil results show the benefit of using arbitrary shaped coils for imaging structures of this nature. The dual coil for this case provides a 26.3 % increase in rSNR compared to the single coil for this case.

The results for the heart model, case 7, provide insight into the optimal coil design for larger volumes and structures. The sample points used to calculate the average rSNR over the surface of this structure range from 12.5 cm to 5.5 cm depth with a slightly larger sample point density at the superior and inferior ends of the model, near its central axis (see Fig. 5). Because of the long length of this structure, it might be expected that coils overlapped in the longitudinal direction would again provide the highest rSNR over its surface. However, because the sample points nearest the surface have the largest intrinsic rSNR, their contribution to the overall cost function is great, and result in an optimal coil design where the coils are overlapped in a transverse manner with respect to B_0. Comparing case 7 with case 3, it can be seen that the coil width radius, a/2 = 3.7 cm, is just slightly larger than that for the single point at 8 cm depth, a/2 = 3.4 cm, accounting for the extra centimeter of the average heart depth. However, in order to account for the length of the heart at such a depth, the coil radius for the longitudinal direction is considerably longer than for the result in case 3. Finally, these results indicate an rSNR increase of approximately 24 % using a dual coil array compared to a single coil.

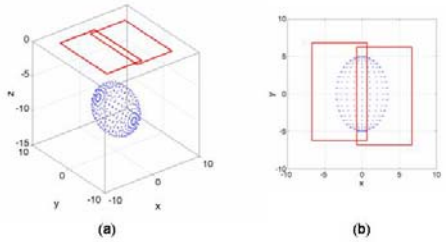

Fig. 5. Case 7: dual coil results show that, for the average rSNR cost function, the coils are still overlapped in the transverse direction even though the structure is long. The dual coil for this case provides a 23.9 % increase in rSNR over the single coil for this case.

The results for the single coil optimizations are in line with intuition and with expected results. Results for the single coil GA are achieved quickly, and can be performed on a standard PC in a matter of minutes. Using the techniques described above on a Dual AMD Opteron, dual core 270 with 4 GB of RAM, case 4 converged in approximately 2.5 hours, and case 7 in approximately 9.55 hours, making these simulations practical to use for specific design applications.

V. DISCUSSION

The purpose of this work was to develop a GA tool that could be used for finding coil geometries and positions that give the highest rSNR for a specific anatomy, and evaluate its usefulness. Modifications were made to the standard GA methods that limit the coil parameter search space to solutions that are practical for imaging the object of interest. Although these simulations were performed for only two coils, it would be natural to extend this work to multi-element arrays. There are challenges in obtaining minimum mutual inductance for three or more coil elements. However, with the use of passive decoupling circuits [28], [63 - 66] and appropriate image reconstruction techniques [65], [67], zero mutual inductance between all adjacent, coils may not be required. With the ability to simulate and optimize multiple coil elements using the GA tool, the number of coil elements that might be used in an array for imaging a specific structure might also be optimized.

In addition to optimizing the number of elements used in a coil array, many other interesting coil design characteristics might be optimized using the GA techniques such as individual coil sizes and relative positions for phased array coil elements, g-factors, and coil element spacing for parallel imaging applications, and any other coil dimension or relative coil position. Cost functions can also be modified to include other

anatomic structure specifications or image acquisition parameters. Recently, Breuer and Griswold have shown that phased array designs may be optimized for specific parallel image acquisition schemes that use different data gridding techniques. [68], [69] Therefore, the results of this study indicate that the use of the GA for optimization of coil design parameters is useful and promising.

The purpose simulating these different cases was to evaluate coil design trends and the effects on rSNR for different imaging applications, providing answers to fundamental coil design questions concerning coil size, position, direction of overlap, etc. These different case studies were also designed to provide insight into the results of designing RF coils for various objects of interest and to better understand how the optimal coil should be configured for these different geometries. It can be seen that coils or arrays of coils that are optimized for a specific point in the sample can provide significantly more rSNR for that point than if the point is only a part of some greater volume or structure that is being imaged with a coil designed for the entire volume.

There are several limitations to this study. First, particularly for complicated anatomies such as the carotid bifurcation, the simple vessel models may be insufficient. More realistic models would include accurate representation of the head, neck and shoulders and full wave solutions to account for all the complicated boundaries of such a model. Such a model would also provide the appropriate sample and correlated loss terms, whereas the infinite half plane model used in these studies may represent a much more dominant load than that of the head, neck and shoulders.

Second, these simulations are based on quasi-static electromagnetic field simulations where it is assumed that the electric and magnetic fields are not coupled and that the magnetic field in the sample is primarily due to the current in the coil conductor. Simulations using these equations combined with the effectively infinite slab model are subject to error, because they do not take into account important effects such as the boundary conditions of actual human anatomy, sample loading, conductive shielding of the fields from the sample, etc. Wright has computed the rSNR for several different coils at 64 MHz and has shown that the results using the quasi-static solutions tend to show all appropriate trends and features of the coils compared to actual measurements [44]. Many other authors have used quasi-static calculations to obtain reasonable estimates of real measurements [9], [20], [38], [56], [70-78]. These simulations seem to work well for situations where the current distributions around the coils are known to be relatively constant across the coil. As the coil dimensions or the frequency increases the changes in phase of the current in the coil become more significant, and these simulations may be inaccurate in predicting appropriate rSNR trends and characteristics.

Finally, it is also important to note that these simulation results are based on a cost function that is computed as the average rSNR over all sample points that define the structure of interest. The cost function also assumes the use of Roemer's full reconstruction algorithm (equation (11)) [38]. These results might be significantly different if the sample points were weighted to emphasize different sections of the structure or if different reconstruction algorithms were used to combine data from multiple coils.

VI. Conclusions

This work demonstrates that the GA can be used as a coil design tool to study rSNR characteristics for imaging applications of specific anatomic structures, where relative trends and tradeoffs of various coil configurations can be understood. Although GAs typically require large amounts of computing power, modifications can be made to decrease the parameter search space and improve the speed of RF coil GA optimizations. Cost functions for the GA coil optimization can be modified to include larger numbers of array elements as well as other interesting coil parameters such as g-factor and array element spacing for parallel imaging applications, as well as size, shape, and total number of elements in an array for optimal rSNR imaging.

The case studies presented in this work demonstrate important characteristics of various coil designs optimized to image specific anatomic structures, and provide answers to fundamental questions concerning the design of RF coils for MRI.

References

[1] M. Alecci, C. M. Collins, J. Wilson, W. Liu, M. B. Smith, and P. Jezzard, "Theoretical and experimental evaluation of detached endcaps for 3 T birdcage coils," *Magn. Reson. Med.,* vol. 49, no. 2, pp. 363 - 370, 2003.

[2] E. Atalar, P. A. Bottomley, O. Ocali, L. C. Correia, M. D. Kelemen, J. A. Lima, and E. A. Zerhouni, "High resolution intravascular MRI and MRS by using a catheter receiver coil," *Magn. Reson. Med*., vol. 36, no. 4, pp. 596 - 605, 1996.

[3] E. Atalar, P. A. Bottomley, and E. A. Zerhouni, *A Flexible Catheter Coil for Imaging and Spectroscopy of Atherosclerotic Plaques*, Nice, p. 988, 1995.

[4] L. Axel and C. Hayes, "Surface coil magnetic resonance imaging," *Arch. Inst. Physiol. Biochim.,* vol. 93, no. 5, pp. 11-18, 1985.

[5] F. Bernstein, G. Slavin, R. A. Day, F. Macaluso, and S. D. Wolff, *A Phased Array Coil Optimized for Carotid Artery Imaging*, Philadelphia, p. 163, 1999.

[6] D. Beyer, W. Steinbrich, G. Friedmann, and J. W. Ermers, "Use of surface coils in magnetic resonance imaging or orbit and knee," *Diagn. Imaging Clin. Med.,* vol. 55, no. 1-2, pp. 84 - 91, 1986.

[7] P. A. Bottomley, C. H. Lugo Olivieri, and R. Giaquinto, "What is the optimum phased array coil design for cardiac and torso magnetic resonance?," *Magn. Reson. Med*., vol. 37, no. 4, pp. 591 - 599, 1997.

[8] M. J. Chelsky, M. D. Schnall, E. J. Seidmon, and H. M. Pollack, "Use of endorectal surface coil magnetic resonance imaging for local staging of prostate cancer," *J. Urol,* vol. 150 (2 Pt 1), pp. 391 - 395, 1993.

[9] C. D. Constantinides, C. R. Westgate, W. G. O'Dell, E. A. Zerhouni, and E. R. McVeigh, "A phased array coil for human cardiac imaging," *Magn. Reson. Med.,* vol. 34, no. 1, pp. 92 - 98, 1995.

[10] J. A. de Zwart, P. J. Ledden, P. van Gelderen, J. Bodurka, R. Chu, and J. H. Duyn, "Signal-to-noise ratio and parallel imaging performance of a 16-channel receive-only brain coil array at 3.0 Tesla," *Magn. Reson. Med.,* vol. 51, no. 1, pp. 22 - 26, 2004.

[11] D. D. Do-Dai and R. A. Youngberg, "MRI of the hip with a shoulder surface coil in off-coronal plane," *J. Comput. Assist. Tomogr.,* vol. 19, no. 2, pp. 336 - 338, 1995.

[12] J. Doornbox, H. A. Grimbergen, P. E. Booijen, L. te Strake, J. L. Bloem, G. J. Vielvoye, and E. Boskamp, "Application of anatomically-shaped surface coils in MRI at 0.5 T.," *Magn. Reson. Med.,* vol. 3, no. 2, pp. 270-281, 1986.

[13] M. Erlichman, "Surface/specialty coil devices and gating techniques in magnetic resonance imaging," *Health Technol. Assess. Rep.,* vol. 3, pp. 1-23, 1990.

[14] A. Ettl, J. Kramer, A. Daxer, and L. Koornneef, "High resolution magnetic resonance imaging of neurovascular orbital anatomy," *Ophthalmology*, vol. 104, no. 5, pp. 869-877, 1997.

[15] T. H. Farmer, G. P. Cofer, and G. A. Johnson, "Maximizing contrast to noise with inductively coupled implanted coils," *Invest. Radiol.,* vol. 25, no. 5, pp. 552-558, 1990.

[16] S. H. Faro, S. Vinitski, H. V. Ortega, F. B. Mohamed, C. Y. Chen, A. E. Flanders, C. F. Gonzales, and R. A. Zimmerman, "Carotid magnetic resonance angiography: Improved image quality with dual 3-inch surface coils," *Neuroradiology*, vol. 38, no. 5, pp. 402-408, 1996.

[17] O. P. Gandhi and X. B. Chen, "Specific absorption rates and induced current densities for an anatomy-based model of the human for exposure to time-varying magnetic fields of MRI," *Magn. Reson. Med.,* vol. 41, no. 4, pp. 816-823, 1999.

[18] J. R. Hadley, B. E. Chapman, J. A. Roberts, D. C. Chapman, K. C. Goodrich, H. R. Buswell, A. L. Alexander, J. S. Tsuruda, and D. L. Parker, "A three-coil comparison for MR angiography," *J. Magn. Reson. Imaging,* vol. 11, no. 4, pp. 458-468, 2000.

[19] J. R. Hadley and D. L. Parker, *A Coil Coupling Model Model for Optimization Algorithms*, Toronto, Ontario, 2003.

[20] J. R. Hadley and D. L. Parker, "Relative RF coil performance in carotid imaging," *Magn. Reson. Imaging,* vol. 23, pp. 629-639, 2005.

[21] C. J. Hardy, P. A. Bottomley, K. W. Rohling, and P. B. Roemer, "An NMR phased array for human cardiac 31P spectroscopy," *Magn. Reson. Med.,* vol. 28, no. 1, pp. 54-64, 1992.

[22] C. E. Hayes, C. M. Mathis, and C. Yuan, "Surface coil phased arrays for high-resolution imaging of the carotid arteries," *J. Magn. Reson. Imaging*, vol. 6, no. 1, pp. 109-112, 1996.

[23] C. E. Hayes, J. S. Tsuruda, and C. M. Mathis, "Temporal lobes: Surface MR coil phased-array imaging," *Radiology*, vol. 189, no. 3, pp. 918-920, 1993.

[24] L. E. Hendrix, J. A. Strandt, D. L. Daniels, L. P. Mark, J. A. Borne, L. F. Czervionke, V. M. Haughton, and A. L. Williams, "Three-dimensional time-of-flight MR angiography with a surface coil: Evaluation in 12 subjects," *AJR Am. J. Roentgenol,* vol. 159, no. 1, pp. 103-106, 1992.

[25] N. Hosten and A. J. Lemke, "A special surface coil for high-resolution ocular MRI," *Front Radiat. Ther. Oncol.,* vol. 30, pp. 20-25, 1997.

[26] R. Jones, *Twelve Antenna Element Lower Extremity/Pelvic Array for MRI(A)*, Sydney, p. 440, 1998.

[27] R. Kier, R. J. Herfkens, R. A. Blinder, G. S. Leight, J. A. Utz, and P. M. Silverman, "MRI with surface coils for parathyroid tumors: Preliminary investigation," *AJR Am. J. Roentgenol.,* vol. 147, no. 3, pp. 497-500, 1986.

[28] J. H. A. Klinge, S. C. Davis, D. D. Gangahedkar, S. A. Lindsay, L. Blawat, and E. B. Boskamp, *An 8 Channel Cardiac SENSE Array*, Honolulu, p. 904, 2002.

[29] K. Y. Kojima, J. Szumowski, and R. C. Sheley, "Lower extremities: MR angiography with a unilateral telescopic phased-array coil," *Radiology*, vol. 196, pp. 871-875, 1995.

[30] M. E. Kooi, K. B. J. M Cleutjens, M. J. A. P. Daemen, P. J. E. H. M. Kitslaar, G. J. Kemerink, and J. M. A. van Engelshoven, *In-vivo and In-vitro MRI of the Carotid Artery Wall Using a Small Diameter Surface Coil*, Denver, p. 1657, 2000.

[31] J. F. Le Bas, M. Hassler, H. Reutenauer, M. Decorps, J. P. Camuset, G. Crouzet, and A. L. Benabid, "MRI of the cervical spine. Creation of a surface coil. Technical and clinical results," *J. Radiol.,* vol. 68, no. 10, pp. 579-586, 1987.

[32] A. Liffers, H. H. Quick, C. U. Herborn, H. Ermert, and M. E. Ladd, "Geometrical optimization of a phased array coil for high-resolution MR imaging of the carotid arteries," *Magn. Reson. Med*, vol. 50, no. 2, pp. 439-443, 2003.

[33] L. Malmgren, B. Geijer, S. Holtas, and F. Stahlbert, *A Two-Channel Phased Array Coil for MR-Angiography of the Extracranial Part of Carotid Artery*, Nice, p. 982, 1995.

[34] W. D. Middleton, S. Macrander, T. L. Lawson, J. B. Kneeland, J. D. Cates, G. M. Kellman, G. F. Carrera, W. D. Foley, A. Jesmanowicz, and J. S. Hyde, "High resolution surface coil magnetic resonance imaging of the joints: Anatomic correlation," *Radiographics*, vol. 7, no. 4, pp. 645-683, 1987.

[35] J. W. Monroe, P. Schmalbrock, and D. G. Spigos, "Phased array coils for upper extremity MRA," *Magn. Reson. Med.,* vol. 33, no. 2, pp. 224-229, 1995.

[36] J. R. Porter, S. M. Wright, and A. Reykowski, "A 16-element phased-array head coil," *Magn. Reson. Med.,* vol. 40, no. 2, pp. 272-279, 1998.

[37] M. Rivera, J. J. Vaquero, A. Santos, J. Ruiz-Cabello, and F. Del Pozo, "MRI visualization of small structures using improved surface coils," *Magn. Reson. Imaging*, vol. 16, no. 2, pp. 157-166, 1998.

[38] P. B. Roemer, W. A. Edelstein, C. E. Hayes, S. P. Souza, and O. M. Mueller, "The NMR phased array," *Magn. Reson. Med.,* vol. 16, no. 2, pp. 192-225, 1990.

[39] B. Roger, M. Laval-Jeantet, N. Delepine, G. Delepine, and F. Tobolski, "Magnetic resonance imaging of tumors of the knee using surface coils," *Rev. Chir. Orthop. Reparatrice Appar. Mot.,* vol. 72, no. 4, pp. 253-258, 1986.

[40] P. Schmalbrock, J. Pruski, L. Sun, A. Rao, and J. W. Monroe, "Phased array RF coils for high-resolution MRI of the inner ear and brain stem," *J. Comput. Assist. Tomogr.,* vol. 19, no. 1, pp. 8-14, 1995.

[41] M. Wiger, K. P. Pruessmann, C. Leussler, P. Roschmann, and P. Boesiger, "Specific coil design for SENSE: A six-element cardiac array," *Magn. Reson. Med.,* vol. 45, no. 3, pp. 495-504, 2001.

[42] R. M. Wilk, S. E. Harms, and L. M. Wolford, "Magnetic resonance imaging of the temporomandibular joint using a surface coil," *J. Oral Maxillofac. Surg.,* vol. 44, no. 12, pp. 935-943, 1986.

[43] M. L. Workman, M. Christensen, H. J. Griffiths and B. L. Cunningham, "Magnetic resonance imaging of the nose with surface coils: A new technique to evaluate functional and aesthetic problems," *Plast. Reconstr. Surg.,* vol. 91, no. 6, pp. 1154 - 1158, 1993.

[44] S. M. Wright and L. L. Wald, "Theory and application of array coils in MR spectroscopy," *NMR Biomed.,* vol. 10, no. 8, pp. 394 - 410, 1997.

[45] X. Zhang, K. Ugurbil, and W. Chen, "Microstrip RF surface coil design for extremely high-field MRI and spectroscopy," *Magn. Reson. Med.,* vol. 46, no. 3, pp. 443 - 450, 2001.

[46] R. A. Zimmerman, L. T. Bilaniuk, M. Yanoff, J. F. Schenck, H. R. Hart, T. H. Foster, W. A. Edelstein, P. A. Bottomley, R. W. Redington, and C. J. Hardy, "Orbital magnetic resonance imaging," *Am. J. Ophthalmol.,* vol. 100, no. 2, pp. 312-317, 1985.

[47] R. L. Haupt and S. E. Haupt, *Practical Genetic Algorithms*, John Wiley & Sons Inc., HoboKen, New Jersey, 2004.

[48] D. E. Goldbert, *Genetic Algorithms in Search, Optimization and Machine Learning*, Addison-Wesley, Reading, MA, 1989.

[49] L. Davis, *Handbook of Genetic Algorithms*, Van Nostrand Reinhold, New York, 1991.

[50] V. Cavaliere, A. Formisano, R. Martone, and M. Primizia, "A genetic algorithm approach to the design of split coil magnets for MRI," *IEEE T. Appl. Supercon,* vol. 10, no. 1, pp. 1376-1379, 2000.

[51] B. J. Fisher, N. Dillon, T. A. Carpenter, and L. D. Hall, "Design of a biplanar gradient coil using a genetic algorithm," *Magn. Reson. Imaging,* vol. 15, no. 3, pp. 369-376, 1997.

[52] D. Yau and S. Crozier, "A genetic algorithm/ method of moments approach to the optimization of an RF coil for MRI applications – theoretical considerations," *PIER (Progress in Electromagnetics Research),* vol. 39, pp. 177-192, 2003.

[53] P. Andris and I. Frollo, "Optimizationof NMR coils by genetic algorithms," *Measurement Science Review,* vol. 2, sec. 2, pp. 13-22, 2002.

[54] B. J. Fisher, N. Dillon, T. A. Carpenter, and L. D. Hall, "Design by genetic algorithm of a z gradient set for magnetic resonance imaging of the human brain," *Measurement Science and Technology,* vol. 6, pp. 904-909, 1995.

[55] N. Lu, J. Jin, E. Michielssen, and R. L. Magin, *Optimization of RF Coil Design Using Genetic*

Algorithm and Simulated Annealing Method, Nice, p. 1002, 1995.

[56] W. R. Smythe, *Static and Dynamic Electricity*, McGraw-Hill Book Company, New York, pp. 290-291, 1968.

[57] M. Misakian, "Equations for the magnetic field produced by one or more rectangular loops of wire in the same plane," *J. Res. Natl. Inst. Stan.,* vol. 105, no. 4, pp. 557-564, 2000.

[58] D. I. Hoult, "The principle of reciprocity in signal strength calculations – A mathematical guide," *Concepts in Magnetic Resonance*, vol. 12, no. 4, pp. 173-187, 2000.

[59] W. L. Stutzman and G. A. Thiele, *Antenna Theory and Design*, John Wiley & Sons Inc., New York, pp. 102-103, 1981.

[60] F. W. Grover, *Inductance Calculations: Working Formulas and Tables,* D. Van Nostrand Company Inc., New York, 1946.

[61] C. E. Hayes, N. Hattes, and P. B. Roemer, "Volume imaging with MR phased arrays," *Magn. Reson. Med,* vol. 18, no. 2, pp. 309-319, 1991.

[62] C. E. Hayes and P. B. Roemer, "Noise correlations in data simultaneously acquired from multiple surface coil arrays," *Magn. Reson. Med.,* vol. 16, no. 2, pp. 181-191, 1990.

[63] E. B. Boskamp, L. Blawat, K. F. King, J. Lorbiecki, and A. B. Tiwari, *A 16-Channel Neurovascular SENSE Array,* Honolulu, p. 852, 2002.

[64] D. J. Weyers and E. B. Boskamp, *An 8-Channel Volume RF Transmit Coil*, Honolulu, p. 901, 2002.

[65] R. F. Lee, R. O. Giaquinto, and C. J. Hardy, "Coupling and decoupling theory and its application to the MRI phased array," *Magn. Reson. Med.,* vol. 48, pp. 203-213, 2002.

[66] K. P. McGee, J. P. Debbins, E. B. Boskamp, L. Blawat, L. Angelos, and K. F. King, "Cardiac magnetic resonance parallel imaging at 3.0 Tesla: Technical feasibility and advantages," *J. Magn. Reson. Imaging*a, vol. 19, no. 3, pp. 291-297, 2004.

[67] G. R. Duensing, H. R. Brooker, and J. R. Fitzsimmons, "Maximizing signal-to-noise ratio in the presence of coil coupling," *J. Magn. Reson. B.,* vol. 111, no. 3, pp. 230-235.

[68] F. A. Breuer, M. Blaimer, M. F. Mueller, R. M. Heidemann, M. A. Griswold, and P. M. Jakob, *Finding the Optimal Sampling Pattern in 2D Parallel Imaging for a Given Receiver Coil Configuration,* Miami, Florida, Morning categorical course, 2005.

[69] M. A. Griswold, *RF Coils for Parallel Imaging*, Miami, Florida, Morning categorical course, 2005.

[70] N. Famili, S. M. Wright, and J. R. Porter, "MR flow measurement using RF phase gradients in receiver coil arrays," *IEEE Trans. Biomed. Eng.,* vol. 40, no. 12, pp. 1243-1249, 1993.

[71] S. M. Wright, R. L. Magin, and J. R. Kelton, "Arrays of mutually-coupled receiver coils: theory and application," *Magn. Reson. Med.,* vol. 17, no. 1, pp. 252-268, 1991.

[72] R. Pascone, T. Vullo, J. Farrelly, and P. T. Cahill, "Explicit treatment of mutual inductance in eight-solumn birdcage resonators," *Magn. Reson. Imaging*, vol. 10, no. 3, pp. 401-410, 1992.

[73] R. J. Pascone, B. J. Garcia, T. M. Fitzgerald, T. Vullo, R. Zipagan, and P. T. Cahill, "Generalized electrical analysis of low-pass and high-pass birdcage resonators," *Magn. Reson. Imaging*, vol. 9, no. 3, pp. 395-408, 1991.

[74] R. Pascone, T. Vullo, J. Farrelly, R. Mancuso, and P. T. Cahill, "Use of transmission line analysis for multi-tuning of birdcage resonators," *Magn. Reson. Imaging,* vol. 11, no. 5, pp. 705-715, 1993.

[75] T. J. Lawry, M. W. Weiner, and G. B. Matson, "Computer modeling of surface coil sensitivity," *Magn. Reson. Med.,* vol. 16, no. 2, pp. 294-302, 1990.

[76] J. Jin, G. Shen, and T. Perkins, "On the field inhomogeneity of a birdcage coil," *Magn. Reson. Med.,* vol. 32, no. 3, pp. 418-422, 1994.

[77] J. Jin, *Electromagnetic Analysis and Design in Magnetic Resonance Imaging,* CRC Press, Boca Raton, Florida, 1999.

[78] T. Vullo, R. Pascone, R. Mancuso, R. Zipagan, and P. T. Cahill, "Transmission line analysis of noncylindrical birdcage resonators," *Magn. Reson. Imaging,* vol. 12, no. 5, pp. 785-797, 1994.

[79] J. R. Hadley, *Design of Optimal Radio Frequency Coil Arrays for Magnetic Resonance Angiography*, Ph.D. Dissertation, Department of Electrical and Computer Engineering, University of Utah, Salt Lake City, UT, 2005.

Modeling of Ground-Penetrating Radar for Detecting Buried Objects in Dispersive Soils

K. P. Prokopidis and T. D. Tsiboukis

Applied and Computational Electromagnetics Laboratory,
Department of Electrical and Computer Engineering,
Aristotle University of Thessaloniki, Thessaloniki, GR 54124, Greece
E-mail: kprokopi@faraday.ee.auth.gr; tsibukis@auth.gr

Abstract – The detection of buried targets with ground-penetrating radars (GPRs) has been an issue of considerable attention during the last decades. In this paper, an efficient three-dimensional (3-D) time-domain numerical method is proposed for the simulation of GPR on dispersive soils. The soil is considered as an M-th order Debye medium with additional static conductivity and an unsplit-field perfectly matched layer (PML) is also presented to terminate such media. The radar unit is modeled with two transmitters and one receiver in order to eliminate undesired signals. The impact of radar frequency, soil parameters and object depth upon the ability to detect buried targets is investigated through several finite-difference time-domain (FDTD) simulations. The detection of multiple dielectric and conducting buried objects in stratified and inhomogeneous soils can be feasible through the tracing of the received energy of B-scan measurements in perpendicular linear paths.

Index Terms – Finite difference time domain (FDTD) method, ground-penetrating radar, dispersive media, perfectly matched layer.

I. INTRODUCTION

There is a growing interest in the propagation of transient electromagnetic signals through the earth and subsurface radar techniques for the detection and location of buried artifacts and structures within the upper regions of the earth's surface [1]-[6]. Ground-penetrating radar (GPR) has a wide range of applications such as geological mapping, object detection, and various archeological, civil and electrical engineering applications. The algorithm uses transmitting and receiving antennas placed near the earth's surface to probe the shallow subsurface. It is well known that at the GPR operating range (50-1000 MHz) soil is dispersive. More specifically, the dielectric constant and conductivity of the earth are functions of the excitation frequency.

The finite-difference time-domain (FDTD) method [7], [8] is inarguably one of the most successful second-order accurate schemes for electromagnetic time-domain simulations. Although the applicability of the original FDTD scheme is restricted to nondispersive media, a number of researchers have extended the conventional Yee's scheme to incorporate dispersive media. There are several techniques, like the recursive convolution (RC) [7], the auxiliary differential equation (ADE) scheme [8], the Z-transform (ZT) [9] and some alternative techniques [10]-[12] for handling dispersive media. An extensive survey of the FDTD methods for dispersive media is found in [13] and in the introduction of [4]. Among the previous techniques, we select a competent modification of the ADE approach [10] and introduce an unsplit-field perfectly matched layer (PML) which is used to terminate the computational domain.

Since the FDTD technique is very easy to implement, versatile and can handle any number and type of scatterers and soils, it has been extensively used to simulate GPR problems [2]-[6]. Usually, in the FDTD simulations, the soil is modeled as a dielectric with constant permittivity. In contrast, this paper presents a complete FDTD simulation with a practical radar configuration and introduces a number of simple techniques for the detection of dielectric and/or conducting buried targets in various realistic ground models.

II. FDTD/PML METHOD FOR THE DEBYE MODEL

Although the determination of the dielectric properties of earth materials remains largely experimental there is always the need of soil modeling. Experimental data indicate that dielectric behavior of wet snow, rocks, soils

This work was supported by IRAKLITOS – Fellowships for Research of A.U. Th. (under Grant 21765), partly funded by the E.U.

and even dry sand follows the Debye relaxation [1], [14]. This good fit to the Debye model with multiple poles is explained by the natural occurring of moisture in varying proportions everywhere in earth. The relative complex dielectric permittivity $\varepsilon_r(\omega)$ for the case of the M-th order Debye medium ($e^{j\omega t}$ time variation is assumed) is described by the following equation

$$\varepsilon_r(\omega) = \varepsilon_{r,\infty} + \sum_{p=1}^{M} \frac{\varepsilon_{r,sp} - \varepsilon_{r,\infty}}{1 + j\omega\tau_p} \tag{1}$$

where $\varepsilon_{r,sp}$, τ_p is the relative static permittivity and the relaxation time of the p pole, respectively, and $\varepsilon_{r,\infty}$ is the infinite relative permittivity usually determined to fit experimental data.

For the FDTD simulations we adopt the efficient technique of [10] and we propose a new PML formulation to terminate the simulation region. The modified Maxwell's equations inside the PML are written as,

$$\nabla \times \tilde{\mathbf{H}} = j\omega\varepsilon_0 \left[\frac{\sigma}{j\omega\varepsilon_0} + \varepsilon_r(\omega) \right] T \cdot \tilde{\mathbf{E}}, \tag{2}$$

$$\nabla \times \tilde{\mathbf{E}} = -j\omega\mu_0 T \cdot \tilde{\mathbf{H}}, \tag{3}$$

where the terminated medium is assumed to be dispersive with relative permittivity $\varepsilon_r(\omega)$ and additional static conductivity σ and $T = \text{diag}\{\zeta_x/(\zeta_y\zeta_z)$, $\zeta_y/(\zeta_z\zeta_x)$, $\zeta_z/(\zeta_x\zeta_y)\}$ is the diagonal "material" tensor of the PML conductivities. The tilde denotes that the fields are in the frequency domain. The stretching factors ζ_s are defined as $\zeta_s = 1/[\kappa_s + \sigma_s/(j\omega)]$, $s = x, y, z$ where κ_s and σ_s are spatially polynomial variables.

Ampere's law, equation (2), is written as

$$\nabla \times \tilde{\mathbf{H}} = \sigma T \cdot \tilde{\mathbf{E}} + j\omega\varepsilon_\infty T \cdot \tilde{\mathbf{E}} + j\omega \sum_{p=1}^{M} \tilde{\mathbf{Q}}_p \tag{4}$$

where $\varepsilon_\infty = \varepsilon_0\varepsilon_{r,\infty}$. The additional variable $\tilde{\mathbf{Q}}_p$ is defined as,

$$\tilde{\mathbf{Q}}_p = \frac{\varepsilon_{sp} - \varepsilon_\infty}{1 + j\omega\tau_p} T \cdot \tilde{\mathbf{E}} \tag{5}$$

with $\varepsilon_{sp} = \varepsilon_0\varepsilon_{r,sp}$. We also introduce variables $\tilde{\mathbf{R}} = T \cdot \tilde{\mathbf{E}}$ and equation (4) takes the following form

$$\nabla \times \tilde{\mathbf{H}} = \sigma\tilde{\mathbf{R}} + j\omega\varepsilon_\infty \tilde{\mathbf{R}} + j\omega \sum_{p=1}^{M} \tilde{\mathbf{Q}}_p. \tag{6}$$

We next transform equations (5) and (6) into the time domain and get

$$\mathbf{Q}_p + \tau_p \frac{d\mathbf{Q}_p}{dt} = (\varepsilon_{sp} - \varepsilon_\infty)\mathbf{R}, \tag{7}$$

$$\nabla \times \mathbf{H} = \sigma\mathbf{R} + \varepsilon_\infty \frac{d\mathbf{R}}{dt} + \sum_{p=1}^{M} \frac{d\mathbf{Q}_p}{dt}. \tag{8}$$

Equations (7) and (8) are approximated using finite differences and the update equations for the variables $\mathbf{Q}_p$ and $\mathbf{R}$ are

$$\mathbf{Q}_p^{n+1} = \frac{2\tau_p - \Delta t}{2\tau_p + \Delta t}\mathbf{Q}_p^n + \frac{(\varepsilon_{sp} - \varepsilon_\infty)\Delta t}{2\tau_p + \Delta t}\left(\mathbf{R}^{n+1} + \mathbf{R}^n\right), \tag{9}$$

$$\mathbf{R}^{n+1} = c_e\mathbf{R}^n + c_m(\nabla \times \mathbf{H})^{n+1/2} + 2c_m \sum_{p=1}^{M} \frac{1}{2\tau_p + \Delta t}\mathbf{Q}_p^n, \tag{10}$$

where Δt is the time step of the FDTD method and the coefficients c_e and c_m are given by

$$c_e = \frac{2\varepsilon_\infty - \sigma\Delta t - 2\sum_{p=1}^{M} \frac{(\varepsilon_{sp} - \varepsilon_\infty)\Delta t}{2\tau_p + \Delta t}}{2\varepsilon_\infty + \sigma\Delta t + 2\sum_{p=1}^{M} \frac{(\varepsilon_{sp} - \varepsilon_\infty)\Delta t}{2\tau_p + \Delta t}},$$
$$c_m = \frac{2\Delta t}{2\varepsilon_\infty + \sigma\Delta t + 2\sum_{p=1}^{M} \frac{(\varepsilon_{sp} - \varepsilon_\infty)\Delta t}{2\tau_p + \Delta t}}. \tag{11}$$

The x-component of the variable $\mathbf{R}$ is $\tilde{R}_x = \zeta_x/(\zeta_y\zeta_z)\tilde{E}_x$ and the update equation for E_x is obtained following the methodology of [15]. The FDTD/PML equations for the other electric and magnetic components can be extracted in the same fashion.

Since all explicit finite-difference schemes are conditionally stable, there is the need for the stability condition of the proposed formulation. The fields are expressed as [16]

$$\mathbf{F}^n = \mathbf{F}_0 Z^n e^{j(I\Delta x\tilde{k}_x + J\Delta y\tilde{k}_y + K\Delta z\tilde{k}_z)} \tag{12}$$

where $\mathbf{F}_0$ is a complex amplitude, indexes I, J, K denote the positions of the nodes in the FDTD grid, $\Delta\beta, (\beta = x, y, z)$ are the sizes of the FDTD cells, $\tilde{k}_\beta, (\beta = x, y, z)$ is the numerical wavenumber in the β-direction and Z is a complex variable. Such solutions are substituted into the difference equations and the characteristic polynomial is yielded (for the case of the one-pole Debye medium is a third-order polynomial). The condition for stability can be written as $|Z_i| \le 1$, where Z_i are the roots of the characteristic polynomial in Z. Since the characteristic polynomial is generally dependent on the Debye parameters, the maximum value of the time step Δt cannot be independently specified as it is with nondispersive media. Given the parameters of the medium and $\Delta\beta$, the selection of Δt is tested by numerically finding the roots of the characteristic polynomial. For the case of the one-pole Debye medium, the stability criterion of the proposed scheme can be expressed as

$$\Delta t \le \frac{1}{c_\infty}\left(\sum_{\beta=x,y,z}\frac{1}{(\Delta\beta)^2}\right)^{-1/2} \quad (13)$$

where $c_\infty = 1/\sqrt{\mu\varepsilon_\infty}$ on condition that $\varepsilon_s \ge \varepsilon_\infty$.

III. SOIL PARAMETERS AND RADAR UNIT

In this paper, the radar unit consists of two identical transmitters (T_1 and T_2) and one receiver (R), called transmitter-receiver-transmitter (TRT) configuration [5], illustrated in Fig. 1. The two alike transmitters, modeled as small electric dipoles aligned at z-axis, are fed 180° out of phase and the receiver is located equidistantly between them. The receiver is implemented as a small dipole which samples and stores the z-component of the electric field at a specific Yee cell. Due to this configuration, the two direct signals D_1 and D_2 are mutually cancelled at the receiver R. Similarly, the two reflected signals G_1 and G_2 are subtracted at the same symmetry plane and they do not contribute to the signal received by the receiver. Finally, the signal collected by the receiver is solely due to the scatterers buried in the ground. Using this configuration, we separate the desired scattered signal $S_1 + S_2$, which is generally weak, from the direct and the reflected from the ground signal, rendering thus, the buried-object detection procedure possible.

An A-scan is performed when the radar unit is

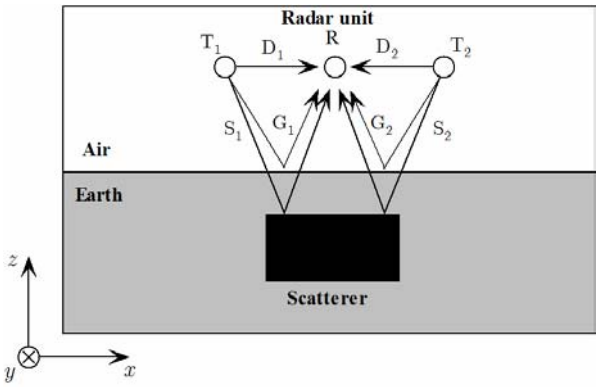

Fig. 1. The TRT configuration of the radar unit with the direct (D_1 and D_2), the reflected (G_1 and G_2), and the scattered (S_1 and S_2) signals depicted.

stationary and the receiver collects data for a time period. When the radar unit travels along a linear path performing repeated A-scan measurements at discrete points above the ground, this is called B-scan [5]. For our simulations the radar unit moves in a linear path performing B-scan simulations. The fields are excited using hard sources at the points of the two transmitters. The time variation of the source is given by $f(n) = e^{-a[(n-b)\Delta t]^2}\cos(2\pi f_c\, n\Delta t)$, where $b = 512$, $a = 16/(\beta\Delta t)^2$, f_c the excitation frequency and n denotes the time step.

IV. NUMERICAL RESULTS

In our FDTD simulations, the Yee cell sizes are selected to be $\Delta = \Delta x = \Delta y = \Delta z = 5\,\text{cm}$ and the time step $\Delta t = 38.516\,\text{psec}$, in order to ensure the stability. The size of the computational domain is $60 \times 60 \times 30$ Yee cells and is truncated with an 8-cell PML described in previous section. The transmitting and receiving antennas are arranged as shown in Fig. 1 and are separated by two cells (10 cm). The radar unit is moving in straight lines and is located 10 cm above the ground surface. We assume three Puerto Rico clay loams modeled with Debye dispersion with parameters listed in Table I [4]. The soil occupies the first 20 cells of the vertical height of the simulation region.

Table I. Model parameters for Puerto Rico clay loams.

Moisture (%)	$\varepsilon_{r,\infty}$	σ (mS/m)	τ_1 (nsec)	τ_2 (nsec)	$\varepsilon_{r,s1}$	$\varepsilon_{r,s2}$
2.5	3.20	0.397	2.71	0.108	3.95	3.50
5.0	4.15	1.110	3.79	0.151	5.95	4.75
10.0	6.00	2.000	3.98	0.251	8.75	6.75

We assume two cubic scatterers: a perfectly electric conductor (PEC) and a dielectric one with permittivity $8\varepsilon_0$. The PEC and the dielectric targets of sizes $5\Delta\times5\Delta\times5\Delta$ and $4\Delta\times4\Delta\times4\Delta$ are buried 4Δ and 5Δ under the ground-air interface, respectively and are separated by 6Δ. In Fig. 2 the electric field at the receiver is depicted when one scatterer, both scatterers and no scatterers are present. The scatterers are buried in 2.5 % moisture soil with parameters taken from Table I. It is obvious, as expected, that the received signal is solely due to buried objects.

In the following, we show two FDTD snapshots of the x-component of the electric field for the TRT radar model above earth modeled with two different Debye media for the aforementioned scenario of the two scatterers. The central frequency of excitation is 200 MHz. In Fig. 3 (a) the earth is modeled with the Debye model of 2.5 % moisture while in Fig. 3 (b) with the 5 % moisture. We can observe the wave propagation in free space and dispersive soil and the scattering from the two targets.

Since the detection of buried targets is performed

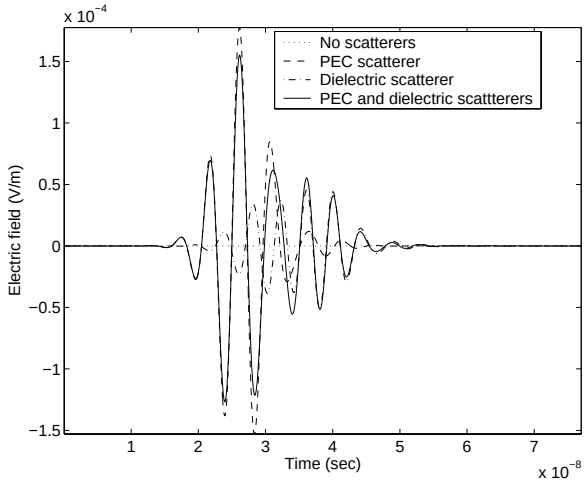

Fig. 2. The electric field at the receiver of a TRT radar as a function of time for different subsurface scenarios (A-scan).

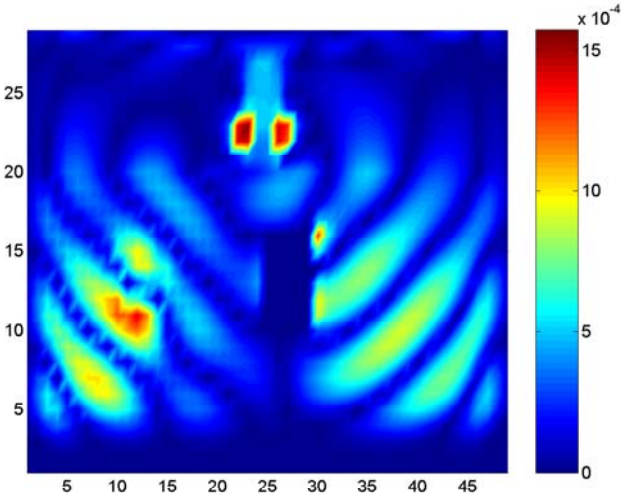

(a)

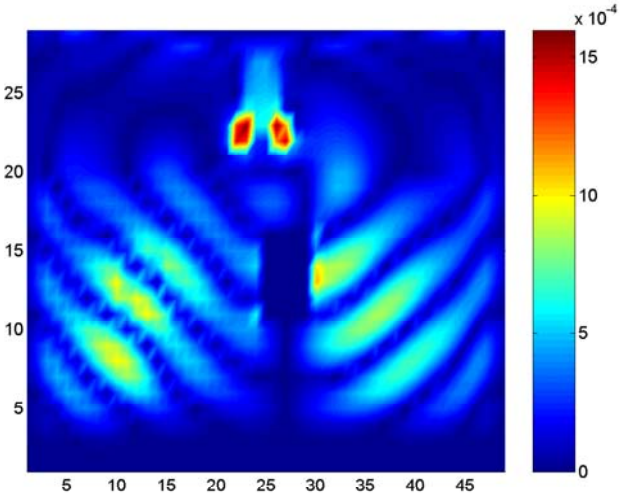

(b)

Fig. 3. Snapshots of the amplitude of the x-component of the electric field. The ground is modeled with Debye medium of (a) 2.5 % and (b) 5 % moisture.

through the received energy due to the presence of the scatterers, we estimate the scattered energy collected by the receiver in an A-scan, as $\mathcal{E} = \sum_n |E^n|^2$, where E^n is the n-th time sample of the corresponding electric field at that A-scan location.

A. *Effect of Frequency*

In order to investigate the effect of excitation frequency upon the operation of the GPR, we assume the aforementioned scenario with the Puerto Rico clay loam of 2.5 % moisture. We perform two simulations: (a) with $f_c = 200\,\text{MHz}$ and (b) with $f_c = 400\,\text{MHz}$ whereas the corresponding energy of the excitation functions is calculated as $\mathcal{E}_{t1} = 80.212$ and $\mathcal{E}_{t2} = 80.212$ (the energies are almost equal due to the value of the parameter b). Each A-scan is normalized with its own maximum and individually plotted in Figs 4 (a) and 4 (b) and form the B-scan plot which is a function of the position of the radar unit (vertical axis) and time (horizontal axis). In Figs 4 (a) and 4 (b), the energies of the A-scans waveforms are depicted as a function of the radar position (vertical axis). The maximum energy collected by the receiver is $\mathcal{E}_{r1} = 85.281$ and $\mathcal{E}_{r2} = 102.123$. The ratios of the received to the transmitted energy for the two frequencies are 1.063 and 1.273, respectively. So, the PEC target is better detected if excitation frequency is $f_c = 400\,\text{MHz}$, although the position of the dielectric target is not very clear for this case. We also remark that the energy peak for the conducting target is greater than that of the dielectric as expected.

B. *Effect of Soil Parameters and Object Depth*

Usually, there is great difficulty in accurate prediction of the electromagnetic propagation behavior of the ground due to the variability of the material parameters and local geological conditions encountered in real life. We now perform another set of numerical simulations in which the parameters of the ground are that of the Puerto Rico clay loam with 5 % moisture (Table I) which describes a wet earth, to investigate the effect of soil parameters. Fig. 5 (a) shows the same scenario as in the previous subsection but in another soil background (with 5 % moisture) for $f_c = 400\,\text{MHz}$. The ratio of the collected to the transmitted energy is now 1.045. In Fig. 5 (b), the excitation frequency is 200 MHz, while the ratio is 0.996. We observe that using a higher frequency (400 MHz) we get 1.05 times more energy (Figs 5 (a) and 5 (b)) for the 5 % moisture model, whereas for the 2.5 % moisture model we obtain 1.2 (Figs 4 (a) and 4 (b)). This is due to the fact that the 5 % moisture soil model

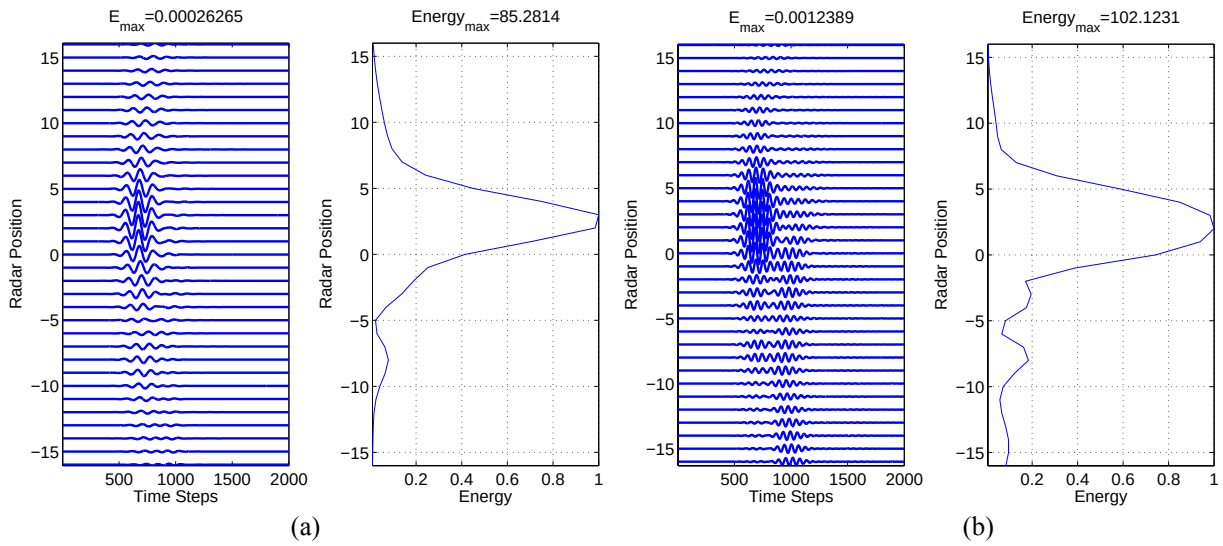

Fig. 4. Simulations results (B-scan and collected energy) of two scatterers (one PEC and one dielectric) buried 20 cm and 25 cm, respectively, under the ground and separated by 30 cm with excitation frequency (a) $f_c = 200\,\text{MHz}$, (b) $f_c = 400\,\text{MHz}$. The earth is a Puerto Rico clay loam with 2.5 % moisture.

containing more moisture than the 2.5 % causes greater attenuation to the scattered energy collected by the receiver. At a given frequency, wet materials exhibit higher dielectric losses than dry ones.

We next consider that the dielectric scatterer is smaller (of size $2\Delta \times 2\Delta \times 2\Delta$) and is buried 7Δ under the surface. The corresponding B-scan results are depicted in Fig. 5 (c). One may note that the dielectric scatterer is, now, invisible to the radar, since the collected energy is practically zero. Obviously, the scattered energy from the dielectric target is very weak due to the attenuation of the wet soil. It is to be stressed that in many practical applications, the GPR results are inconclusive because of the significant attenuation caused by the dispersive soil. Such problems can usually be solved with a proper frequency selection. Additionally, it is not plain to predict, before the FDTD simulation, which frequency is suitable, leads to less dielectric losses and to clear subsurface image.

C. *Multiple Target Detection in Stratified Soil*

One of the important goals of the GPR applications is to image metallic, dielectric scatterers and cavities in the near subsurface. We now assume a scenario with two perfectly conducting scatterers of sizes $3\Delta \times 3\Delta \times 3\Delta$ buried 4Δ under the ground. The earth model is assumed to be inhomogeneous and consists of a 25 cm thick layer of Puerto Rico clay loam with 5 % moisture near the surface and the rest of a 10 % moisture soil (with parameters listed in Table I). The locations of the targets are illustrated in Fig. 6. Two linear, perpendicular paths (linear paths A and B in Fig. 6) are regarded. We perform B-scans upon the prementioned linear paths and the results are demonstrated in Figs 7 (a) and 7 (b). The maxima in the plots correspond to the energy scattered by the two targets, while the energy magnitudes are generally functions of the sizes, locations, depths and constitutive properties of the scatterers. Since in the examined scenario, the targets are the same in size and dielectric properties and are buried in the same depth, the energy peaks just indicate their locations. The prescribed procedure serves as a simple algorithm for the detection of buried targets and if combined with other measurements or calculations can provide an accurate subsurface image.

D. *Target Detection in Inhomogeneous Soil*

We now assume a more realistic scenario of earth model considering 50 small dielectric scatterers with permittivity $8\varepsilon_0$ of sizes and positions selected randomly embedded in a 2.5 % moisture soil background. The maximum size of the dielectric scatterers is $5\Delta \times 5\Delta \times 5\Delta$ and the excitation frequency is 200 MHz. A PEC target of size $5\Delta \times 5\Delta \times 5\Delta$ is buried 4Δ deep as shown in Fig. 8 (a). The maximum of the collected energy in Fig 8 (b) is due to PEC scatterer (this can be extracted by comparisons with previous B-scan simulations where the PEC scatterer was in the same position) although the

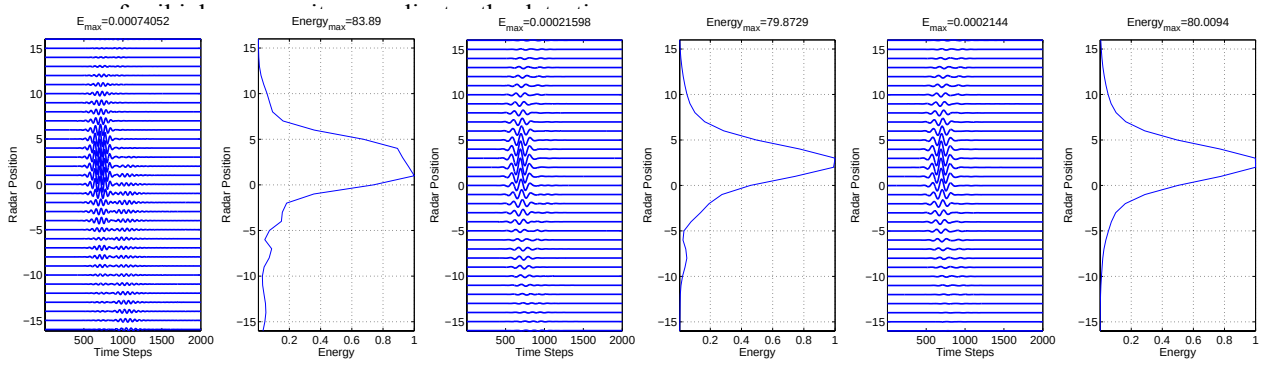

Fig. 5. Simulations results (B-scan and collected energy) of two scatterers (one PEC and one dielectric) (a), (b) buried 20 cm and 25 cm, respectively, under the ground and separated by 30 cm and (c) buried 20 cm and 35 cm, respectively, under the ground and separated by 40 cm with excitation frequency (a) $f_c = 400\,\text{MHz}$ and (b), (c) $f_c = 200\,\text{MHz}$. The earth is a Puerto Rico clay loam with 5.0 % moisture.

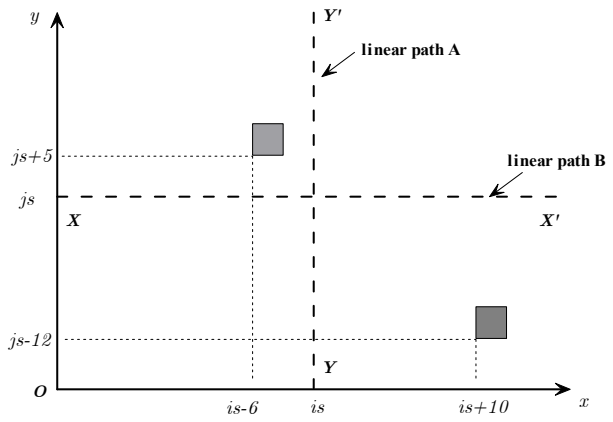

Fig. 6. Subsurface model with two perfectly electric conducting scatterers.

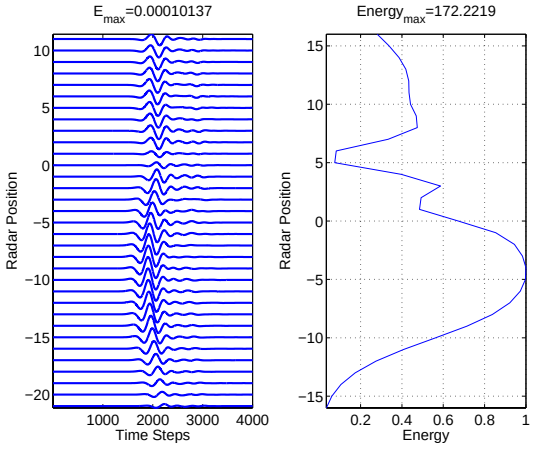

Fig. 7. Simulations results (B-scan and collected energy) of two perfectly electric conducting scatterers buried 4 cells under the ground: (a) linear path A and (b) linear path B.

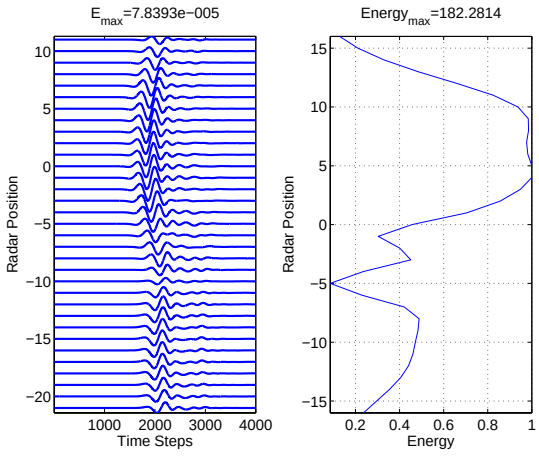

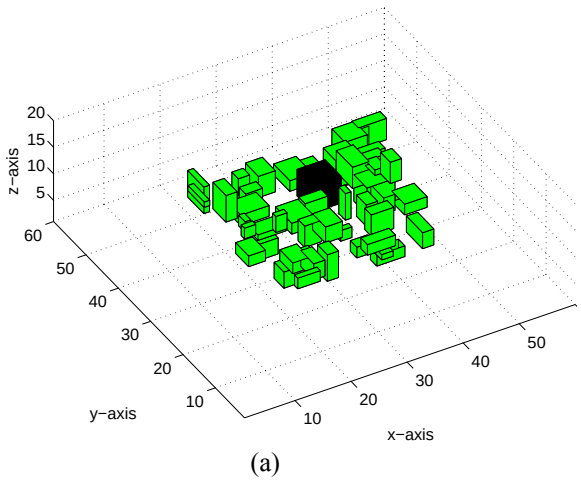

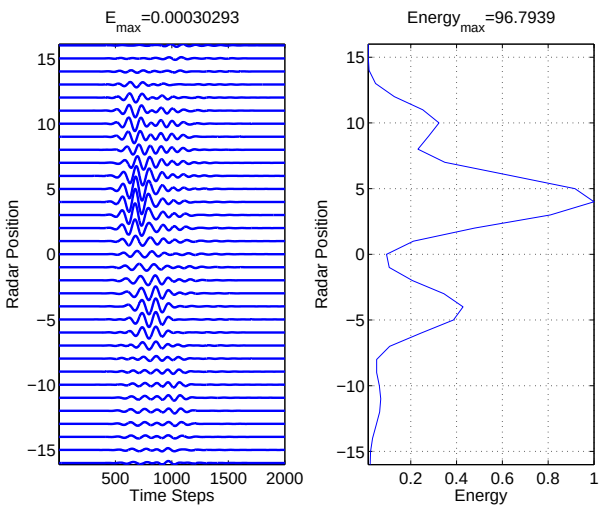

(b)

Fig. 8. (a) Inhomogeneous earth model (the PEC target and the dielectric scatterers are depicted) and (b) simulation results (B-scan and collected energy) for the inhomogeneous earth model with excitation frequency $f_c = 200\,\mathrm{MHz}$.

V. CONCLUSIONS

The application and importance of the realistic ground model in the 3-D FDTD simulations of GPR scenarios are presented. The earth is modeled as a Debye medium with two poles and static conductivity and an efficient FDTD scheme is used to simulate the wave propagation inside stratified and inhomogeneous dispersive soils. An unsplit-field PML is also proposed for the termination of the computational domain and its effectiveness and accuracy is proved in numerous GPR problems with different (PEC or dielectric) targets and soil parameters. The effect of the excitation frequency upon the ability to detect buried objects is studied and the difficulty to recognize dielectric targets is discussed. The simulation results show that the detection of metal and dielectric buried objects is possible through the collected energy at the receiver and a simple and efficient algorithm is also introduced for the detection of multiple targets. The FDTD/PML technique presented in this paper provides a vigorous and effortless method for accurate GPR simulations and facilitate the analysis and design of GPR systems.

REFERENCES

[1] D. J. Daniels, *Surface-Penetrating Radar*, London, UK: IEE, 1996.

[2] J. M. Bourgeois and G. S. Smith, "A fully three-dimensional simulation of a ground-penetrating radar: FDTD theory compared with experiment," *IEEE Trans. Geosci. Remote Sensing*, vol. 34, pp. 36-44, Jan. 1996.

[3] T. Bergmann, J. O. A. Robertsson, and K. Holliger, "Finite-difference modeling of electromagnetic wave propagation in dispersive and attenuating media," *Geophysics*, vol. 63, pp. 856-867, May-June 1998.

[4] F. L. Teixeira, W. C. Chew, M. Straka, M. L. Oristaglio, and T. Wang, "Finite-difference time-domain simulation of ground penetrating radar on dispersive, inhomogeneous, and conductive soils," *IEEE Trans. Geosci. Remote Sensing*, vol. 36, pp. 1928-1937, Nov. 1998.

[5] L. Gurel and U. Oguz, "Three-dimensional FDTD modeling of a ground-penetrating radar," *IEEE Trans. Geosci. Remote Sensing*, vol. 38, pp. 1513-1521, July 2000.

[6] D. Uduwawala, M. Norgren, and P. Fuks, "A complete FDTD simulation of a real GPR antenna system operating above lossy and dispersive grounds," *Progress in Electromagnetics Research*, vol. 50, pp. 209-229, 2005.

[7] K. Kunz and R. Luebbers, *The Finite Difference Time Domain Method for Electromagnetics*, Boca Raton, FL: CRC, 1993

[8] A. Taflove and S. C. Hagness, *Computational Electrodynamics: The Finite-Difference Time-Domain Method*, Norwood, MA: Artech House, 2000.

[9] D. M. Sullivan, "Frequency-dependent FDTD methods using Z transforms," *IEEE Trans. Antennas Propagat.*, vol. 40, pp. 1223-1230, Oct. 1992.

[10] Y. Takayama and W. Klaus, "Reinterpretation of the Auxiliary Differential Equation method for FDTD," *IEEE Microw. Wireless Components Lett.*, vol. 12, pp. 102-104, Mar. 2002.

[11] J. A. Pereda, A. Vegas, and A. Prieto, "FDTD modeling of wave propagation in dispersive media by using the Mobius transformation technique," *IEEE Trans. Microw. Theory Tech.*, vol. 50, pp. 1689-1695, July 2002.

[12] K. P. Prokopidis, E. P. Kosmidou, and T. D. Tsiboukis, "An FDTD algorithm for wave propagation in dispersive media using higher-order schemes," *J. Electromagn. Waves Applicat.*, vol. 18, pp. 1171-1194, 2004.

[13] J. L. Young and R. O. Nelson, "A summary and systematic analysis of FDTD algorithms for linearly dispersive media," *IEEE Antennas Propagat. Mag.*, vol. 43, pp. 61-77, Feb. 2001.

[14] C. Matzler, "Microwave permittivity of dry sand," *IEEE Trans. Geosci. Remote Sensing*, vol. 36, pp. 317-319, Jan. 1998.

[15] S. D. Gedney, "An anisotropic perfectly matched layer-absorbing medium for the truncation of FDTD lattices," *IEEE Trans. Antennas Propagat.*, vol. 44, pp. 1630-1639, Dec. 1996.

[16] J. A. Pereda, L. A. Vielva, A. Vegas, and A. Prieto, "Analyzing the stability of the FDTD technique by combining the von Neumann method with Routh-Hurwitz criterion," *IEEE Trans. Microw. Theory Tech.*, vol. 49, pp. 377-381, Feb. 2001.

Konstantinos P. Prokopidis was born in Florina, Greece, on August 10, 1976. He received his Diploma Degree from the Department of Electrical and Computer Engineering (DECE), Aristotle University of Thessaloniki (A.U.Th.), Thessaloniki, Greece in 1999. From 2000 to 2001 he served as sergeant in the Hellenic Army (infantry). In 2001 he joined the Applied and Computational Electromagnetics Laboratory of the DECE, A.U.Th, where he is now pursuing his Ph. D. Degree. His research interests focus on finite difference time domain method, perfectly matched layers, higher-order schemes, dispersive media, antenna design, and signal processing. He is the recipient of a number of scholarship distinctions, including Technical Chamber of Greece Award and IRAKLITOS-Fellowship of research of the A.U.Th. Mr. Prokopidis is a member of the Technical Chamber of Greece and the Applied Computational Electromagnetics Society.

Theodoros D. Tsiboukis received the Diploma Degree in Electrical and Mechanical Engineering from the National Technical University of Athens, Greece, in 1971 and the Doctor Engineer Degree from the Aristotle University of Thessaloniki (A.U.Th.), Greece, in 1981. From 1981 to 1982, he joined the Electrical Engineering Department of the University of Southampton, England, as a senior research fellow. Since 1982 he has been working at the Department of Electrical and Computer Engineering (DECE) of the A.U.Th., where he is now a Professor. His main research interests include electromagnetic field analysis by energy methods, computational electromagnetics (FEM, BEM, Vector Finite Elements, MoM, FDTD, ABCs), inverse and EMC problems. He has authored or co-authored 6 books, more than 115 refereed journal articles, and more than 100 international conference papers. Prof. Tsiboukis was the Guest Editor of a special issue of the International Journal of Theoretical Electrotechnics (1996) and the Chairman of the local organizing committee of the 8th International Symposium on Theoretical Electrical Engineering (1995). He has served in many administrative positions, including Director of the Division of Telecommunications at the DECE (1993-1998) and Chairman of the DECE (1997-1998). Prof. Tsiboukis was awarded several distinctions and is member of various societies, associations, chambers and institutions.

Inverse Scattering of Inhomogeneous Dielectric Cylinders Buried in a Slab Medium by TE Wave Illumination

C. H. Huang, C. C. Chiu, C. J. Lin, and Y. F. Chen

Electrical Engineering Department, Tamkang University
Tamsui, Taipei, R.O.C.

Abstract **–** The inverse scattering of inhomogeneous dielectric cylinders buried in a slab medium by transverse electric (TE) wave illumination is investigated. Dielectric cylinders of unknown permittivities are buried in second space and scattered a group of unrelated waves incident from first space where the scattered field is recorded. By proper arrangement of the various unrelated incident fields, the difficulties of ill-posedness and nonlinearity are circumvented, and the permittivity distribution can be reconstructed through simple matrix operations. The algorithm is based on the moment method and the unrelated illumination method. Numerical results are given to demonstrate the capability of the inverse algorithm. Good reconstruction is obtained even in the presence of additive Gaussian random noise in measured data. In addition, the effect of noise on the reconstruction result is also investigated.

I. INTRODUCTION

In the last few years, inverse scattering problems of objects buried in slab medium have been a growing importance in many different fields of applied science, with a large potential impact on geosciences and remote sensing applications. Typical examples are the detection of water pipes buried in the wall, power and communication cables buried in the wall, archaeological remains and so on. However, the solutions are considerably more difficult than those involving objects in free space or a half space. This is due to the interaction between the air-earth interface and the object, which leads to the complicated Green's function for this three layer problem. Most microwave inverse scattering algorithms developed are for TM wave illuminations in which the vectorial problem can be simplified to a scalar one [1 - 10]. On the other hand, much fewer works have been reported on the more complicated TE case [11 - 17]. In the TE wave excitation case, the presence of polarization charges makes the inverse problem more nonlinear. As a result, the reconstruction becomes more difficult. However, the TE polarization case is useful because it provides additional information about the object. To the best of our knowledge, in TE case, there is still no investigation on the inverse scattering of inhomogeneous dielectric cylinders buried in a slab medium by unrelated illumination method.

In this paper, the inverse scattering of inhomogeneous dielectric cylinders buried in a slab medium by TE wave illumination is investigated. An efficient algorithm is proposed to reconstruct the permittivity distribution of the objects by using only the scattered field measured outside. The algorithm is based on the unrelated illumination method [9], [13], [15 - 16]. In section II, the theoretical formulation for electromagnetic inverse scattering is presented. Numerical results for objects of different permittivity distributions are given in section III. Finally, conclusions are drawn in section IV.

II. THEORETICAL FORMULATION

Let us consider dielectric cylinders buried in a lossless homogeneous half-space as shown in Fig. 1.

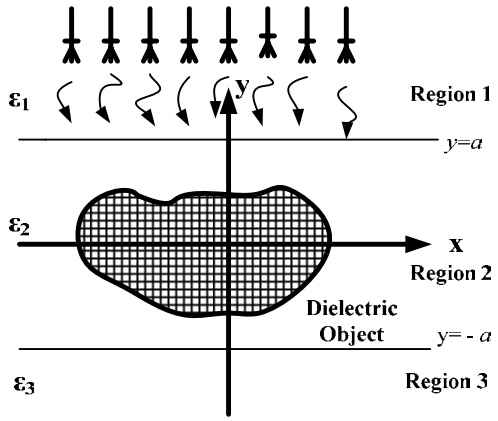

Fig. 1. Geometry of problem in the x-y plane.

$(\varepsilon_i, \sigma_i)$ $i = 1, 2, 3,$ denote the permittivities and conductivities in each region. The permeability is μ_0 for all material including the scatterers. The axis of the buried cylinder is the z-axis; that is, the properties of the scatterer may vary with the transverse coordinates only. A group of unrelated incident wave with magnetic field parallel to the z-axis (i.e., transverse electric, or TE, polarization) is illuminated upon the scatterers.

Owing to the interface, the incident plane wave

generates three waves that would exist in the absence of the conducting object. Let the unperturbed field be represented by

$$\vec{E}^i(x,y)=\begin{cases}\left(E_x^i\right)_1(x,y)\hat{x}+\left(E_y^i\right)_1(x,y)\hat{y}, & y\ge a,\\ \left(E_x^i\right)_2(x,y)\hat{x}+\left(E_y^i\right)_2(x,y)\hat{y}, & a>y>-a,\\ \left(E_x^i\right)_3(x,y)\hat{x}+\left(E_y^i\right)_3(x,y)\hat{y}, & y\le -a.\end{cases} \tag{1}$$

Using the vector potential techniques, the internal total electric field defined as

$$\vec{E}(x,y)=E_x(x,y)\hat{x}+E_y(x,y)\hat{y}=(E_x^i+E_x^s)\hat{x}+(E_y^i+E_y^s)\hat{y}$$

and the external scattered field,

$$\vec{E}^s(x,y)=E_x^s(x,y)\hat{x}+E_y^s(x,y)\hat{y}$$

can be expressed by the following equations,

$$E_x(\vec{r})=-\left(\frac{\partial^2}{\partial x^2}+k_2^2\right)\left[\int_s G(\vec{r},\vec{r}')(\varepsilon_1(\vec{r}')-1)E_x(\vec{r}')ds'\right]$$
$$-\frac{\partial^2}{\partial x\partial y}\left[\int_s G(\vec{r},\vec{r}')(\varepsilon_2(\vec{r}')-1)E_y(\vec{r}')ds'\right]+E_x^i(\vec{r}), \tag{2}$$

$$E_y(\vec{r})=-\frac{\partial^2}{\partial x\partial y}\left[\int_s G(\vec{r},\vec{r}')(\varepsilon_1(\vec{r}')-1)E_x(\vec{r}')ds'\right]$$
$$-\left(\frac{\partial^2}{\partial y^2}+k_2^2\right)\left[\int_s G(\vec{r},\vec{r}')(\varepsilon_2(\vec{r}')-1)E_y(\vec{r}')ds'\right]+E_y^i(\vec{r}), \tag{3}$$

$$E_x^s(\vec{r})=-\left(\frac{\partial^2}{\partial x^2}+k_2^2\right)\left[\int_s G(\vec{r},\vec{r}')(\varepsilon_1(\vec{r}')-1)E_x(\vec{r}')ds'\right]$$
$$-\frac{\partial^2}{\partial x\partial y}\left[\int_s G(\vec{r},\vec{r}')(\varepsilon_2(\vec{r}')-1)E_y(\vec{r}')ds'\right], \tag{4}$$

$$E_y^s(\vec{r})=-\frac{\partial^2}{\partial x\partial y}\left[\int_s G(\vec{r},\vec{r}')(\varepsilon_1(\vec{r}')-1)E_x(\vec{r}')ds'\right]$$
$$-\left(\frac{\partial^2}{\partial y^2}+k_2^2\right)\left[\int_s G(\vec{r},\vec{r}')(\varepsilon_2(\vec{r}')-1)E_y(\vec{r}')ds'\right], \tag{5}$$

with

$$G(x,y;x',y')=\begin{cases}G_{1s}(x,y:x',y'), & y\ge a,\\ G_{2s}(x,y;x',y'), & -a<y<a,\\ G_{3s}(x,y;x',y'), & y\le -a,\end{cases} \tag{6a}$$

$$G_{1s}(x,y;x',y')=\frac{1}{2\pi}\int_{-\infty}^{\infty}je^{-j\gamma_1(y-a)}$$
$$\frac{\left(\left(\gamma_2+\gamma_3\right)e^{j\gamma_2(y'+a)}+\left(\gamma_2-\gamma_3\right)e^{-j\gamma_2(y'+a)}\right)\times e^{-j\alpha(x-x')}}{\left(\gamma_1+\gamma_2\right)\left(\gamma_2+\gamma_3\right)e^{j\gamma_2(2a)}+\left(\gamma_1-\gamma_2\right)\left(\gamma_2-\gamma_3\right)e^{-j\gamma_2(2a)}}d\alpha, \tag{6b}$$

$$G_{2s}(x,y;x',y')=G_{2sf}(x,y;x',y')+G_{2ss}(x,y;x',y'), \tag{6c}$$

$$G_{3s}(x,y;x',y')=\frac{1}{2\pi}\int_{-\infty}^{\infty}je^{j\gamma_1(y+a)}$$
$$\frac{\left(\left(\gamma_1+\gamma_2\right)e^{-j\gamma_2(y'-a)}+\left(\gamma_2-\gamma_1\right)e^{j\gamma_2(y'-a)}\right)\times e^{-j\alpha(x-x')}}{\left(\gamma_1+\gamma_2\right)\left(\gamma_2+\gamma_3\right)e^{j\gamma_2(2a)}+\left(\gamma_1-\gamma_2\right)\left(\gamma_2-\gamma_3\right)e^{-j\gamma_2(2a)}}d\alpha, \tag{6d}$$

where

$$G_{2sf}(x,y;x',y')=\frac{j}{4}H_0^{(2)}\left(k_2\sqrt{(x-x')^2+(y-y')^2}\right),$$

$$G_{2ss}(x,y,x',y')=$$
$$\frac{1}{2\pi}\times\int_{-\infty}^{\infty}\frac{je^{-j\alpha(x-x')}}{2r_2}\left\{\left[\frac{(r_2-r_1)(r_2-r_3)\left[e^{-jr_2\left[|y-y'|+2a\right]}+e^{jr_2\left[|y-y'|-2a\right]}\right]}{(r_1+r_2)(r_2+r_3)e^{jr_2(2a)}+(r_1-r_2)(r_2-r_3)e^{-jr_2(2a)}}\right]\right.$$
$$\left.+\left[\frac{(r_2-r_1)(r_2+r_3)e^{jr_2\left(y+y'\right)}+(r_2-r_3)(r_1+r_2)e^{-jr_2\left(y+y'\right)}}{(r_1+r_2)(r_2+r_3)e^{jr_2(2a)}+(r_1-r_2)(r_2-r_3)e^{-jr_2(2a)}}\right]\right\}d\alpha$$

$\gamma_i^2=k_i^2-\alpha^2$, $i=1,\ 2,\ 3$, $\mathrm{Im}(r_i)\le 0$, $-a<y'<a$.

Here, k_i denotes the wave number in region i and ε_r is the relative permittivity of the dielectric objects. $G(x,y;x',y')$ is the Green's function, which can be obtained by the Fourier transform [18]. For numerical implementation of Green's function, we might face some difficulties in calculating this function. This Green's function is in the form of an improper integral, which must be evaluated numerically. However, the integral converges very slowly when (x,y) and (x',y') approach the interface $y=a$. Fortunately we find that the integral in G_{1s}, G_{2s}, and G_{3s} may be rewritten as a closed-form term plus a rapidly converging integral [2]. Thus, the whole integral in the Green's function can be calculated efficiently.

The direct scattering problem is to calculate the scattered field $\vec{E}^s$ in region 1, while the permittivity distribution of the buried objects is given. This can be achieved by first solving the total field $\vec{E}$ in equations (2) and (3) as well as calculating $\vec{E}^s$ in equations (4) and (5). For numerical implementation of the direct problem, the dielectric objects are divided into *N* sufficient small cells. Thus the permittivity and the total field within each cell can be taken as constants. Then the moment method is used to solve equations (2) to (5) with a pulse basis function for expansion and point matching for testing [19]. Equations (2) to (5) can then be transformed into a matrix form

$$\begin{pmatrix}E_x^i\\ E_y^i\end{pmatrix}=\left\{\begin{bmatrix}[G_1] & [G_2]\\ [G_2] & [G_3]\end{bmatrix}\begin{bmatrix}[\tau] & 0\\ 0 & [\tau]\end{bmatrix}+\begin{bmatrix}[I] & 0\\ 0 & [I]\end{bmatrix}\right\}\begin{pmatrix}E_x\\ E_y\end{pmatrix}, \tag{7}$$

$$\begin{pmatrix} E_x^s \\ E_y^s \end{pmatrix} = \left\{ -\begin{bmatrix} [G_4] & [G_5] \\ [G_5] & [G_6] \end{bmatrix} \begin{bmatrix} [\tau] & 0 \\ 0 & [\tau] \end{bmatrix} \right\} \begin{pmatrix} E_x \\ E_y \end{pmatrix}, \tag{8}$$

where (E_x^i) and (E_y^i) represent the *N*-element incident field column vectors and, (E_x) and (E_y) are the *N*-element total field column vectors. (E_x^s) and (E_y^s) denote the M-element scattered field column vectors. Here, M is the number of measurement points. The matrices [G_1], [G_2], and [G_3] are $N \times N$ square matrices. [G_4], [G_5], and [G_5] are $M \times N$ matrices. The element in matrices [G_i], i =1, 2, 3…6 can be obtained by tedious mathematic manipulation (see Appendix). [τ] is a $N \times N$ diagonal matrix whose diagonal element are formed from the permittivities of each cell minus one. [I] is an identity $N \times N$ matrix.

For the inverse scattering problem, the permittivity distribution of the dielectric objects is to be computed by the knowledge of the scattered field measured in region 1. In the inversion procedure, 2*N* different incident column vectors are used to illuminate the object, the follow equations are obtained,

$$[E_t^i] = [[G_{t1}][\tau_t] + [I_t]] \ [E_t], \tag{9}$$

$$[E_t^s] = -[G_{t2}] \ [\tau_t] \ [E_t] \tag{10}$$

where

$$[E_t^i] = \begin{bmatrix} E_x^i \\ E_y^i \end{bmatrix}, \quad [E_t] = \begin{bmatrix} E_x \\ E_y \end{bmatrix}, \quad [E_t^s] = \begin{bmatrix} E_x^s \\ E_y^s \end{bmatrix},$$

$$[G_{t1}] = \begin{bmatrix} [G_1] & [G_2] \\ [G_2] & [G_3] \end{bmatrix}, [G_{t2}] = \begin{bmatrix} [G_4] & [G_5] \\ [G_5] & [G_6] \end{bmatrix}$$

$$[\tau_t] = \begin{bmatrix} [\tau] & 0 \\ 0 & [\tau] \end{bmatrix}, \quad [I_t] = \begin{bmatrix} [I] & 0 \\ 0 & [I] \end{bmatrix},$$

Here, $[E_t^i]$ and $[E_t]$ are both $2N \times 2N$ matrices. $[E_t^s]$ is an $M \times 2N$ matrix. It is worth mentioning that other than matrix $[G_{t2}]$, the matrix $[G_{t1}][\tau_t] + [I_t]$ is always a well-posed one in any case, therefore we can first solve $[E_t^i]$ in equation (9) and substitute into equation (10), and then [τ_t] can be found by the following equation

$$[\Psi_t][\tau_t] = [\Phi_t] \tag{11}$$

where

$$[\Phi_t] = -[E_t^s][E_t^i]^{-1}$$

$$[\Psi_t] = [E_t^s][E_t^i]^{-1}[G_{t1}] + [G_{t2}]$$

From equation (11), all the diagonal elements in the matrix [τ] can be determined by comparing the element with the same subscripts which may be any row of both $[\Psi_t]$ and $[\Phi_t]$,

$$(\tau)_{nn} = \frac{(\Phi_t)_{mn}}{(\Psi_t)_{mn}}, \quad n \le N \tag{12a}$$

or

$$(\tau)_{(n-N)(n-N)} = \frac{(\Phi_t)_{mn}}{(\Psi_t)_{mn}}, \quad n \ge N+1. \tag{12b}$$

Then the permittivities of each cell can be obtained as follow,

$$\varepsilon_n = (\tau)_{nn} + 1. \tag{13}$$

Note that there are a total of 2M possible values for each element of τ. Therefore, the average value of these 2M data is computed and chosen as final reconstruction result in the simulation.

In the above derivation, the key problem is that the incident matrices $[E_t^i]$ must not be a singular matrix, i.e., all the incident column vectors that form the $[E_t^i]$ matrices, must be linearly unrelated. Thus, if the object is illuminated by a group of unrelated incident waves, it is possible to reconstruct the permittivity distribution of the objects. Note that when the number of cells becomes very large; it is difficult to make such a great number of independent measurements. In such a case, some regularization methods must be used to overcome the ill-posedness

III. NUMERICAL RESULTS

In this section, we report some numerical results obtained by computer simulations using the method described in section II. Consider a lossless three- layer structure ($\sigma_1 = \sigma_2 = \sigma_3 = 0$) and the width of the second layer is 0.2m. The permittivity in each region is characterized by $\varepsilon_1 = \varepsilon_0$, $\varepsilon_2 = 2.25\varepsilon_0$ and $\varepsilon_3 = \varepsilon_0$, respectively, as shown in Fig. 1. The frequency of the incident wave is chosen to be 3 GHz. The incident waves are generated by numerous groups of radiators operated simultaneously.

Each group of radiators is restricted to transmit a narrow-bandwidth pattern that can be implemented by antenna array techniques. By changing the beam direction and tuning the phase of each group of radiators, one can focus all the incident beams in turn at each cell of the object. This procedure is known as *Beam Focusing* [9]. Note that this focusing should be set when the scatterer is absent. Clearly, an incident matrix formed in this way is diagonally dominant and its inverse matrix exists. The measurement is taken from 0.4 m to -0.4 m in region 1 at equal spacing. The number of measurement points is set to be 9 for each illumination. For avoiding trivial inversion of finite dimensional problems, the discretization number for the direct problem is four times that for the inverse problem in our numerical simulation.

In the first example, the buried cylinder with a 70 ×

21 mm rectangular cross section is discretized into 20 × 6 cells, and the corresponding dielectric permittivities are plotted in Fig. 2. The model is characterized by simple step distribution of permittivity. Each cell has 3.5 × 3.5 mm cross-sections. The reconstructed permittivity distributions of the object are plotted in Fig. 3. The root-mean-square (RMS) error is about 0.9 %. It is apparent that the reconstruction is good.

In the second example, the buried cylinder with a 36 × 36 mm square cross section is discretized into 10 × 10 cells, and the corresponding dielectric permittivities are plotted in Fig. 4. The model is characterized by a four-layer contrast of permittivity. Each cell has 3 × 3 mm cross-sections. The reconstructed permittivity distributions of the object are plotted in Fig. 5. The root-mean-square (RMS) error is about 1.21 %. We can see the reconstruction is also good.

For investigating the effect of noise, we add to each complex scattered field a quantity b+cj,

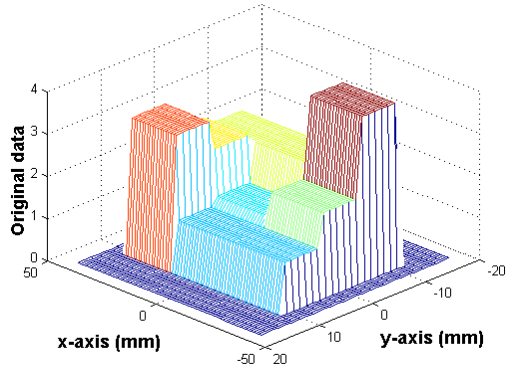

Fig. 2. Original relative permittivity distribution for example 1.

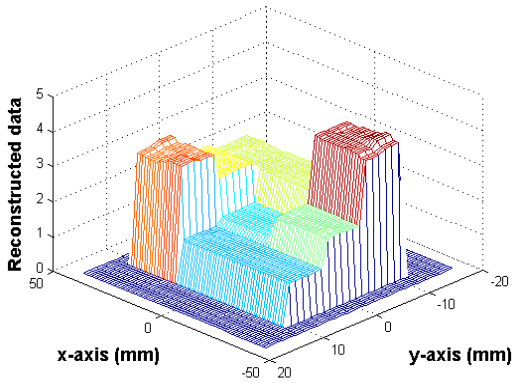

Fig. 3. Reconstructed relative permittivity distribution for example 1.

where b and c are independent random numbers having a Gaussian distribution over 0 to the noise level times the RMS value of the scattered field. The noise levels applied include 10^{-5}, 10^{-4}, 10^{-3}, 10^{-2}, and 10^{-1} in the simulations. The numerical results for examples 1 and 2 are plotted in Figs. 6 and 7, respectively. They show the effect of noise is tolerable for noise levels below 1%.

Our method depends on the condition number of $[E_t^i]$; that is, on having 2N unrelated measurements. The procedure will generally not work when the number of unknowns gets very large. This is due to the fact that it is difficult to make such a great number of measurements and make them all unrelated. As a result, the condition number of $[E_t^i]$ will become large while the number of unknowns is very large. In such a case, the regularization method should be employed to overcome the ill-posedness. For instance, the pseudoinverse transform techniques [7] can be applied for the inversion of the $[E_t^i]$ matrix.

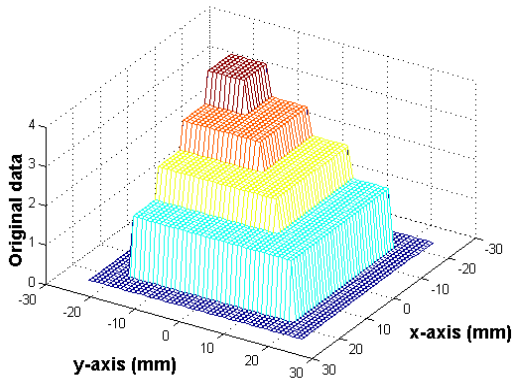

Fig. 4. Original relative permittivity distribution for example 2.

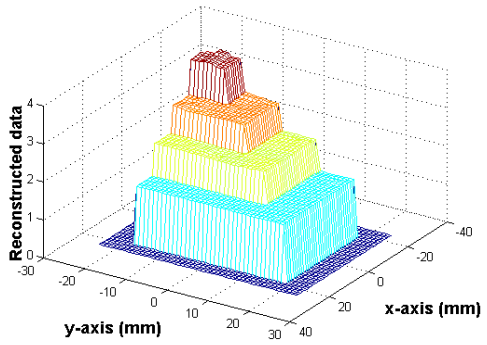

Fig. 5. Reconstructed relative permittivity distribution for example 2.

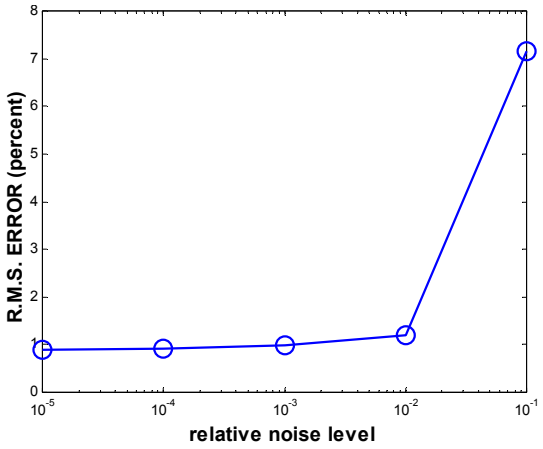

Fig. 6. Reconstructed error as a function of noise level for example 1.

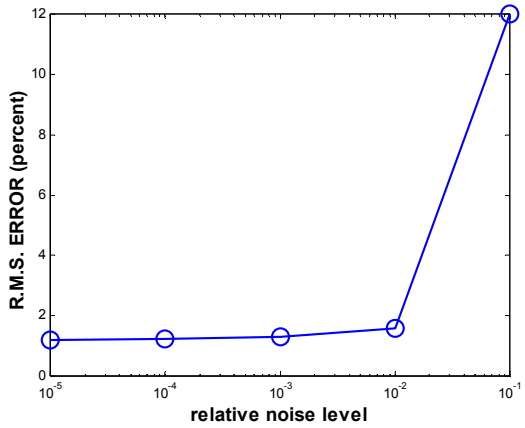

Fig. 7. Reconstructed error as a function of noise level for example 2.

IV. CONCLUSIONS

Imaging algorithm for TE case is more complicated than that for the TM case, due to the added difficulties in the polarization charges. Nevertheless, the polarization charges cannot be ignored for this two-dimensional problem and all three-dimensional problems. In this paper, an efficient algorithm for reconstructing the permittivity distribution of inhomogeneous dielectric cylinders buried in a slab medium, illuminated by TE waves, has been proposed. By properly arranging the direction of various unrelated waves, the difficulty of ill-posedness and nonlinearity is avoided. Thus, the permittivity distribution can be obtained by simple matrix operations. The moment method has been used to transform a set of integral equations into matrix form. Then these matrix equations are solved by the unrelated illumination method. Numerical simulation for imaging the permittivity distribution of an inhomogeneous dielectric cylinder buried in a slab medium has been carried out and good reconstruction has been obtained even in the presence of Gaussian noise in measured data. This algorithm is very effective and efficient, since no iteration is required.

APPENDIX

The element in the matrix $[G_1]$ can be written as

$$(G_3)_{mn} = \left[\left(\frac{\partial^2}{\partial x^2} + k_2^2\right)\cdot \iint_{cell\ n} G_2(x,y;x',y')dx'dy'\right]_{\substack{x=x_m\\y=y_m}}$$

where (x_m, y_m) is the observation point located in the center of the mth cell. For a sufficient small cell, we can replace the cell by a circular cell with the same cross section [20]. Let the equivalent radius of the nth circular cell be a_n. The $(G_1)_{mn}$ can be expressed in the following form

$$(G_3)_{mn} = \begin{cases} \left.\dfrac{\partial^2 G_s(x,y;x_n,y_n)}{\partial x^2}\right|_{\substack{x=x_m\\y=y_m}}\cdot \Delta S_n \\ +G_s(x_m,y_m;x_n,y_n)\cdot k_2^2\cdot \Delta S_n \\ +\dfrac{j\pi a_n J_1(k_2 a_n)}{2\rho_{mn}^3} k_2\rho_{mn}(y_m-y_n)^2 H_0^{(2)}(k_2\rho_{mn}) \\ +\left((x_m-x_n)^2-(y_m-y_n)^2\right)H_1^{(2)}(k_2\rho_{mn}), \quad m\neq n \\ \\ \left.\dfrac{\partial^2 G_s(x,y;x_n,y_n)}{\partial x^2}\right|_{\substack{x=x_m\\y=y_m}}\cdot \Delta S_n \\ +G_s(x_m,y_m;x_n,y_n)\cdot k_2^2\cdot \Delta S_n \\ +\dfrac{j}{4}\left[\pi k_2 a_n H_1^{(2)}(k_2 a_n) - 4j\right], \quad m=n \end{cases}$$

with $\rho_{mn} = \sqrt{(x_m-x_n)^2+(y_m-y_n)^2}$, where J_1 is Bessel function of the first order and (x_n, y_n) is the center of the cell n. ΔS_n denotes the area of the nth cell. Similarly,

$$(G_2)_{mn} = \begin{cases} \left.\dfrac{\partial^2 G_{2ss}(x,y;x_n,y_n)}{\partial x\partial y}\right|_{\substack{x=x_m\\y=y_m}}\cdot \Delta S_n \\ +\dfrac{j\pi a_n J_1(k_2 a_n)}{2\rho_{mn}^3}(x_m-x_n)(y_m-y_n)\times \\ 2H_1^{(2)}(k_2\rho_{mn}) - k_2\rho_{mn}H_0^{(2)}(k_2\rho_{mn}), \quad m\neq n \\ \\ 0, \quad m=n \end{cases}$$

$$
\left(G_3\right)_{mn}=\begin{cases}
\left.\dfrac{\partial^2 G_{2ss}\left(x,y;x_n,y_n\right)}{\partial y^2}\right|_{\substack{x=x_m\\ y=y_m}}\cdot\Delta S_n \\
+G_{2ss}\left(x_m,y_m;x_n,y_n\right)\cdot k_2^2\cdot\Delta S_n \\
+\dfrac{j\pi a_n J_1\left(k_2 a_n\right)}{2\rho_{mn}^3} \\
\times\begin{bmatrix} k_2\rho_{mn}\left(x_m-x_n\right)^2 \\ \times H_0^{(2)}\left(k_2\rho_{mn}\right) \\ +\begin{pmatrix}\left(y_m-y_n\right)^2 \\ -\left(x_m-x_n\right)^2\end{pmatrix} \\ \times H_1^{(2)}\left(k_2\rho_{mn}\right)\end{bmatrix}, & m\neq n \\
\left.\dfrac{\partial^2 G_{2ss}\left(x,y;x_n,y_n\right)}{\partial y^2}\right|_{\substack{x=x_m\\ y=y_m}}\cdot\Delta S_n \\
+G_{2ss}\left(x_m,y_m;x_n,y_n\right)\cdot k_2^2\cdot\Delta S_n \\
+\dfrac{j}{4}\left[\pi k_2 a_n H_1^{(2)}\left(k_2 a_n\right)-4j\right], & m=n
\end{cases}
$$

$$
\left(G_4\right)_{mn}=\left.\frac{\partial^2 G_{1s}\left(x,y;x_n,y_n\right)}{\partial x^2}\right|_{\substack{x=x_m\\ y=y_m}}\cdot\Delta S_n + G_{1s}\left(x_m,y_m;x_n,y_n\right)\cdot k_2^2\cdot\Delta S_n \quad ,
$$

$$
\left(G_5\right)_{mn}=\left.\frac{\partial^2 G_{1s}\left(x,y;x_n,y_n\right)}{\partial x^2}\right|_{\substack{x=x_m\\ y=y_m}}\cdot\Delta S_n + G_{1s}\left(x_m,y_m;x_n,y_n\right)\cdot k_2^2\cdot\Delta S_n \quad ,
$$

$$
\left(G_6\right)_{mn}=\left.\frac{\partial^2 G_{1s}\left(x,y;x_n,y_n\right)}{\partial y^2}\right|_{\substack{x=x_m\\ y=y_m}}\cdot\Delta S_n + G_{1s}\left(x_m,y_m;x_n,y_n\right)\cdot k_2^2\cdot\Delta S_n \quad .
$$

REFERENCES

[1] S. Caorsi, G.L. Gragnani, and M. Pastorino, "Numerical electromagnetic inverse-scattering solution for two-dimensional infinite dielectric cylinders buried in a lossy half-space," *IEEE Trans. Antennas Propagat.*, vol. AP-41, pp. 352 - 356, Feb. 1993.

[2] C. C. Chiu and Y. M. Kiang, "Inverse scattering of a buried conducting cylinder," *Inv. Prob.*, vol. 7, pp. 187 - 202, April 1991.

[3] C. C. Chiu and C. P. Huang, "Inverse scattering of dielectric cylinders buried in a half space," *Microwave and Optical Technology Letters*, vol. 13, pp. 96 - 99, Oct. 1996.

[4] F. Soldovieri and R. Persico, "Reconstruction of an embedded slab from multifrequency scattered field data under the distorted born approximation", *IEEE Trans. Antennas Propagat.*, vol. 52, pp. 2348 - 2356, Sept. 2004.

[5] O. M. Bucci, L. Crocco, T. Isernia, and V. Pascazio, "Inverse scattering problems with multifrequency data: reconstruction capabilities and solution strategies," *IEEE Trans. Geoscience and Remote Sensing*, vol. 38, pp. 1749 - 1756, July 2000.

[6] V. A. Mikhnev and P. Vainikainen, "Two-step inverse scattering method for one-dimensional permittivity profiles," *IEEE Trans. Antennas Propagat.*, vol. 48, pp. 293 - 298, Feb. 2000.

[7] M. M. Ney, A. M. Smith, and S. S. Stuchly, "A solution of electromagnetic imaging using pseudoinverse transformation," *IEEE Trans. Med. Imag.*, vol. MI-3, pp. 155 - 162, Dec. 1984.

[8] S. Caorsi, G. L. Gragnani, and M. Pastorino, "An approach to microwave imaging using a multiview Moment Method solution for a two-dimensional infinite cylinder," *IEEE Trans. Microwave Theory and Techniques*, vol. MTT-39, pp. 1062 - 1067, June 1991.

[9] W. Wang and S. Zhang, "Unrelated illumination method for electromagnetic inverse scattering of inhomogeneous lossy dielectric bodies," *IEEE Trans. Antennas Propagat.*, vol. AP-40, pp. 1292 - 1296, Nov. 1992.

[10] K. A. Nabulsi and D. G. Dudley, "A new approximation and a new measurable constraint for slab profile inversion," *IEEE Trans. on Geoscience and Remote Sensing*, vol. 34, no. 3, May 1996.

[11] N. Joachimowicz, C. Pichot, and J. P. Hugonin, "Inverse scattering: an iterative numerical method for electromagnetic imaging," *IEEE Trans. Antennas Propagat.*, vol. AP-39, pp. 1742 - 1752, Dec. 1991.

[12] G. P. Otto and W. C. Chew, "Inverse scattering of Hz waves using local shape function imaging: a T-Matrix formulation," *Int. J. Imaging Syst.*

Technol., vol. 5, pp. 22 - 27, 1994.
[13] C. C. Chiu and P. T. Liu, "Image reconstruction of a complex cylinder illuminated by TE waves," *IEEE Trans. Microwave Theory Tech.*, vol. 44, pp. 1921 - 1927, Oct. 1996.
[14] C. P. Chou and Y. W. Kiang, "Inverse scattering of dielectric cylinders by a cascaded TE-TM method," *IEEE Trans. Microwave Theory and Techniques*, pp. 1923 - 1930, vol. 47, Oct. 1999.
[15] C. C. Chiu and C. J. Lin, "Image reconstruction of buried uniaxial dielectric cylinders," *Journal of Electromagnetic Waves and Applications*, vol. 22, no. 2, pp. 97 - 112, Feb. 2002.
[16] C. C. Chiu and C. J. Lin, "Image reconstruction of buried dielectric cylinders by TE wave illumination," *Journal of Electromagnetic Waves and Applications*, vol. 16, no. 2, pp. 243 - 245, Feb. 2002.
[17] B. J. Kooij, "Contrast source inversion of a buried object in TE-scattering," *Antennas and Propagation Society International Symposium*, vol. 2, pp. 714 - 717, June 1998.
[18] J. R. Wait, *Electromagnetic Waves in Stratified Media,* Macmillan, New York, 1962.
[19] R. F. Harrington, "Field Computation by Moment Methods," *New York: Macmillan*, 1968.
[20] J. H. Richmond, "TE-wave scattering by a dielectric cylinder of arbitrary cross-session shape," *IEEE Trans. Antennas Propagat.*, vol. 14, pp. 460 - 464, July 1966.

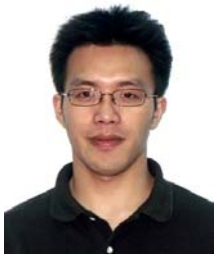

Chung-Hsin Huang was born in Tucheng, Taiwan, Republic of China, on February 1, 1980. He is currently working toward Ph.D. degree in the Department of Electrical Engineering, Tamkang University. His current research interests include numerical techniques in electromagnetics and indoor wireless communications.

Chien-Ching Chiu was born in Taoyuan, Taiwan, Republic of China, on January 23, 1963. He received the B.S.C.E. degree from National Chiao Tung University, Hsinchu, Taiwan, in 1985 and M.S.E.E. and Ph.D degrees from National Taiwan University, Taipei, Taiwan, in 1987 and 1991, respectively. From 1987 to1989, he served in the ROC Army Force as a communication officer. In 1992 he joined the faculty of the Department of Electrical Engineering, Tamkang University, where he is now an Professor. He was a visiting scholar at the MIT and University of Illinois, Urbana from 1998 to 1999. His current research interests include microwave imaging, numerical techniques in electromagnetics and indoor wireless communications.

Chun Jen Lin was born in Tamsui, Taiwan, Republic of China, on February 19, 1977. He is now a graduate student in the Department of Electrical Engineering, Tamkang University. His current research interests include numerical techniques in electromagnetics and indoor wireless communications

Ying-Feng Chen was born in Chai-Yi, Taiwan, Republic of China, on August 13, 1982. He is currently working toward M.S.E.E. degree in the Department of Electrical Engineering, Tamkang University. His current research interests include numerical techniques in electromagnetics and indoor wire less communications.

A Wavefront Launching Model for Predicting Channel Impulse Response

Michael Robinson

Syracuse Research Corporation
6225 Running Ridge Road
North Syracuse, NY 13212

Abstract **–** Maintaining the topology of an expanding wavefront surface allows for a simpler time-domain wave ray launching model that is free from the problems associated with ray catching. In addition to the usual ray location and direction information, the wavefront launching model stores which rays are adjacent in the advancing wavefront surface. The added information allows interpolation over this surface, so the model easily incorporates diffracted waves and power density changes from beam spreading.

I. INTRODUCTION

Ray tracing and launching methods have become popular for predicting wave propagation in complex geometries. Ray tracing methods trace "dominant" paths from source to receiver [1]. This can result in a large number of redundant rays being traced if the model has many receiver points. Ray launching reduces this computational burden by tracing a fixed number of rays from the source, which are followed as they scatter around the geometry. If they pass sufficiently close to a receiver point, they contribute to that receiver's response. This leads to the problem of "ray catching," where rays can be "double counted" at a receiver [2].

This paper describes a method of ray launching that avoids double counting by respecting the topological structure of the moving wavefront. Unlike ray catching, in which the wavefront is *extrapolated* to the receiver point, this method *interpolates* the wavefront to the receiver point. This avoids causing errors associated with extending the wavefront beyond its true extent. The topological information also allows accurate wavefront power densities to be computed purely from geometric considerations.

II. TOPOLOGICAL ASPECTS OF WAVEFRONT PROPAGATION

The aim of this paper is to present a method for computing the solution to the scalar wave equation in a region Ω, with a transmitted signal f,

$$\nabla^2 u - \frac{1}{c^2}\frac{\partial^2 u}{\partial t^2} = f(x,t),\ (x,t) \in \Omega \times \mathbb{R}^+ \qquad (1)$$

where the parameter c describes the wave propagation speed, which depends on the medium in which the wave propagates [3]. This equation can be used to predict electromagnetic wave propagation where polarization is not expected to be an issue, or in small-amplitude acoustic settings. In the case of acoustic waves, u describes the pressure at a given point, while for electromagnetic waves, it describes a component of the electric field vector. Typical indoor or outdoor urban environments do not show marked differences in electromagnetic wave propagation due to polarization, so it is reasonable to choose a component of the electric field parallel to the radiating elements [4].

A. Waves in Unbounded Media

When the spatial domain Ω is of odd dimension, Huygen's principle ensures that there are well-defined wavefronts [3]. In an unbounded spatial domain, where $\Omega = \mathbb{R}^3$, this is apparent from the Green's function of equation (1),

$$G_u(x,\xi,t,\tau) = \frac{\delta\left(|x-\xi| - c(t-\tau)\right)}{4\pi\left(|x-\xi| - c(t-\tau)\right)}. \qquad (2)$$

The locus of points where $G(x,\xi,t,\tau) \neq 0$ is called a "wavefront". In general, the "wavefront set" shall be defined as

$$W(\xi,\tau) = \left\{(x,t) \in \Omega \times \mathbb{R}^+ \,\middle|\, G(x,\xi,t,\tau) \neq 0\right\} \qquad (3)$$

where G is the Green's function relevant to the particular spatial geometry Ω. In unbounded media, the wavefront set does not change topologically with time; it is always spherical.

B. Reflecting Half-Space

If an infinite, flat boundary is introduced, the method of images leads to a new Green's function for equation (1),

$$G_h(x,\xi,t,\tau) = G_u(x,\xi,t,\tau) - G_u(x,\xi',t,\tau) \qquad (4)$$

where ξ' is the image of ξ reflected across the boundary. It is evident that the wavefront set of this Green's function does not undergo topological change. Like the unbounded case, it is always topologically equivalent to a sphere.

C. Diffraction and Topological Change

Diffraction causes the topology of the wavefront set to change in the vicinity of convex boundary edges. The wavefront set is no longer confined to a thin surface once diffraction occurs, due to dispersion. The Uniform Theory of Diffraction (UTD) predicts that diffracted wave power falls off like $t^{-3/2}$ at a given point (equation (16) of [5]). In light of this, it is reasonable to assume that the diffracted wave can be approximated by confining its power to the "leading edge" of the wavefront set. This removes the dispersive effects of diffraction, and makes diffracted waves easy to model with the wavefront approach. This approximation restricts the frequencies the model can accurately treat and introduces a small time delay error. Further, a scalar wave model ignores the polarization-dependent effects of electromagnetic wave diffraction. To mitigate these concerns, frequency- and polarization-specific diffraction coefficients must be chosen for the operating frequency and incident polarization. Alternatively, one may use empirical diffraction coefficients that explicitly ignore frequency, phase delay, and polarization [6].

Having motivated a non-dispersive scalar approximation for diffraction, we now look at how diffraction changes wavefront topology. Diffraction occurs when a wavefront crosses an edge in the boundary; wavefront points on one side of the edge are sent off at vastly different angles from those on the other side. The continuity of the wavefront is disrupted along such an edge, cutting the incident wavefront into two distinct pieces. This discontinuity is smoothed out by the introduction of a diffracted wave, as shown in Fig. 1. Using the UTD approximation, the edge begins to emit a diffracted wave when it is touched by an incident wavefront [5].

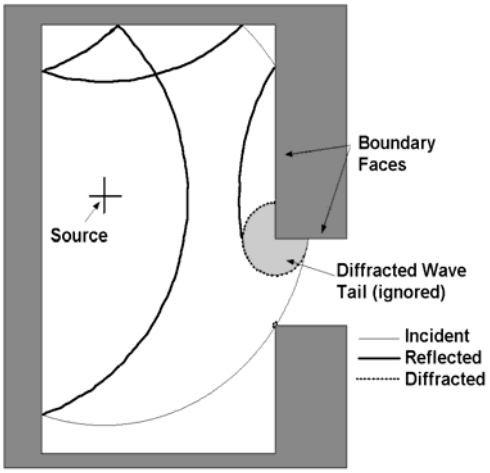

Fig. 1. An example of the topological changes of a wavefront: Waves near the left side of the room maintain their topology after being reflected at flat surfaces and concave corners. Waves at the convex corners (exit of the room) undergo a topology change as a distinct diffracted wave is created.

III. STORAGE OF TOPOLOGICAL INFORMATION

In the wavefront launching model, the wavefront set is sampled both in space and in time, resulting in a collection of discrete points. A unit vector representing the motion of the wavefront is tied to each of these points and fills the same role as rays do in ray tracing or launching models. The topology of the wavefront is represented by maintaining links between adjacent points both in space and in time. This allows new points or rays to be interpolated anywhere in the wavefront set.

A group of four wavefront points that form a link-connected loop in space is called a "patch". Two patches that are linked in the time dimension are called a "cube". (See Fig. 2) It is often of interest to know if a wavefront crosses a particular point in space $\boldsymbol{x}$ over a given interval of time $[t_0, t_1]$: that is, if $\boldsymbol{x}$ belongs to the set $W(\xi,\tau)\cap\Omega\times[t_0,t_1]$. This problem may be solved computationally by checking if the point of interest can be found in any of the wavefront's cubes that are valid on the time interval of interest. This eliminates the problem of ray-catching, since the wavefront is interpolated rather than extrapolated to the point. Further, the incident power density at any point on the patch is easy to calculate: the wave power at the four points on the patch is smoothly distributed over the surface of the patch.

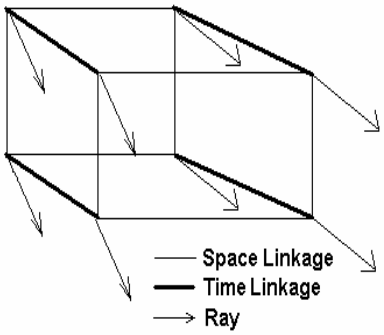

Fig. 2. Points, rays, and linkages of a "cube".

IV. PROPAGATION OF THE WAVEFRONT

The wavefront model generates the wavefront set by propagating snapshots of the wavefront at earlier times. It uses two previous snapshots (points, rays, and spatial linkages) W_{i-1} and W_i to generate a new one W_{i+1}, where each W_n is valid over $t \in [t_{n-1}, t_n]$. Where rays do not cross a diffracting edge, they are propagated according to the usual rules of ray tracing. (See, for example, [1] or [2])

When a point on the wavefront comes near a diffracting edge, the wavefront model checks to see if any of the cubes containing that point intersect the edge. If so, then a new diffracted wavefront will be launched from that edge. The incident wavefront's rays will be unaffected by

the diffracting edge, although the links of the incident wavefront will be broken along the edge.

The structure of the diffracted wave is created from the incident wave by decomposing the patches incident on the edge. It is important to realize that a diffracted wave develops as different patches of the incident wavefront cross the edge at different times. It is important to allow these patches to duplicate points and rays along the edges if there is no explicit topological linkage between them. That way, the diffracted wave can form over several time steps. (This is not the most memory efficient approach, but it is simple and fast.)

Once the patches for generating the diffracted wave are found, each one is used to create a family of diffracted wave patches. Since the diffracting edge generates the diffracted wave, the diffracted wave patches must be launched from that edge. The launch points are found by projecting each incident patch onto the edge. To simplify matters geometrically, the two points that are farthest apart are used as launch points for the diffracted patches. Then the rays are built by decomposing them into components. The ray component parallel to the edge is computed by projecting the incident ray onto the edge,

$$\frac{\mathbf{e}\bullet\mathbf{v}}{\|\mathbf{e}\|^2} \tag{5}$$

where **v** is the incident ray, and **e** is parallel to the edge.

The components normal to the edge are built by the following formula,

$$\mathrm{F}(\theta)=\frac{\mathrm{t}_1\cos\theta+\mathrm{t}_2\sin\theta}{\left\|\mathrm{t}_1\cos\theta+\mathrm{t}_2\sin\theta\right\|} \tag{6}$$

where the parameter θ is controlled by

$$\theta\in\begin{cases}\left[\frac{\pi}{2},2\pi\right] & \text{if} \quad \mathrm{t}_1\bullet\mathrm{t}_1+\mathrm{t}_1\bullet\mathrm{t}_2>0 \\ & \text{and} \\ \left[0,\frac{\pi}{2}\right] & \text{otherwise} \quad \mathrm{t}_2\bullet\mathrm{t}_2+\mathrm{t}_1\bullet\mathrm{t}_2>0\end{cases} \tag{7}$$

and the vectors $\boldsymbol{t_1}$ and $\boldsymbol{t_2}$ are normal to **e** and contained in the faces adjacent to the edge. Then the ray directions can be computed as,

$$\mathrm{D}(\theta)=\left\|\mathrm{v}-\frac{\mathrm{e}\bullet\mathrm{v}}{\|\mathrm{e}\|^2}\mathrm{e}\right\|\mathrm{F}(\theta)+\frac{\mathrm{e}\bullet\mathrm{v}}{\|\mathrm{e}\|^2}\mathrm{e}. \tag{8}$$

Observe that by sweeping θ over the range of values specified in equation (7), a family of diffracted patches is generated for the incident patch. The diffracted wave power levels are then assigned to each point using UTD [5] or a similar approximation [6], and the diffracted wave topology is assembled using the topology induced by D(θ).

V. INSTRUMENTATION

One of the most attractive features of ray models is that the impulse response of the channel is easy to compute [1]. From this, useful parameters such as the RMS delay spread can be extracted to yield predictions of coverage. The ray tracing, ray launching, and the wavefront launching methods sample the impulse response at given locations in space. The impulse response data contains wavefront arrival time, direction, and power density. The arrival direction allows the user to explore the use of directional antennas to cure multipath problems.

VI. RESULTS

A. Discussion of Images

Figure 3 shows the results of this model on a two room geometry. Despite appearances, the model is three dimensional. There is a single source, which appears near the center of the left room. This source emits a uniformly distributed spherical wavefront, and so is a simple model of an acoustic source or a electrically small antenna. Each of the walls is perfectly reflective, and there is a 3 dB attenuating window in the middle of the hallway. The plots on the left side of the figure are peak power density plots, and those on the right are RMS delay spread. The left plots indicate the signal strength of the dominant path. The RMS delay spread plots give an indication of multipath.

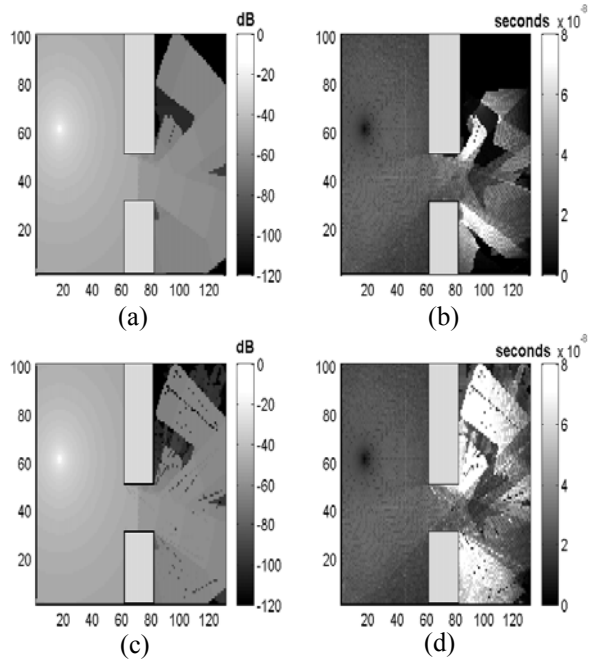

Fig. 3. (a) Relative power density (dB) without diffraction, (b) RMS delay spread (s) without diffraction, and (c) Relative power density (dB) with diffraction, (d) RMS delay spread (s) with diffraction.

The simulation was stopped after most of the signal had entered the right room, but before it reflected too many times. One can still see the wavefront structure in the upper half of the right room. It is evident that the diffracted waves contribute strongly to the multipath situation in the shadowed region of the right room. A strong diffracted wave reaches into the shadowed region well before the specular components from the incident wave. This results in a large delay spread, and would be problematic for wideband digital communications. Near the transmitter, the coherence bandwidth is roughly 16 MHz. In the shadowed region, the coherence bandwidth drops to 6 MHz, which represents a 266 % loss in available bandwidth.

B. Discretization Problems

The wavefront method avoids most discretization problems associated with ray launching, since it interpolates the wavefront between points on the wavefront set. However, discretization becomes evident when using a diffraction model, since diffracting edges cut apart incident wavefronts. If the wavefront is not sampled with enough points, these cuts will become jagged. This leaves gaps between the diffracted wavefront and the incident wavefront, which result in lost impulse response data. Some of these gaps can be seen in the lower plots of Fig. 3, where they look a little like streaky noise. The best solution for this problem is to resample incident wavefronts along a diffracting edge so that the cuts do not become jagged.

VII. FUTURE WORK

A. Ray Resampling

Like all numerical solvers for the wave equation, the wavefront model loses accuracy after a long period of simulation. This occurs when adjacent points become quite far apart. The wavefront set gradually becomes poorly sampled, and interpolating points on it is likely to be inaccurate. It seems that this problem could be alleviated by interpolating new points and rays onto the surface of the wavefront as time elapses. This would help avoid the discretization that appears in the diffraction results, and would also yield more accurate power density calculations.

B. Vector-Wave Models

The model presented here is a scalar model, which is assumed to be a good approximation of electromagnetic phenomena even though electromagnetic waves are polarized. The reflection and diffraction coefficients of many materials respond differently to waves of different polarization, so a vector wave formulation would allow the wavefront model to handle these sorts of materials.

VIII. CONCLUSIONS

Maintaining the topology of the wavefront allows for a simpler time-domain wave propagation model that is free from the problems associated with ray catching. Using interpolation over the surface of the wavefront, this model naturally incorporates diffracted waves and power density changes from beam spreading. The measurable quantities are automatically power densities, which do not need to be weighted by ray counts. It is also possible that this model can compensate for errors associated with discretization of the signal into rays, by carefully interpolating them over the wavefront. However, this particular aspect of the model has not been investigated.

REFERENCES

[1] H. R. Anderson, “A ray-tracing propagation model for digital broadcast systems in urban areas,” *IEEE Transactions on Broadcasting*, vol. 39, no. 3, pp. 309–317, 1993.

[2] G. Durgin, N. Patwari, and T. S. Rappaport, “Improved 3d ray launching method for wireless propagation prediction,” *Electronics Letters*, vol. 33, no. 16, pp. 1412–1413, 1997.

[3] L. C. Evans, *Partial Differential Equations*, American Mathematical Society, 1998.

[4] D. Chizhik, J. Ling, and R. A. Valenzuela, “The effect of electric field polarization on indoor propagation,” *Proc. Int. Conf. Universal Personal Communications (ICUPC 98)*, Florence, Italy, pp. 459–462, 1998.

[5] T. W. Veruttipong, “Time domain version of the uniform GTD,” *IEEE Transactions on Antennas and Propagation*, vol. 38, no. 11, pp. 1757–1764, Nov. 1990.

[6] G. Wölfle, R. Hoppe, T. Binzer, and F. M. Landstorfer, “Radio network planning and propagation models for urban and indoor wireless communication networks,” *Millenium Conference on Antennas and Propagation (AP2000)*, Davos, Switzerland, April 2000.

Michael Robinson is a graduate student in the Center for Applied Mathematics at Cornell University, and also works part-time at Syracuse Research Corporation. He received his BS in Electrical Engineering and MS in Mathematics at Rensselaer Polytechnic Institute, in 2002 and 2003, respectively. His research interests involve using topological information to understand and simplify the solution of differential equations.

2007 INSTITUTIONAL MEMBERS

AUSTRALIAN DEFENCE LIBRARY
Northcott Drive
Canberra, A.C.T. 2600 Australia

BAE SYSTEMS
W. Hanningfield Road
Technology Center Library
Great Baddow, Chelmsford
UK CM2 8HN

BEIJING BOOK COMPANY, INC
701 E Lindon Ave.
Linden, NJ 07036-2495

DARTMOUTH COLL-FELDBERG LIB
6193 Murdough Center
Hanover, NH 03755-3560

DSTO-DSTORL EDINBURGH
Jets AU/33851-99, PO Box 562
Milsons Point, NSW
Australia 1565

DTIC-OCP/LIBRARY
8725 John J. Kingman Rd. Ste 0944
Ft. Belvoir, VA 22060-6218

ELLEDIEMME SRL
C.P. 69 Poste S. Silvestro
Roma, Italy 00187

ELSEVIER
Bibliographic Databases
PO Box 2227
Amsterdam, Netherlands 1000 CE

ENGINEERING INFORMATION, INC
PO Box 543
Amsterdam, Netherlands 1000 Am

ETSE TELECOMUNICACION
Biblioteca, Campus Lagoas
Vigo, 36200 Spain

FGAN-FHR
Neuenahrerstrasse 20
Wachtberg, Germany 53343

FLORIDA INTERNATIONAL UNIV
10555 W. Flagler Street
Miami, FL 33174

GEORGIA TECH LIBRARY
225 North Avenue, NW
Atlanta, GA 30332-0001

HANYANG UNIVERSITY
Paiknam Academic Info. Ctr Library
17 Haengdang-Dong
Seongdong-Ku
Seoul, South Korea 133-791

HRL LABS, RESEARCH LIBRARY
3011 Malibu Canyon
Malibu, CA 90265

IEE INSPEC/Acquisitions Section
Michael Faraday House
6 Hills Way
Stevenage, Herts UK SG1 2AY

INSTITUTE FOR SCIENTIFIC INFO.
Publication Processing Dept.
3501 Market St.
Philadelphia, PA 19104-3302

IPS RADIO & SPACE SERVICES
PO Box 1386
Haymarket NSW Australia 1240

ISRAEL AIRCRAFT INDUSTRIES
Ben-Gurion Airport
70100 Israel

LEMA-EPFL
ELB-ECUBLEMS
Lausanne, Switzerland
CH-1020

LIBRARY – DRDC OTTAWA
3701 Carling Avenue
Ottawa, Ontario, Canada K1A OZ4

LIBRARY of CONGRESS
Reg. Of Copyrights
Attn: 40T Deposits
Washington DC, 20559

LINDA HALL LIBRARY
5109 Cherry Street
Kansas City, MO 64110-2498

MISSISSIPPI STATE UNIV LIBRARY
PO Box 9570Mississippi State, MS
39762

MIT LINCOLN LABORATORY
Periodicals Library
244 Wood Street
Lexington, MA 02420

NAVAL POSTGRADUATE SCHOOL
Attn:J. Rozdal/411 Dyer Rd./ Rm 111
Monterey, CA 93943-5101

NAVAL RESEARCH LABORATORY
Code 3516
4555 Overlook Avenue SW
Washington, DC 20375-5334

NDL KAGAKU
C/0 KWE-ACCESS
PO Box 300613 (JFK A/P)
Jamaica, NY 11430-0613

OHIO STATE UNIVERSITY
1320 Kinnear Road
Columbus, OH 43212

OVIEDO LIBRARY
PO BOX 830679
Birmingham, AL 35283

PENN STATE UNIVERSITY
126 Paterno Library
University Park, PA 16802-1808

PHILIPS RESEARCH LABORATORY
Cross Oak Lane, Stella Cox
Salfords, Redhill
UK RH1 5HA

RENTON TECH LIBRARY/BOEING
PO BOX 3707
SEATTLE, WA 98124-2207

SOUTHWEST RESEARCH INSTITUTE
6220 Culebra Road
San Antonio, TX 78238

SWETS INFORMATION SERVICES
160 Ninth Avenue, Suite A
Runnemede, NJ 08078

TECHNISCHE UNIV. DELFT
Mekelweg 4, Delft, Holland, 2628 CD
Netherlands

TELSTRA
TRL/M2/770 Blackburn Road
Clayton, Victoria, Australia 3168

TIB & UNIV. BIB. HANNOVER
DE/5100/G1/0001
Welfengarten 1B
Hannover, Germany 30167

TU DARMSTADT
Schlossgartenstrasse 8
Darmstadt, Hessen
Germany D-64289

UNIV OF CENTRAL FLORIDA LIB.
4000 Central Florida Boulevard
Orlando, FL 32816-8005

UNIV OF COLORADO LIBRARY
Campus Box 184
Boulder, CO 80309-0184

UNIVERSITY OF MISSISSIPPI
John Davis Williams Library
PO Box 1848
University, MS 38677-1848

UNIV OF MISSOURI-ROLLA LIB.
1870 Miner Circle
Rolla, MO 65409-0001

UNIV POL DE CARTAGENE
PO Box 830470
Birmingham, AL 35283

USAE ENG. RES. & DEV. CENTER
Attn: Library/Journals
72 Lyme Road
Hanover, NH 03755-1290

ACES COPYRIGHT FORM

This form is intended for original, previously unpublished manuscripts submitted to ACES periodicals and conference publications. The signed form, appropriately completed, MUST ACCOMPANY any paper in order to be published by ACES. PLEASE READ REVERSE SIDE OF THIS FORM FOR FURTHER DETAILS.

TITLE OF PAPER:

AUTHORS(S)

PUBLICATION TITLE/DATE:

RETURN FORM TO:

Dr. Atef Z. Elsherbeni
University of Mississippi
Dept. of Electrical Engineering
Anderson Hall Box 13
University, MS 38677 USA

PART A - COPYRIGHT TRANSFER FORM

(NOTE: Company or other forms may not be substituted for this form. U.S. Government employees whose work is not subject to copyright may so certify by signing Part B below. Authors whose work is subject to Crown Copyright may sign Part C overleaf).

The undersigned, desiring to publish the above paper in a publication of ACES, hereby transfer their copyrights in the above paper to The Applied Computational Electromagnetics Society (ACES). The undersigned hereby represents and warrants that the paper is original and that he/she is the author of the paper or otherwise has the power and authority to make and execute this assignment.

Returned Rights: In return for these rights, ACES hereby grants to the above authors, and the employers for whom the work was performed, royalty-free permission to:

1. Retain all proprietary rights other than copyright, such as patent rights.
2. Reuse all or portions of the above paper in other works.
3. Reproduce, or have reproduced, the above paper for the author's personal use or for internal company use provided that (a) the source and ACES copyright are indicated, (b) the copies are not used in a way that implies ACES endorsement of a product or service of an employer, and (c) the copies per se are not offered for sale.
4. Make limited distribution of all or portions of the above paper prior to publication.
5. In the case of work performed under U.S. Government contract, ACES grants the U.S. Government royalty-free permission to reproduce all or portions of the above paper, and to authorize others to do so, for U.S. Government purposes only.

ACES Obligations: In exercising its rights under copyright, ACES will make all reasonable efforts to act in the interests of the authors and employers as well as in its own interest. In particular, ACES REQUIRES that:

1. The consent of the first-named author be sought as a condition in granting re-publication permission to others.
2. The consent of the undersigned employer be obtained as a condition in granting permission to others to reuse all or portions of the paper for promotion or marketing purposes.

In the event the above paper is not accepted and published by ACES or is withdrawn by the author(s) before acceptance by ACES, this agreement becomes null and void.

AUTHORIZED SIGNATURE — TITLE (IF NOT AUTHOR)

EMPLOYER FOR WHOM WORK WAS PERFORMED — DATE FORM SIGNED

Part B - U.S. GOVERNMENT EMPLOYEE CERTIFICATION

(NOTE: if your work was performed under Government contract but you are not a Government employee, sign transfer form above and see item 5 under Returned Rights).

This certifies that all authors of the above paper are employees of the U.S. Government and performed this work as part of their employment and that the paper is therefor not subject to U.S. copyright protection.

AUTHORIZED SIGNATURE — TITLE (IF NOT AUTHOR)

NAME OF GOVERNMENT ORGANIZATION — DATE FORM SIGNED

PART C - CROWN COPYRIGHT

(NOTE: ACES recognizes and will honor Crown Copyright as it does U.S. Copyright. It is understood that, in asserting Crown Copyright, ACES in no way diminishes its rights as publisher. Sign only if *ALL* authors are subject to Crown Copyright).

This certifies that all authors of the above Paper are subject to Crown Copyright. (Appropriate documentation and instructions regarding form of Crown Copyright notice may be attached).

AUTHORIZED SIGNATURE TITLE OF SIGNEE

NAME OF GOVERNMENT BRANCH DATE FORM SIGNED

Information to Authors

ACES POLICY

ACES distributes its technical publications throughout the world, and it may be necessary to translate and abstract its publications, and articles contained therein, for inclusion in various compendiums and similar publications, etc. When an article is submitted for publication by ACES, acceptance of the article implies that ACES has the rights to do all of the things it normally does with such an article.

In connection with its publishing activities, it is the policy of ACES to own the copyrights in its technical publications, and to the contributions contained therein, in order to protect the interests of ACES, its authors and their employers, and at the same time to facilitate the appropriate re-use of this material by others.

The new United States copyright law requires that the transfer of copyrights in each contribution from the author to ACES be confirmed in writing. It is therefore necessary that you execute either Part A-Copyright Transfer Form or Part B-U.S. Government Employee Certification or Part C-Crown Copyright on this sheet and return it to the Managing Editor (or person who supplied this sheet) as promptly as possible.

CLEARANCE OF PAPERS

ACES must of necessity assume that materials presented at its meetings or submitted to its publications is properly available for general dissemination to the audiences these activities are organized to serve. It is the responsibility of the authors, not ACES, to determine whether disclosure of their material requires the prior consent of other parties and if so, to obtain it. Furthermore, ACES must assume that, if an author uses within his/her article previously published and/or copyrighted material that permission has been obtained for such use and that any required credit lines, copyright notices, etc. are duly noted.

AUTHOR/COMPANY RIGHTS

If you are employed and you prepared your paper as a part of your job, the rights to your paper initially rest with your employer. In that case, when you sign the copyright form, we assume you are authorized to do so by your employer and that your employer has consented to all of the terms and conditions of this form. If not, it should be signed by someone so authorized.

NOTE RE RETURNED RIGHTS: Just as ACES now requires a signed copyright transfer form in order to do "business as usual", it is the intent of this form to return rights to the author and employer so that they too may do "business as usual". If further clarification is required, please contact: The Managing Editor, R. W. Adler, Naval Postgraduate School, Code EC/AB, Monterey, CA, 93943, USA (408)656-2352.

Please note that, although authors are permitted to re-use all or portions of their ACES copyrighted material in other works, this does not include granting third party requests for reprinting, republishing, or other types of re-use.

JOINT AUTHORSHIP

For jointly authored papers, only one signature is required, but we assume all authors have been advised and have consented to the terms of this form.

U.S. GOVERNMENT EMPLOYEES

Authors who are U.S. Government employees are not required to sign the Copyright Transfer Form (Part A), but any co-authors outside the Government are.

Part B of the form is to be used instead of Part A only if all authors are U.S. Government employees and prepared the paper as part of their job.

NOTE RE GOVERNMENT CONTRACT WORK: Authors whose work was performed under a U.S. Government contract but who are not Government employees are required so sign Part A-Copyright Transfer Form. However, item 5 of the form returns reproduction rights to the U. S. Government when required, even though ACES copyright policy is in effect with respect to the reuse of material by the general public.

APPLIED COMPUTATIONAL ELECTROMAGNETICS SOCIETY JOURNAL
http://aces.ee.olemiss.edu

INFORMATION FOR AUTHORS

PUBLICATION CRITERIA

Each paper is required to manifest some relation to applied computational electromagnetics. **Papers may address general issues in applied computational electromagnetics, or they may focus on specific applications, techniques, codes, or computational issues.** While the following list is not exhaustive, each paper will generally relate to at least one of these areas:

1. **Code validation.** This is done using internal checks or experimental, analytical or other computational data. Measured data of potential utility to code validation efforts will also be considered for publication.

2. **Code performance analysis.** This usually involves identification of numerical accuracy or other limitations, solution convergence, numerical and physical modeling error, and parameter tradeoffs. However, it is also permissible to address issues such as ease-of-use, set-up time, run time, special outputs, or other special features.

3. **Computational studies of basic physics.** This involves using a code, algorithm, or computational technique to simulate reality in such a way that better, or new physical insight or understanding, is achieved.

4. **New computational techniques** or new applications for existing computational techniques or codes.

5. **"Tricks of the trade"** in selecting and applying codes and techniques.

6. **New codes, algorithms, code enhancement, and code fixes.** This category is self-explanatory, but includes significant changes to existing codes, such as applicability extensions, algorithm optimization, problem correction, limitation removal, or other performance improvement. **Note: Code (or algorithm) capability descriptions are not acceptable, unless they contain sufficient technical material to justify consideration.**

7. **Code input/output issues.** This normally involves innovations in input (such as input geometry standardization, automatic mesh generation, or computer-aided design) or in output (whether it be tabular, graphical, statistical, Fourier-transformed, or otherwise signal-processed). Material dealing with input/output database management, output interpretation, or other input/output issues will also be considered for publication.

8. **Computer hardware issues.** This is the category for analysis of hardware capabilities and limitations of various types of electromagnetics computational requirements. Vector and parallel computational techniques and implementation are of particular interest.

Applications of interest include, but are not limited to, antennas (and their electromagnetic environments), networks, static fields, radar cross section, inverse scattering, shielding, radiation hazards, biological effects, biomedical applications, electromagnetic pulse (EMP), electromagnetic interference (EMI), electromagnetic compatibility (EMC), power transmission, charge transport, dielectric, magnetic and nonlinear materials, microwave components, MEMS, RFID, and MMIC technologies, remote sensing and geometrical and physical optics, radar and communications systems, sensors, fiber optics, plasmas, particle accelerators, generators and motors, electromagnetic wave propagation, non-destructive evaluation, eddy currents, and inverse scattering.

Techniques of interest include but not limited to frequency-domain and time-domain techniques, integral equation and differential equation techniques, diffraction theories, physical and geometrical optics, method of moments, finite differences and finite element techniques, transmission line method, modal expansions, perturbation methods, and hybrid methods.

Where possible and appropriate, authors are required to provide statements of quantitative accuracy for measured and/or computed data. This issue is discussed in "Accuracy & Publication: Requiring, quantitative accuracy statements to accompany data," by E. K. Miller, *ACES Newsletter,* Vol. 9, No. 3, pp. 23-29, 1994, ISBN 1056-9170.

SUBMITTAL PROCEDURE

All submissions should be uploaded to ACES server through ACES web site (http://aces.ee.olemiss.edu) by using the upload button, journal section. Only pdf files are accepted for submission. The file size should not be larger than 5MB, otherwise permission from the Editor-in-Chief should be obtained first. Automated acknowledgment of the electronic submission, after the upload process is successfully completed, will be sent to the corresponding author only. It is the responsibility of the corresponding author to keep the remaining authors, if applicable, informed. Email submission is not accepted and will not be processed.

PAPER FORMAT (INITIAL SUBMISSION)

The preferred format for initial submission manuscripts is 12 point Times Roman font, single line spacing and single column format, with 1 inch for top, bottom, left, and right margins. Manuscripts should be prepared for standard 8.5x11 inch paper.

EDITORIAL REVIEW

In order to ensure an appropriate level of quality control, papers are peer reviewed. They are reviewed both for

technical correctness and for adherence to the listed guidelines regarding information content and format.

PAPER FORMAT (FINAL SUBMISSION)

Only camera-ready electronic files are accepted for publication. The term **"camera-ready" means that the material is neat, legible, reproducible, and in accordance with the final version format listed below.**

The following requirements are in effect for the final version of an ACES Journal paper:

1. The paper title should not be placed on a separate page. The title, author(s), abstract, and (space permitting) beginning of the paper itself should all be on the first page. The title, author(s), and author affiliations should be centered (center-justified) on the first page. The title should be of font size 16 and bolded, the author names should be of font size 12 and bolded, and the author affiliation should be of font size 12 (regular font, neither italic nor bolded).

2. An abstract is required. The abstract should be a brief summary of the work described in the paper. It should state the computer codes, computational techniques, and applications discussed in the paper (as applicable) and should otherwise be usable by technical abstracting and indexing services. The word "Abstract" has to be placed at the left margin of the paper, and should be bolded and italic. It also should be followed by a hyphen (—) with the main text of the abstract starting on the same line.

3. All section titles have to be centered and all the title letters should be written in caps. The section titles need to be numbered using roman numbering (I. II. ….)

4. Either British English or American English spellings may be used, provided that each word is spelled consistently throughout the paper.

5. Internal consistency of references format should be maintained. As a guideline for authors, we recommend that references be given using numerical numbering in the body of the paper (with numerical listing of all references at the end of the paper). The first letter of the authors' first name should be listed followed by a period, which in turn, followed by the authors' complete last name. Use a coma (,) to separate between the authors' names. Titles of papers or articles should be in quotation marks (" "), followed by the title of journal, which should be in italic font. The journal volume (vol.), issue number (no.), page numbering (pp.), month and year of publication should come after the journal title in the sequence listed here.

6. Internal consistency shall also be maintained for other elements of style, such as equation numbering. As a guideline for authors who have no other preference, we suggest that equation numbers be placed in parentheses at the right column margin.

7. The intent and meaning of all text must be clear. For authors who are not masters of the English language, the ACES Editorial Staff will provide assistance with grammar (subject to clarity of intent and meaning). However, this may delay the scheduled publication date.

8. Unused space should be minimized. Sections and subsections should not normally begin on a new page.

ACES reserves the right to edit any uploaded material, however, this is not generally done. It is the author(s) responsibility to provide acceptable camera-ready pdf files. Incompatible or incomplete pdf files will not be processed for publication, and authors will be requested to re-upload a revised acceptable version.

COPYRIGHTS AND RELEASES

Each primary author must sign a copyright form and obtain a release from his/her organization vesting the copyright with ACES. Copyright forms are available at ACES, web site (http://aces.ee.olemiss.edu). To shorten the review process time, the executed copyright form should be forwarded to the Editor-in-Chief immediately after the completion of the upload (electronic submission) process. Both the author and his/her organization are allowed to use the copyrighted material freely for their own private purposes.

Permission is granted to quote short passages and reproduce figures and tables from and ACES Journal issue provided the source is cited. Copies of ACES Journal articles may be made in accordance with usage permitted by Sections 107 or 108 of the U.S. Copyright Law. This consent does not extend to other kinds of copying, such as for general distribution, for advertising or promotional purposes, for creating new collective works, or for resale. The reproduction of multiple copies and the use of articles or extracts for commercial purposes require the consent of the author and specific permission from ACES. Institutional members are allowed to copy any ACES Journal issue for their internal distribution only.

PUBLICATION CHARGES

All authors are allowed for 8 printed pages per paper without charge. Mandatory page charges of $75 a page apply to all pages in excess of 8 printed pages. Authors are entitled to one, free of charge, copy of the journal issue in which their paper was published. Additional reprints are available for a nominal fee by submitting a request to the managing editor or ACES Secretary.

Authors are subject to fill out a one page over-page charge form and submit it online along with the copyright form before publication of their manuscript.

ACES Journal is abstracted in INSPEC, in Engineering Index, DTIC, Science Citation Index Expanded, the Research Alert, and to Current Contents/Engineering, Computing & Technology.